



DOCTORAL THESIS

Adsorption and degradation of water pollutants on TiO₂

Author:
Filippo BALZARETTI

First Reviewer:
Dr. Susan KÖPPEN
Second Reviewer:
Prof. Dr. Thorsten
KLÜNER

*A thesis submitted in fulfillment of the requirements
for the degree of Doctor rerum naturalium in Physics*

in the

Faculty of Physics and Electrical Engineering
UNIVERSITY OF BREMEN

Hybrid
Materials
Interfaces Group 

Day of oral examination: 11 November 2021

Declaration of Authorship

I, Filippo BALZARETTI, declare that this thesis titled *Adsorption and degradation of water pollutants on TiO₂* and the work presented in it are my own. I confirm that:

- This work was done wholly or mainly while in candidature for a research degree at this University.
- Where any part of this thesis has previously been submitted for a degree or any other qualification at this University or any other institution, this has been clearly stated.
- Where I have consulted the published work of others, this is always clearly attributed.
- Where I have quoted from the work of others, the source is always given. With the exception of such quotations, this thesis is entirely my own work.
- I have acknowledged all main sources of help.
- Where the thesis is based on work done by myself jointly with others, I have made clear exactly what was done by others and what I have contributed myself.

Signed:

Date:

Thoroughly conscious ignorance is the prelude to every real advance in science.

James Clerk Maxwell

Abstract

Given the enormous presence of organic pollutants in aquatic environments, it is essential to study an effective way to eliminate them. Titanium dioxide (TiO_2) is one of the most widely used materials for promoting photocatalytic activity. Thanks to its oxidation-reduction reactions can be generated, capable of degrading adsorbant contaminants into substances that are no longer harmful. Experimental data indicate the feasibility of this process, but do not explain the specific way in which the functional groups of pollutants interact with the surface of TiO_2 . Computational chemistry must therefore take note of this and support the research from an atomistic point of view.

In this work, the problem is addressed through several levels of theory that allow the development of a top-down protocol. The dynamic evolution of nine water pollutants is investigated on an amorphous TiO_2 surface in order to observe their main adsorption modes. Among them glyphosate (GGG), a very powerful herbicide harmful for our health, shows a force of attraction much higher than that of the other molecules. Its adsorption and possible degradation are then studied in detail on a pristine surface rutile-(110), obtaining results in line with experiments. The interaction of water with two reconstructed surfaces validated on pristine models is also investigated beforehand in a direct comparison between density functional theory (DFT) and density functional tight-binding (DFTB).

Through this work we want to understand the interaction of organic molecules of different species at the interface with TiO_2 . We ask about the effect of complexities such as material roughness, competition between molecules of the same species, and the role that the solvent plays. Especially this last factor can in fact be decisive also during degradation processes and needs special attention.

Acknowledgements

Thank you, Susi, for introducing me to this world that was completely unknown to me before and for following me with such perseverance and patience especially during this last period. You have always encouraged me to travel, to meet new people in the scientific environment and to always give my best in research: if the supervisor had been me, I would have done exactly the same!

Thank you, Lucio, for being the kind of professor I would like to become one day. For you work is pure passion and your enthusiasm can involve up to the bottom of your heart.

Thank you, Maria, for being a precious friend and colleague. Your scientific contribution and your corrections have made this thesis a work which I can only be proud of.

Thank you, Wilke, for standing my nagging requests and often trivial questions. Possessing a knowledge of chemistry even remotely close to yours would be for me one of the best achievements of my life.

Thank you Isabel for being a wonderful office colleague, even though these recent hard times have not given us the opportunity to see each other often.

Thank you Eric and Stefan for taking care of the working stations, I can hardly remember any days in the last four years when I had troubles with the computer.

Thank you Britta for literally being the best secretary in the world, always patient, helpful and efficient.

I would also like to thank Roozbeh, Lorenzo, Wolf and all the other new members of the HMI group who, although we have known each other too little, I am sure are excellent scientists.

Of course, special thanks also go to all the former group members, including André, Massimo, Jing Feng, Monika, and Thorben, especially for the endless discussions about the quality of the food in the mensa.

I would like to thank all the Research Training Group members, from professors to PhD students, for being such a nice community, full of persons from different faculties with one common love: material science. A special thank goes to Tim, for being such a great organizer, and to Balint and his precious help and discussions on DFTB.

Thank you Verena for being the best person I could ever wish for to contribute with for my first publication. Your patience is admirable and I am so happy I could meet you.

Thank you, Luca, for your incredible ability to clearly explain complex concepts such as excited state calculations. Degrading glyphosate with you was a pleasure more than a duty.

Thank you, Tim, for making me realize how competent a person must be to become a junior professor. Following your JEDI teachings as a young padawan I will try to do it too, someday.

I thank my mother and my brother who, despite the distance, manage to stay close to me and give me their support from Turin. I hope in the future to be able to visit you more often and spend incredible days together again.

Thank you, Alby, for being my best friend since we were in kindergarten. There is no distance that can break our super-covalent bond.

Thank you, Marcel and Andrea, for being such important friends to me ever since my Erasmus experience in Osnabrück. If I fell in love with Germany back then it was especially for your presence there.

Thank you Chris, Christian and Christina for being my three new friends in Germany with identical names so that I could get confused every time. Bremen is a nice city, but with you it's simply amazing.

Thank you, dear Eelda's League friends and colleagues, for always being with me and believing in our project.

Last, but not least, my greatest thank goes to Laura. When I came here I had just met you, but as I once told you « flying between Bergamo and Bremen will be even faster than taking the train from Turin ». And it was. Starting a new life together with you here was one of the best decisions of my life.

Contents

Declaration of Authorship	iii
Acknowledgements	ix
1 Motivations and aim	1
2 Basics of Molecular Dynamics	9
2.1 Equations of motion	10
2.2 System management	12
3 Pristine and reconstructed surfaces of rutile	21
3.1 Theoretical background	25
3.1.1 Density Functional Theory	26
3.1.2 Density Functional Tight-Binding	36
3.1.3 Methods of analysis	38
3.2 Calculations protocols	44
3.3 Pristine slab models	51
3.4 Reconstructed slab models	54
3.4.1 Reconstruction of rutile-(100)	55
3.4.2 Reconstruction of rutile-(001)	57
3.5 Interaction with water	60
3.5.1 A special mention: water on (001)-rec	67
3.6 Summary	73
4 Water pollutants on amorphous TiO₂	75
4.1 Theoretical background	80
4.1.1 Force Fields	80
4.2 Calculations protocols	85
4.3 Force-distance curves	87
4.4 Dynamic multi-sampling	90
4.4.1 A special mention: glyphosate	95
4.5 Summary	96

5	Adsorption and degradation of glyphosate on rutile-(110)	99
5.1	Theoretical background	101
5.1.1	Molecular analysis	102
5.1.2	Defining reaction pathways	105
5.1.3	Time-Dependent Density Functional Theory (TD-DFT)	109
5.2	Calculations protocols	112
5.3	Adsorption of glyphosate on rutile-(110)	117
5.4	Properties of the bidentate \perp mode	121
5.5	Degradation of the bidentate \perp mode	124
5.5.1	Thermal degradation	124
5.5.2	Photo-degradation	130
5.6	Summary	133
6	Conclusions and final remarks	135
	Appendix	152

List of Abbreviations

ACE	Acetaminophen
AFM	Atomic Force Microscopy
AMPA	Aminomethylphosphonic acid
BEN	Benzene
B3LYP	Becke, 3-parameter, Lee–Yang–Parr
CAF	Caffeine
CAS	Complete Active Space
CP	Cole-Perdew
CRB	Carbamazepine
DCL	Dichloromethane
DFT	Density Functional Theory
DFTB	Density Functional Tight Binding
DFT-Dx	Density Functional Theory with Dispersion term x
DOS	Density of States
ECP	Effective Core Potentials
ES	Excited State
FF	Force Field
FP	Fine Particle
GGA	Generalized Gradient Approximation
GGG	Glyphosate
Gr	Ground water
GROMACS	Groningen Machine for Chemical Simulations
GS	Ground State
HF	Hartree-Fock
HOMO	Highest Occupied Molecular Orbital
HSE	Heyd–Scuseria–Ernzerhof
IBU	Ibuprofen
IR	Infrared
JEDI	Judgment of Energy Distribution
LAPACK	Linear Algebra Package
LDA	Local Density Approximation
LEED	Low Energy Electron Diffraction

LUMO	Lowest Unoccupied Molecular Orbital
Ma	Marine water
MD	Molecular Dynamics
MEP	Minimum Energy Path
ML	Monolayer
MP	Model Potentials
NEB	Nudged Elastic Band
NP	Nanoparticle
NVE	Number of particles, Volume and Energy
NpT	Number of particles, pressure and Temperature
NVT	Number of particles, Volume and Temperature
OPC	Optimal Point Charge
PAW	Projector-Augmented Wave
PBE	Perdew-Burke-Ernzerhof
PBC	Periodic Boundary Conditions
PCF	Point Charge Field
PDOS	Projected Density of States
PP	Pseudopotential
PPC	Polarizable Point Charge
PZC	Point of Zero Charge
PW91	Perdew-Wang
PZ81	Perdew-Zunger
QTAM	Quantum Theory of Atoms in Molecules
Rv	River waters
SCC	Self Consistent Charge Error
SCF	Self Consistent Field
Sf	Surface waters
SFG	Sum Frequency Generation
SLC	Salicylic Acid
SPC	Simple Point Charge
STM	Scanning Tunneling Microscopy
SVP	Split Valence Polarization
TD-DFT	Time Dependent-Density Functional Theory
TiO₂	Titanium dioxide
TI_xP	Transferable Intermolecular Potential with x Points
TTR	Tetracycline
TZVP	Triple Zeta Valence Plus Polarization
UV	Ultraviolet
VASP	Vienna Ab-initio Simulation Package
VdW	Van der Waals
VBE	Valence Band Edge
VMD	Visual Molecular Dynamics
VTST	Transition State Tools for VASP
VWN	Vosko-Wilk-Nusair
WTE/I	Water Treatment Effluents/Influents
XPS	X-ray Photoelectron Spectroscopy
ΔSCF	Delta Self Consistent Field

*TO LAURA, LOVE AND SYMBOL OF MY NEW
WONDERFUL LIFE IN GERMANY.*

CHAPTER 1

Motivations and aim

Aquatic pollution is one of the most complicated environmental challenges of our time. As the population, industrialization processes and medical advances increase, so does the impurity of water resources. The huge presence of (micro)plastics in water has attracted the attention of media and scientific community [1, 2, 3, 4], but contamination due to organic agents remains one of the most urgent environmental challenges of our time [5, 6, 7, 8]. Pharmaceuticals in hospital drains [9, 10, 11, 12, 13], chemicals from factories [14, 15, 16, 17, 18], cosmetics or everyday goods [19, 20, 21, 22, 23] as well as compounds heavily used in agriculture [24, 25, 26, 27, 28] are major threats for our ecosystem. Especially in the agriculture sector, pesticides and herbicides are found in our food and drinking water at high concentrations [29, 30, 31]. Whenever such a chemical is released on plants or directly onto the soil, a major part of it percolates in the ground right underneath, as briefly illustrated in fig. 1.1. This

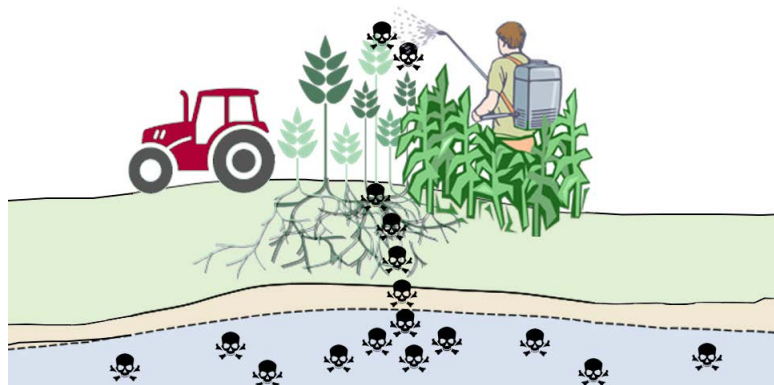


Figure 1.1: Schematic representation of the percolation of an agriculture pesticide into ground aquifers.

results in both the contamination of the humus, which is the most chemically and physically active part of the soil organic matter, as well as in the nesting of these products within the underlying aquifers. The compounds reach then our water sources to end up in our sinks at home. In addition to the harm caused to humans, these products also threaten many animal species, aquatic and non-aquatic [32, 21, 12, 33].

Despite the inclusion of several regulatory actions over time, the abuse of polluting substances shows no sign of stopping. Even if their use would end in a few years, the damage has been done: many pollutants are already present in rivers and groundwaters all over the world [34, 33, 35, 23]. The development of new technologies that can clean up our water resources is therefore of fundamental importance and urgency. They, in turn, must not generate further environmental impact, transferring the problem of water pollution in other areas such as, for instance, in the atmosphere. The goal is then to find a technology that can be environmentally friendly, affordable, efficient and non-toxic, which is far from being a trivial task.

Over the last decades, the main approach has been focusing on the exploitation of sunlight in chemical cleaning processes involving semiconductors. These materials are able to remove dissolved and undissolved smaller contaminants, addressing non-biodegradable agents with high environmental footprint [36]. Among them, the interaction with metal oxides represents the most optimal way to degrade water organic pollutants under UV light. The Advanced Oxidation Processes (AOPs) are often chosen as an alternative able to destroy resilient pesticides, biozides and pharmaceuticals [37, 38]. They consist of the generation of highly reactive species, such as hydroxyl radicals, which are capable of destroying molecules of interest in the aquatic environment. Moreover, if the exploited source is the ultraviolet (UV) light then one talks about the *photocatalytic activity*: the sunlight is in principle able to excite the electrons of a material in order to activate oxidation-reduction reactions that otherwise would not occur or would need much longer time to take place.

Titanium dioxide (TiO_2) is well-known to be one of the most efficient semiconductors around the world [39, 40, 41, 42, 43, 44, 45, 46]. Thanks to its high reactivity and low selectivity, it is widely studied and applied. In the past, photocatalysis with TiO_2 has already been employed to destroy bacteria, viruses, fungi and protozoa [37, 38], with successful applications especially in the nanoscience and technological field [39, 47, 48]. Compounds based on TiO_2 are then no longer limited in cosmetics or in construction dyes, although the medical field still benefits from dental and bone implants based on this metal oxide [49, 50, 51].

Today's most intense research mainly focuses on its photochemical properties. Its two main phases, anatase and rutile, proved to be able of major photocatalytic activity under UV light irradiation, which turned out to be a powerful tool for relevant engineering applications such as water splitting [52, 53] or environmental cleaning [54, 55, 56]. Moreover, TiO_2 powders with negligible rate of impurities can be synthesized at very affordable prices [57], enabling it to reach a primary role with respect to other materials. When talking about photocatalysis, one should actually use the term *heterogeneous* in front. This is because

the photocatalytic activity of a semiconductor is a very broad field of study: it is the combination of materials and surface science, spectroscopy, catalysis and photochemistry [58]. The interest in this type of research is mainly provided by ecological reasons. The ability to exploit the photocatalytic activity of a material makes it possible to degrade some of the most harmful pollutants on our planet, present in both water and air. All of this is performed by harnessing the sun, a source of energy that we can consider inexhaustible and, of course, clean. The applications of photocatalysis extend to many areas [59], such as dental implants [49, 50, 51], hydrogen generation through water splitting, CO_2 reduction into energy fuels and solar batteries.

Photocatalytic processes are usually very fast and their specific mechanism is different from pollutant to pollutant. Thanks to the joint forces of both experimental and theoretical studies, a description of the general procedure has been outlined over time (fig. 1.2). Depending on the adsorbed molecule on the TiO_2

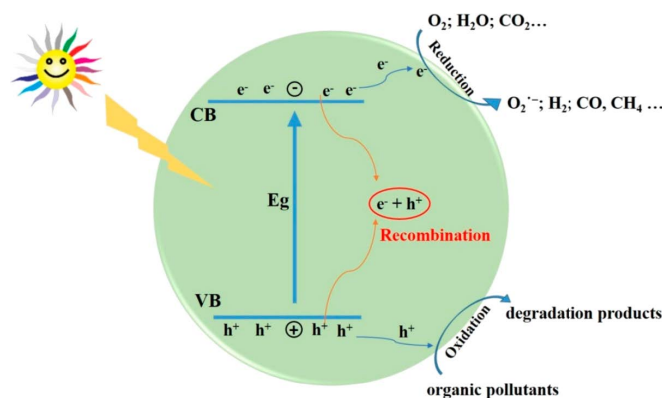


Figure 1.2: Sketched mechanism of the reactions occurring during photocatalysis. Illustration is taken from the work of Kang et al. [59].

surface, this can act either as an oxidant or a reducing agent: in other terms, as an electron acceptor or donor [52]. Whenever a ray of light with an energy greater than the band gap of the material hits the surface, one electron is likely to be excited and jump into the conduction band. This leaves behind a positive hole in the valence band which can then be occupied by its next energetically close electron. This electron, feeling again the excitation, can then move onto the conduction band as well. The combination of the electron-hole fluxes creates a negative and positive current in the semiconductor. If the electron-hole pair, also named *exciton*, encounters a strong separation, then adsorbing molecules can be affected by reduction or oxidation mechanisms. The two processes can be performed in a direct or indirect way. In the first case, the bounded pollutant degrades by electronic exchange from its own structure. In the second case, the creation of highly reactive species within the surrounding solvent brings the contaminant to its unfolding. When a reduction occurs, superoxide ($\text{O}_2\bullet^-$) and hydroxyl radicals ($\bullet\text{OH}$) can be created [59]. They can also be generated via oxidation by the positive current provided by the holes.

The phenomenon of recombination of the exciton is taking place more often. Despite the jump onto the conduction band, the electron still feels the Coulomb attraction towards its left hole spot in the valence band. If the band gap is too

small, i.e. the semiconductor has a more metallic character rather than an insulator one, then the electron can easily turn back to its original energetic level and no photo-induced mechanism is occurring. On the other hand, small band gap values are usually what one aims for. Solar illumination accounts for 4% of UV radiation, while as much as 40% of visible light. A photo-induced mechanism activated by visible light (380 - 780 nm) then would be more desirable but, in order to happen, the band gap of the material should lay between 1.98 - 3.26 eV. Finding the right balance between exciton recombination probability and a low band gap value is therefore far from being a trivial task. The electronic structure of the bulk phase and, above all, the presence of defects play a determinant role in this regard. This can act as charge traps, holding holes or electrons on their site and preventing their recombination. Among them, the presence of vacancies, morphological reconstructions and ion doping inside the material or in its surface layer are the most frequent characteristics.

Experiments are a strong and valuable source of information. Thanks to them it is possible to evaluate the degradation rates of contaminants together with their pH dependence [10, 19, 12, 24, 13, 60, 55, 24, 61], but also light-induced and in-dark thermal activations [61, 62] or the direct observation of competitive behaviors [63, 64, 65]. The analytical techniques used are mostly spectroscopic and are able to detect and quantify the chemical elements involved in the reactions. However, direct observation with a definition that can identify the process in its entirety, with the specific characterization of the functional groups involved and the effects that the solvent has on the adsorbate, remains a challenging or even impossible task [66]. For this reason, lab results shall further be complemented by the use of computational chemistry. Through computer simulations carried out at different levels of theory, accurate models can be created to confirm or disprove experimental results. A major obstacle lies however in the complexity of the systems being considered. When a problem is approached through a physical-mathematical model, it is always necessary to break down these complex systems into simpler approximations. If the model is too complicated, taking into account more factors than necessary, it risks to be inefficient. On the other hand, if it is too simplistic, it will not be able to achieve significant results. Since the treatment of adsorption and degradation processes under photocatalytic activity requires high levels of precision, the tendency is to create overly simplistic models. For example, a single organic pollutant, represented by a simple sphere in fig. 1.3 with eventually an electrical charge, is placed in a vacuum cell on a smooth TiO₂ surface in order to trigger an electronic transfer. There are, however, several complexities to take into account (fig. 1.3).

Water itself, as well as the concentration of ions within the solvent, is able to influence the adsorption mode of a contaminant. An organic pollutant approaching the surface must first be able to overcome the barrier formed by the water molecules in the first adsorption layer. It has however been demonstrated through several studies that the mode of water adsorption changes under the action of photocatalytic activity [67, 68]. By becoming more reactive, H₂O molecules could turn out to be active agents of the photocatalytic reaction, binding to the approaching molecule, by contributing in its degradation. Also

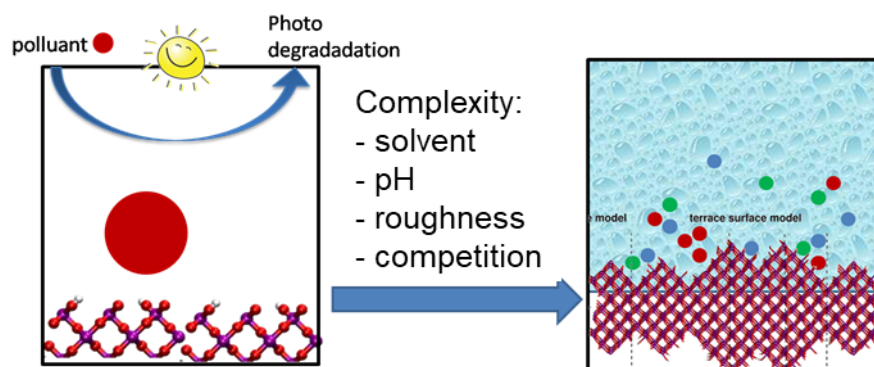


Figure 1.3: Scheme on the complexities to take into account when computationally modelling a degradation reaction. The image was taken as the representative of project P6 within the RTG-QM³.

the pH value of the system plays a major role, as the total charge present on the surface of TiO_2 varies with it [69, 70, 71, 72, 73]. The point of zero charge (PZC) resides in fact at a pH value of approximately 5.8: under acidic conditions the surface become slightly positively charged due to an increased presence of $\text{Ti}_2\text{O-H}$ species, whereas under basic conditions it becomes negatively charged due to a greater presence of Ti-OH species. One shall also not forget that in nature a material is never either perfectly stoichiometric or with a totally flat and regular surface. This kind of impurity gives the surface a change not only in structural terms, but also in its electronic properties. With the presence of kinked sites and their physic-chemical properties, it is then not trivial to guess a priori what path the organic pollutant should take when reaching its optimal adsorption configuration. Finally, there are high concentrations of pollutants of the same or different species present in an aquatic environment. These molecules, even before reaching the TiO_2 surface, could interact with each other creating a more complex compound. Their mixture is then unpredictable and it has been reported cases in which different compounds, individually harmless, showed detrimental effects only once mixed with each other [63, 64, 65].

The amount of complexities that can be taken into account in a system strongly depends on the size of the considered TiO_2 surface. This semiconductor is found in nature as a fine powder. While the human eye may find it difficult to observe a grain of TiO_2 , thus is actually huge from a microscopic point of view. Different than those fine particles (FPs), which have sizes of about $0.1 - 2.5 \mu$, nanoparticles proved to have efficient physicochemical properties thanks to their much smaller diameter size ($1 - 100 \text{ nm}$) and larger surface area per unit mass [74]. They are basic building blocks already widely used in the technological industry [75]. NPs composed mostly of anatase are more efficient in terms of photocatalytic activity [76, 77]. Nevertheless, some studies believe that NPs formed from a higher rutile content are in general less toxic [78, 79]. Thanks to the rather small size, experiments are here able to meet the computational perspective as well. However, the treatment at the level of quantum mechanics is not possible: no ab-initio theory is able to deal with such large and complex systems. That is why one should follow a sort of top-down approach instead. They can be studied theoretically through *coarse-grained*

methods which, by treating groups of atoms or molecules as pseudo-particles in a classical way, allows an impressive computational speed to be achieved [80, 81]. Fig. 1.4 (a) outlines though how TiO_2 NPs may appear very smooth at a first glance, but in reality their surface is composed of a succession of amorphous structures which arises in nature due to various formation processes of annealing and quenching. Through methods such as *Force Fields* (FF), amorphous and

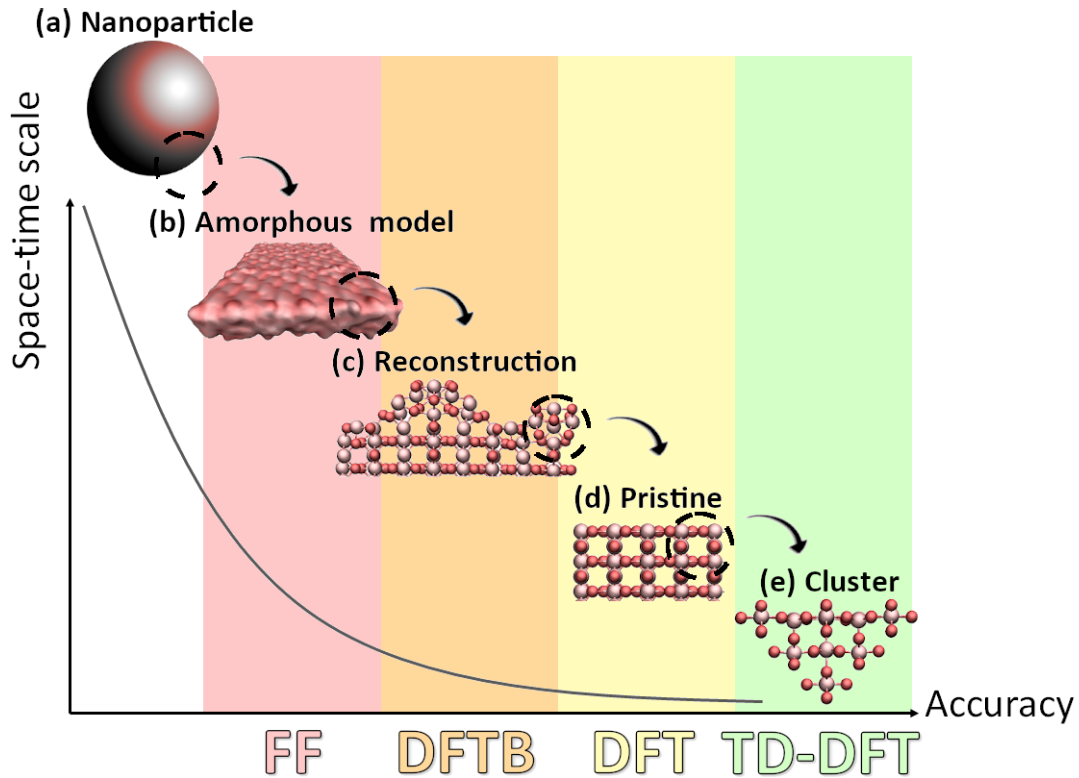


Figure 1.4: Representative scheme from the nano-world downward. The mentioned method are those applied in this work.

crystalline structures (surfaces of about 100 nm^2) can be investigated by directly accessing the atomic information [26, 81] (1.4 (b)). This is still a classical method, in which the forces acting on the system are derived by a sum of external potentials parametrized on ab-initio methods. While FF approaches manage to deal with relatively large surfaces as well as simulation times (up to hundreds of nanometers and nanoseconds, respectively), they have no access to the electronic information and therefore cannot observe the breaking and formation of new bonds between atoms. In order to deal with this aspect, one could investigate interfaces by means of semi-empirical methods. *Density functional tight binding* (DFTB) is able to treat those systems by accessing the ab-initio information through parametrizations [82, 83, 84]. Reconstructed surfaces (5 – 10 nm long) represent the building blocks of extended amorphous structures and are here well suited to be studied (1.4 (c)). *Density functional theory* (DFT) is however considered by the scientific community to be among the most accurate and reliable [85]. The systems analyzed within this method are limited to approximately 1 nm^2 and simulation times of 10 ps, but the electronic part can be described, in principle, in an exact way (1.4 (d)). Finally,

creating a cluster from the pristine surface allows us to exclude its periodicity. In this way methods such as TD-DFT are able to study properties such as the excited state (ES), otherwise very expensive computationally.

The goal of this thesis is multifaceted. On the one hand, we are interested in understanding the electrochemical properties of pollutants-TiO₂ interfaces, according to the reasons listed so far. On the other hand, we want to illustrate how powerful a combination of several methods at different levels of theory can be. Each of them has in fact access to information that the others cannot achieve, whereas their limitations offset each other.

A full ab-initio knowledge of the electronic configurations of pristine and reconstructed surfaces is mandatory, as will be made clear in chapter 3. In nature, however, large amorphous structures are what to expect. For this reason in chapter 4 a classical multi-sampling approach was performed. It consists of considering 25 molecules per pollutant simultaneously on an amorphous TiO₂ surface to observe their dynamic evolution for a relatively long time (from 10 to 110 ns). Again, the study of chemical processes such as degradation can however only be done in depth on small surfaces through ab-initio methods. The need to use outcomes from every possible level of theory becomes therefore even more clear. An example of this multi-level approach will be given in chapter 5, where a top-down approach was performed to achieve a full understanding of both the adsorption and degradation processes of glyphosate on a pristine rutile-(110) surface. The set of analyses carried out in each chapter has one common basis: molecular dynamics simulations, which are an extremely powerful computational tool. The thesis starts then with an introduction to the basis of this method in chapter 2.

CHAPTER 2

Basics of Molecular Dynamics

As the name implies, the molecular dynamics (MD) method consists in the representation of the trajectories of the atoms present in the system. It is to solve numerically and iteratively the equations of motion through the Hamiltonian formalism for the many-body problem. There exist mainly two types of MDs, the main distinction of which lies in how the potential of the system is treated. Ab-initio MDs (AIMDs) are based on the electronic information provided by quantum mechanics, meaning that the potential of the system takes explicitly into account electron-electron, electron-ion and ion-ion interactions. The Hamiltonian of the many-body problem is treated here via the Born-Oppenheimer approximation [86, 87]. As we will see in chapter 3, it consists in considering the ions of the system as parameters computable through classical equations of motion, leaving the treatment at the quantum level to the electronic Hamiltonian only. Solving the Schrödinger equation for this Hamiltonian requires calculations based on a self-consistent cycle, which therefore increases the computational effort. Ab-initio MDs scale with the cube of the atoms in the system, namely $O(N^3)$, and in some cases can even reach $O(N^7)$ [88]. For this reason, they are limited to systems of about 10 – 20 Å per dimension and time scales of 10 – 30 ps. Classical MD methods, such as force fields (FF), allow instead the study of larger systems (up to 100 – 200 Å per dimension) at longer time scales (up to 1 – 3 μ s) [26, 81]. Here, all interactions belonging to the potential of the system are approximated mainly with harmonic functions. The direct effects of electrons in the system are considered within the total potential through parameters derived from ab-initio methods such as DFT [89, 90] or Hartree-Fock [91, 92, 93]. The same parameters can also be experimentally determined via measurements deriving from infrared spectroscopy or similar approaches. For this reason, the accuracy of the results of classical MDs can never exceed that of the methods on which it relies for parameterization. While this does not allow

a direct observation of the creation or breaking of chemical bonds, the speed of calculation for the dynamics gets greatly accelerated. The computational effort of a classical MD usually scales quadratically with the number of involved atoms N , but it can be dragged down from $O(N^2)$ to $O(N)$ by using spherical cut-offs or other techniques [88].

2.1 Equations of motion

In this section, the Hamiltonian formalism is briefly introduced. Next, the numerical methods used primarily in solving the equations of motion are explained.

The Hamiltonian formalism

Most systems considered in molecular/atomistic simulations are under the effect of only conservative forces. Macroscopic phenomena such as friction or heat dissipation, in fact, are rather an effect of the action of the atoms of a system and not a component present on its own. Excluding external actions, therefore, it is correct to consider systems as conservative. Given a molecular system composed by N atoms, each of them can be found at an arbitrary time t in a position described by the vector

$$\begin{aligned} \vec{r}_i : \mathbb{R}^+ &\longrightarrow \mathbb{R}^N \\ t &\longmapsto \vec{r}_i(t) \end{aligned} \quad (2.1)$$

and the total potential acting on them is then a function with domain in \mathbb{R}^N , namely:

$$\begin{aligned} V : \quad \quad \quad \mathbb{R}^N &\longrightarrow \mathbb{R} \\ (\vec{r}_1, \vec{r}_2, \dots, \vec{r}_N) &\longmapsto V(\{\vec{r}_i\}_i) \end{aligned} \quad (2.2)$$

Within this potential all the information one needs to study the dynamics of the system is collected.

The motion of a dynamical system can be treated analytically mainly by referring to the Euler-Lagrange equations or Hamilton equations. Both formalisms are equivalently applicable, since they identify Newton's classical equations of motion anyway. Given $\{\vec{v}_i\}_i$ Lagrangian velocities and $\{\vec{p}_i\}_i$ moments associated to the particles in the system, it is possible to transform the Lagrangian $\mathcal{L}(\{\vec{r}_i\}_i, \{\vec{v}_i\}_i)$ in the Hamiltonian $\mathcal{H}(\{\vec{r}_i\}_i, \{\vec{p}_i\}_i)$ (and vice versa) via the Legendre transform:

$$\begin{aligned} \mathcal{H}(\{\vec{r}_i\}_i, \{\vec{p}_i\}_i) &= \sum_{i=1}^N \vec{v}_i \cdot \vec{p}_i - \mathcal{L}(\{\vec{r}_i\}_i, \{\vec{v}_i\}_i) \\ &= \frac{1}{m} \sum_{i=1}^N \|\vec{p}_i\|^2 - K + V = K + V \end{aligned} \quad (2.3)$$

In the above expression, $K = \frac{1}{2m} \sum_{i=1}^N \|\vec{p}_i\|^2$ and V are the kinetic energy and the potential respectively. The Hamiltonian formalism is used as the main one in conventional terms. This is because quantum mechanics itself, on which FF theory also relies, uses the Hamiltonian operator to determine the eigenvalues of the Schrödinger equation. The dynamics of the system can then be traced back to Newton's equations through the famous Hamilton equations:

$$\begin{cases} \frac{d}{dt} \vec{p}_i = -\frac{\partial H}{\partial \vec{r}_i} \\ \frac{d}{dt} \vec{r}_i = \frac{\partial H}{\partial \vec{p}_i} \end{cases} \quad (2.4)$$

Due to the complexity of the many-body problem, this set of equations is not solvable analytically and requires the use of numerical methods.

Numerical approaches

Given a conservative system, the force acting on the i -th atom is directly related to the gradient of the total potential when derived in its correspondent Cartesian coordinates:

$$\vec{F}(\vec{r}_i) = -\nabla_{\vec{r}_i} V(\vec{r}_1, \vec{r}_2, \dots, \vec{r}_N) \quad (2.5)$$

By integrating over the time t , one can then obtain the velocity

$$\vec{v}_i(t) = \dot{\vec{r}}_i(t) = \vec{v}_i(t_0) + \int_{t_0}^t \frac{1}{m} \vec{F}(\vec{r}_i(s)) ds, \quad (2.6)$$

with t_0 being the initial time of reference for the dynamics. In order to solve the Cauchy problem with a defined solution, both the initial positions and velocities at the time t_0 shall be known. In the first case, they are simply determined by the geometrical configuration of the system before starting the simulation. This is usually a minimum equilibrium of the ionic potential, derived by a geometry optimization to ensure stability [94]. The initial velocities are instead usually randomly assigned by the simulation program from a Maxwell-Boltzmann distribution.

Due to the big size of the system and the complexity of the potential, an analytical integration of equation 2.6 is not possible. Therefore, it is necessary to proceed via numerical methods in order to obtain the equation of motion for each of the atom. The first step is to exploit the information provided by the potential by evaluating the velocity by use of a simple numerical integration such as, for instance, the Euler algorithm of finite differences:

$$\vec{v}_i(t) = \vec{v}_i(t_0) + \frac{1}{m} \vec{F}(\vec{r}_i(t_0)) \Delta t \quad (2.7)$$

The choice of the time step Δt is crucial. The value, in fact, should be sufficiently small enough to ensure numerical accuracy. A good reference would be one that allows to observe the total oscillation of the fastest molecule in the system. In case of water, for instance, this would be less than 10 fs, due to the stretching frequency of 3400 cm^{-1} between its O-H atoms. On the other hand, however, small time step choices provide higher computational times. Once it

is set, we can proceed by evaluating the i -th position vector. Note that its definition depends on the velocity of the previous step: for the very first one, this corresponds to $\vec{v}_i(t_0)$.

$$\vec{r}_i(t) = \vec{r}_i(t_0) + \vec{v}_i(t_0)\Delta t \quad (2.8)$$

At this point, the potential itself can be updated with the new N position vectors and the procedure can be iterated by first evaluating $\vec{v}_i(t + \Delta t)$ and then $\vec{r}_i(t + \Delta t)$ which, this time, will use the information of $\vec{v}_i(t)$ instead.

The Euler algorithm can be interpreted mathematically as a truncated, first-order Taylor approximation in a neighborhood of the point t_0 . If, on one hand, this is a quick computational method, on the other it is unstable for oscillatory motions. For this reason, it is rather preferable to use the Verlet algorithm instead [95]. This approach is based on both the forward and backward positions of the ions in terms of time, $\vec{r}_i(t + \Delta t)$ and $\vec{r}_i(t - \Delta t)$, respectively. Here, by expanding the Taylor series up to the third order, one obtains the following system:

$$\begin{cases} \vec{r}_i(t + \Delta t) = \vec{r}_i(t) + \frac{d}{dt}\vec{r}_i(t)\Delta t + \frac{1}{2}\frac{d^2}{dt^2}\vec{r}_i(t)\Delta t^2 + \frac{1}{6}\frac{d^3}{dt^3}\vec{r}_i(t)\Delta t^3 + o(\Delta t^3) \\ \vec{r}_i(t - \Delta t) = \vec{r}_i(t) - \frac{d}{dt}\vec{r}_i(t)\Delta t + \frac{1}{2}\frac{d^2}{dt^2}\vec{r}_i(t)\Delta t^2 - \frac{1}{6}\frac{d^3}{dt^3}\vec{r}_i(t)\Delta t^3 + o(\Delta t^3) \end{cases} \quad (2.9)$$

Adding term to term, those of first and third order, corresponding respectively to the velocity and the derivative of acceleration, are eliminated. Therefore, only the information on the position and the information provided by the second derivative remain, which can be obtained directly from the potential of the system:

$$\vec{r}_i(t + \Delta t) = 2\vec{r}_i(t) - \vec{r}_i(t - \Delta t) + \frac{1}{m}\vec{F}(\vec{r}_i(t))\Delta t^2 + o(\Delta t^3) \quad (2.10)$$

Although the velocities do not appear directly, it is still possible to calculate them through estimation, for example, at half time-step:

$$\vec{v}_i\left(t + \frac{1}{2}\Delta t\right) = \frac{\vec{r}_i(t + \Delta t) - \vec{r}_i(t)}{\Delta t} \quad (2.11)$$

In conclusion, this algorithm is able to deal with oscillatory behaviors more efficiently than Euler's one. Nevertheless, one needs to perform one iteration of Euler method (or similar) in order to obtain a guess of the backward position corresponding to the initial time t_0 , namely $t_0 - \Delta t$. Without this, Verlet algorithm could not start.

2.2 System management

During the development of an MD it is necessary to take into account some parameters that play a fundamental role. In this section we introduce three of the most important ones. The first is the solvent, which can be treated implicitly or explicitly and can actively influence the dynamics of the system. We next

find an explanation of how to handle periodic systems, which is necessary to greatly speed up the computational effort. Finally, the concept of ensemble is described, as well as the use of the main thermostats and barostats, which allow control over the thermodynamic quantities of the system.

Types of solvent

When performing a simulation, the environment surrounding the molecule of interest must be considered. The latter, in fact, can be in the vacuum or embedded in a solvent. Simulations in vacuum represent the gas-phase of the structure and are faster than when a solvent is present. This approach, however, does not provide a model applicable to most situations, such as adsorption to a surface, since the chemical processes that occur in nature and that we are interested in in this thesis do not take place in a vacuum chamber. Moreover, the adsorbate mobility itself depends on its diffusion in the solvent, which can either cooperate or compete in the adsorption. Explicit molecules belonging to the solvent can, in fact, structure themselves around the adsorbate in the solvation shell [96, 97]. On the other hand, the formation of a double layer by an electrolyte aqueous solution often occurs in the proximity of a charged surface. Hence, a molecule reaching the surface should first be able to overcome the barrier provided by the solvent itself. The introduction of a solvent is therefore necessary, which can be of two types.

- **Implicit solvent.** This method does not introduce additional molecules into the system and works directly on the total electrostatic potential. In this way, the computational effort required is less expensive than that of an explicit solvent calculation. The action that the solvent would have on the solute is here mediated by changing the dielectric constant in vacuum ε_0 to that of the respective medium ε within the electrostatic Poisson-Boltzmann equation. If $V_E(\{\vec{r}_i\}_i)$ is the Coulomb potential of the system, this is given by

$$\Delta V_E(\{\vec{r}_i\}_i) = -\frac{\rho(\{\vec{r}_i\}_i)}{\varepsilon}, \quad (2.12)$$

where ρ is the charge density. Solving this equation allows to compute the electrostatic potential in the most accurate way available, but it can be rather expensive in terms of computational effort. A numerical solution, in fact, relies on a predefined grid able to characterize the charge density. If the used algorithm is not optimal, this implicit solvent approach can even turn out to be as expensive as for an explicit solvent calculation. Approximations of the Poisson-Boltzmann approach are possible, such as the generalized Born approach [98, 99], which help to overcome this problem.

- **Explicit solvent.** This method consists in the introduction of explicit molecules in the system (in our case, H₂O molecules). In this way, all the electrostatic effects that a solvation model would bring in the system are evaluated with use of the Coulomb potential present in the FF, once

ensured that the energy cut-off is properly set. The water molecules inserted differ from model to model. In fact, they can be rigid, flexible, polarizable or dissociable. Although there is a slight difference in terms of angles and O-H distance, what distinguishes one model from another is the distribution of electrical charge. In the SPC [100] and TIP3P [101] models, a partial negative charge is located in correspondence of the oxygen atom. In the OPC [102] and TIP4P [101] approaches this charge is instead inside the molecular virtual triangle, whereas it is outside in the PPC [103] model. Nevertheless, the positive partial charge is always located at the positions of the hydrogen atoms. Finally, in the ST2 and TIP5P [101] models, the charge is divided in two and distributed outside of the triangle. The presence of an explicit solvent in the system requires great care in terms of the equilibrium of the system, as explained in the next section 2.2.

Periodic boundary conditions

Simulations performed using FF theory (but also DFT / DFTB theory) use Periodic Boundary Conditions (PBC). It is a method that allows to reproduce the simulation cell in a periodic way along the three Cartesian directions. The images, which follow each other with periodicity $\mathbf{n}L$ in the case of cubic lattice positions, with $\mathbf{n} \in \mathbb{Z}^3$ and $L \in \mathbb{R}_0^+$, are perfect copies of the original system, as shown in fig. 2.1. Using this approach, infinite systems such as a crystalline

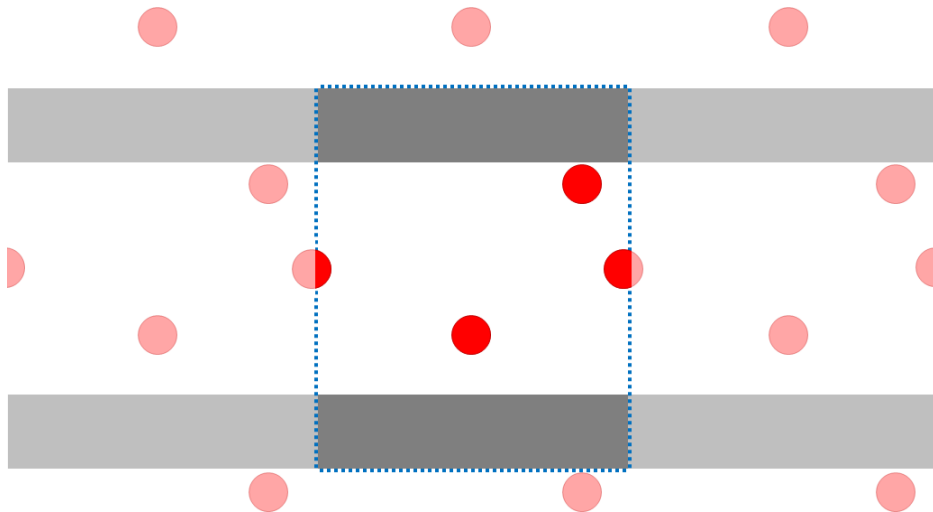


Figure 2.1: Schematized illustration of a 2D Periodic Boundary Conditions. The blue, dotted line represents the simulation box. Brighter colors are the mirrored images.

surfaces can be reproduced by exploiting their structural periodicity rather than manually creating them by inserting additional atoms. A solute molecule is also able to diffuse freely in the system without encountering dummy walls, eventually crossing box edges without encountering nonphysical effects. While this method brings great advantages, it also raises some technical issues. First of all, it is necessary to make sure that the distance between one slab and the

other is sufficiently large, since a molecule in the middle must feel the attraction/repulsion of only one of the two surfaces to avoid fictitious interactions. The total charge in the system can also be a big problem: in case the surface is not neutral, in fact, the excess charge is reproduced by the effect of PBC, resulting in a system with infinite charge. The most classical way to solve this problem is to insert counterions, typically Na^+ or Cl^- , inside the solvent in order to balance the excess charge [104]. Over the years, however, methods using a charged background have also been developed. The latter are in fact preferable, as the counterions themselves can create active interactions with the solute, typically creating double layers right above the surface [105, 106]. Finally, the biggest problem is due to long-range interactions. In fact, it must be ensured that the interaction of a particle with itself and the other solvent molecules belonging to the mirrored images is treated correctly. It has been shown that interactions decaying slower than $\|\vec{r}\|^{-n}$, with n dimensionality of the system (usually $n = 3$), have a non negligible effect even at distances greater than half the smallest length of the simulation box. Although the VdW potential does not fall into this category (it decays with $\|\vec{r}\|^{-6}$ according to Lennard-Jones as well as in the Buckingham potential, see chapter 4), the Coulomb interaction is completely subject to it (it decays with $\|\vec{r}\|^{-1}$). Trying to solve this issue by using a proper energy cut-off is not a good choice. If it is chosen shorter than the smallest length of the simulation box, crucial parts of the potential energy will be neglected, which should be taken into account instead in order not to work with an artifact model. On the other hand, if it is chosen longer than it, then each particle would feel the repulsion with itself, which must be absolutely avoided.

So far, the most widely used method to treat this problem is provided by Ewald summations [107, 108] or their improved algorithms. For sake of simplicity, we briefly introduce Ewald's approach for a simulation cell consisting in cubic lattice positions of length L and periodicity $\mathbf{n} = (n_x, n_y, n_z)$. In this case, the electrostatic potential obtained by analytically solving the Poisson-Boltzmann equation 2.12 is the following:

$$V(\{\vec{r}_i\}_i) = \frac{1}{2} \sum_{i=1}^N \sum_{j=1}^N \sum_{\mathbf{n} \in \mathbb{Z}_0^3} \frac{q_i}{4\pi\epsilon} \frac{1}{\|\vec{r}_i - \vec{r}_j + \mathbf{n}L\|} \quad (2.13)$$

The evaluation of this sum is very time consuming, as it converges really slow. For this reason, it gets split into two parts which consist, in turn, in the Ewald summation. One term refers to the short-range part and it is developed in the same space of $\{\vec{r}_i\}_i$ (referred to as *real space*). The second term, instead, takes into account the long-range interactions and it is structured in the space of wave vectors $\{\vec{K}_i\}_i$ provided by a Fourier transformation (referred to as *reciprocal space*). Different from the total sum of eq. 2.13 and provided the introduction of two further correction terms, the two new potentials quickly converge in real and reciprocal space, respectively. The first step to derive the Ewald summation is to consider the charge density of the whole system at an arbitrary position

\vec{r} , which it is expressed via Dirac delta function:

$$\rho(\vec{r}) = \sum_{i=1}^N \sum_{\mathbf{n} \in \mathbb{Z}^3} q_i \delta(\vec{r} - \vec{r}_i + \mathbf{n}L) \quad (2.14)$$

In order to split the total potential of eq. 2.13, we divide the density into a (real) short-range and (reciprocal) long-range part. One starts by defining the long-range density ρ_{l-r} as the convolution of the total density ρ with, typically, a Gaussian function of the form $\gamma = \frac{\alpha^3}{\pi^{3/2}} e^{-\alpha^2 \vec{r} \cdot \vec{r}}$. Hence, one has that

$$\begin{aligned} \rho_{l-r}(\vec{r}) &= (\rho * \gamma)(\vec{r}) = \int_{\mathbb{R}^3} \rho(\vec{r}') \gamma(\vec{r} - \vec{r}') d\vec{r}' \\ &= \frac{\alpha^3}{\pi^{3/2}} \int_{\mathbb{R}^3} \rho(\vec{r}') e^{-\alpha^2 (\|\vec{r}'\|^2 + \|\vec{r} - \vec{r}'\|^2 - 2\vec{r}' \cdot \vec{r})} d\vec{r}' \end{aligned} \quad (2.15)$$

where $d\vec{K} = dk_x dk_y dk_z$. Note that already in the above definition the Fourier transform of ρ appears as part of the whole convolution. The short-range density is then provided by simple complementary difference, namely $\rho_{s-r} = \rho - \rho_{l-r}$. The Poisson equation can now be solved separately for ρ_{s-r} and ρ_{l-r} , giving rise to the two new short-range and long-range potentials:

$$\begin{aligned} V_{s-r}(\{\vec{r}_i\}_i) &= \frac{1}{2} \sum_{i=1}^N \sum_{j=1}^N \sum_{\mathbf{n} \in \mathbb{Z}_0^3} \frac{q_i q_j}{4\pi\epsilon} \frac{2}{\sqrt{\pi}} \frac{\int_{-\infty}^{+\infty} e^{-s^2} ds}{\|\vec{r}_i - \vec{r}_j + \mathbf{n}L\|} \\ V_{l-r}(\{\vec{r}_i\}_i) &= \frac{1}{2} \sum_{i=1}^N \sum_{j=1}^N \sum_{\vec{K} \in \mathcal{M}} \frac{q_i q_j}{\epsilon} \frac{1}{\|\vec{K}\|^2 L^3} e^{-\|\vec{K}\|^2 / 4\alpha^2} e^{i\vec{K} \cdot (\vec{r}_i - \vec{r}_j)} \end{aligned} \quad (2.16)$$

In the second expression, the wave vector \vec{K} can be interpreted as a numerical triplet \mathbf{k} running in the specific reciprocal set $\mathcal{M} = \{2\pi\mathbf{n}/L | \mathbf{n} \in \mathbb{Z}_0^3\}$. In order for the Ewald summation not to encounter errors due to fictitious effects, it is necessary to intervene by adding two corrective terms. The first one is due to the self-interaction error, since in the short-range action potential the summation on the index j includes also the eventuality $j = i$. To solve this problem, we re-solve the Poisson equation 2.12 for a Gaussian charge distribution centered at the arbitrary position \vec{r} , using the spherical symmetry of the Gaussian charge cloud:

$$\rho_{self}(\vec{r}) = q_i (\gamma * \delta(\vec{r})) \quad (2.17)$$

with q_i specifically referring to the charge of the self-interaction. The resulting potential provides then the first correction term:

$$V_{self} = -\frac{1}{2} \sum_{i=1}^N \frac{\alpha q_i^2}{2\pi^{3/2}\epsilon} \quad (2.18)$$

The second correction refers instead to the dielectric boundary conditions in infinity and acts instead on the reciprocal space. Its mathematical derivation is complicated and would be outside the scope of this thesis. Therefore, we limit

ourselves here to reporting its expression,

$$V_{diel} = \frac{1}{2L^3\varepsilon(2\varepsilon'_r + 1)} \left(\sum_{i=1}^N q_i \vec{r}_i \right)^2, \quad (2.19)$$

where ε'_r is a non-infinite relative dielectric constant, as if non-metallic boundary conditions were assumed.

In conclusion, adding the two expressions 2.16 with 2.18 and 2.19 one obtains Ewald summation and the Coulomb interaction in PBC is well-treated.

Thermostats, barostats and ensembles

Since we are dealing with chemical systems, the average speed at which the atoms move is directly related to quantities such as temperature and pressure. It is absolutely necessary to have a sort of manual control on these two quantities, because not only laboratory experiments are carried out under precise room conditions, but also because, mathematically, the system would risk to collapse. If one employs Verlet's algorithm without any control over temperature and pressure, then we would be in the microcanonical ensemble. Here the number of particles in the system N , the volume V , and the total energy E are conserved, barring numerical errors, in the latter case. For this reason, it is referred to as the NVE ensemble. The lack of control over temperature and pressure (or, equivalently, average particle velocity) causes these two terms to fluctuate without a precise value. Thus, the correct approach is to bring the system to equilibrium through the use of a thermostat and then a barostat (or vice versa), as briefly schematized in fig. 2.2. The idea is first to heat/cool the

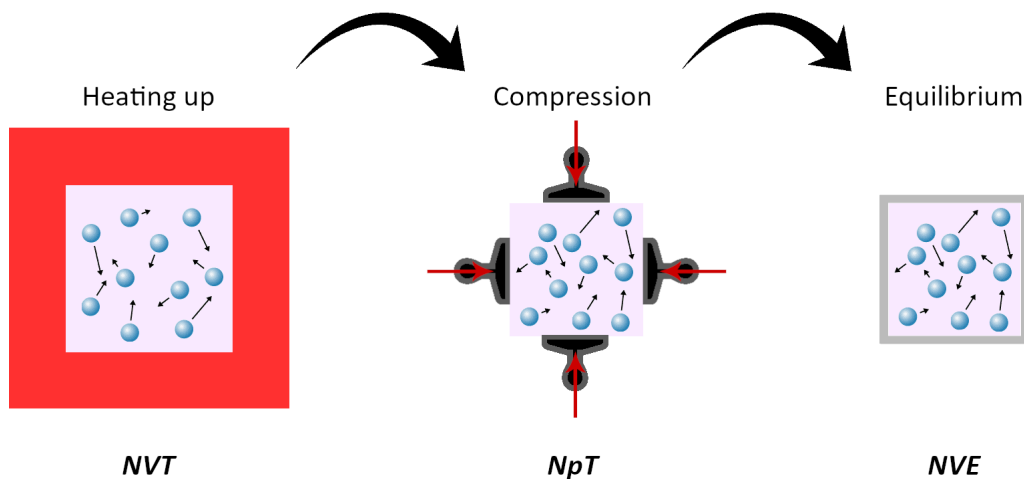


Figure 2.2: Schematized illustration of the ensembles used in the procedure towards a production run.

system up/down to the desired temperature (typically around 300 K, room temperature) by embedding it in a heat bath. Then, one proceeds with a volumetric compression until a specific pressure (or, usually, a density of 1000 Kg/m³) is reached for the solvent inside.

The main methods of temperature management include *velocity rescaling* [109], *Berendsen thermostat* [110] and *Nosé-Hoover thermostat* [111].

- **Velocity rescaling.** In this method, one supposes that on each particle with velocity $\vec{v}_i(t)$ a common scaling parameter $\lambda \in \mathbb{R}$ is applied to reach a target temperature. In order to do this, we shall refer to the equations of a perfect gas, which hold as an acceptable approximation for systems with an explicit solvent.

$$\begin{aligned} \langle K \rangle &= \frac{3}{2} N k_B T & (2.20) \\ \Rightarrow T &= \frac{2}{3} \frac{\langle K \rangle}{N k_B} \\ &= \frac{2}{3} \frac{\frac{1}{2} \sum_{i=1}^N m_i (\vec{v}_i \cdot \vec{v}_i)}{N k_B} \\ &= \frac{1}{3 N k_B} \sum_{i=1}^N m_i (\vec{v}_i \cdot \vec{v}_i) \end{aligned}$$

In the above equation, $\langle K \rangle$ is the mean kinetic energy of the system, N the total number of particles in it, k_B the Boltzmann constant and T the temperature. Note that, classically, $K = \frac{1}{2} \sum_{i=1}^N m_i (\vec{v}_i \cdot \vec{v}_i) = \frac{1}{2} \sum_{i=1}^N m_i (v_{i_x}^2 + v_{i_y}^2 + v_{i_z}^2)$, but since we are dealing with the kinetic theory of gases, one can stochastically assume that $v_{i_x} = v_{i_y} = v_{i_z}$. This explains the number 3 in the above expression. One can now evaluate the difference between the target temperature, the velocities of which are defined by $\lambda \vec{v}_i$, and the current one:

$$\Delta T = T_{target} - T_{current} = \frac{1}{3 N k_B} \sum_{i=1}^N m_i (\lambda \vec{v}_i \cdot \lambda \vec{v}_i - \vec{v}_i \cdot \vec{v}_i) \quad (2.21)$$

By solving the equation as a function of λ , one obtains:

$$\Delta T = \frac{(\lambda^2 - 1)}{T_{current}} \Rightarrow \lambda = \sqrt{\frac{T_{target}}{T_{current}}} \quad (2.22)$$

Hence, this is the value all the velocities in the system shall be multiplied of at each current step in order to reach the desired temperature.

- **Berendsen thermostat.** Also in the case of the Berendsen thermostat, the velocities of the individual particles are scaled at each time step. In this case, however, a differential equation is introduced that describes the rate of temperature exchange with the heat bath:

$$\frac{dT}{dt} = \frac{1}{\tau} (T_{bath} - T) \quad (2.23)$$

Here, τ is a parameter representing how tight the bath and the system are coupled together. According to Berendsen assumption, the temperature of the system decays exponentially to the target temperature. This affects

directly the dynamics of the whole system, by adding in the Newton's equations a frictional term:

$$m_i \frac{d^2}{dt^2} \vec{r}_i(t) = \vec{F}_i + m_i \frac{1}{2\tau} \left(\frac{T_{bath}}{T} - 1 \right) \frac{d}{dt} \vec{r}_i \quad (2.24)$$

By treating eq. 2.23 numerically, one can introduce also in this case a velocity scaling parameter λ . The equation, in fact, can be rewritten as

$$\begin{aligned} \frac{\Delta T}{\Delta t} &= \frac{1}{\tau} (T_{bath} - T) \\ \Rightarrow \Delta T &= \frac{\Delta t}{\tau} (T_{bath} - T), \end{aligned} \quad (2.25)$$

which can then be inserted in eq. 2.21, identifying T_{target} as T_{bath} . Hence, the proportional scaling of the velocities per time step is given by the following expression:

$$\lambda = \sqrt{1 + \frac{\Delta t}{\tau} \left(\frac{T_{bath}}{T_{current}} - 1 \right)} \quad (2.26)$$

- **Nosé-Hoover thermostat.** Unlike before, the Nosé-Hoover thermostat acts directly on the total energy of the system and not as a velocity rescaling method. In this case, the heat bath acts as a reservoir with an own potential and kinetic energy. Its coupling to the real system influences the temperature fluctuations in a way that the ensemble average equals that of the canonical ensemble within time. For this reason, the Nosé-Hoover thermostat is widely used to reach an equilibrium before the production run in NVE.

First, the coordinates originally used in the system, say $(\vec{r}_i^{(or)}, \vec{p}_i^{(or)}, t^{(or)})$, are replaced by virtual coordinates according to the following transformation:

$$\begin{cases} \vec{r}_i^{(or)} = \vec{r}_i \\ \vec{p}_i^{(or)} = \vec{p}_i \\ t^{(or)} = \int_{t_0}^t \frac{d\tau}{s} \end{cases} \quad (2.27)$$

The term s is an additional, one-dimensional degree of freedom introduced in the system, the correlated one-dimensional momentum of which is then given by $p_s = \frac{1}{Q} \frac{d}{dt} s$. In order to define this latter expression, a fictitious mass Q is required. This parameter shall be chosen carefully, since it can strongly influence the whole dynamics. The new Hamiltonian is then defined as it follows:

$$\mathcal{H}(\{\vec{r}_i\}_i, \{\vec{p}_i\}_i, p_s, s) = \sum_{i=1}^N \frac{\|\vec{p}_i\|^2}{2ms^2} + V(\{\vec{r}_i\}_i) + \frac{p_s^2}{2Q} + gk_B T \log s \quad (2.28)$$

In the above expression, g is the number of independent momentum degrees of freedom of the system (usually $g = 3N$), whereas T is the externally set temperature we want to have control on. By applying Hamilton's

equations, one obtains that:

$$\begin{aligned}
\frac{d}{dt}\vec{r}_i &= \frac{\partial\mathcal{H}}{\partial\vec{p}_i} = \frac{\vec{p}_i}{m_i s^2} \\
\frac{d}{dt}\vec{p}_i &= -\frac{\partial\mathcal{H}}{\partial\vec{r}_i} = -\frac{\partial V}{\partial\vec{r}_i} \\
\frac{ds}{dt} &= \frac{\partial\mathcal{H}}{\partial p_s} = \frac{p_s}{Q} \\
\frac{dp_s}{dt} &= -\frac{\partial\mathcal{H}}{\partial s} = -\frac{1}{s} \left(\sum_{i=1}^N \frac{\|\vec{p}_i\|^2}{2m_i s^2} - gk_B T \log s \right) \quad (2.29)
\end{aligned}$$

It can be proven that, if $t \rightarrow +\infty$, the equations reported above allows the canonical ensemble of the original system to be conserved. On the other hand, the behavior is non-ergodic, which means that not all parts of the phase space will be visited. For this reason new algorithms, such as Nosé-Hoover chains or Bauer–Bulgac–Kusnezov schemes were introduced to remedy this problem.

The use of barostats follows the same principles as that of thermostats. The volumetric compression of the simulation cell can in fact be thought of as a sort of "pressure bath" acting externally. In the case of the Berendsen barostat, we will have that the pressure of the system will be scaled at each step by the following parameter:

$$\mu = \sqrt[3]{1 + \frac{\Delta t}{\tau_p} \beta_T (p - p_{bath})} \quad (2.30)$$

In the above equation, $\beta_T = -\frac{1}{V} \frac{\partial V}{\partial p}$ is the isothermal compressibility and τ_p is the coupling strength to the external pressure bath. In terms of coordinates, the scaling applies with $\vec{r}'_i = \mu \vec{r}_i$, producing a total compression of $V' = \mu^3 V$. Following the same principle, a barostat analogous to Nosé-Hoover thermostat can be generated by introducing in the Hamiltonian an additional degree of freedom. In this case, though, it will not be the temperature T to appear as a contribution in the additional potential, but rather the pressure p .

Other approaches, such as Andersen's [112], are of course also present and frequently used.

CHAPTER 3

Pristine and reconstructed surfaces of rutile

Most metal oxides undergo the phenomenon of polymorphism. These are different structures dependent on pressure and temperature that the material can assume while maintaining the same stoichiometry. The main phases of TiO_2 are named anatase, rutile and brookite (see fig. 3.1). As a basic matrix, all

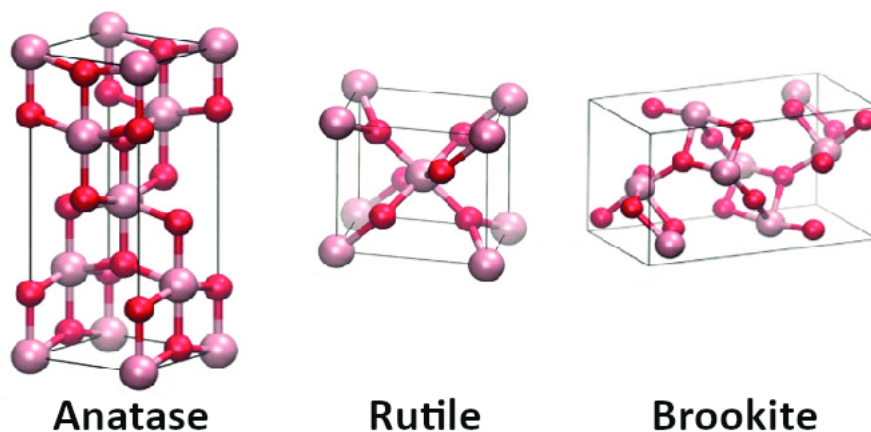


Figure 3.1: Anatase, rutile and brookite crystal structures. Red spheres refer to O atoms, pink ones to Ti atoms. The image has been taken from reference [113] and slightly modified.

three have the combination of octahedra with a Ti atom at the center and six O atoms bonded to it. The arrangement of the symmetry group (I_4^1md for anatase, $C_{4v}nm$ for rutile and $C_{2v}bca$ for brookite) generates their different bulk crystallization. This leads to a variation of their properties such as the photocatalytic efficiency. Especially this point raises a question that has been under

debate for a long time: which of the three TiO_2 polymorphs shall be considered to conduct photocatalytic studies? We have a straight answer to it: all of them. It is pointless to dispute which of them is the best, because it is the very definition of *best* being unclear. Depending on various aspects, each of the three phases has advantages and disadvantages. Since there are relatively few studies on brookite, considering that it is the rarest structure to be obtained in the laboratory, the discussion is mainly between anatase and rutile.

Anatase is in principle to be considered the most efficient in terms of photocatalytic activity. Despite a band gap of 3.20 eV, compared to the smaller one of rutile (3.02 eV), anatase is able to generate more redox reactions than rutile (fig. 3.2 (a)). Among the possible reasons there is the fact that anatase

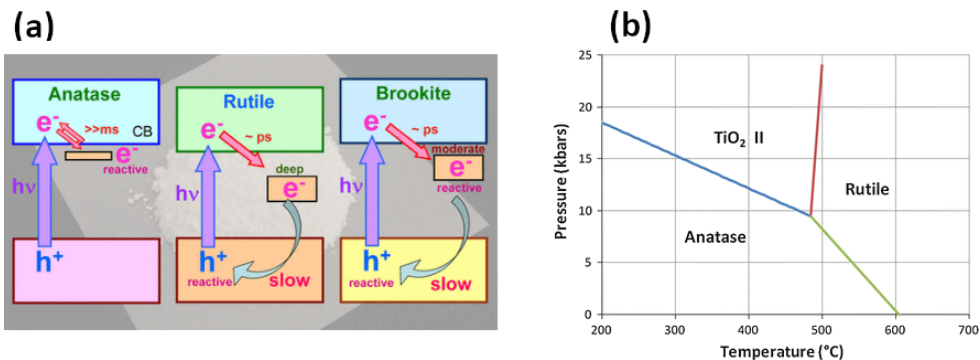


Figure 3.2: (a) Valence and conduction bands, with their schematic band gap, are shown for anatase, rutile and brookite. The illustration was taken from the work of Monai et al. [114]. (b) The phase transition boundaries from anatase to rutile depending on temperature and pressure. TiO_2 II stands for srilankite, an orthorhombic polymorph not relevant to the discussion of this thesis. The illustration was taken from the work of Hanaor et al. [115].

has a larger surface area per unit cell. This implies the presence of a higher density of localized states, leading to less frequent recombination of excitons. An experimental study by Luttrell et al. [116] demonstrated within an epitaxial growth process that at least in part this depends also on the bulk structure itself. Finally, anatase has an indirect band gap lower than its direct band gap, whereas in rutile there is not much of a difference. Semiconductors with an indirect band gap are more prone in carrying excitons for longer time, being less likely to recombine.

On the other hand, rutile is at all temperatures and pressures a more stable phase than anatase [115]. Indeed, anatase is considered to be a metastable polymorph. As shown in fig. 3.2 (b), at constant atmospheric pressure anatase transforms irreversibly into rutile at around 900 K through a process of reconstruction and settlement of the crystal structure. Rutile is therefore the phase with which one must inevitably work in devices involving high-temperature processes and applications, such as gas sensors and porous gas separation membranes. It has moreover been reported that rutile has a higher surface enthalpy and higher surface free energy than anatase. This implies that rutile possesses a higher hydrophilicity than anatase. Hence, rutile exhibits a higher density of adsorbed species than anatase.

Brookite, as mentioned above, is by far the least studied TiO_2 polymorph. A relatively recent work by Monai et al. [114] has pointed out that it may well be brookite the phase one should investigate at most. Its band gap has not yet been precisely defined and is in the range of 3.1 - 3.4 eV. Energetically, however, brookite would have trap states deeper than those of anatase and shallower than those of rutile. This would result in virtually perfect diffusion of the excitons, since the trap-depth in anatase is considered too shallow, while in rutile it is considered too deep.

In conclusion, one cannot rely solely and exclusively on arguments relating to band structure. When investigating the electronic properties of a semiconductor, it shall be remembered that various defects such as vacancies or reconstructions can be a game changer. The investigation of this thesis is focused on rutile. As part of other collaborations within the RTG-QM³ other studies have also been carried out on the anatase surface, which are not reported here.

Given the small sizes of the systems that ab-initio methods are able to handle, it is not possible to reproduce an amorphous surface without falling into the regularities dictated by the repetition of PBCs. Rutile-(110), (100) and (001) facets have been extensively investigated over the years and are still a hot topic for discussions and debates nowadays. Many theoretical studies focused on finding proper values of rutile's surface energy, agreeing on the order $\gamma_{(110)} < \gamma_{(100)} < \gamma_{(001)}$, when compared with each other [117, 118, 119, 120].

Despite the huge progress made in the past few decades, accurate atomistic models of TiO_2 /water interfaces [121, 122, 123, 124, 125, 126, 127] still rarely consider complex reconstructions. The interaction of metal oxides with liquid water in terms of solvent and as single molecules is of main relevance: if not directly in a river, a lake or a sea, almost no environmental reaction would take place in a system which does not involve at least some humid conditions. It is already well known in literature how water tends to form strong bilayers at TiO_2 surfaces, which represent a physical and energetic barrier for other molecules to overcome before reacting with the material [128, 129, 130]. An accurate chemical study of such exchanges is still an open question: the character of the interaction strongly depends on the geometry, on the considered phase and on the pH conditions the material is embedded into. In theoretical chemistry, the description of water networks is a task as meaningful as difficult to handle. Metal oxide surfaces with a combination of exposed surface oxygen and metal atoms are known to promote adsorption of water mainly in three different ways [131, 127, 122, 132]. As schemed in fig. 3.3 for TiO_2 , water can adsorb in a molecular way, via splitting into one hydroxyl and a proton or by forming a hydrogen bond with the surface. In the first case of molecular adsorption the

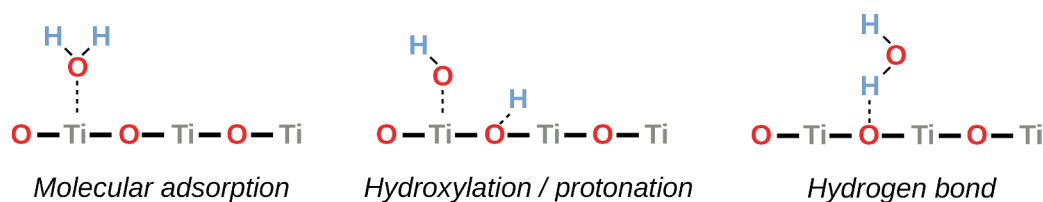


Figure 3.3: Three main adsorption modes of water on a TiO_2 surface, independently on its phase.

water molecule gets adsorbed with a strong bond between its oxygen atom and a surface metal atom. Here the two hydrogen atoms tend to lie towards the water network or can form hydrogen bonds with oxygen surface atoms. If the metal oxide structure supports a splitting of water upon adsorption, it ends up in the formation of a hydroxyl and a proton. As in the molecular case, the hydroxyl gets adsorbed with a bond between the water oxygen atom and the surface metal atom. The pulled proton feels the attraction of a surface oxygen atom and gets adsorbed on it. In the last state, water molecules often form direct hydrogen bonds with one or sometimes two surface oxygen atom(s). This last case represents the least attractive configuration due to the weakness of the hydrogen bond [133].

The first layer of formation of water on the surface represents both an energetic and physical barrier for other molecules attempting to approach the material. Moreover, it has been shown that due to the photocatalytic action molecularly adsorbed H_2O on the surface change their mode by dissociating [67, 68, 134]. This may allow the contaminant to interact directly with the surface. For this reason it is necessary to possess a clear and correct idea of what the adsorption modes of water are on different TiO_2 surfaces. Only in this way one could proceed with investigations moving from ground states (GS) to excited states (ES).

Rutile-(110), being the most stable case, is also the most studied one both theoretically and experimentally. Nowadays many doubts are still unresolved for what concerns the ability of this surface to adsorb water. Although some researches assume that the hydroxylated states are the ones being promoted [122] through dissociation at the surface, the main opinion holds onto the molecular adsorption [135, 136, 127]: more complex types of theoretical investigations, such as peptides recognition [137] or kinked sites effects [138], have been recently carried out by giving this last configuration as the correct one. Different studies attributed this discrepancy to the dependence of the adsorption mechanism on mainly two factors: the number of layers in the chosen slab model and the coverage of water present at the surface [132, 139, 140].

In the common natural rutile powder, the (100) facet is present with a proportion of at least 20% [117]. This surface is quite different from rutile-(110), although the coordination number of O and Ti atoms is exactly the same. Upon annealing at more than 800 K under UHV conditions, rutile-(100) tends to reconstruct along (110) microfacets in a 1×3 surface with a roof-like shape [39, 141]. Therefore both the smooth and reconstructed cases have been taken into account during time for structural validations [142, 143] and interactions with different molecules at the surface [128, 129, 130]. The 1×3 rutile-(100) geometry promotes the formation of 1×5 and 1×7 surfaces as well, which were observed after annealing at higher temperatures.

In the past years, also rutile-(100) was controversially discussed about the adsorption modes of water molecules at the surface. The debate ranged again between the completely molecular and partially dissociative adsorption hypothesis [128, 122, 127]. According to the latest literature researches, though, water molecules approaching the surface of rutile-(100) prefer the molecular adsorption mode.

Due to its metastability, rutile-(001) is the facet with the least available information, although this crystal orientation promotes the highest electrical conductivity [39]. Some first investigations on the annealing of this surface were performed in the eighties [144, 145] and then retaken into account only in 1999 by Nörnberg [146]. In his work, he was able to clearly observe a $(7\sqrt{2} \times \sqrt{2})R45^\circ$ reconstruction of the surface, but only Fukui and Tero [147, 148] provided a valid chemical stairs-like model found after annealing the sample at temperatures about 1050 K. This consists of a Ti_7O_{12} stoichiometry at the surface, with interstitial Ti atoms which were forming during the Ar ion sputtering process. Such a reconstruction was also found via epitaxial growth [149] and with pulsed laser irradiation [150]. Recently, low energy electron diffraction (LEED) experiments proposed a similar model for (011)-faceted rutile-(001) when annealed at 683 K [151], leading to a theoretical stoichiometric reconstructed surface [152] which has been lately considered of main interest for the adsorption of CH_3OH and H_2O molecules [153].

In this chapter, static and dynamic computational analysis on all of the aforementioned slab models are presented, which allowed to investigate the atomistic structure and relative thermodynamic stability. A special focus on the reconstructed cases of rutile-(100) and (001) is reported. The reactivity of water on the rutile surfaces was extensively studied also via Molecular Dynamics (MD) simulations. A direct comparison between the standard *Density Functional Theory* (DFT) and the approach of *Self-Consistent-Charge Density Functional Tight-Binding* (DFTB) was here depicted. We firmly trust that a combination of the two methods might represent, in the near future, one path to move towards larger systems and time scales without lack of ab-initio information.

3.1 Theoretical background

When one wants to study in detail a process of adsorption or degradation of a pollutant, as well as the specific properties of the crystalline surface with which it interacts, the use of quantum mechanics is inevitable. Only solids formed from the noble elements or pure ionic combinations can still be described essentially in classical terms [154], but this category is very limiting. In quantum physics, the solution of the Schrödinger equation for the many-body problem provides all the information about the probability of detecting particles in the system at time t in a specific configuration $(\{\vec{R}_H(t)\}_H, \{\vec{r}_h(t)\}_h)$, where the first position vectors refer to ions, the second to electrons. Until the 1960s the total wavefunction $|\Psi(\{\vec{R}_H(t)\}_H, \{\vec{r}_h(t)\}_h)\rangle$ was the main tool for investigating the physics of quantum systems. Thanks to it, in fact, we can define the time evolution of the system and the average value associated with the observables of interest, such as total energy and angular momentum. Although it provides a complete description, only for hydrogen atom and slightly more complex systems it is possible to access to an analytical solution of many-body problem. A simple oxygen molecule O_2 , in fact, should take into account 2 ions and 16 total electrons. Even just limiting it to valence electrons, one would have a system with $3 \times (2 + 12) = 42$ degrees of freedom. Furthermore, since the electrons are

identical fermions, it is necessary for the total wavefunction to be antisymmetric under the exchange of any pair of them. Inevitably, therefore, heavy approximations had to be made so that the electronic information of the system could be derived with acceptable computational effort. Beyond the universally accepted Born-Oppenheimer approximation [86], methods such as Hartree-Fock [91, 92, 93] and configuration interaction [155] were the first to emerge. An alternative approach, introduced in 1965 by Hohenberg and Kohn, instead exploits the electron density at an arbitrary position, $\rho(\vec{r})$, as a fundamental function of their theory. The amazing thing about Density Functional Theory (DFT) [89, 90] is not only the culling from $3n$ degrees of freedom to 3 only, but also the fact that the method guarantees the exact solution of the system. This is, however, only in principle: one element of the Kohn-Sham equations, the heart of the method, is not known and is therefore subject to approximations. Nevertheless, the DFT is still recognized as one of the most efficient methods in its field [85].

3.1.1 Density Functional Theory

In contrast to the 2.1 section, where we had a classical many-body system consisting of N ions, this time we have to consider n additional electrons. In the following discussion, Dirac's *bra-ket* notation will be used. Each electron is identified by a position vector \vec{r}_i , with $i \in \{1, 2, \dots, n\}$, mass $m_e = -1.602 \times 10^{-19}C$ and electric charge $e = -9.109 \times 10^{-31}Kg$. Ions are described by the position vectors \vec{R}_I , with $I \in \{1, 2, \dots, N\}$, mass M_I and electric charge $Z_I e$, which is proportional to that of an electron. Since the system is conservative, the potential has no direct dependence on time. This allows us to consider the stationary Schrödinger equation:

$$\hat{H} |\Psi\rangle = E |\Psi\rangle \quad (3.1)$$

The term \hat{H} indicates the Hamiltonian operator which is composed as it follows:

$$\begin{aligned} \hat{H} = & \underbrace{-\frac{\hbar^2}{2m_e} \sum_{i=1}^n \Delta_i}_{\text{electronic kinetic term}} - \underbrace{\frac{\hbar^2}{2} \sum_{I=1}^N \frac{1}{M_I} \Delta_I}_{\text{ionic kinetic term}} \\ & + \underbrace{\sum_{i=1}^{n-1} \sum_{j>i}^n \frac{e^2}{\|\vec{r}_i - \vec{r}_j\|}}_{\text{electron-electron interaction}} + \underbrace{\sum_{I=1}^{N-1} \sum_{J>I}^N \frac{Z_I Z_J}{\|\vec{R}_I - \vec{R}_J\|}}_{\text{ion-ion interaction}} + \underbrace{-\sum_{I=1}^N \sum_{i=1}^n \frac{e^2 Z_I}{\|\vec{R}_I - \vec{r}_i\|}}_{\text{electron-ion interaction}} \end{aligned} \quad (3.2)$$

Despite the Born-Oppenheimer approximation (see appendix 6), solving the Schrödinger equation analytically for the electron Hamiltonian is far from being a trivial task. The most complicated term to handle is V_{e-e} , as it is the only one that has a summation with double entry from the variables. If only \hat{K} and V_{ext} appeared in the equation, which have only one entry of the variables in the summation, the problem would not exist. Instead of trying to go through a direct analytical solution via integration, therefore, we rather refer to the Rayleigh-Ritz principle [156].

Theorem 1 (Rayleigh-Ritz principle). *Given the many-body, stationary, electronic Schrödinger equation, the expectation value of the electronic hamiltonian operator \hat{H}_e on any wavefunction cannot be lower than the GS energy of the system.*

A proof of this theorem is given in the appendix 6. An alternative method of solving the stationary electronic Schrödinger equation is then to look for the normalized wavefunction $|\Psi\rangle$ to which the GS energy corresponds. The problem of integrating a differential equation then shifts to one of minimizing the expectation value of an operator. The domain Q over which we wish to minimize is a space of functions and not numerical and it is therefore necessary to use variational methods. If, on one hand, this approach greatly simplify the research of the solution, it can only find the GS energy of the system. Therefore, if one is interested in its excited states (ES), for instance due to a photocatalytic activity, other methods need to be implemented, as explained in chapter 4.

The development of DFT theory since the 1960s earned the Nobel Prize in Chemistry in 1998 to Walter Kohn and John A. Pople, the latter "for his development of computational methods in quantum chemistry." Early approaches to finding GS energy from the Rayleigh-Ritz principle were based on a heavy approximation of the wavefunction $|\Psi\rangle$. In Hartree's method, for example, the wavefunction was thought of as if the electrons were non-interacting particles. In the later Hartree-Fock (HF) approach [91, 93], the approximation was further weighted down with the introduction of the Slater determinant [92], so that the Pauli exclusion principle could also be taken into account. In the DFT theory, not only we do not use any kind of approximation on the shape of the wavefunction, but we approach the problem from another point of view: that of the electronic density. The electronic density at an arbitrary electronic position $\vec{r}_j := \vec{r}$ is given by

$$\rho_{\Psi}(\vec{r}) = n \int_{\mathcal{Q}^{3(n-1)}} \Psi^*(\vec{r}_1, \dots, \vec{r}_n) \Psi(\vec{r}_1, \dots, \vec{r}_n) d\vec{r}_1 \dots d\vec{r}_{j-1} d\vec{r}_{j+1} \dots d\vec{r}_n, \quad (3.3)$$

where the symbol $*$ indicates the complex conjugate and $\mathcal{Q}^n = \mathcal{Q}_1 \times \mathcal{Q}_2 \times \dots \times \mathcal{Q}_n$ represents the Cartesian product of the volumes in which each \vec{r}_i are defined. Electronic density has, in this context, the same meaning as probability density. When integrated in turn into the variable \vec{r} , then, the result corresponds to the probability of finding the electronic configuration dictated by $|\Psi\rangle$ somewhere in space, i.e. $\int_{\mathcal{Q}^3} \rho_{\vec{r}} d\vec{r} = 1$. In defining this quantity we must therefore refer to a wavefunction $|\Psi\rangle$. In 1964, Hohenberg and Kohn showed instead that it is the wavefunction $|\Psi\rangle$ itself that can be defined by the electronic density ρ , provided it is that of the GS, namely $|\Psi_0(\{\vec{r}_i\}_i)\rangle$. In this sense, $|\Psi_0\rangle$ is dependent on the electronic density at the GS, i.e. ρ_0 , so it is its functional (hence the name of the theory): $|\Psi_0\rangle = |\Psi_0[\rho_0]\rangle$. In turn, all observables \hat{O} of the system (including energy) become a functional of it: $\langle \Psi_0[\rho_0] | \hat{O} | \Psi_0[\rho_0] \rangle$. In order to prove this, we shall first rewrite the stationary electronic Schrödinger equation A.3 in terms of electronic density. The two terms $\langle \Psi_0 | \hat{K} | \Psi_0 \rangle$ and $\langle \Psi_0 | V_{e-e} | \Psi_0 \rangle$ can not be written down explicitly as functionals of ρ . In the first case, indeed,

the application of Δ_i either on Ψ^* or Ψ inside the integral does not allow to explicitly get ρ . Similarly, in V_{e-e} the presence of the term $1/\|\vec{r}_i - \vec{r}_j\|$ acts in the integrand without being able to explicate ρ in any way. The external potential, on the other hand, can be written explicitly (see appendix 6). We can then introduce the famous Hohenberg-Kohn's theorem.

Theorem 2 (first theorem of Hohenberg-Kohn). *Given the many-body, stationary, electronic Schrödinger equation, there exists a bijection between the GS electronic density $\rho_{\Psi_0}(\vec{r})$ and the external potential $V_{ext}(\vec{r})$ of the system.*

A proof of this theorem is given in the appendix 6. The whole system therefore depends on ρ , which means that so does the total energy. With their second theorem, Hohenberg and Kohn proved that the Rayleigh-Ritz principle holds true when minimizing the expectation value on $\rho_{\Psi} \in C^0(\mathcal{Q}^3)$, with $C^0(\mathcal{Q}^3) = \{\rho_{\Psi} : \mathcal{Q}^3 \rightarrow \mathbb{R} | \rho \text{ is continuous}\}$ instead that on $\Psi \in Q$. At this point, then, it is not necessary to write Ψ in ρ_{Ψ} , as Ψ itself also depends on ρ . The energy of the system can then be expressed as

$$E[\rho] = \langle \Psi | \hat{K} + V_{ee} | \Psi \rangle + V_{ext}[\rho] \quad (3.4)$$

The first term does not change if we change external potential, hence it is to be considered as an *universal functional* of ρ , namely $\hat{F}[\rho]$. Although the introduction of the electron density has dramatically improved the problem of finding the energy of the GS, the lack of an explicit expression of $\hat{F}[\rho]$ with respect to the electron density does not allow us to find an analytical solution. One year after their publication, Kohn and Sham developed a simple method for carrying-out DFT calculations in practice. This, however, implies the use of some approximations that detract accuracy from the completeness of DFT. An explanation of them is given in the appendix 6, together with the derivation of the Kohn-Sham equations:

$$\left[-\frac{\hbar^2}{2m_e} \Delta_{\vec{r}} + V_{eff}[\rho](\vec{r}) \right] |\psi(\vec{r})\rangle = \varepsilon_i |\psi(\vec{r})\rangle \quad (3.5)$$

Note that the effective potential is a function of the density itself which, in turn, is obtainable only by solving the equations through the single-particle states. For this reason, eqs. 3.1.1 have a self-consistency character (SCF). This is not a major issue, since the solution can then be found iteratively by assuming an initial form of $\rho(\vec{r})$. On the other hand, solving a self-consistent loop at each ionic step costs computational time, as it usually needs up to 60 iterations before a sufficient convergence is reached.

That being said, the major problem is rather to find a suitable approximation for the exchange-correlation term $E_{xc}[\rho]$. To this extent, we introduce here some major methods that have been used in our work.

- **Local-density approximation (LDA)**. This is the simplest type of estimate [90, 157]. It consists of locally approximating the exchange and correlation energy through the contribution of a corresponding homogeneous electron gas system, also called *Jellium*, giving rise to the same electron density. For a Jellium structure, the atomic nuclei are assumed to be

uniformly distributed. We speak of *local* in the sense that the exchange-correlation energy at each point in space is a function of the electron density at that point alone (and not from its derivatives). Hence, one assumes that the density can be treated locally as in a uniform electron gas. At each point of an uniform electron gas, one has an exchange-correlation energy per particle ϵ_{xc} of density ρ . By adding up this energy per density in a continuous way, we obtain the following integral formulation:

$$E_{xc}^{\text{LDA}}[\rho] = \int_{Q^3} \epsilon_{xc}[\rho(\vec{r})]\rho(\vec{r})d\vec{r} \quad (3.6)$$

Its functional derivative provides us then the expression to be inserted in eqs. 3.1.1:

$$\frac{\delta E_{xc}[\rho(\vec{r})]}{\delta \rho(\vec{r})} = \epsilon_{xc}[\rho(\vec{r})] + \rho(\vec{r})\frac{\partial \epsilon_{xc}(\rho)}{\partial \rho} \quad (3.7)$$

What is the explicit expression of $\epsilon_{xc}[\rho(\vec{r})]$, though? Among different possibilities, the most accepted one consists of splitting this functional into an exchange and correlation term, respectively ϵ_x and ϵ_c . The first one is determined by the assumption of being in a homogeneous electron gas, for which one can use the Dirac functional:

$$\epsilon_x^{\text{LDA}} = -\frac{3}{4}\sqrt{\frac{3}{\pi}}\rho(\vec{r}) \quad (3.8)$$

For the correlation term, analytic expressions are known only in the limiting cases of high and low densities which correspond, respectively, to correlations of infinitely-weak and infinitely-strong character. With use of Quantum Monte-Carlo simulations, cases of intermediate densities can also be determined by interpolation. The most famous approaches to explicitly describe ϵ_c are those of Vosko-Wilk-Nusair (VWN) [158], Perdew-Zunger (PZ81) [159], Cole-Perdew (CP) [160] and Perdew-Wang (PW92) [161].

The LDA method works remarkably well and, since the functional ϵ_{xc} depends only on ρ , it is also relatively fast in terms of computational effort. On the other hand, however, it can only describe very well systems in which the density does not vary quickly. As we will see within this same chapter, LDA is thus an excellent approach to determine the properties of crystalline structures, but gives serious problems in describing a dynamical water network.

- **Generalized gradient approximation (GGA)**. An improvement to LDA which takes into account densities that undergo rapid changes can be done by considering also the gradient of ρ as an active variable:

$$E_{xc}^{\text{GGA}} = \int_{Q^3} \epsilon_{xc}(\rho, \nabla \rho)\rho(\vec{r})d\vec{r} \quad (3.9)$$

Theoretically, since the pioneering work of Hohenberg, Kohn, and Sham,

density gradients have been thought of as natural tools for the development and systematic improvement of the exchange and correlation functional with respect to local approximation. For two decades these attempts gave disappointing results until, thanks to Perdew [162, 163], were understood the reasons for failure and the principles on which to base a development in density gradients such as not to violate some basic rules of sum. The presence of the gradient describes eventual non-uniformity of the density in the neighborhood of \vec{r} and is reabsorbed in the case of homogeneous electron gas (being the gradient of a constant equal to the null vector). The most accepted assumption of LDA failure was in that it was especially the exchange term that was affected by non-homogeneous densities. For this reason, Perdew proposed an accurate shape exchange term, namely

$$E_x^{\text{GGA}} = \int_{\mathcal{Q}^3} \epsilon_x(\rho) \rho(\vec{r}) F_x(s) d\vec{r}, \quad (3.10)$$

where $s = \nabla \rho(\vec{r}) / \rho(\vec{r})^{4/3}$ is a replacement variable consisting in a dimensionless density gradient. F is a function which shall be fitted case by case depending on the desired GGA method. In our work, we relied on the Perdew-Burke-Ernzerhof approach [162, 163], for which this function has the following expression:

$$F_x(s) = 1 + k + \frac{k}{1 + \frac{\mu s^2}{k}}, \quad (3.11)$$

with $k = 0.804$ being a mathematical constant and $\mu \approx 0.21951$ being the effective gradient coefficient of exchange.

- **Becke, 3-parameter, Lee–Yang–Parr (B3LYP)**. Another way to deal with approximations of the exchange and correlation term is to introduce hybrid functionals. These are approaches in which the exact exchange functional of HF, namely

$$E_x^{\text{HF}} = -\frac{1}{2} \sum_{i=1}^n \sum_{j=1}^n \int \int_{\mathcal{Q}^6} \psi_i^*(\vec{r}_1) \psi_j^*(\vec{r}_2) \frac{1}{\|\vec{r}_1 - \vec{r}_2\|} \psi_i(\vec{r}_1) \psi_j(\vec{r}_2) \quad (3.12)$$

is mixed in a certain amount within the exchange and correlation term found through other approaches. Deciding how much each energy term weighs is a set of parameters that must be fitted or experimental values. The B3LYP method is one of the most widely used hybrid functionals [164, 165]. It consists in considering a fraction of the exact exchange of eq. 3.12 within a three-parameter combination (hence the 3 in the acronym) between LDA and GGA:

$$E_{xc}^{\text{B3LYP}} = E_x^{\text{LDA}} + \alpha_0 (E_x^{\text{HF}} - E_x^{\text{LDA}}) + \alpha_x (E_x^{\text{GGA}} - E_x^{\text{LDA}}) + E_c^{\text{LDA}} + \alpha_c (E_c^{\text{GGA}} - E_c^{\text{LDA}}) \quad (3.13)$$

with $\alpha_0 = 0.20$, $\alpha_x = 0.72$ and $\alpha_c = 0.81$. Since the functional takes into account five different terms (E_x^{HF} , E_x^{LDA} , E_x^{GGA} , E_c^{LDA} , E_c^{GGA}), it requires

considerable computational effort. In general, any hybrid method such as HSE [166] or PBE0 [167, 168], can only deal with very small systems and should therefore be used for static calculations that require a lot of precision, such as densities of states.

Electronic structures in crystals

Regular crystal structures are characterized by the repetition of a unit cell in the three spatial directions. In chapter 2 we have already observed how the use of Periodic Boundary Conditions (PBC) helps in the creation of very large structures and the diffusion of adsorbates throughout the simulation box. Perhaps the biggest advantage of using PBCs lies in the simplification they allow for computational calculations of the electronic structure. If \vec{a}_1 , \vec{a}_2 and \vec{a}_3 are the lattice vectors of the primitive unit cell, we can reach each point of a mirrored image by use of a lattice vector of the form

$$\vec{R} = n_1\vec{a}_1 + n_2\vec{a}_2 + n_3\vec{a}_3, \quad n_1, n_2, n_3 \in \mathbb{Z} \quad (3.14)$$

Let us now suppose that the crystal is composed of N_j repetitions of the unit cell along \vec{a}_j , with $j = 1, 2, 3$. The proper boundary conditions for the single-particle states within an infinite crystal can be given by the Born-von Karman approach [169, 170]:

$$\psi_{\vec{k}}(\vec{r}) = \psi_{\vec{k}}(\vec{r} + N_j\vec{a}_j) \quad (3.15)$$

where \vec{r} lies inside the primitive unit cell. With use of Bloch's theorem statement (appendix 6), we have then that

$$\begin{aligned} e^{i\vec{k} \cdot (N_j\vec{a}_j)} = 1 &\iff e^{i2\pi k_j N_j} = 1 \iff 2\pi k_j N_j = 2\pi h_j \\ &\iff k_j = \frac{h_j}{N_j}, \text{ with } h_j \in \mathbb{Z} \end{aligned}$$

Note that \vec{k} may take up to $N = N_1 N_2 N_3$ distinct values, since h_j can take only N_j inequivalent values that satisfy the above equation. We can assume that they can be any any N_j consecutive integer values: beyond and within this range, h_j would correspond to adding integer multiples of $2\pi i$ to the argument of the exponential and it would therefore give equivalent results. This restricts non-equivalent values of \vec{k} to a specific volume corresponding to the primitive unit cell of the reciprocal space \mathcal{R} , named the first Brillouin zone. This volume in reciprocal space is known as the first Brillouin Zone. Finally, we can ask what happens in the case where the crystal is endowed with an infinitely coarse periodicity, that is, when $N_j \rightarrow \infty$. In this case, we shall first evaluate the differential volume change in \vec{k} . In order to do that, we can make use of eq. A.26 together with the fact that $\Delta h_j = 1$ for any $j = 1, 2, 3$:

$$\begin{aligned} \Delta^3 \vec{k} &= \Delta \vec{k}_1 \cdot (\Delta \vec{k}_2 \times \Delta \vec{k}_3) \\ &= \frac{\Delta h_1 \vec{b}_1}{N_1} \cdot \left(\frac{\Delta h_2 \vec{b}_2}{N_2} \times \frac{\Delta h_3 \vec{b}_3}{N_3} \right) = \left\| d\vec{k} \right\| = \frac{(2\pi)^3}{N\Omega_{PUC}} \end{aligned} \quad (3.16)$$

From the above expression it is clear that an increase in size of the primitive unit cell leads to a null differential, namely a constant value of \vec{k} . In other terms, the bigger the primitive unit cell is, the less k-points are needed to obtain accurate results and viceversa. This concept leads to a very important benchmark when it comes to energy calculations, as it is important to distribute an enough amount of k-points in the reciprocal space in order to obtain precise outcomes. Care must be taken, however, not to use k-points when it is not necessary, as the computational effort that is expended increases significantly with the use of dense meshes. In the case of ab-initio MDs, it is therefore advisable to use only one k-point, which coincides with the center of the Brillouin zone. This is denoted as Γ -point and, together with other points of the Brillouin zone (M, R, X, K, L, U, ...), it plays a key role in the study of electronic band structures.

All DFT calculations performed in this thesis are based on a code that develops the $u_{h,\vec{k}}(\vec{r})$ in plane-waves, with h indicating the h -atomic orbital index:

$$u_{h,\vec{k}} = \frac{1}{\sqrt{\Omega_{\text{PUC}}}} \sum_{\vec{G} \in \mathcal{R}} c_{h,\vec{G},\vec{k}} e^{i\vec{G} \cdot \vec{r}} \quad (3.17)$$

In the above expression, $c_{h,\vec{G},\vec{k}} \in \mathbb{C}$ are Fourier complex coefficient. In terms of single-particle Kohn-Sham wavefunctions, it immediately follows that

$$\psi_{h,\vec{k}}(\vec{r}) = u_{h,\vec{k}} e^{i\vec{k} \cdot \vec{r}} \frac{1}{\sqrt{\Omega_{\text{PUC}}}} \sum_{\vec{G} \in \mathcal{R}} c_{h,\vec{G},\vec{k}} e^{i(\vec{G} + \vec{k}) \cdot \vec{r}} \quad (3.18)$$

Of course, it is not possible to develop the basis set in all wave vectors of the reciprocal space \mathcal{R} and that is why cut-off energy sets are needed: only wave vectors satisfying the relation $\frac{1}{2} \left\| \vec{G} + \vec{k} \right\|^2 \leq E_{\text{cut-off}}$ will be considered in the summation. This assumption brings an additional advantage to plane-waves: the convergence of the energy can be controlled directly by increasing or decreasing the single parameter of the cut-off energy.

The main disadvantage of this approach is that it is necessary to sum many plane-waves to obtain a proper energy description, which results in high energy cut-offs and more expensive computational costs. The problem arises from the description of tightly bound states, which are spacially strong localized, and contributing electrons with fast oscillations in the wavefunction. These are mostly core electrons, which usually possess very high energy: electrons belonging to the 1s shell contribute with values up to $-13.6Z^2$ eV, where Z is the atomic number. Since these energies rapidly go to zero as the distance from the center of the nucleus increases, a trivial idea to solve this issue might be to eliminate their contributions completely. This, however, would result in slight errors that gradually accumulate and end up dominating the scene. A better approach consists in the frozen core approximation [154], in which the contribution of the core electrons is pre-calculated at the very beginning of the simulation and then kept constant without allowing any variation of their corresponding wavefunctions. An even more effective method is to completely remove the core orbitals to include an orthogonality constraint to them with the Coulomb potential. This produces an effective potential acting on the valence electrons,

called pseudopotential, which mimics the original one from some distance \vec{r}_c , as shown in fig. 3.4. Pseudopotentials allow one to achieve energy convergence

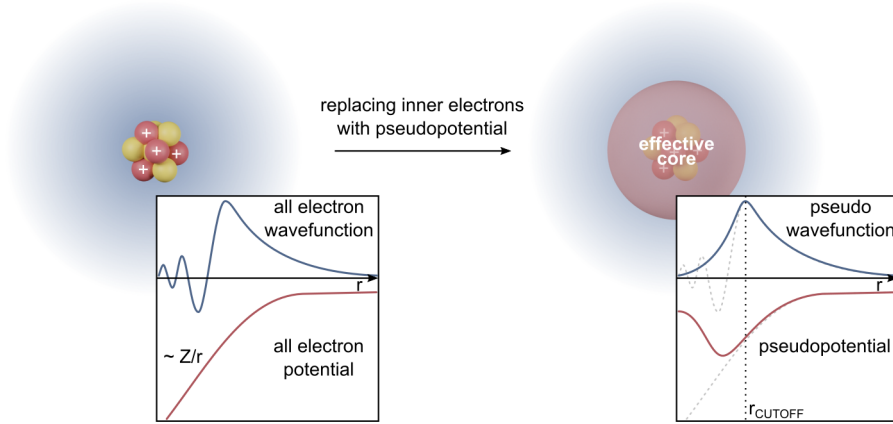


Figure 3.4: Representation of an electrostatic potential $V \approx \frac{Z}{\|\vec{r}\|}$ (red curve in the left panel), with Z being the nuclear charge number, and a corresponding pseudopotential $V_{\text{pseudo}}(\|\vec{r}\|)$ (red curve in the right panel). In the upper part of the graphs the relative wavefunctions are also shown. Image under free license by [Edvin Fako](#).

of the basis set very quickly, but they incur several problems. First, there is no single pseudopotential for each element and it is relatively easy to construct one that fails without noticing it. The estimate of core electrons is also still too rough, leading to a priori assumptions about them that turn out to be wrong. Among the latest and most accurate methods developed to address these additional issues is Projector-Augmented Wave (PAW), which was developed in 1994 by Peter Blöchl [171]. The idea is to use some auxiliary functions $|\tilde{\psi}_h(\vec{r})\rangle$ within an augmentation sphere. Its radius \vec{r}_c represents a boundary beyond which the auxiliary functions coincide with the true ones:

$$|\tilde{\psi}_h(\vec{r})\rangle = |\psi_h(\vec{r})\rangle \iff \|\vec{r}\| \geq \|\vec{r}_c\| \quad (3.19)$$

The region inside is instead where the core electrons need to be treated properly. We want to construct the auxiliary functions in a way that they can be analytically representable as a plane-wave expansion, corresponding to a smoothed version of the true $|\psi_h(\vec{r})\rangle$. Therefore, we want to define an operator \hat{U} such that

$$|\tilde{\psi}_h(\vec{r})\rangle = \hat{U} |\psi_h(\vec{r})\rangle \iff \|\vec{r}\| \leq \|\vec{r}_c\| \quad (3.20)$$

Our interest actually lies in the inverse operator, $\hat{T} := \hat{U}^{-1}$, for which the following holds:

$$|\psi_h(\vec{r})\rangle = \hat{T} |\tilde{\psi}_h(\vec{r})\rangle \iff \|\vec{r}\| \leq \|\vec{r}_c\| \quad (3.21)$$

If we now insert the above expression into the corresponding Kohn-Sham equation we obtain:

$$\left(\hat{T}^\dagger \hat{H} \hat{T} - \hat{T}^\dagger T \epsilon_h \right) \hat{T} |\tilde{\psi}_h(\vec{r})\rangle = 0 \quad (3.22)$$

with \hat{T}^\dagger adjoint operator of \hat{T} . The Kohn-Sham equations are easily solvable for the auxiliary wavefunctions as long as the operator \hat{T} is known. This should be linear and non-local. We assume that it is of the form of

$$\hat{T} = 1 + \sum_{\alpha} \hat{T}_{\alpha} \quad (3.23)$$

which means it is composed of many operators \hat{T}_{α} , each of one acts on the atomic index α . They can be identified by inserting this structure in eq. 3.21 for the atomic index α_i :

$$\begin{aligned} |\psi_j(\vec{r})\rangle &= |\tilde{\psi}_j(\vec{r})\rangle + \hat{T}_{\alpha_i} |\tilde{\psi}_j(\vec{r})\rangle = \\ \hat{T}_{\alpha_i} |\tilde{\psi}_j(\vec{r})\rangle &= |\psi_j(\vec{r})\rangle - |\tilde{\psi}_j(\vec{r})\rangle = \sum_{j=1}^n \left(|\psi_j(\vec{r})\rangle - |\tilde{\psi}_j(\vec{r})\rangle \right) \underbrace{\langle \tilde{p}_i | \psi_j \rangle}_{\delta_{ij}} \\ \Rightarrow \hat{T} &= 1 + \sum_{j=1}^n \left(|\psi_j(\vec{r})\rangle - |\tilde{\psi}_j(\vec{r})\rangle \right) \langle \tilde{p}_j | \end{aligned}$$

with \tilde{p}_i being projector functions.

Dispersion corrections

According to Hohenberg-Kohn theorem, DFT is an exact method for detecting the GS energy of a system. The presence and effects of Van der Waals (VdW) interactions is then, in principle, automatically implemented as a consequence of this exactness. Approximations of the exchange-correlation functional, though, generate an inaccuracy that is then inherited by VdW effects. As long as one is interested in the electronic properties of crystal solids, VdW interactions are negligible. The same does not apply, however, when an adsorbate approach a surface or when a water net bulk is present as an explicit solvent, which is our case in this thesis. It is therefore necessary to apply an energetic correction term able to describe in a proper manner this important dispersion. The main approaches developed so far consists of semi-empirical methods (DFT-D2)[172, 173], models with environmental dependencies (DFT-D3, Tkatchenko-Scheffler) [174, 175], specifically defined functionals (VdW-DF) and techniques going beyond pairwise interactions such as the development of many-body dispersion terms or random-phase approximations. In our work, both for DFT and DFTB calculations, we used the zero-damping DFT-D3 dispersion correction of Grimme. This approach follows the general idea of DFT-D2 (see appendix 6). It consists of improving the dispersion correction by changing the coupled dispersion coefficients $C_{6,J}^{(D2)}$ into new ones, here named $C_{6,J}^{(D3)}$, which depend on the molecular geometry. Among the three variants of DFT-D3, we present here the zero-damping DFT-D3 method of Grimme. Its name comes from the fact that two damping functions $f_{d,n}$ are defined to show a maximum contribution for medium-range distances to then damp down very fast. The index $n = 6, 8$ represents how strong the damping is ($n = 6$ in DFT-D2). Values of n smaller

than 6 would provide too strong interactions (remember that also in the classical approach, with Lennard-Jones and Buckingham potentials they use this rate), whereas values higher than $n = 8$ proved to contribute in a completely negligible way. The definition of the two DFT-D3 damping functions is given by

$$\begin{cases} \frac{1}{1+6\left(\frac{\|\vec{R}_I-\vec{R}_J\|}{s_{r,6}R_{0IJ}^{(D3)}}\right)^{-\alpha_6}} & \text{if } n = 6 \\ \frac{1}{1+6\left(\frac{\|\vec{R}_I-\vec{R}_J\|}{R_{0,IJ}^{(D3)}}\right)^{-\alpha_6-2}} & \text{if } n = 8 \end{cases} \quad (3.24)$$

Again, $s_{r,6}$ is a functional-dependent scaling factor, whereas α_6 is a parameter determining the steepness of the damping function. The energetic dispersion term $E_{\text{corr}}^{(\text{DFT-D3})}$ to add to the total Kohn-Sham energy $E^{(\text{DFT})}$ is then given by

$$E_{\text{disp}}^{(\text{D3})} = -\frac{1}{2}s_6 \sum_{I=1}^N \sum_{J=1}^N \sum_{n=6,8} s_n \frac{C_{n,IJ}^{(\text{D2})}}{\|\vec{R}_I - \vec{R}_J\|^n} f_d^{(\text{D2})}(\|\vec{R}_I - \vec{R}_J\|) \quad (3.25)$$

The question is now to understand how the coupled dispersion coefficients are defined, which shall depend on the molecular geometry. This is done by relating them to the coordination number, which describes how many neighbor atoms are close to the I -th atom considered. In order to do this, we first define the fractional coordination number as

$$CN(I) = \sum_{I=1}^N \sum_{J=1}^N \frac{1}{1 + e^{-16 \left[\left(\frac{4R_{I,\text{cov}} + R_{J,\text{cov}}}{3\|\vec{R}_I - \vec{R}_J\|} \right) - 1 \right]}}, \quad (3.26)$$

where $R_{I,\text{cov}}$, $R_{J,\text{cov}}$ are Pyykkö-Atsumi covalent radii. At this point, we need to introduce the six-ordered reference dispersion coefficients of the environment $C_{6,IJ}^{(\text{D3-ref})}(CN(I), CN(J))$, which are then used to define the coupled six-ordered dispersion coefficients $C_{6,IJ}^{(\text{D3})}(CN(I), CN(J))$, in a way similar to DFT-D2. Their expression is based on a modified variant of the Casimir-Polder formula [172, 173, 176]:

$$C_{6,IJ}^{(\text{D3-ref})}(CN(I), CN(J)) = \frac{3}{\pi} \int_0^{+\infty} \left\{ \frac{1}{m} [\alpha_{I_m H_n}(i\omega) - \frac{n}{2} \alpha_{H_2}(i\omega)] \times \frac{1}{k} [\alpha_{J_k H_l}(i\omega) - \frac{1}{2} \alpha_{H_2}(i\omega)] \right\} d\omega \quad (3.27)$$

Here we have element hydrides as reference compounds, named after $I_m H_n$ and $J_k H_l$, where m , n , l and k are stoichiometric coefficients. We have to consider that energetically low-lying atomic states would influence the polarizabilities $\alpha(i\omega)$, with ω imaginary frequency, by leading to large dispersion coefficients. Hydrides were then chosen instead in order to avoid this issue, as they are simple and well-defined. We can now define the coupled six-ordered dispersion

coefficients by the following expression:

$$C_{6,IJ}^{(D3)}(CN(I), CN(J)) = \frac{\sum_{a=0}^{N_a} \sum_{b=0}^{N_b} C_{6,IJ}^{(D3-ref)}(CN(I)_a, CN(J)_b) L_{ab}}{\sum_{a=0}^{N_a} \sum_{b=0}^{N_b} L_{ab}} \quad (3.28)$$

The generation of these coefficients is performed by letting the fractional coordinates $CN(I)$ and $CN(J)$ span a 2-dimensional grid with N_a and N_b mesh points. The term L_{ab} is a Gaussian-type function describing the distance between grid points and it is given by

$$L_{ab} = e^{-4\{[CN(I)-CN(I)_a]^2 + [CN(J)-CN(J)_b]^2\}} \quad (3.29)$$

Having the six-ordered dispersion coefficients, the eight-ordered ones can be defined straight away:

$$C_{8,IJ}^{(D3)} = 3C_{6,IJ}^{(D3)} \sqrt{\frac{1}{4} \sqrt{Z_I Z_J} \frac{\langle R^4 \rangle_I \langle R^4 \rangle_J}{\langle R^2 \rangle_I \langle R^2 \rangle_J}} \quad (3.30)$$

In the above expression, Z_I and Z_J are the nuclear charges of atoms I and J , respectively, whereas symbols $\langle \cdot \rangle$ represent expectation values of dipoles (for R^2) and quadrupoles (for R^4), which can be derived by atomic densities.

Now that we possess all the terms, it is possible to insert them into the eq. 3.25 to obtain the dispersion energy and finally correct the Kohn-Sham total energy.

3.1.2 Density Functional Tight-Binding

DFT is undoubtedly a very valid method that has been incredibly successful over the years [82]. Despite its computational speed compared to other ab-initio methods, such as HF, DFT struggles to support systems with more than 1000 atoms and time scales longer than a dozen picoseconds. FF theory can be a viable alternative, but as already explained in the 2 chapter, it does not allow to study the electronic structure adequately and thus to observe chemical reactions such as bond formation or breaking. The meeting point between these two methods is represented by the semi-empirical tight-binding approaches, which have been existing from the very beginning. In the mid-90s Eschrig, Seifert, Frauenheim and co-workers developed the method of Density Functional Tight-Binding (DFTB) [83]. They are based on a parameterization and fitting of the potentials of the ab-initio methods, without exploiting classical approximations such as those found in FF. The name *tight-binding* derives from the approximation of the system Hamiltonian to a one related to a single form of the atomic orbital. The fundamental assumption consists of working with atomic orbitals of very small size relative to lattice distances, for which their interaction with neighboring states is pretty limited. In this way, it is possible to keep the electronic information within the system while drastically accelerating the computation of Kohn-Sham solutions. Although this approach was therefore developed to work well with covalently bonded systems, such as hydrocarbons, it can generally be used for other materials as well.

In the following derivation (which is the conventional one), we are going to work with $\frac{\hbar^2}{m_e} = 4\pi\epsilon_0 = e = 1$. In the many-body, stationary, electronic hamiltonian [A.1](#) we consider the ion-ion potential as well, here denoted as $V_{\text{ions}}(\{\vec{R}_H\}_H)$. The method of DFTB, as the name suggests, is based on DFT. The idea is to perform a perturbation $\delta\rho$ of the GS electronic density ρ_{GS} . Since the total DFT energy functional $E[\rho]$ is smooth (variational) with respect to the density, for a sufficiently small $\delta\rho_0$ we can assume the existence of another density ρ_0 which, although it does not minimize $E[\rho]$, gets close to it: $E[\rho_{\text{GS}}] = E[\rho_0 + \delta\rho]$. This justifies a Taylor expansion of the energy functional in ρ_0 which, for the scope of this thesis, can be truncated at the second order:

$$E[\delta\rho] = \sum_{i=1}^n \langle \psi_i | -\frac{\Delta_i}{2} + V_{\text{ext}}(\vec{r}) + \int_{\mathcal{Q}^3} \frac{\rho'_0(\vec{r})}{\|\vec{r} - \vec{r}'\|} d\vec{r}' + V_{\text{xc}}[\rho_0] | \psi_i \rangle + \quad (3.31)$$

$$+ \frac{1}{2} \int \int_{\mathcal{Q}^6} \left(\frac{\delta^2 E_{\text{xc}}[\rho_0]}{\delta\rho\delta\rho'} + \frac{1}{\|\vec{r} - \vec{r}'\|} \right) \delta\rho\delta\rho' d\vec{r}d\vec{r}' + \quad (3.32)$$

$$- \frac{1}{2} \int \int_{\mathcal{Q}^6} \frac{\rho_0(\vec{r})\rho'_0(\vec{r}')}{\|\vec{r} - \vec{r}'\|} d\vec{r}d\vec{r}' + E_{\text{xc}}[\rho_0] - \int_{\mathcal{Q}^3} V_{\text{xc}}[\rho_0](\vec{r})\rho_0(\vec{r})d\vec{r} + V_{\text{ions}} \quad (3.33)$$

The above expression can be written as the sum of specific energetic terms. Expressions [3.31](#), [3.32](#) and [3.33](#) are defined as the band-structure energy $E_{\text{b-s}}[\delta\rho]$, the charge fluctuation energy $E_{\text{coul}}[\delta\rho]$ and the repulsive energy E_{rep} , respectively. Hence, the same expression can be rewritten as:

$$E[\delta\rho] = E_{\text{b-s}}[\delta\rho] + E_{\text{coul}}[\delta\rho] + E_{\text{rep}} \quad (3.34)$$

Some approximations of the last two terms need then to be introduced (see [appendix 6](#)).

The tight-binding approach assumes that the description of the electrons is provided by a minimal local basis set. This means that there exists only one basis function for each orbital μ at atom I , which in turn consists of the commonly used real spherical harmonics $\tilde{Y}(\theta, \varphi)$ of angles θ and φ . Each single electronic orbital can then be expanded as

$$|\psi_i(\vec{r})\rangle = \sum_{\mu} c_{\mu}^I \left| \phi_{\mu}(\vec{r} - \vec{R}_I) \right\rangle, \quad (3.35)$$

where $\left| \phi_{\mu}(\vec{r} - \vec{R}_I) \right\rangle = R_{\mu}(\vec{r})\tilde{Y}(\theta, \phi)$, with $R_{\mu}(\vec{r})$ being an auxiliary function. The index μ is here described to run up to a pre-defined maximal number of atomic orbitals. We can now observe how the expression of the band-structure

energy $E_{\text{b-s}}[\delta\rho]$ changes when this form of $|\psi_i(\vec{r})\rangle$ is inserted into it:

$$E_{\text{b-s}}[\delta\rho] = \sum_{I=1}^N \sum_{\mu} \sum_{\nu} c_{\mu}^{I*} c_{\nu}^I \underbrace{\langle \phi_{\mu} | -\frac{\Delta_i}{2} + V_{\text{ext}}(\vec{r}) + \int_{\mathcal{Q}^3} \frac{\rho'_0(\vec{r}')}{\|\vec{r} - \vec{r}'\|} d\vec{r}' + V_{\text{xc}}[\rho_0] | \phi_{\nu} \rangle}_{H_{\mu\nu}^0} \quad (3.36)$$

The matrix $H_{\mu\nu}^0$ is strictly connected both to the Kohn-Sham hamiltonian operator as well as the two minimal basis functions ϕ_{μ} and ϕ_{ν} . Hence, the core of the tight binding concept is strictly related to this numerical matrix which is, in turn, what one needs to parametrize in order to perform any DFTB calculation. The same replacement can be done for the electron populations Δq_I , since we know from DFT that $\delta\rho = \sum_{i=1}^n \|\psi_i(\vec{r})\|_{\mathbb{C}}^2$. From eq. A.36 it follows that

$$\begin{aligned} q_I &= \int_{V_I} \rho(\vec{r}) d\vec{r} = \sum_{i=1}^n \int_{V_I} \|\psi_i(\vec{r})\|_{\mathbb{C}}^2 d\vec{r} \\ &= \sum_{i=1}^n \sum_{\mu} \sum_{\nu} c_{\mu}^I c_{\nu}^I \int_{V_I} \phi_{\mu}^*(\vec{r}) \phi_{\nu}(\vec{r}) d\vec{r} \end{aligned} \quad (3.37)$$

Here, only three possible situations can occur. First, if μ and ν belongs to the same atomic volume V_I , then the expression will be roughly 0. Similarly, if μ and ν are both part of the same volume, then the results will roughly be given by Kronecker delta $\delta_{\mu\nu}$, since the corresponding functions are building an orthonormal basis of the Hermitian space. Finally, the situation in which $\mu \in V_I$, but $\nu \notin V_I$ gives rise to the overlap matrix $S_{\mu\nu}$:

$$\int_{V_I} \phi_{\mu}^*(\vec{r}) \phi_{\nu}(\vec{r}) d\vec{r} = \frac{1}{2} \int_V \phi_{\mu}^*(\vec{r}) \phi_{\nu}(\vec{r}) d\vec{r} := \frac{1}{2} S_{\mu\nu} \quad (3.38)$$

We have now all the ingredients to write down the total energy $E[\delta\rho]$ by adding all the assumptions and approximations introduced. Its variation, following the Rayleigh-Ritz theorem together with Lagrangian multipliers ε_i constraining the orthonormality of $|\psi_i\rangle$ as in DFT, produces the DFTB Kohn-Sham equations:

$$\sum_{\nu=1}^N c_{\nu}^i (H_{\mu\nu} - \varepsilon_i S_{\mu\nu}) = 0 \quad (3.39)$$

where $H_{\mu\nu}^0 = H_{\mu\nu} + \frac{1}{2} S_{\mu\nu} \sum_{K=1}^N (\gamma_{IK} + \gamma_{JK}) \Delta q_k$. Also in this case, these equations need to be solved self-consistently, with an initial guess based on $\{\Delta q^I\}_I$.

3.1.3 Methods of analysis

In this section we are going to introduce some useful tools for analyzing our results. All of them use the electronic properties of the system, previously

evaluated, to provide significant additional information, such as the stability of a configuration or the possibility of accessing an excited state (ES).

Surface energies

A crystalline surface is for all intents and purposes a defect in the solid, since it consists of the breaking of its molecular bonds. Exposed atoms are therefore undercoordinated and can promote reactions with molecules in their surroundings to seek saturation. To break a crystal structure it is necessary to exploit external energy, which happens all the time in nature through mostly mechanical forces. Compared to pure bulk structure, a crystal surface it is less energetically favorable. The so-called surface energy is an important quantity that can be derived both experimentally and analytically. It represents the energy at the surface, resulting from incomplete bonding. The surface energy is a measurement of the stability of a slab: the higher it is, the more the solid acquires a propensity of degenerating into reconstructions.

We derive here the method used in DFT calculations for metal oxides, specifically referring to TiO_2 . Here we talk of surface *free* energy, as they are related to the Gibbs (Helmoltz) free energy. If the crystal is stoichiometric, the surface energy can directly be evaluated by using the expression

$$\gamma_{\text{surf}} = \frac{E_{\text{slab}} - N_{\text{Ti}}E_{\text{bulk}}}{2A} \quad (3.40)$$

where E_{slab} is the total energy of the slab model containing N_{Ti} atoms (namely TiO_2 units) and E_{bulk} is the energy of a single bulk unit. The exposed surface area is then twice the area A of the $\{x, y\}$ plane in the surface primitive cell, since the slab model is usually created by symmetrically cutting the bulk structure both from the top and from the bottom, leaving two exposed surfaces. Thanks to this formula it is possible to relate the surface energy with the number of layers taken into account. If one wants to perform calculations on crystalline surfaces it is necessary to make sure that the bulk structure in the slab is sufficiently stable. A too poor cut, which takes into account less than 3 layers, would result in the creation of an unstable structure or with strong interactions between the surface above and below, like a 2D-material like graphene. On the other hand, too rich a cut would increase the computational burden, as each layer considered adds degrees of freedom to the system. For this reason it is necessary to find a good compromise by observing the typical oscillations of the surface free energy with respect to the number of layers. They are due to several factors, such as the creation of a dipole in the case where the surface above was not cut symmetrically with respect to the one below, a phenomenon that often occurs when the number of layers considered is odd. As the number of layers increases, the structure (which is from time to time appropriately brought to a local minimum energy through a geometry optimization) becomes more and more stable and the surface energy finds a plateau along a horizontal asymptote.

In case of unstoichiometric systems, it is necessary to modify the expression 3.40 in a proper way [177]. In order to do this, we should first understand

how DFT is actually calculating the energy term E_{slab} . Let us then consider the metal oxide as if it was embedded in an atmosphere oxygen reservoir at a certain temperature T and pressure p . This means that the O_2 molecules can either increase at the TiO_2 interface or be taken out from it, leading to unstoichiometric systems. The right energy to take into account when describing such an interaction would be the Gibbs free energy $G(T, p, N_{\text{Ti}}, N_{\text{O}})$, for which the surface free energy can be evaluated similarly to 3.40:

$$\gamma_{\text{surf}} = \frac{G(T, p, N_{\text{Ti}}, N_{\text{O}}) - N_{\text{Ti}}\mu_{\text{Ti}}(T, p) - N_{\text{O}}\mu_{\text{O}}(T, p)}{2A} \quad (3.41)$$

The two terms $\mu_{\text{Ti}}(T, p)$ and $\mu_{\text{O}}(T, p)$ are the chemical potentials of the corresponding elements at a temperature T and pressure p . We now suppose that the bulk structure, which is stoichiometric, contains enough atoms such that the following relationship holds:

$$g_{\text{TiO}_2}^{\text{bulk}}(T, p) = \mu_{\text{Ti}}(T, p) + 2\mu_{\text{O}}(T, p) \quad (3.42)$$

In the above expression, $g_{\text{TiO}_2}^{\text{bulk}}(T, p)$ is the Gibbs free energy per formula unit at temperature T and pressure p . By inserting it in the surface free energy 3.41 we then obtain a dependence only in terms of one chemical potential, for instance from our reservoir represented by μ_{O} :

$$\gamma_{\text{surf}} = \frac{G(T, p, N_{\text{Ti}}, N_{\text{O}}) - N_{\text{Ti}}g_{\text{TiO}_2}^{\text{bulk}}(T, p) + (2N_{\text{Ti}} - N_{\text{O}})\mu_{\text{O}}(T, p)}{2A} \quad (3.43)$$

The issue of this formalism lies exactly in the Gibbs free energy, which does not correspond to the resulting total energy computed in DFT. The latter is actually the Helmholtz free energy of the system at zero temperature $E_{\text{total}}^{(\text{DFT})}(V, N_{\text{Ti}}, N_{\text{O}})$, which also depends on the volume V of the used supercell. This energy is also neglecting zero-point vibrations; the real Helmholtz free energy of the system $F(V, N_{\text{Ti}}, N_{\text{O}})$ should then take them into account through an additional vibrational term $F_{\text{vib}}(T, V, N_{\text{Ti}}, N_{\text{O}})$:

$$\begin{aligned} F(T, V, N_{\text{Ti}}, N_{\text{O}}) &= E_{\text{total}}^{(\text{DFT})}(V, N_{\text{Ti}}, N_{\text{O}}) + F_{\text{vib}}(T, V, N_{\text{Ti}}, N_{\text{O}}) \\ &= E_{\text{total}}^{(\text{DFT})}(V, N_{\text{Ti}}, N_{\text{O}}) + E_{\text{vib}}(T, V, N_{\text{Ti}}, N_{\text{O}}) - TS_{\text{vib}}(T, V, N_{\text{Ti}}, N_{\text{O}}) \end{aligned} \quad (3.44)$$

The vibrational term was decomposed in vibrational energy $E_{\text{vib}}(T, V, N_{\text{Ti}}, N_{\text{O}})$, which includes zero-point vibrations, and entropic contribution $S_{\text{vib}}(T, V, N_{\text{Ti}}, N_{\text{O}})$. We can now relate the Gibbs free energy to the Helmholtz free energy:

$$G(T, p, N_{\text{Ti}}, N_{\text{O}}) = F(T, p, N_{\text{Ti}}, N_{\text{O}}) + pV(T, N_{\text{Ti}}, N_{\text{O}}) \quad (3.45)$$

A simple dimensional analysis shows though that the pV term is completely negligible, since it would contribute with energies (normalized to the surface area) about at magnitude of 10^{-8} meV/ \AA^2 , whereas in the pressure range DFT calculations are usually performed the order of magnitude is of 1 meV/ \AA^2 . The question is then now to understand if and under which conditions one can consider also the vibrational part $F_{\text{vib}}(T, V, N_{\text{Ti}}$ negligible. According to Reuter

and Scheffler's approach [177], one possible way is to consider the Einstein model to approximate the phonon density of states by using just one characteristic frequency ω for each atom type. In their work, they showed that for RuO₂ bulk values of $\omega_{\text{O}} = 80$ meV and $\omega_{\text{Ti}} = 25$ meV [178, 179] were sufficiently low to let this term contributing as much as the same order as the numerical uncertainty of DFT calculations (about $\pm 10\%$ meV/Å²). With all of these considerations, we can then rewrite eq. 3.41 in a DFT-computable fashion as it follows:

$$\gamma_{\text{surf}} = \frac{E_{\text{slab}} - N_{\text{Ti}}E_{\text{bulk}} + (2N_{\text{Ti}} - N_{\text{O}})\mu_{\text{O}}(T, p)}{2A} \quad (3.46)$$

The final piece of the puzzle consists then in the explicit introduction of the chemical potential of oxygen μ_{O} :

$$\mu_{\text{O}}(T, p) = \mu_{\text{O}}^0 + \frac{1}{2}k_{\text{B}}T\ln\left(\frac{p_{\text{O}_2}}{p^0}\right) \quad (3.47)$$

The term p^0 can correspond to the reference pressure used in an experiment the results of which one tries to reproduce. By letting p^0 being a simple parameter, one can evaluate how the surface energy $\gamma_{\text{surf}}(T, p^0)$ depends on the temperature. From the point where its graph intersects the constant value of the corresponding stoichiometric surface, the nonstoichiometric surface is likely to form. Values for μ_{O}^0 can be taken experimentally from, for instance, the JANAF thermochemical tables [180], which are referred though to the chemical potential of an oxygen molecule $\mu_{\text{O}_2}^{\text{JANAF}}(T, p^0)$. For this reason, one shall add to it the additional term $\frac{1}{2}E_{\text{O}_2}^{\text{DFT}}$ of an oxygen molecule total energy computed in DFT at $T = 0$ K. This allows the surface energy $\gamma_{\text{surf}}(T, p^0)$ to be in the oxygen-poor limit regime, which is a safe reference for DFT calculations, as explained more in detail by Reuter and Scheffler [177]. In conclusion, the formula we used in our calculations is:

$$\mu_{\text{O}}(T, p) = \frac{1}{2}\left[E_{\text{O}_2}^{\text{DFT}} + \mu_{\text{O}_2}^{\text{JANAF}}(T, p^0) + k_{\text{B}}T\ln\left(\frac{p_{\text{O}_2}}{p^0}\right)\right] \quad (3.48)$$

Density of States

As we have seen for both DFT and DFTB, the solution of the many-body Schrödinger equation can be (approximately) found in its GS configuration through the Kohn-Sham equations (A.22 in DFT and 3.39 in DFTB). The collection of solutions $\{|\psi_h(\vec{r})\rangle\}_h$ provides insights into how the electrons are arranged in the system, whereas the correspondent eigenvalues $\{\varepsilon_h\}_h$ gives rise to the band structure. An understanding of this information is fundamental, as it explains the way in which the electrons would respond to external perturbations. Through the band structure one can evaluate the width of the band gap as well as its property of being direct or indirect. Moreover, one can also read out the possible excitations that determine in turn optical properties such as color and reflectivity.

A key tool to analyze the band structure of a solid is provided by the density of states (DOS) [154]. As the name suggests, it consists of evaluating how many electronic states that are to be occupied are present per unit volume Ω

in a small energy range, say $\varepsilon + d\varepsilon$. Thanks to its graphical representation, one can immediately identify whether a material is a metal, an insulator or a semiconductor. If the DOS function is broken by an interval in which it has constant value equal to zero, then the left part of its graph collects the states of the valence band, while the one on the right those of the conduction band. When the Fermi level is located in correspondence of a non-zero area spaced by DOS, then the material is a metal: there is no distinction between valence and conduction band. If the Fermi level is instead located in a null area of DOS, then according to the width of the band gap the material can be considered insulator ($E_{\text{gap}} > 5.5$ eV at room temperature) or semiconductor (1.0 eV $< E_{\text{gap}} < 5.5$ eV at room temperature).

Let us now derive the general analytical form of the DOS. Supposing the energy levels are discrete and countable, then the DOS is defined by the following double sum over their total number N and wave-vectors \vec{k} in the reciprocal space \mathcal{R} :

$$g(\varepsilon) = \frac{1}{\Omega} \sum_{i=1}^N \sum_{\vec{k} \in \mathcal{R}} \delta(\varepsilon - \varepsilon_{\vec{k}}^{(i)}) \quad (3.49)$$

Here, δ is the Dirac delta function and $\{\varepsilon_{\vec{k}}^{(h)}\}_h$ are the energy levels uniquely characterized by their corresponding wave-vector \vec{k} . Note that, in this formalism, we are not taking into account spin degeneracy (which would contribute by a factor of 2) since all of the calculations performed in this work were not spin-polarized. Let us now consider the simple situation of $\Omega = L^3$, meaning that our system consists of a box of length L . In this case, the wave-vector differential $d\vec{k}$ is given by

$$d\vec{k} = \left(\frac{2\pi}{L}\right)^3 \quad (3.50)$$

and we can then assume that the sum becomes an integral over the reciprocal space as $L \rightarrow +\infty$:

$$g(\varepsilon) = \left(\frac{L}{2\pi}\right)^3 \sum_{i=1}^N \int_{\mathcal{R}} \delta(\varepsilon - \varepsilon_{\vec{k}}^{(i)}) d\vec{k} \quad (3.51)$$

Due to the properties of the Dirac delta function, we know that the integral argument will correspond to 1 over an energy surface $\partial\varepsilon^{(i)}$ on which $\varepsilon_{\vec{k}}^{(i)}$ is constant and equal to ε :

$$g(\varepsilon) = \left(\frac{L}{2\pi}\right)^3 \sum_{i=1}^N \int_{\partial\varepsilon^{(i)}} d\vec{k} \quad (3.52)$$

We can now choose a new coordinate system $\vec{k}' = (k'_x, k'_y, k'_z)$ such that one direction, say k'_z , lies perpendicular to the surface $\partial\varepsilon^{(i)}$ and then parallel to the gradient of $\varepsilon_{\vec{k}}^{(i)}$. Hence, we obtain that

$$d\varepsilon^{(i)} = \|\nabla_{\vec{k}} \varepsilon\| dk'_z \quad (3.53)$$

We then proceed by substitution in the integral to obtain the following double-integral:

$$g(\varepsilon) = \left(\frac{L}{2\pi}\right)^3 \sum_{i=1}^N \int \int_{\partial\varepsilon^{(i)}} \frac{1}{\|\nabla_{\vec{k}}\varepsilon\|} dk'_x dk'_y \quad (3.54)$$

An important consequence of this expression lies in the analysis of the critical points of the DOS. In fact, whenever we have wave-vectors \vec{k} for which $\varepsilon_{\vec{k}}^{(i)}$ has an extremum, the integrand in the DOS diverges. These roots of the denominator are of first order and introduce sharp features in $g(\varepsilon)$, called *van Hove singularities*. It can be proven that there exist four types of van Hove singularities in the three-dimensional space: they correspond to non-differentiable local minima, maxima or two different kinds of saddle points in the DOS. When computed numerically, the DOS of a system requires then a high number of k-points to ensure a proper evaluation of the integral as well as to correctly resolve these critical points.

Projected DOS are also possible, in which one focuses on a single element or on specific orbitals in order to achieve a more direct information on their contributions.

Energy of adsorption

An effective method to understand the intensity of attraction of a molecule to a surface is provided by the energy of adsorption [127, 122, 132]. Using Helmholtz free energies provided by DFT, it is possible to evaluate the energy of adsorption *per molecule* directly through the following formula:

$$\Delta E_{\text{ads}}^{\text{mol}} = \frac{1}{N_{\text{mol}}} (E_{\text{slab} + \text{mol}} - E_{\text{slab}} - N_{\text{mol}} E_{\text{mol}}) \quad (3.55)$$

In the above expression, $E_{\text{slab} + \text{mol}}$ is the total energy of the system with the adsorbing molecules on the surface, E_{slab} is the surface total energy, E_{mol} the energy of a single adsorbing molecule and N_{mol} the total number of adsorbing molecules. The lower and more negative the values of the adsorption energy, the stronger the interaction created at the molecule-surface interface. On the other hand, a positive value means that there is a repulsive force and therefore the adsorption reaction is unfavorable. The adsorption energy formula is straightforward and easy to compute, but needs some technical attention. First, it is advisable to always have a symmetric situation on both sides of the slab model. This means that the molecules whose reaction is observed are at least two, positioned in correspondence to two points of the surface corresponding in symmetry. This not only doubles the observation of the geometrically optimized configuration, ensuring that there is consistency between the bonds formed in the structure above and below the surface, but also ensures that no electric dipole is created in the case of a slab with few layers. Finally, it is necessary to ensure that the geometric optimization of each component of the system is performed in the same box and with the same number of k-points. In the first case, a sufficiently large molecule that feels an attraction even with its repeated image via PBC conditions in the system with the surface must possess the same interaction even when isolated. Instead, a consistent number of k-points ensures

that the reciprocal state remains consistent, preventing the creation of contrived errors.

3.2 Calculations protocols

The computational settings used in this chapter are listed below.

Exchange-correlation functionals

The DFT calculations were performed with the two exchange-correlation functionals of LDA and GGA-PBE and their results compared. Due to the better performance of GGA-PBE, only this one was used in all of the MD simulations as well as in all calculations of chapter 5. The *Self Consistent Field* (SCFs) absolute errors were set to 10^{-4} eV.

Benchmark of the bulk structure

the bulk structure of rutile-TiO₂ belongs to the group of tetragonal systems, in which a 3-fold coordinated Ti atom is surrounded by six 3-fold coordinated O atoms, forming an octahedron. In order to reproduce this structure in a controlled way, a single unit cell consisting in two TiO₂ molecules was taken into account, as shown in fig. 3.5. A supercell consisting in its repetition along the three cartesian coordinates was then built by using as starting lattice parameters the experimental values reported in Diebold's review ($a = b = 4.587\text{\AA}$, $c = 2.953\text{\AA}$) [39]. The first simulations conducted on the supercell

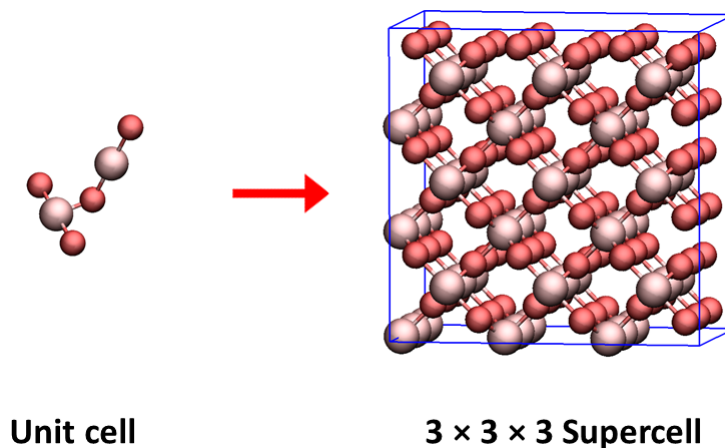


Figure 3.5: Ball-and-stick model of the unit cell of rutile-TiO₂ (left). It was repeated along the three cartesian directions up to a $3 \times 3 \times 3$ supercell (right).

consisted single point calculations performed at the default energy cut-off of 400 eV and Γ -point only mesh. By evaluating the total energy of the system with respect to the cell size, a size was found which could fit well for all further investigations. Here, the choice of the right pick was guided by two factors. First, one should ensure to have a sufficiently big size of the model, since in the

planned simulations the adsorption of glyphosate had to be taken into account. This molecule is in fact large enough to risk an interaction with its repeated image through the PBC conditions in case the supercell has a too narrow size. Secondly, the bigger the supercell, the more computational resources are needed to perform any calculation. A good balance composed by a $3 \times 3 \times 3$ repetition was then detected with a difference of 0.01 eV from the $2 \times 3 \times 3$ and of 0.04 eV from the $3 \times 3 \times 4$ cases, as shown in fig. 3.6. Using a Γ -point only mesh scheme

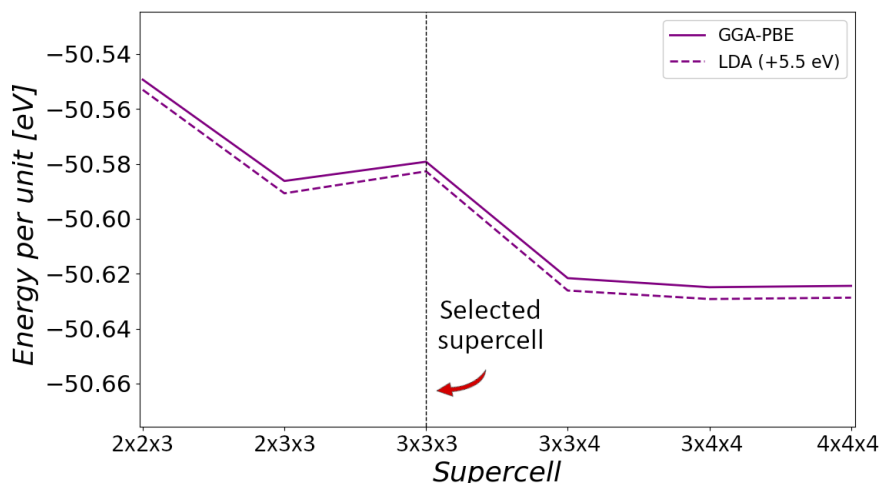


Figure 3.6: GGA-PBE and (shifted) LDA total energies per unit cell were evaluated with respect to the supercell size. The calculation was performed with the default cut-off energy value of 400 eV and a Γ -point only mesh. The supercell composed of a $3 \times 3 \times 3$ repetition was picked as the best candidate to proceed with for our further investigations.

is not sufficient for precise static energy evaluations such as the calculation of the optimal lattice parameters. For this reason, the k-points meshes were chosen case by case using a $3 - 3 - 3$ setting for the bulk supercell of the crystal and, in case of slab models, by lowering the k-coordinate perpendicular to the surface to 1. As shown in fig. 3.7, the main difference between any k-point mesh lies in the Γ -point only scheme. All MD simulations were performed sampling the cell only at the Γ -point. This results in a maximum error of about 0.06 eV in the adsorption energy of a single water molecule with respect to a $(3 \times 3 \times 1)$ k-points grid, which we considered accurate enough for the purpose of the simulated reactions. By doing so, an optimal computational effort was ensured. The next step was the optimization of the energy cut-off. The 400 eV value used so far was the default one, automatically read by VASP as the maximum value between the energy cut-off of O and Ti present stated in their pseudopotentials. In fig. 3.8 it can be observed that the default value of 400 eV was already sufficiently precise by performing single point calculations. Nevertheless a cut-off of 700 eV in our further static calculations was used. This large value was necessary to keep the error associated with the evaluation of water adsorption energy below 0.05 eV per molecule. At this point, the right optimized bulk lattice parameters had to be identified. The procedure consisted of two phases. First, a steer and stretch of the supercell was carried out with a step of 0.05 \AA . At each deformation,

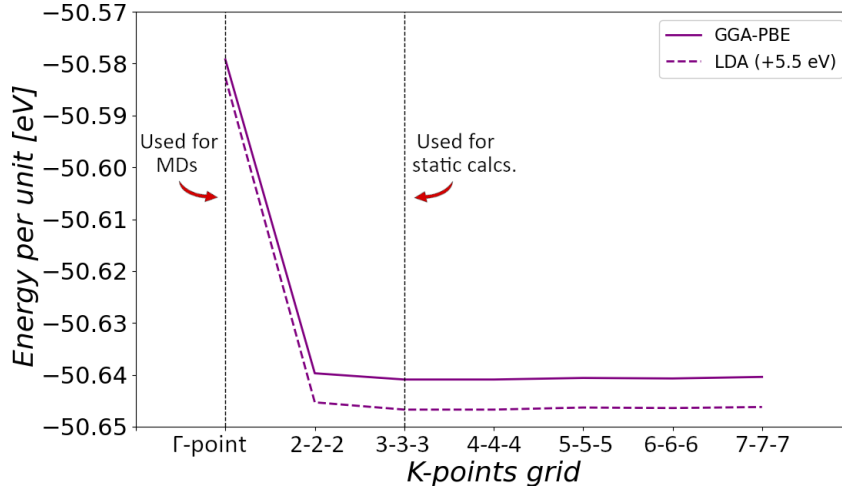


Figure 3.7: GGA-PBE and (shifted) LDA total energies per unit cell were evaluated with respect to the k-points mesh. The calculation was performed with the default cut-off energy value of 400 eV on the previously selected $3 \times 3 \times 3$ supercell. The $3 - 3 - 3$ k-points mesh was taken into account for any further static calculation reported in this chapter, whereas the Γ -point only scheme was used on any further dynamical simulation in order to spare in terms of computational time.

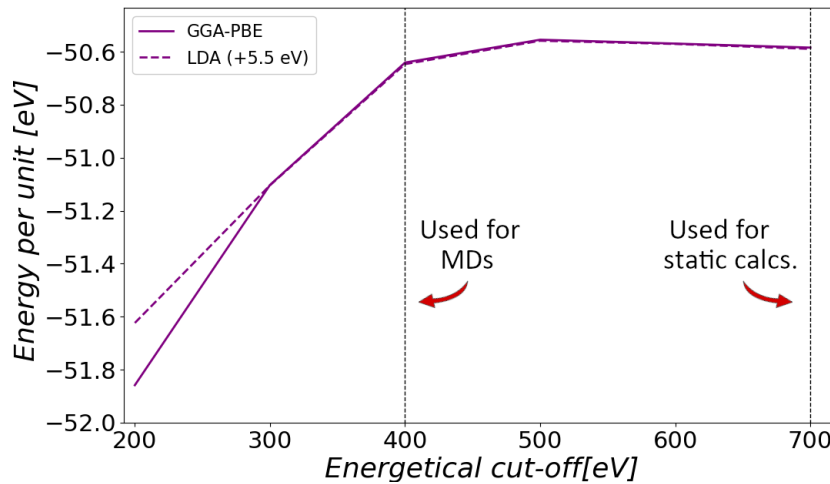


Figure 3.8: GGA-PBE and (shifted) LDA total energies per unit cell were evaluated with respect to the cut-off energy. The calculation was performed with the $3 - 3 - 3$ k-points mesh and the previously selected $3 \times 3 \times 3$ supercell. As depicted in the graph, a cut-off energy of 700 eV ensures for both of the two methods accurate energetic values for any further static calculation, whereas the 400 eV default value was then used for dynamical simulations only in order to spare computational time.

the energy was evaluated with a single point calculation, whereas a quadratic fitting was afterwards performed within the three lowest energy values found (fig. 3.9). Despite the discrepancy of up to 5.5 eV among the used methods, as also reported in our previous figs. 3.6-3.8, the relevant references to take into account here are the length, width and height which form the volume of the cell corresponding to the minimum of the curves. The vertex of the parabola

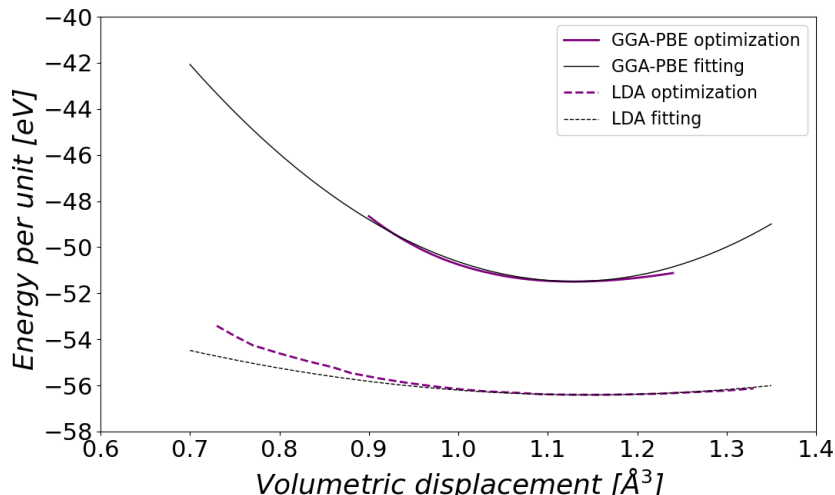


Figure 3.9: GGA-PBE and LDA total energies per unit cell were evaluated with respect to the volumetric displacement. The minima of the curves were respectively fitted with a quadratic approximation and then taken into account as initial guesses for the final optimization.

could be thought as a good initial guess to proceed with the second step, which consisted in a full lattice vector and geometry relaxation with the conjugate gradient routine.

The same supercell size was taken into account for DFTB calculations¹ and the k-points meshes were then chosen in agreement with DFT calculations. The research of the optimized lattice parameters was directly performed within the DFTB+ code routine.

In tab. 3.1 the different lattice parameters obtained in comparison with experimental values [39] are shown.

Table 3.1: Rutile lattice parameters derived from different approaches¹.

Method	a = b	c
LDA	4.570 Å	2.931 Å
GGA-PBE	4.663 Å	2.968 Å
Tiorg	4.671 Å	2.993 Å
Tiorg-smooth	4.677 Å	2.971 Å
Exp. [39]	4.587 Å	2.953 Å
HF [181]	4.575 Å	2.999 Å
B3LYP [181]	4.639 Å	2.974 Å

Cut of the surface models

All surface models were constructed symmetrically with respect to the z axis perpendicular to the surface, ensuring that no spurious macroscopic dipole

¹The DFTB lattice parameters were computed by Verena Gupta with two parametrization sets (Tiorg and Tiorg-smooth), starting from the optimized DFT rutile bulk structure.

builds up in any simulation cell.

Treatment of core and valence electrons

The PAW method was used in the DFT calculations with O and Ti atoms described by 6 and 4 valence electrons only, respectively.

Dispersion corrections

The GGA-PBE exchange-correlation functional has been extended with the zero damping DFT-D3 method of Grimme [172] implemented in VASP [182]. No appreciable effects were observed by using the D3 correction also in models without water, with lattice constants differences less than 0.01 Å and differences of the electronic-state energies lower than 0.01 eV. The same implementation was reproduced in DFTB² with the parameters $s_{r,6} = 1.217$ and $s_8 = 0.722$ provided with respect to the GGA-PBE functional by the *Mulliken Center for Theoretical Chemistry* [184].

DFTB parametrizations

The DFTB² calculations rely on two variations of the Tiorg Slater-Koster file set of parameters [185]. We refer to the first one as *Tiorg*, which can be found online under the [dftb+ website](#). Its electronic part is parametrized based on GGA-PBE, whereas the repulsive one on B3LYP. The second set of parameters, in the following named *Tiorg-smooth*, has the repulsive potential of Tiorg smoothed by polynomial fits. These modifications are very close to the original set, but vanish much smoother at their cutoffs. This was considered a necessary correction since in the Tiorg set the repulsive potential has some numerical noise. The electronic part between the two sets of parameters remained unchanged. The Self Consistent Charge Error (SCC) was set to 10^{-6} electrons and the forces were allowed to relax to values below 10^{-4} a.u. (2.7×10^{-3} eV).

Unstoichiometric surface energy

The computation of the surface energy for unstoichiometric cases was necessary in the rutile-(001) reconstructed model. The pressure was kept as a fixed parameter by plotting the curve with respect to the temperature. The use of the Einstein model was well suited since the phononic characteristic frequency of $\omega_{Ti} = 25$ meV can be taken into account for hcp titanium at room temperature and ambient pressure [186].

Settings of PDOS

Both DFT and DFTB (P)DOS calculations were performed with the use of $9 \times 9 \times 1$ k-points in cases involving the pristine surfaces or the rutile-(100)

²DFTB calculations with the two sets of parameters and with/without dispersion term were performed by Verena Gupta, the results of which have been discussed with all the co-authors [183].

reconstruction introduced in this chapter. Due to the increased system size, a mesh consisting of $6 \times 6 \times 1$ k-points was chosen to compute the PDOS of the rutile-(001) reconstruction. The DFT analysis were carried out through the free software *vaspkit* [187], whereas in DFTB they were obtained directly within the *dftb+ code* routine².

Adsorption energies

All calculations concerning water adsorption were performed by including individual molecules on both sides of the slab. In the unique case of a complete monolayer for rutile-(110), the molecules were 6 per side.

MD settings

The timestep in DFT and DFTB was set to $\Delta t = 0.5$ fs for both vacuum and water systems, in which the Deuterium mass for H atoms was established in the DFT calculations. In this way, it was possible to ensure a sufficiently small time step able to describe H_2O oscillations in a proper manner.

Two main types of thermodynamical ensembles were considered. First, an NVT ensemble with temperature ramping for 1 ps was carried out via a Nosé-Hoover thermostat. This thermalization time was considered long enough to achieve an equilibrium structure for bulk water, as reported for the time evolution of the MD potential energy of rutile-(110) (fig. 3.10). The final temperature

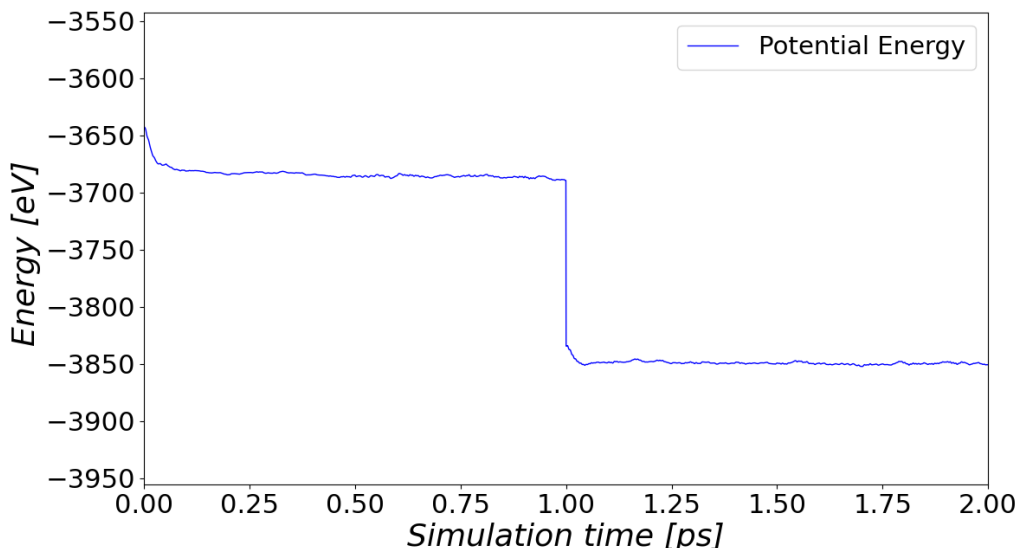


Figure 3.10: Time evolution of the potential energy of rutile-(110) during a heating-up process performed from 0 to 320 K within an NVT ensemble for 1 ps, which was followed by stabilization at 320 K within an NVE ensemble.

of the systems was then scaled to 320 K to avoid overstructures of liquid water, which is a known problem of GGA simulations [188]. This was followed by long-time NVE micro canonical ensembles, which provided more reliable and stable

temperatures. Due to the huge size of the (001)-rec system, its MD simulations were performed with an energy cutoff of 400 eV, whereas the temperature was increased up to 320 K.

Both in DFT and DFTB, the temperature rescaling in NVT simulations was performed every 25 steps, which also corresponds to the sampling frequency in both NVT / NVE ensembles, using a Nosé-Hoover thermostat. Here the fully solvated system was obtained by the iterative addition of H₂O molecules through the *GROMACS* box solvation tool [189], which fills the unit cell up to a standard water density of 1000 g/l. This procedure can be thought of as a manual generation of an NpT ensemble. Once the water was added, simulations within an NVT ensemble were performed for about 1.5 ps. Due to the structuring of a high ordered water layer near the titania surface, vacuum spots were observed after the simulation. These spots left behind were then refilled once again by the solvation tool. The procedure was repeated until no more water molecules were added. The resulting water densities for the pristine surfaces are shown in fig. 3.11.

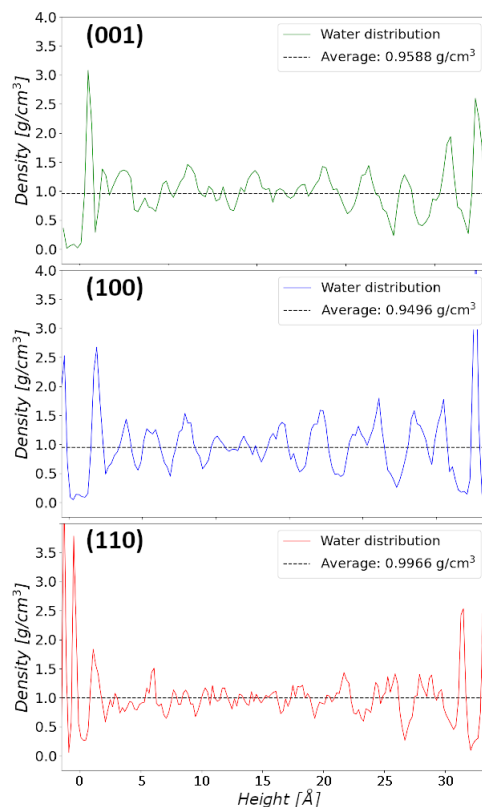


Figure 3.11: Water density profiles for pristine rutile-(110), (100) and (001). The results refer to the last step of the manual NpT procedure performed with the *GROMACS* box solvation tool [189]. The averages are also reported, with values around the desired density of 1 g/l.

DFT calculations with an implicit solvation model of water were performed with use of the VASPsol code [190, 191, 192], which enabled to set the relative permittivity to 80 in the Poisson equation.

3.3 Pristine slab models

In this section are introduced the pristine models of rutile-(110), (100) and (001) that have been considered for our further analysis. Their cuts were obtained by carving in the respective direction, leaving a vacuum of at least 15 Å with the bottom of the periodically repeated slab in DFT calculations. During geometry relaxations only, this distance was increased up to 60 Å in DFTB simulations since this method is well suited for such system sizes. The two slab models of rutile-(100) and (001) were represented by a repetition of $3 \times 3 \times 1$ of the unit cell. Due to the development along the diagonal of the xy plane, rutile-(110) was cut instead with proportions of $2\sqrt{2} \times 3 \times 1$. To avoid formation of electronic dipoles forming inside the structures, the surfaces were cut symmetrically.

In fig. 3.12 the profiles of the three pristine slab models composed by 6 layers are shown. By carving in the (110) direction, the first exposed oxygen atoms

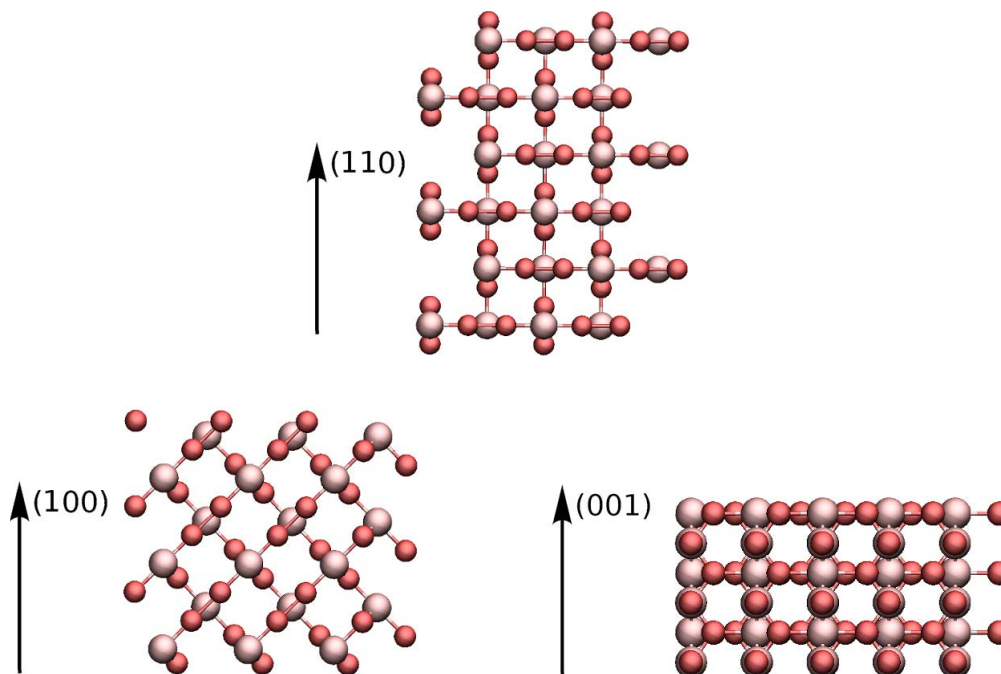


Figure 3.12: Side view of the 6-layered pristine rutile-(110), (100) and (001) studied in this thesis.

are two-fold coordinated, bridging above the underlying titania. Furthermore, 3-fold coordinated surface oxygen atoms connect the unexposed 6-fold coordinated titania with the corresponding 5-fold coordinated ones. A cut in the (100) direction brings to a unique *sawtooth* shape [117]. Again, the only atoms representative of reactive sites are the 2-fold coordinated oxygen atoms and 5-fold coordinated titania at the surface, similar to rutile-(110). Rutile-(001), on the other hand, has 4-fold and not 5-fold coordinated titania surface atoms and therefore the facet is rather unstable and more reactive.

The three different stabilities were confirmed by the evaluations of their surface energy. The energetic values of the slabs were computed with respect to the number of layers, starting from a thickness of 4. This turned out to produce

an oscillating behavior of the surface energies depending on whether or not the number of layers are even or odd. The curves are presented in fig. 3.13 with their relative converging values in tab. 3.2. The surface energies are in very good agreement with previous theoretical works both for DFT [117, 118, 119, 120] and DFTB [185, 193]. The order $(110) < (100) < (001)$ and the fluctuations of the curves were adequately described in all the different methods. The surface energy curve belonging to rutile-(100) does not oscillate in an appreciable way and its surface energy value remains rather constant, whereas rutile-(001) shows the most aggressive fluctuations.

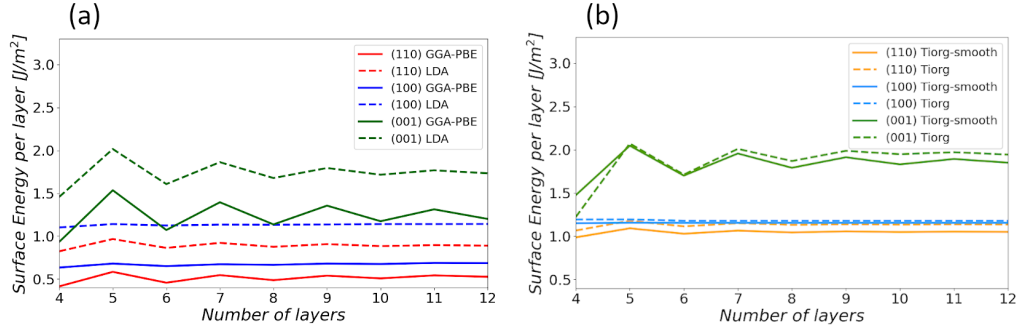


Figure 3.13: The surface energies γ_{surf} of the pristine surfaces are reported with respect to the number of layers for (a) DFT and (b) DFTB. The colors differentiate between them: red for (110), blue for (100) and green for (001). Lighter colors are used DFTB ³.

Table 3.2: Comparison between DFT, DFTB³ and other methods for the surface energies in $\frac{J}{m^2}$ of γ_{Surf} .

	LDA	GGA-PBE	Tiorg	Tiorg-smooth	HF [119]	B3LYP [119]
(001)	1.75	1.26	1.94	1.87	2.08	1.45
(100)	1.15	0.69	1.18	1.16	1.13	0.70
(110)	0.89	0.53	1.14	1.05	0.92	0.46

Despite the same qualitatively behaviors, the surface energy values differ significantly depending on the applied method used. LDA calculations show a fairly good agreement with both of the two Tiorg sets of parameters in DFTB with discrepancies smaller than $0.25 \frac{J}{m^2}$. Especially for rutile-(100) the difference between LDA and Tiorg-smooth was less than $0.01 \frac{J}{m^2}$. Such agreement was not found in GGA-PBE. A known problem of this functional relies in its significant underestimation of the surface energies for materials with a large correlation energy such as titanium dioxide [194]. It is notable that Tiorg-smooth provided a pronounced contrast between the surface energy values of rutile-(110) and rutile-(100). Although the difference between Tiorg and Tiorg-smooth in the latter case is low (0.04 eV), it is high in the (110) model (0.11 eV). This is a very

³The structural and energetic validation of each model per layer in DFTB has been implemented by Verena Gupta and the results compared together with all co-authors [183].

important difference as it allows to define in a proper way the two slabs also from an energetic point of view. The results therefore suggest that Tiorg-smooth is slightly more reliable than Tiorg.

Slab models composed of 6 layers for each of the surfaces were chosen for any further investigation. In the most unstable case of rutile-(001), the convergence was defined at less than $0.3 \frac{J}{m^2}$ both in DFT and DFTB. In tab. 3.3 the size of the three adopted systems composed by 6 layers are reported together with the involved number of atoms.

Table 3.3: Size of the pristine slab models together with the total number of atoms. The reported supercell values refer to GGA-PBE only.

Surface	Supercell (\AA^3)	Atoms in slab
(110)	$13.19 \times 8.90 \times 55.00$	216
(100)	$13.99 \times 8.90 \times 43.00$	162
(001)	$13.99 \times 13.99 \times 33.00$	162

Since the main scientific interest on TiO_2 regard its photocatalytic activity, it is important to collect information on how the electrons are arranged in all the proposed models. Through the analysis of the DOS the different band gaps of the pristine surfaces given by the contribution of the surface atoms were computed. In fig. 3.14 the DOS of the pristine surface atoms are shown, all shifted at the *valence band edge* (VBE). Although the absolute band gap

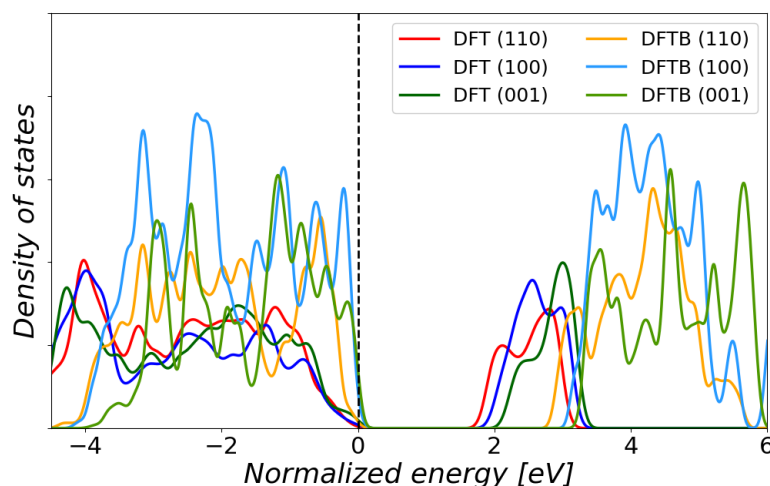


Figure 3.14: Density of States (DOS) of the surface atoms for rutile-(110), (100) and (001) with GGA-PBE and Tiorg-smooth⁴. The curves were smoothed with Gaussians and shifted to the VBE.

values are not quantitatively in agreement between the two levels of theory, fixed difference ranging at around 1.1 eV (tab. 3.4) is observed. It is well established in

⁴The DFTB DOS calculations were computed by Verena Gupta directly within the `dftb+routine`, which smooths the curves with Gaussians automatically.

Table 3.4: Band gap values (eV) of the pristine surfaces for GGA-PBE and Tiorg-smooth⁴.

Surface	DFT (GGA-PBE)	DFTB (Tiorg-smooth)	Difference
(110)	1.75	2.87	1.12
(100)	1.94	3.14	1.20
(001)	2.18	3.26	1.08

literature that DFT calculations are usually underestimating band gap values with consequent tendency to delocalization due to the self-interaction error [163, 195]. This issue is resolved in DFTB [185] by adjusting the compression radii in the repulsive part of the Slater-Koster files. Another important difference is the very steep increase of the DOS at the valence-band edge obtained with DFTB, whereas DFT predicts a much smoother band edge. This is attributable to the larger electron density on the O atoms, which contribute for the largest part to the valence-band edge, whereas the Ti atoms curves appear mostly to the conduction-band edge above the band gap.

3.4 Reconstructed slab models

Although working with regular surfaces can help us manage electronic configurations more easily, there are no perfect substances in nature. During the formation of an oxide such as TiO_2 , defects are often created: among them vacancies, doping atoms and kinked sites are most common. In addition to the three smooth surfaces of rutile-(110), (100) and (001), reconstructed models of the (100) and (001) slabs were investigated, the latter non-stoichiometric. For sake of simplicity we refer to the two reconstructed structures as (100)-rec and (001)-rec, respectively. The slab model of rutile-(100)-rec is represented by a $3 \times 3 \times 1$ repetition of the unit cell, as in the pristine cases of rutile-(100) and (001). Instead, in order to reproduce properly the stairs-like structure of the (001)-rec model the supercell was scaled up to a $4\sqrt{2} \times 2\sqrt{2} \times 1$ repetition. In tab. 3.5 the size of the two adopted systems is reported together with the involved number of atoms. The surfaces of (100)-rec and (001)-rec were

Table 3.5: Size of the reconstructed slab models together with the total amount of atoms. The reported supercell values refer to GGA-PBE only.

Surface	Supercell (\AA^3)	Atoms in slab
(100)-rec.	$13.99 \times 8.90 \times 50.00$	243
(001)-rec.	$26.38 \times 13.19 \times 27.00$	488

carved from the 11-layered (100) and 13-layered (001) pristine facets. To avoid formation of electronic dipoles inside the structures, the surfaces are symmetric.

3.4.1 Reconstruction of rutile-(100)

In fig. 3.15 the profile of our (100)-rec model is shown. This surface is composed by exactly two facets of rutile-(110). The repetition of its image creates a roof-like shape, with wide valleys formed by saturated TiO_2 units. At the tip of the structure, the bridging oxygen atoms are bonded to 5-fold coordinated Ti atoms, which is different from the regular case of rutile-(110). This confers a defective characteristic to the site and these unsaturated titania are able to promote reactions. The geometry relaxation of this model converged only when

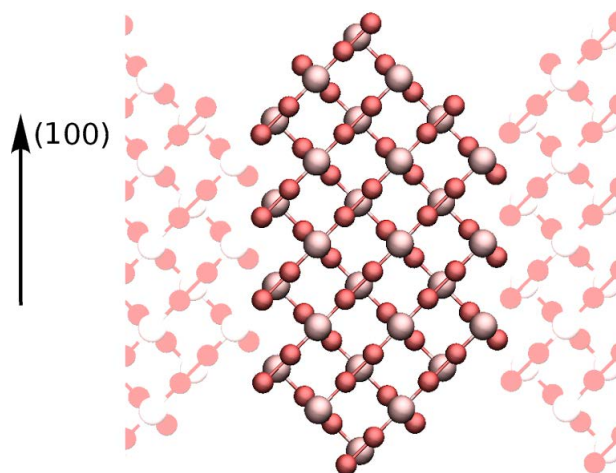


Figure 3.15: Ball-and-stick model of rutile-(100)-rec. The valley that the structure forms with its periodic image is highlighted with lighter colors.

the 2-fold coordinated bridging oxygen atoms at the tip moved towards the symmetry axis vertical to the surface. The angle shifted from 45° to about 65° in all of the used methods, as shown in fig. 3.16. This antenna-like structure

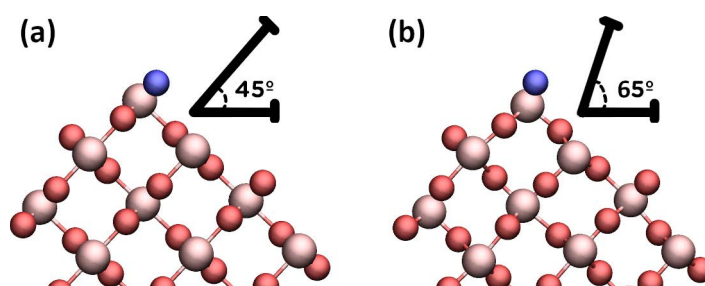


Figure 3.16: Ball-and-stick model of rutile-(100)-rec before (a) and after (b) the GGA-PBE geometry relaxation. The change in the angle formed by the oxygen atoms (blue) at the tip with the y-axis is reported.

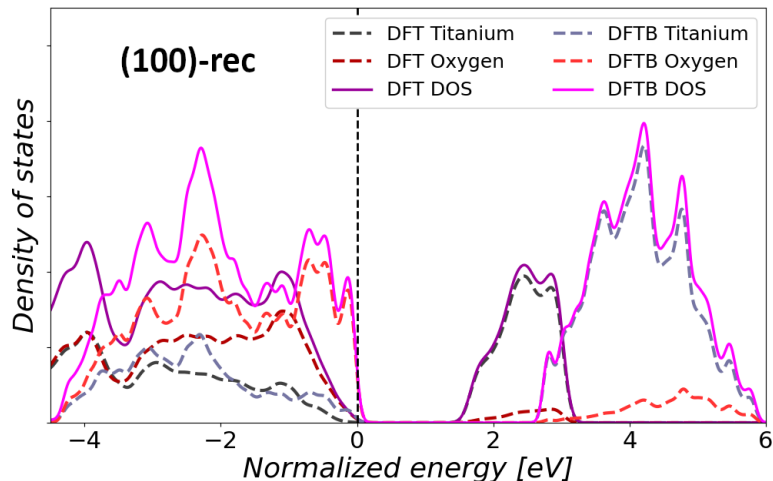
is chemically justified by O atoms balancing the unsaturation provided by the underlying 5-fold titania at the triangular site. Since the model was obtained by cutting rutile-(100) along the (110) and $(\bar{1}\bar{1}0)$ axes, the same relaxations occurring in rutile-(110) appear at the sides of the structure. It is therefore reasonable to expect the same surface energy of this latter case multiplied by

Table 3.6: Value of the surface energy in $\frac{J}{m^2}$ for (100)-rec ⁵.

	γ_{Surf}	Ratio w.r.t. (110)
LDA	1.26	$1.41 \sim 1.00\sqrt{2}$
GGA-PBE	0.73	$1.38 \sim 0.97\sqrt{2}$
Tiorg	1.47	$1.29 \sim 0.91\sqrt{2}$
Tiorg-smooth	1.42	$1.35 \sim 0.95\sqrt{2}$

approximately a factor of $\sqrt{2}$. In tab. 3.6 the agreement with this suggestion is clear. Although the LDA approach provides a proportional value of exactly 1.00, we shall consider that the roof-like structure presents a defective site rather than two perfect and infinitely reproduced (110) surfaces. In fact, the oxygen atoms consisting in the tip of the model are shared in common within the two facets and therefore a multiplication by exactly $\sqrt{2}$ is not possible. The best agreement is therefore given by GGA-PBE and by the Tiorg-smooth set of parameters.

Instead of performing simple DOS calculations, *partial density of states* (PDOS) were computed for Ti and O surface atoms in order to evaluate the contribution of the two different species. The structure of (100)-rec model presents a band gap even lower than the pristine rutile-(110) (tab. 3.4), as shown in fig. 3.17, which forms its two sides: 1.59 eV (DFT) against 2.78 eV (DFTB), with a difference of 1.19 eV between the two values.

**Figure 3.17:** Projected density of states (PDOS) computed on the surface atoms of the (100)-rec model with GGA-PBE and Tiorg-smooth ⁶. The curves were smoothed with Gaussians and shifted to the VBE.

⁵The DFTB model of (100)-rec was implemented and validated by Verena Gupta by referencing to the corresponding DFT structure.

⁶The DFTB PDOS calculations were computed by Verena Gupta directly within the `dftb+routine`, which smooths the curves with Gaussians automatically.

3.4.2 Reconstruction of rutile-(001)

In fig. 3.18 the profile of the (001)-rec model is shown. The structure has an unstoichiometric surface formed by units of Ti_7O_{12} . The overabundance of interstitial titania atoms gives an unusual 5-fold coordination to the oxygen atoms in the middle of the second layer of each island. The exposed surface is formed by the original (001) structure and by (011) facets along the oblique directions. Moreover, the steepness of the DFT curve found in the pristine cases (fig. 3.14) is exaggerated. A geometry optimization provided two different final

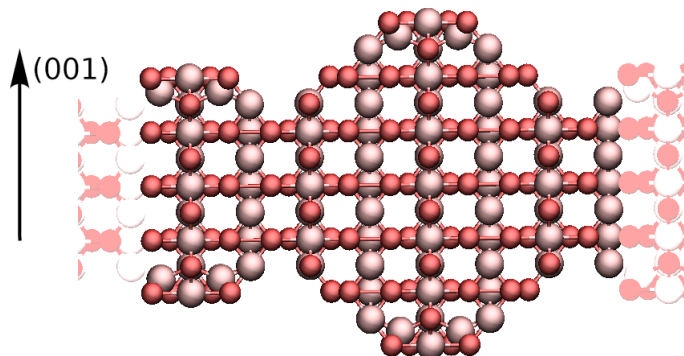


Figure 3.18: Ball-and-stick model of rutile (001)-rec. The valley that the structure forms with its periodic image is highlighted with lighter colors.

configurations between DFT and DFTB, as shown in fig. 3.19.

In our DFT calculations and independently on the exchange-correlation functional considered, the structure relaxed showing a plane formation at the valley site, in contrast with the model proposed from experiments. The Ti atoms lying at the third layer of the lower island moved towards the center of the valley during the relaxation. The attraction to the valley promoted bond breaking and new bond formations with the next O atoms belonging to the opposite slope. On the higher island, 5-fold coordinated Ti atoms in the sub-surface layers became 4-fold coordinated and relaxed towards the outer part of the slope by generating small kinked sites. Overall, the final structure found in DFT recalls the model proposed by Ikuma et al. [151] for rutile-(001). In their work, the sample was annealed at 683 K, whereas our surface was proposed for temperatures above 1050 K [147, 148]. For this reason the two models are not completely matching. The steep valley present before relaxing was however also found flattened in their results as well as the presence of kinks along the (011) directions.

In the DFTB simulation a more elongated, but still ordered surface was found either with the Tiorg or Tiorg-smooth set of parameters⁷. In this situation both of the rugs presented exactly the same relaxation. The first observed dislocation was given by the interstitial Ti atoms, which broke the two bonds with the oxygen atoms right underneath. In this way, they became 2-fold coordinated. This generated an overall movement in the (001) direction towards

⁷The starting (001)-rec model of the DFTB calculations performed by Verena Gupta was created by multiplying the DFT structure with the right ratio of DFTB lattice parameters 3.1.

the vacuum. With the interstitials Ti becoming a sharp tip at the surface, also the 3-fold coordinated oxygen atoms at the surface of the rug broke one bond with the Ti belonging to the second layer of the structure. As a consequence, the Ti atoms became 3-fold coordinated rather than 5-fold.

The main experimental information available on this reconstruction are provided either with STM, AFM or LEED, which analyze the sample from a top view perspective only. This approach does not allow to assume which one of the proposed final configurations between DFT and DFTB is the most likely to be observed in the laboratory, since the two models are barely distinguishable from the top view: on the surface plane, the measured distances do not allow to discriminate between one and the other structure. The analysis of the surface energy of this model can help in solving this issue. Due to its unstoichiome-

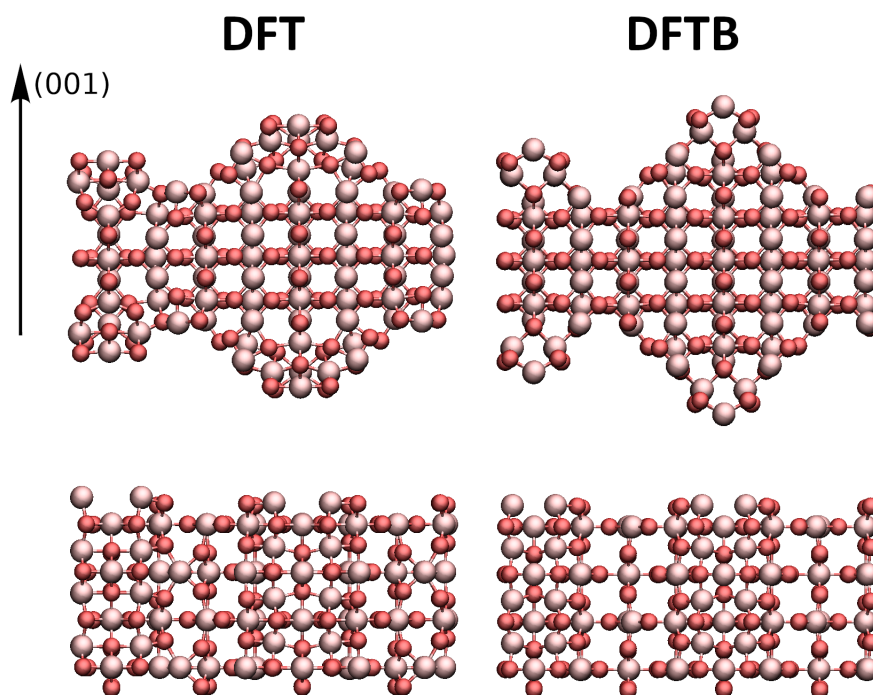


Figure 3.19: Geometrically optimized final structures of rec-(001) computed with GGA-PBE and Tiorg-smooth from the side and top views⁷

try, the computation of the surface energy for this reconstructed case shall be treated differently, as explained in our method section. The resulting curves belonging to the optimized configurations are shown in fig. 3.20 (a). The pressure was set up at $5 \cdot 10^{-8}$ atm as proposed in Tero et al. [148]. According to their work, the reconstructed surface was clearly observed right above 1050 K, whereas it was found at 1027 K in Nörenberg’s experiment [146]. As reported in the left column of tab. 3.7, the outcome of the GGA-PBE relaxation was 1048 K, which is in agreement with these values. However, the model obtained by relaxing the proposed surface with DFTB tends to overestimate the temperature considerably, independently from the used set of parameters.

In order to understand whether or not the relaxed structures were different due to methodological reasons rather than insurmountable energy barriers,

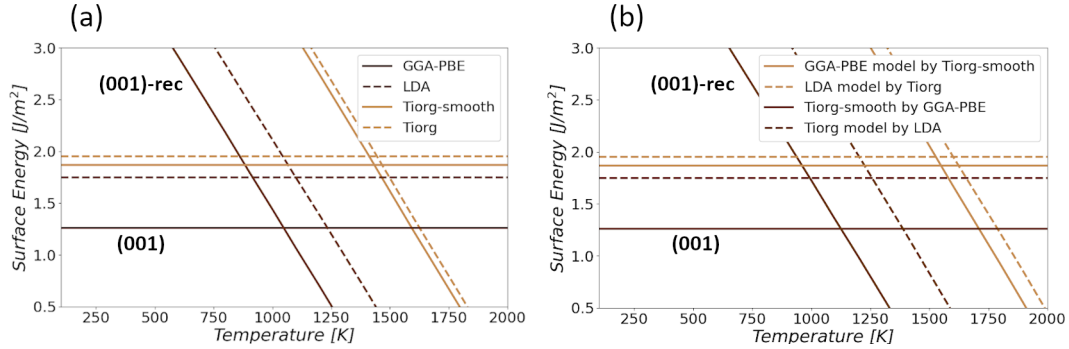


Figure 3.20: (a) The surface energy γ_{Surf} of (001)-rec slab model is plotted with respect to temperature for DFT and DFTB⁸. (b) The same type of calculation was performed in a reverse way: DFT optimized the DFTB structure and vice versa.

the calculations were reversed so that DFT was optimizing the DFTB final geometry and the other way around. No changes could however be observed in the final configurations however, meaning that both the proposed models are local minima of the Helmholtz free energy. Nevertheless, in both cases the surface energy values were much higher, as depicted in fig. 3.20 (b): the DFTB structure is therefore only metastable for DFT and vice versa. In conclusion,

Table 3.7: Computed temperatures at which the reconstruction of rutile-(001) is likely to take place⁸

	Standard relaxation	Reversed relaxation
GGA-PBE	1048 K	1131 K
LDA	1098 K	1257 K
Tiorg	1445 K	1601 K
Tiorg-smooth	1433 K	1549 K

we can make use of two different criteria to state that the DFT configuration represents the most realistic surface model in order to proceed in our further investigations. First, the structure obtained in DFT calculations provides an advantage in terms of total coordination of the atoms, since the relaxed species which are not oversaturated are either maintaining their electronic states or adding one more bond. This is not the case for the DFTB structure, in which the interstitial Ti atoms lower their coordination as well as the surface oxygen atoms, therefore providing a chemical disadvantage rather than an advantage. Secondly, the temperature found in GGA-PBE calculations for the DFT relaxed structure is in a very good agreement with experiments and even simulations with the LDA functional are not giving unreasonable values. Our results are quite similar to the ones of Ikuma et al. [151] for lower temperature ranges.

As for the case of the (100)-rec model, a PDOS investigation of the surface atoms was needed rather than a simple DOS. The resulting curves are shown

⁸The DFTB calculations on the (001)-rec model were computed by Verena Gupta. The final DFT structure in the reversed optimization was computed by her as well.

in fig. 3.21. This shifts the reconstruction from a semiconductor to a metallic

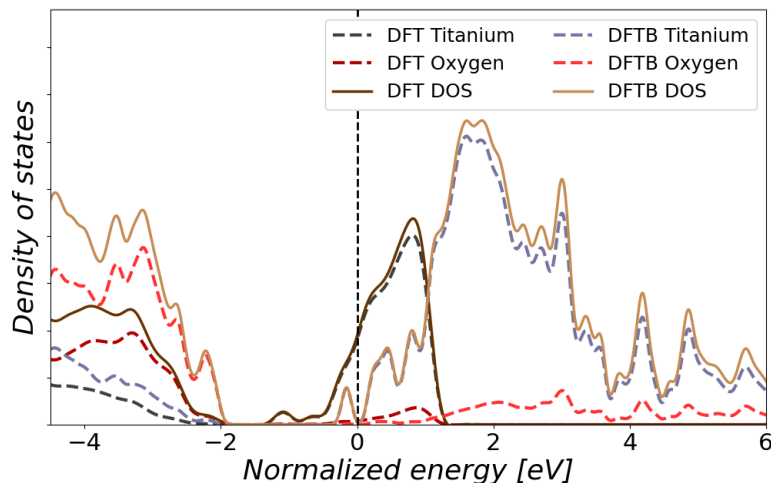


Figure 3.21: Projected density of states (PDOS) computed on the surface atoms of the (001)-rec model with GGA-PBE and Tiorg-smooth⁹. The curves were smeared with Gaussians and shifted to the VBE.

character, with the conduction-band edge shifting below the Fermi level to a larger and more evident extent in DFT than DFTB. While DFTB is in principle able to describe metallic systems correctly, both the Tiorg and Tiorg-smooth sets predicted the wrong structure and energetics for this particular reconstruction. However, it is not easy to determine the reason of this mismatch, as it could rather be the combination of three main factors. First, the difference in the geometry already results in different electronic structures. Secondly, the gap sizes in the two methods are not the same and the Slater-Koster parametrization should be specifically picked for the metallic or the insulator case.

3.5 Interaction with water

In general, a right evaluation of hydrogen bonds is often a crucial challenge. In the following calculations, particular attention will be attributed to the ability of Tiorg-smooth set¹⁰ to agree with GGA-PBE results.

We first present static calculations regarding the adsorption of waters at the different rutile surfaces. Thanks to the following evaluations, we were able to understand in which cases DFTB is in good agreement with DFT. As a first step, a single H₂O molecule was placed above a Ti surface atom of the pristine rutile (110), (100) and (001). Here, two scenarios were taken into account: a molecular adsorbed configuration and a dissociative mode, in line with much of the known literature [127, 122, 132]. Another configuration was also investigated where the hydrogen atoms of the water molecule oriented towards the upper oxygen atoms

⁹The DFTB DOS calculations were computed by Verena Gupta directly within the `dftb+routine`, which smooths the curves with Gaussians automatically.

¹⁰Both static and dynamic DFTB calculations were performed by Verena Gupta on the geometrically optimized DFTB rutile slab models previously validated by her.

consisting in the tip of the (100)-rec structure. The final optimized geometries are shown in fig. 3.22 and the corresponding adsorption energies per molecule are reported in Table 3.8.

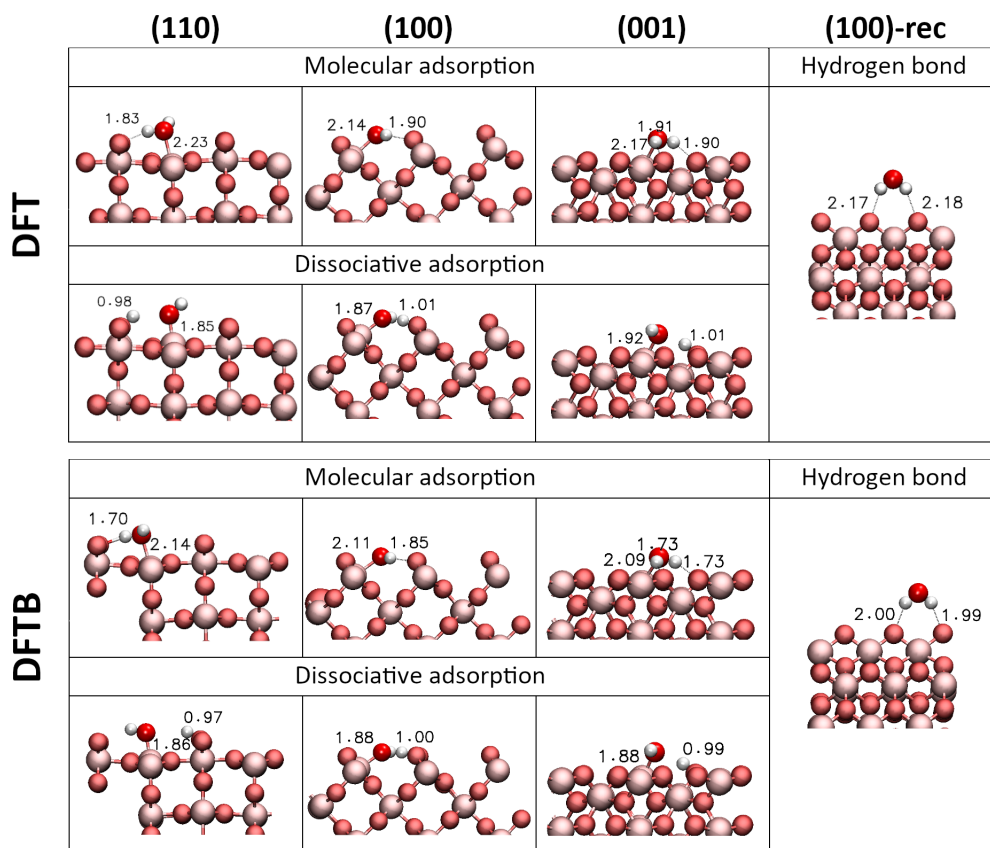


Figure 3.22: Geometrically optimized structures of a single water molecule adsorbing on the pristine surfaces and on (100)-rec. DFT results refer to GGA-PBE calculations only, DFTB to the Tiorg-smooth set of parameters¹¹. The most relevant bond distances in Å are labeled.

In the case of molecular adsorption, stable geometries with Ti-O distances of about 2.23 (110), 2.14 (100) and 2.17 (001) Å were found in DFT on all of the three pristine surfaces with Ti(surf)-O(water) distances slightly larger than the usual Ti(bulk)-O(bulk) value of 1.95 Å [39]. The configurations were further stabilized by hydrogen bonds with adjacent O surface atoms. Comparable geometries were found in the DFTB systems with systematically slightly shorter hydrogen bond distances, but in overall good agreement with the DFT references. In the case of dissociative adsorption, the Ti(surf)-O(surf) interaction of the covalently bound OH group was reduced to about 1.85 (110), 1.87 (100) and 1.92 Å, thus even shorter than the Ti(bulk)-O(bulk) spacing. The corresponding proton created a covalent bond with an adjacent bridging oxygen atom to form a hydrogen bridge with the adsorbed hydroxyl group. This configuration was found on all of the three pristine surface models according to the

¹¹Static water DFTB calculations were performed by Verena Gupta on DFTB optimized rutile models which were prepared beforehand on my own by inserting the H₂O molecules manually.

surface geometry. Also in this case, DFTB reproduced the geometries in good agreement with DFT. The additional configuration, which regarded exclusively hydrogen bonds at the tip of the (100)-rec structure, provided again the same geometry in DFT and in DFTB.

Table 3.8: Adsorption energies per molecule (eV) of H₂O referred to the adsorption modes of fig. 3.22. The most stable configurations are highlighted in bold ¹²

Coverage	Surface	Ads. mode	DFT (GGA-PBE)	DFTB (Tiorg-smooth)
1 H ₂ O				
	(110)	Mol.	-0.99	-1.00
		Diss.	-0.82	-1.29
	(100)	Mol.	-1.21	-1.28
		Diss.	-0.97	-0.94
	(001)	Mol.	-1.23	-1.46
		Diss.	-1.09	-1.61
	(100)-rec	Hydr.	-0.21	-0.38
1 ML				
	(110)	Mol.	-1.11	-1.52
		Diss.	-0.84	-1.86
		Mix.	-1.25	-1.56

The resulting sets of adsorption energies are well compared with literature values [132, 140, 139, 196, 127]. Although the two methods agree on all the structural details of the final configurations, a comparison between their energetics provides different considerations in terms of preferences of adsorption. In rutile-(110) we observed a perfect concordance between DFT / DFTB adsorption energies (-0.77 eV against -0.76 eV) for the molecular adsorption mode. However, in DFTB we have -1.07 eV for the dissociative case and -0.58 eV in DFT. Hence, in DFT calculations the water molecule is more likely to end up in a molecular adsorption, while in DFTB it is rather the other way around. The same consideration is applied on rutile-(001), which provided an even more discrepancy between the energies of the two methods. Like in the previous case, also here DFTB promotes a preference towards a dissociative adsorption, whereas for DFT it is the molecular one that should occur. The difference lies here at around 0.14 eV (-1.23 and -1.09 eV for DFT, -1.46 and -1.61 eV for DFTB). Considering such a small value and the fact that even the highest energy found is not at a negligible rate, we shall expect a comparable probability of adsorption for both modes at a coverage given by one single water

¹²Both structures and energetics from DFTB calculations were provided by Verena Gupta, the adsorption energies of which were then compared and computed together.

molecule. Once again, such a discrepancy was not reported geometrically as the final configurations were in excellent agreement in the two methods. According to the reported values, the single water molecule tends to adsorb molecularly at the surface in both DFT and DFTB in the only case of rutile-(100). Here, the difference between the dissociative (-0.97 eV for DFT, -0.94 for DFTB) and molecular adsorption (-1.21 eV for DFT, -1.28 for DFTB) is instead quite significant (0.24 eV in DFT, 0.34 eV in DFTB). We believe that the inconsistency in the cases of pristine rutile-(110) and (001) comes from two factors. First, such evaluations suggest that DFTB is not able to properly reproduce the strength attributed to hydrogen bond interactions, which is a problem already known in literature [197]. Configurations with a larger amount of in-surface H-bonds, such as the ones rich in terminal OH groups, become over-stabilized. Therefore, it does not come as a surprise that in the only case in which the two methods agree (the rutile-(100) pristine surface) the water molecule is double bound via its hydrogen atoms with the surface bridging oxygen atoms. Secondly, we can assume from our PDOS calculations (see Figures 3.14) that the O atoms of the surface, including those of water adsorbates that saturate Ti dangling bonds, have larger electronegativity in DFTB if compared with DFT. This was evident by the steeper valence-band edges and larger electron density in the PDOS stemming from O atoms. As a result of the stronger electron donation from Ti into the O atom of the adsorbing water molecule, the O-H bonds become more polarized than in the DFT case. They are thus more prone for a proton transfer to a neighboring O acceptor. This overestimation is again proven by the adsorption occurring in the (100)-rec model. Here, the values of DFT (-0.21 eV) and DFTB (-0.38 eV) point towards a stronger bond in the second case. The water molecule adsorbed symmetrically above the rows composed by the bridging oxygen atoms, forming two hydrogen bonds simultaneously. In DFTB we found H(water)-O(surf) distances of 0.17 Å shorter than in DFT.

In order to further investigate the discrepancy between the two methods, adsorption energies were computed for water molecules that are stabilized in their own network. Three different coverages of 1 monolayer (ML) on rutile-(110) were introduced, as suggested by Harris et al. [140]. They consisted of a complete molecular adsorption, a complete dissociation and a mixed situation. Overall, the DFT results were similar to the ones reported for a coverage of a single water molecule, the values of which are also reported in tab. 3.8. DFT evaluations now suggest a preference towards the mixed situation, whereas DFTB ones stay stick to the dissociative reaction. Moreover, not only the adsorption energies decreased of about 0.5 eV with respect to the single molecule case in DFTB calculations, but the starting configuration of the molecular adsorption even changed to dissociation during the relaxation of the system. Such results report then a strong influence of the number of H_2O molecules present at the surface, which motivated to proceed in our research through ab-initio MD simulations in presence of liquid water.

MD simulations of bulk water on the different rutile surface models were then performed. The final configurations at the top and at the bottom of the surfaces always occurred in an equivalent way but for (001)-rec, for which both sides are then discussed. Since DFTB was not able to predict the correct structure and

energetics (fig. 3.19) of this model, in this case only DFT simulations were carried out with the GGA-PBE exchange-correlation functional.

In tab. 3.9 the size of all the adopted systems are reported together with the involved number of explicit water molecules in the box, in DFT and DFTB respectively. In terms of adsorption modes at the surface, the same discrepancy

Table 3.9: Total amount of water molecules in the DFT and DFTB investigated systems ¹³.

Surface	Water molecules
(110)	134 ^{DFT} , 143 ^{DFTB}
(100)	132 ^{DFT} , 130 ^{DFTB}
(001)	159 ^{DFT} , 163 ^{DFTB}
(100)-rec.	138 ^{DFT} , 107 ^{DFTB}
(001)-rec.	128 ^{DFT}

found in our previous static calculations on the pristine slab models (tab. 3.8) could still be detected on rutile-(110). However, a concordance between the two methods was observed not only for the expected case of rutile-(100), but even for rutile-(001).

The calculations on rutile-(110) lasted for 8.5 ps in both DFT and DFTB. In the first method, the interaction mode was provided by molecular adsorption. The DFTB MD simulation was instead dominated by dissociative adsorption. For the molecularly adsorbed molecules, the same behavior of DFT could be observed. In the dissociative cases the hydrogen of the hydroxyl molecules never felt the attraction to the bridging oxygen atoms and were redirected towards the second layer of adsorption. The results of our DFT MD simulation are in contrast with the expectations of tab. 3.8, which should lead to a mixed situation. In order to understand if it was just a matter of an energetic local minimum in which the simulation got stuck, a new MD with a mixed first water layer was performed for 4 ps. Almost instantly, two hydrogen atoms got attracted by the correspondent hydroxyl groups. After 3.06 ps, also the last recombination took place by interacting with a water molecule from the second layer of adsorption through a two-steps Grotthuss mechanism. It is then clear that the presence of a second water layer right upon the surface plays a fundamental role, allowing the H₂O molecules to stabilize in a molecular adsorption mode, avoiding any dissociative or mixed case.

At the surface of rutile-(100) the molecular adsorption mode was dominating after a 10 ps run in DFT and 6 ps in DFTB (fig. 3.24). For both methods, a well established second water layer could be identified, which stabilized the molecular adsorption of the first water layer. During the simulation the H₂O oscillated around their equilibrium position providing only a single hydrogen bond, whereas the second hydrogen felt the attraction of the above water network.

¹³The MD simulations in DFTB were computed by **Verena Gupta**. The addition of the water molecules in the systems was performed on my own and then forwarded to her.

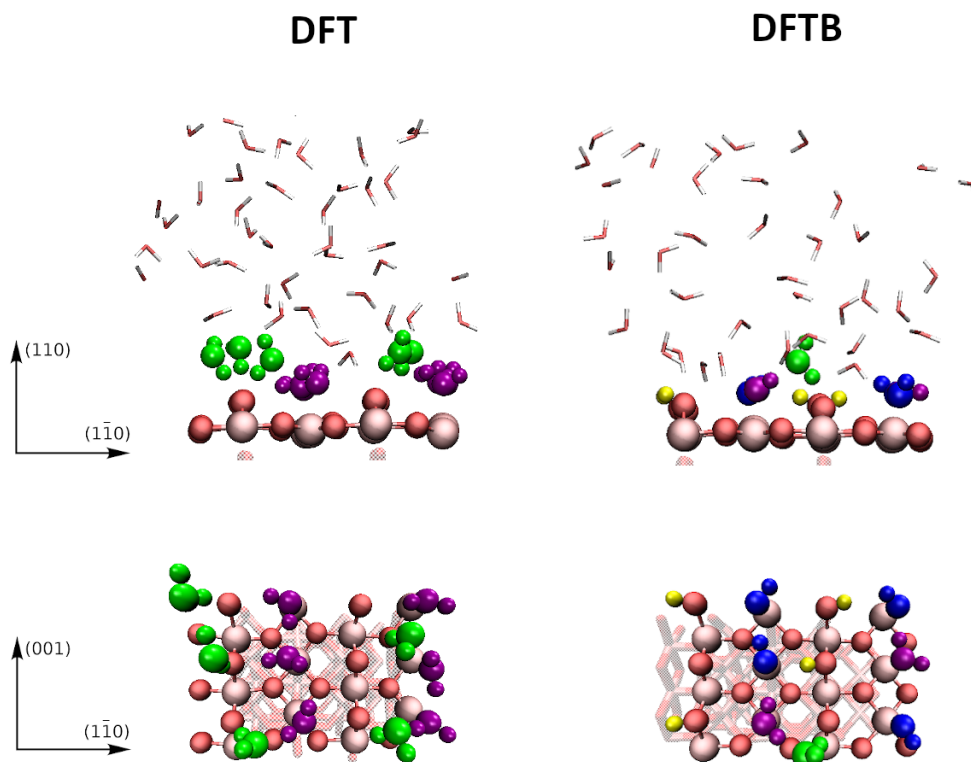


Figure 3.23: Final configurations of water adsorbing at the surface of rutile-(110). Purple molecules represent molecular adsorption, blue ones the hydroxyl case, yellow stands for a proton transfer, green for the formation of a hydrogen bond. Water molecules not involved in any adsorption are shown as single sticks¹³.

The MDs of water on rutile-(001) were performed for 6 ps in both DFT and DFTB (fig. 3.25). Out of 9 reactive TiO_2 surface units we observed 5 molecular adsorptions and 4 dissociative states for a full coverage. In DFT, the molecularly adsorbed H_2O did not form any hydrogen bond with the surface as in their relative static calculation (fig. 3.22). In DFTB this behavior could still be detected in most of the cases. Nevertheless, the configuration of the hydroxyl in both of the two levels of theory was in perfect agreement as for their single water molecule coverage study. Finally, hydrogen bonds between the surface atoms and liquid water molecules were also likely to appear, forming a second structural layer.

Since the facets of the (100)-rec surface are carved along the (110) direction, the same behavior of rutile-(110) for both DFT and DFTB (figs. 3.23 and 3.26) could be detected. In DFTB a mixed situation of dissociated states and few molecularly adsorbed water molecules was identified. The MD runs lasted for 10 ps and 12 ps for the first and second method, respectively. At the tip of the reconstructed model we observed for both DFT and DFTB the usual formation of hydrogen bonds, which are then orienting towards one or the other side of the slope. Water molecules forming a hydrogen bond on one of the two slopes further interacted with the closest molecularly adsorbed water. Some hydrogen

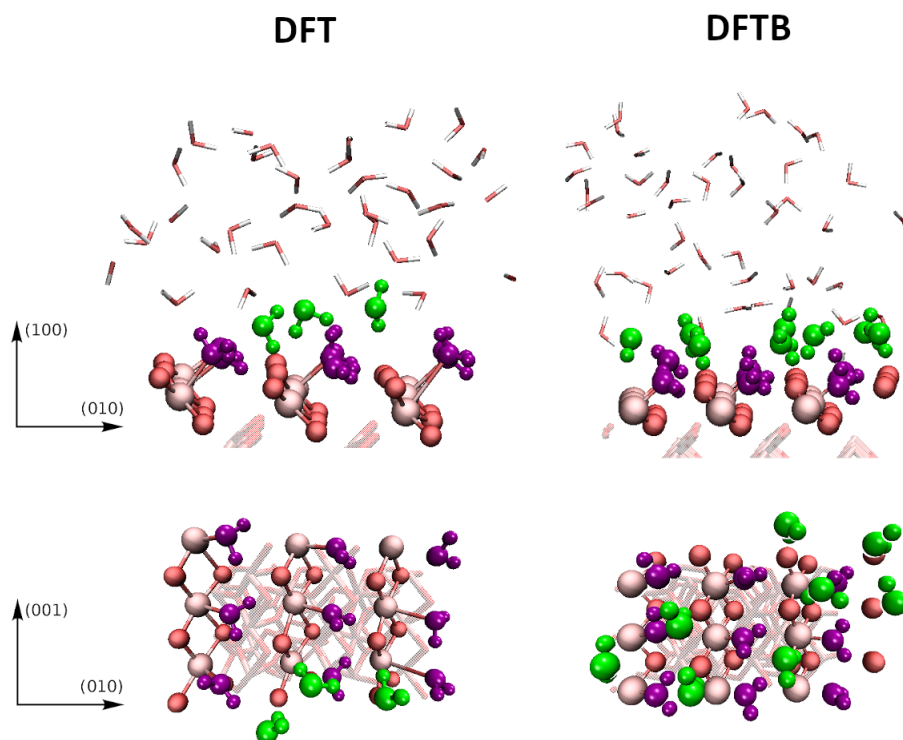


Figure 3.24: Final configurations of water adsorbing at the surface of rutile-(100). The adsorption configuration mode of the water molecule is represented with the color scheme used so far. Water molecules not involved in any adsorption are shown as single sticks¹³.

bonded H_2O are found as well at the bridging oxygen rows of the (110) facets. Finally, this reconstruction presents an interesting behavior especially when it comes to the valley formed with its periodic image. Both in DFT and DFTB calculations, the water molecules got adsorbed on the final part of the slope at which the 5-fold coordinated Ti atoms are present. Since on the opposite slope the first reactive site is given by a row of bridging oxygen atoms, the main tendency here is the formation of a hydrogen bond with them. As a consequence, right in the middle of the valley the second hydrogen atom points perpendicularly to the (100) direction, towards the water network. However, one H_2O molecule in DFT as well as in DFTB shows a different behavior. In the first method, we observed a double hydrogen bonding between the two H atoms belonging to the molecularly adsorbed water and two bridging oxygen atoms in front. On the other hand, in DFTB calculations one H atom belonging to the same H_2O got attracted by one of the oxygen atoms of the opposite bridging rows at the end of the simulation.

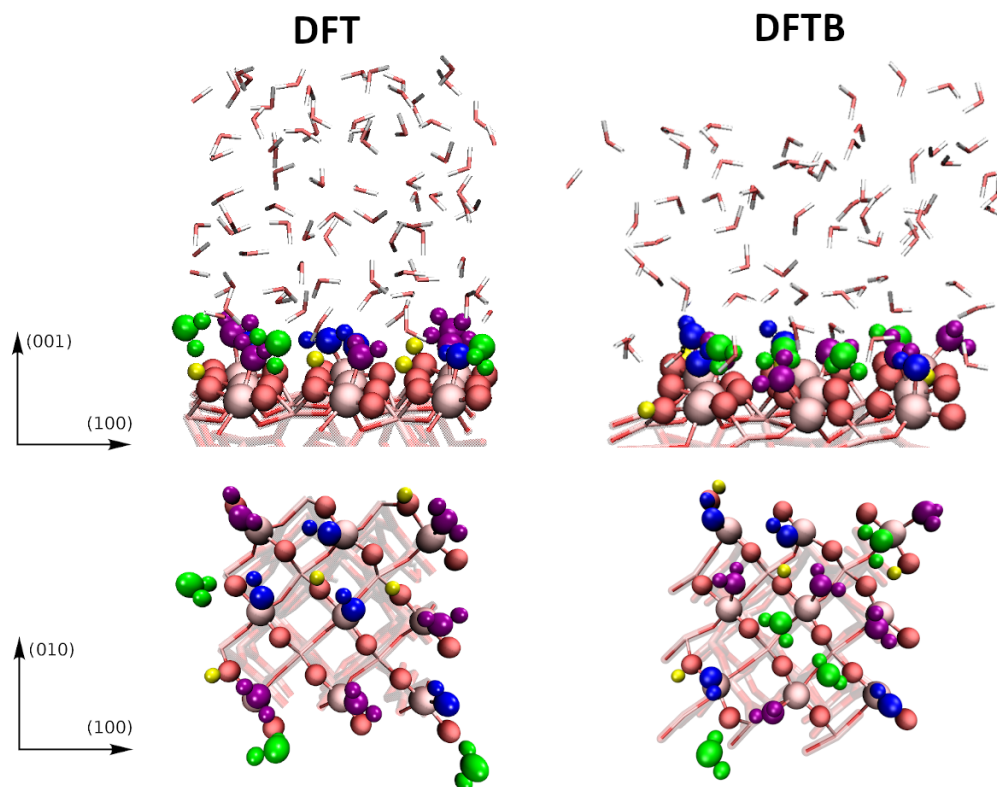


Figure 3.25: Final configurations of water adsorbing at the surface of rutile-(001). The adsorption configuration mode of the water molecule is represented with the color scheme used so far. Water molecules not involved in any adsorption are shown as single sticks¹³.

3.5.1 A special mention: water on (001)-rec

Water reactions on the surface of the (001)-rec model were carried out in an extensive way. Since this system has an unstoichiometric reconstruction, investigation of the interaction with a liquid aquatic environment could provide relevant considerations for other types of TiO_2 reconstructions as well. Those could be the ones occurring after treatment of low-Miller-index single-crystal facets at high temperatures or as the result of relaxation of high-Miller-index facets [198]. Moreover, the abundant presence of excess Ti interstitials in the system, given the overall reduced character of the surface, could support reactions that are imputable to more general surfaces with Ti^{3+} defects, which are well known to form after interaction of titania with UV light [199, 200, 201].

Due to the enormous size of the solvated (001)-rec surface system, we were able to reach a simulation time only of 6 ps with a reasonable computational effort. As mentioned before, our results on this structure refer to DFT calculations only and are shown in fig. 3.27. Here, all of the three modes of water adsorption could be recognized, with the molecular one dominating the scene. This is in agreement with the lower energy value for the molecular adsorption of water on pristine (001) as well as with its correspondent MD simulation. Despite the mirrored symmetry of the structure, the (001)-rec is the only case in

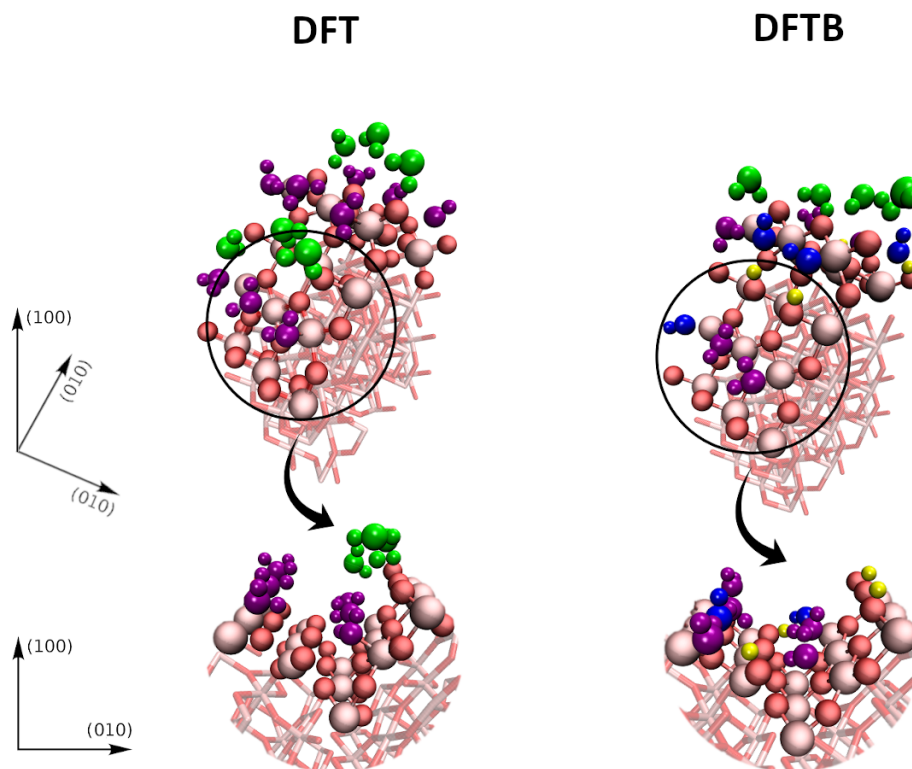


Figure 3.26: Final configurations of water adsorbing at the (100)-rec surface. The adsorption configuration mode of the water molecule is represented with the color scheme used so far¹⁴.

which different ratios of adsorption between the top and the bottom facets were observed. We attribute this feature to the big size of the system, which enhances the possible statistical sampling. In the first one, we detected 11 molecular adsorptions, 8 dissociative cases and 7 adsorptions led by formation of hydrogen bonds. At the bottom, we observed 13 molecular adsorptions, but only 4 dissociative cases and the double amount of hydrogen bound molecules, namely 14. These different ratios show how a lower presence of dissociative adsorption allows the formation of a larger amount of hydrogen bound molecules: the splitting of H_2O in OH^- and H^+ leaves less room for hydrogen bonds to form. Moreover, unlike the other structures studied so far, hydrogen-bound molecules lying horizontally were detected. This happens in both sides of the structure, more specifically in the two valleys: a double hydrogen bond was created, similar to the static calculations for (100)-rec (see fig. 3.22). The high dissociability of water was expected given the presence of exposed fourfold-coordinated Ti atoms on the surface, which have been observed to lead this type of adsorption in the presence of bulk water also for amorphous TiO_x layers grown on Ti in a previous work [202]. In all other systems, where the Ti surface atoms are at least

¹⁴The MD simulations in DFTB were computed by Verena Gupta. Also in case of the reconstructed case of (100)-rec, the addition of the water molecules in the systems was performed on my own and then forwarded to her.

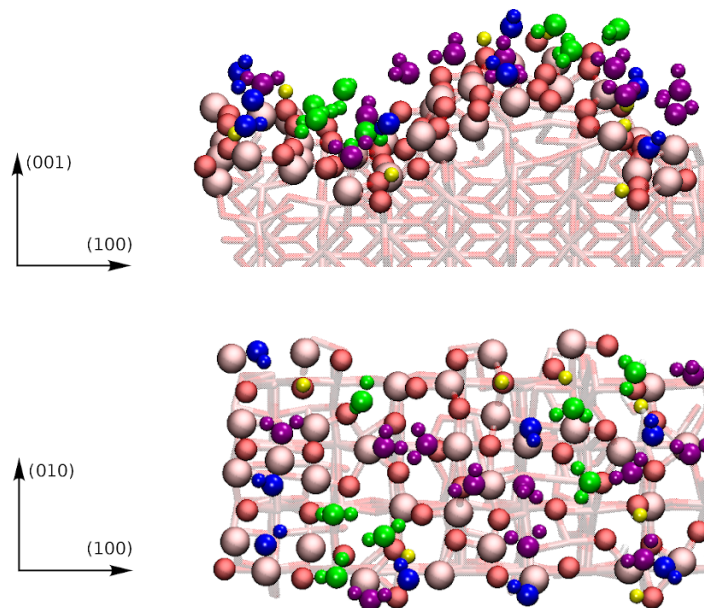


Figure 3.27: Final configurations of water adsorbing at the (001)-rec surface. The adsorption configuration mode of the water molecule is represented with the color scheme used so far. Water molecules not involved in any adsorption are shown as single sticks.

fivefold-coordinated, water adsorbed molecularly and did not dissociate for the entire duration of the simulations up to more than 10 ps. Of course we cannot exclude that dissociation could still take place, at least to some extent, after a longer time period. However, the observation is in line with the most favourable adsorption mode predicted by the static calculations described above.

In this structurally complex situation, hydrogen-bonded molecules play a much more pronounced role than in the previous cases as they are often the result of a combined reaction. As shown in Fig 3.28 for some representative examples, $\text{H}^+ - \text{O}_{surf}$ pairs tend to tear the structure apart towards the water bulk. This allow the formation of hydrogen-bound molecules through the help of a Grotthuss mechanism. Sometimes the presence of OH^- at Ti_{surf} atoms promotes a similar effect, but the stretching here is not as appreciable as for the surface oxygen atoms. In the first case (b), a water molecule that was first molecularly adsorbed with a Ti atom from the main island, desorbed to form two hydrogen bonds with two of the oxygen atoms present at the valley. As a result, one of them was pulled forcefully towards the water network, which also caused a slight local displacement of the nearby Ti atoms. The 3-fold coordinated oxygen atom of the case (c) belonged instead to the lower valley. The molecular adsorption of a water molecule on a nearby Ti atom, enlarged the structure locally and caused the O atom to move upwards. In this way, the weak long-range bond (2.3 Å) with the Ti_{bulk} below got broken and the oxygen atom became 2-fold coordinated. Due to this extreme undercoordinated site, it created a kinked-site in the valley that lasted for 2.5 ps. The atom returned then being 3-fold coordinated with the Ti_{bulk} , but the structure was too unstable to remain as it was, thus reforming the kinked-site. Such oscillations were driven by the high temperature of the system (320 K). We do not exclude that the

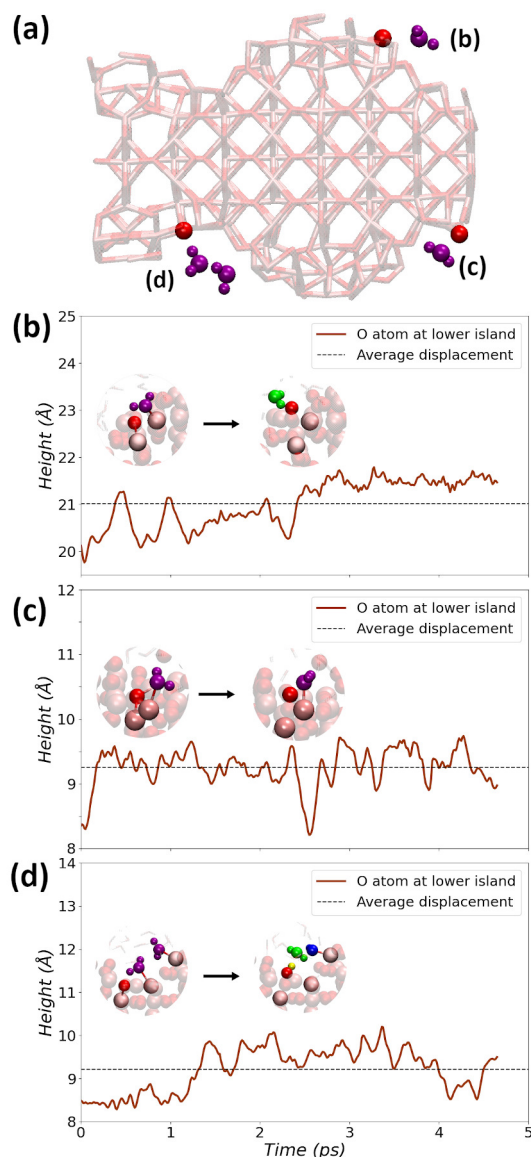


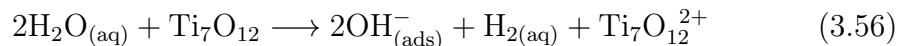
Figure 3.28: Three reactive oxygen surface atoms from either the island (b) or valley positions (c, d) and the corresponding adsorbed water molecules are highlighted. The adsorption configuration mode of the water molecule is represented with the color scheme used so far. The displacements of these oxygen atoms are plotted in (b), (c) and (d). The z coordinate is illustrated over time as a brown solid line. The mean height is plotted as a black dashed line.

alternation between 2-fold / 3-fold coordinated could continue over time, but on average it is clear that the first situation is the most favourable.

Case (d) consisted again of a 3-fold coordinated O atom in the valley near the lower island. At first, it did not feel the influence of any water molecule, but after 1 ps an H₂O that was molecularly adsorbed to the slope of the lower island desorbed, breaking apart into a proton and a hydroxyl, that was immediately re-adsorbed by the structure. The proton also adsorbed to the involved oxygen atom and dragged it towards itself. Also in this situation, the oxygen atom was forced to break the (weak) bond with its underlying Ti_{bulk}. Moreover, the

valleys played a fundamental role in terms of both reaction and recombination. It was possible to observe the migration of a hydroxyl from one adsorption site to another through a concatenated effect with the water-bulk first layer. The OH^- was at first bonded with a Ti in the valley, but after a recombination it was transferred to the slope of the main island. No dissociative adsorption was observed directly at the site between the two islands. Finally, there was a general tendency for the 4-fold coordinated Ti atoms close to the peaks of the two islands to adsorb two H_2O molecules simultaneously. This behavior did not happen in the pristine (001) case and it is reasonable to assume that it relates to the presence of interstitial atoms in the substrate, which make the structure non stoichiometric. The phenomenon was detected with two molecular adsorptions in which the bond lengths were at around 2 Å each and alternated the oscillations in a complementary way. Moreover, it was possible in one case to observe such a double adsorption involving a water molecule and a hydroxyl instead.

The high reactivity of the (001)-rec surface model suggests that a water splitting reaction could be energetically favourable and therefore takes place. The presence of excess Ti interstitials may promote thermally activated redox reactions with development of H_2 , as a consequence of direct surface oxidation upon adsorption of water molecules. The creation of molecular hydrogen at titanium dioxide interfaces is a well-investigated research field [52, 53, 203]. Here, the following pathway was assumed as a possible mechanism. First, two molecularly adsorbed water molecules get split into two hydroxyls, which remain at their adsorbing site and into two protons interacting with each other to form one H_2 molecule into the water net. This process is described by the following equation:



In order to understand whether or not such a reaction could in principle take place, the (001)-rec structure derived from our ab-initio MD was simplified to a system with only its first hydration shell. A geometry optimization was then performed, resulting in an overall configuration which recalls the original one at 0K (fig. 3.29). In both the lower and upper islands the Ti atoms felt the molecular adsorption of water and were dragged out of the underlying bulk. The same behavior involved the surface O atoms, which interacted with the H_2O molecules via hydrogen-bond formation. Furthermore, the Ti and O atoms, that tended to be torn apart by water during the previous MD (fig. 3.28), stabilized without moving back to their original position. To test whether the previously described reaction may occur, the total energy of the (001)-rec model was compared with three other systems in which two protons were displaced in a pseudo-random way and then coupled in the vacuum consisting of the implicit solvent [190]. The adsorbed water involved in this removal were at the valleys, at the top of the islands and at the islands' slopes. The total energy of the original model optimized after the ab-initio MD proved to be favorable to the reaction in all of the three cases. Only in the case of the extraction from the valley the energy turned out to be in the same regime as the original one with a difference of about 0.1 eV, whereas in the other two cases the total energy *decreased* by -2.8 eV (slope sites) and -3.0 eV (islands' top sites). Considering a correction

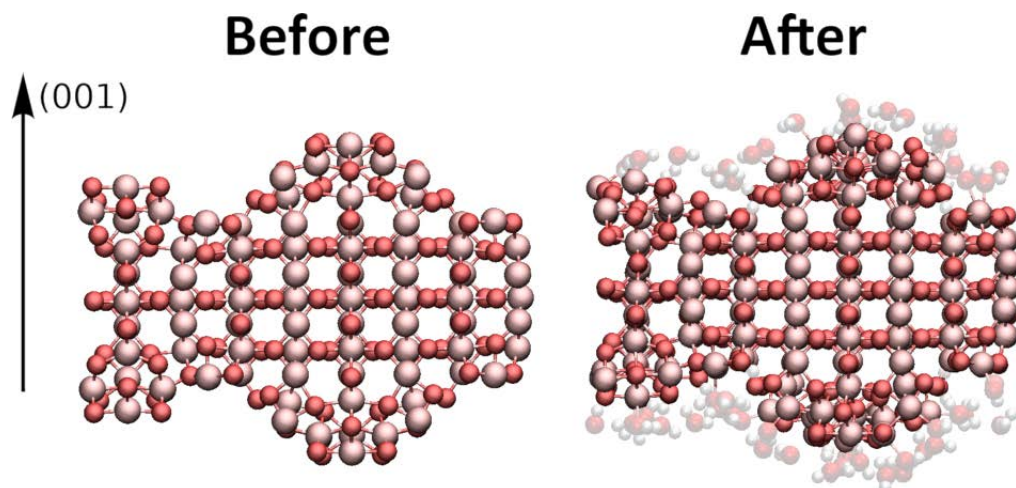


Figure 3.29: Ball-and-stick models of the (001)-rec structure obtained via geometry optimizations before and after performing the ab-initio MD with water at 320K. Water molecules are shown in transparent in order to highlight the kinked surface.

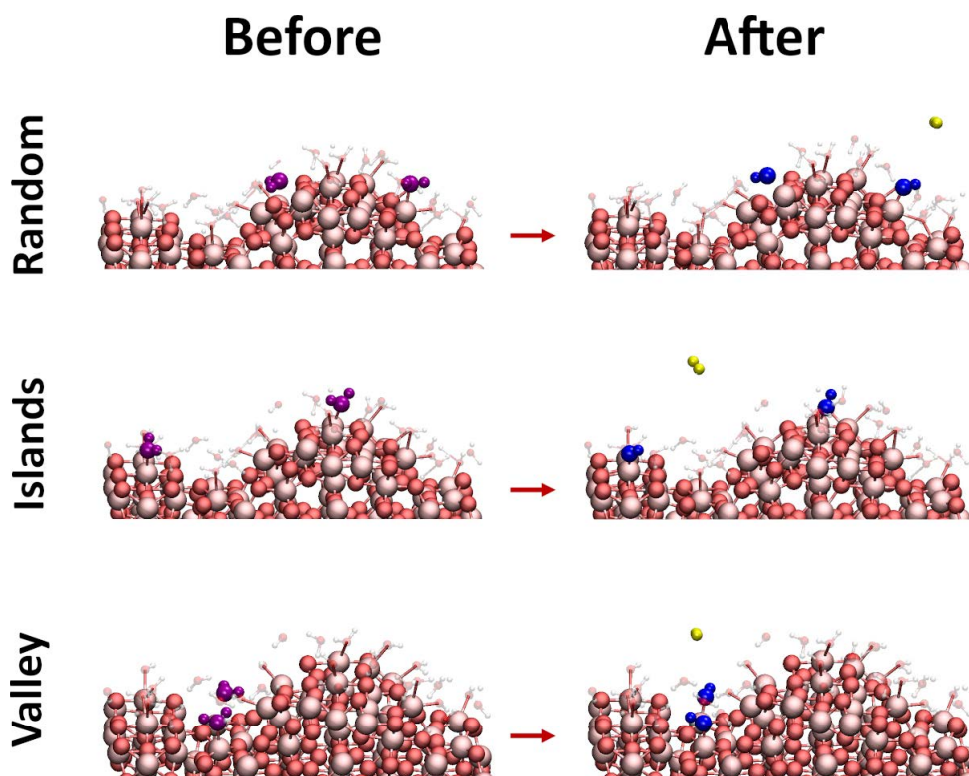


Figure 3.30: Three different scenarios were investigated for the process of water splitting and the formation of molecular H_2 upon reaction of adsorbed H_2O molecules on the reactive reconstructed (001) surface. From the top to the bottom, water molecules were randomly chosen in the islands or valley positions: the chosen molecular waters before the suggested reaction turn to surface hydroxyls and molecular hydrogen in its geometry optimized configuration.

of those values for the Gibbs free energy of solvation of an H_2 molecule from a reference gas state at 1 atm to bulk liquid water at 300 K, which amounts to

+6.6 kcal/mol [203, 204] (about +0.3 eV), we can estimate a driving force of at least ± 2.5 eV for the development of the reaction. This suggests that water splitting can be promoted by TiO₂ surfaces in case of the presence of partially reduced Ti sites as long as there is an external driving force able to sustain the creation of these sites, such as an externally applied potential or a sufficiently strong electromagnetic field. It is of course unknown if such mechanisms do play a role during the photocatalytic water splitting, which opens a new perspective to be investigated.

3.6 Summary

In this chapter it has been showed how several rutile surfaces (both pristine and reconstructed) provide different electronic properties, especially when water comes into play. Moreover, we have proven that DFTB was not able to fully confirm results coming from DFT.

The Tiorg-smooth DFTB+ set provides a powerful semi-empirical approach and can be trusted in the description of different surface energies up to unstoichiometric systems with metallic character. However, it tends to overestimate the values of surface energies and the electron affinity of surface O species. The DFTB evaluation of the band gaps was instead shifted by a constant value from the DFT one, but a lower band gap for the structure of (100)-rec as well as a metallic behavior for (001)-rec could be observed in both cases. The experimental work published so far for the (001)-rec unstoichiometric system provides only a top view of the surface model. Their 3-dimensional interpretation of the structure has resulted in different final geometries in DFT and DFTB+ which look the same in top view, making it difficult to decide which model is closer to the experimental data. We assume that our DFT calculations are more reliable than DFTB ones. In fact, not only tight binding approaches still encounter serious difficulties when dealing with metallic systems, but also the formation temperature found in the DFT calculations is in very good agreement with the reported experimental one [148].

In the systems involving water our DFT calculations generally support a predominantly molecular adsorption at a very low coverage (in line with experimental findings [39, 47, 48, 153]), a mixed situation on rutile-(110) at 1 ML and again a wholly molecular adsorption at larger coverages such as bulk liquid. The latter is a situation less accessible to experiments and would require *first rinciple* MD simulations. Therefore, only very specific H-bond patterns are able to partially stabilize dissociative adsorption. The same trend was reproduced on the surface of (100)-rec, for which the disagreement between DFT and DFTB was clear. Exceptions occur in the presence of peculiar in-surface hydrogen-bound patterns such as on the (110) facet at the water coverage of 1 monolayer, and whenever Ti atoms are strongly undercoordinated (4-fold or less), such as on the pristine (001) facet. This gives us confidence that the DFT predictions should be trusted and that DFTB has a tendency to overestimate the degree of dissociation in most of the cases. This behavior has been already observed for water on ZnO [205].

The unstoichiometric case of (001)-rec in water is a challenge for DFT due to the size of the system. Despite this, different reactions at both sides of the structure could be observed. Also in this case the molecular adsorption mode is the one to be preferred. In many of its sites, a trend for this surface to aggressively react with water could however be detected. Such actions shall be imputed to the unstoichiometry of the system as well as the high amount of undercoordinated atoms all over the surface. Within a simulation time of only 6 ps, one should not expect to achieve a proper and complete description of the full reaction pattern that water promotes at the (001)-rec structure. Finally, with the help of static calculations performed by geometry optimizations, we suggest that this surface can also promote the thermally-activated splitting of water by releasing H₂ molecules. This finding opens up the possibility that such reactions may occur during a photocatalytic water splitting upon exposure to UV light and creation of under-oxidised Ti superficial defects or in sub-surface sites.

In the work described in this chapter, it became clear that the model of a perfectly planar surface with exactly one adsorbate molecule is outdated nowadays. As one of the main tasks of our time, it is necessary to find a way to adequately describe material interface systems by means of approximated quantum chemical methods that move towards more complex configurations. Reconstructions, unstoichiometric systems and defects are the challenges of the next stage. With DFT we have reached a size and time limit that are not able to represent processes in such systems in a meaningful and long-time range statistical way. In this sense, semi-empirical approaches such as tight binding could replace ab-initio methods in the future in order to expand system sizes and time scales without the loss of meaningful information.

CHAPTER 4

Water pollutants on amorphous TiO_2

Organic contaminants are still a main threat nowadays which needs more investigations [6, 7, 8]. To date, most of the information on their dismantling is provided by experiments that are able to report macroscopic data such as degradation rates and pH dependence [10, 19, 12, 24, 13, 60, 55, 24, 61]. For instance, Dai et al. [55] reported that the mineralization rate of methamidophos dropped slightly of about 20% for pH values between the range 2.0 – 4.0 and between 10 – 12, while it increased significantly up to 90% after a pH value of 4 with a peak at 10. A similar trend towards higher degradation rates in basic environments was also reported in many other water contaminants [10, 12, 24, 13], but this does not exclude cases at acidic pH values [19].

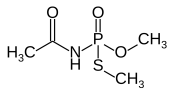
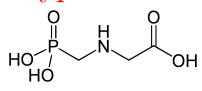
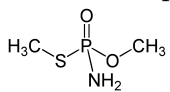
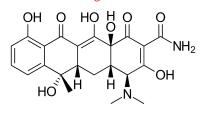
Despite access to this valuable information, the experimental description of the exact reaction mechanisms is very limited [66]. It is therefore necessary to proceed with computational simulations that allow to study first of all contaminants' adsorption modes.

Due to the use of TiO_2 in the biological and medical field, especially for dental implants, there are many studies concerning the protein- TiO_2 interface [206, 207, 208, 209, 210]. Most research in this area is conducted experimentally and it is mainly based on the identification of the bond formed by shifting the adsorption spectrum through vibrational frequencies as a fundamental parameter [211]. The used spectroscopic techniques are X-ray Photoelectron (XPS), InfraRed (IR), Raman, Sum frequency generation spectroscopy (SFG) and Circular Dichroism. These several works do provide important hints on how water pollutants may bind to different TiO_2 surfaces. Most of them share in fact a common structure to amino acids, since the collection of their side chains contains representatives to the functional groups. To give a few examples, one of the most studied amino acids in literature is Cysteine. Experimentally [209] and theoretically [208] the high chemical activity of thiol groups in the molecule

at surface oxygen vacancies is well-known. This amino acid also forms covalent bonds with TiO₂, driven by the interaction of the carboxyl group. For the amino acid Histidine also the backbone amine group and the imidazole side chain interact with the TiO₂ surface [210]. Finally, a carboxylate coordination was identified in some large lysine peptides. According to the study conducted by Roddick-Lanzilotta [212], this was only possible due to the increased flexibility of the polymer backbone. Only with a twisting of the molecule with respect to its gas phase adsorption could therefore take place.

In 2017, Tran et al. carried out a study where they gathered water contaminants concentrations before and after treatment [23]. With a cross reference work ¹, some of the major organic pollutants that are systematically found in waste waters are listed in tables 4.1, 4.2, 4.3 and 4.4. All of the reported contaminants were investigated on TiO₂ upon adsorption. They are classified in four categories: agricultural compounds, pharmaceuticals, industrial chemicals and daily usage. For each of them, their concentrations found in either ground water (Gr), marine water (Ma), surface waters (Sf), river waters (Rv), water treatment influents (WTI) or water treatment effluents (WTE) are also reported.

Table 4.1: Agricultural compounds treated with TiO₂. **Gr:** Ground Water, **Ma:** Marine Water, **SW:** Surface waters, **Rv:** River Water, **WTI:** Water treatment influents, **WTE**¹: Water treatment effluents. Red colors refer to pollutants investigated in this work.

Contaminant	Concentration	Application	TiO ₂ Literature
Acephate: 		Insecticide	Han et al. 2008 [213]
Glyphosate: 	Gr:1.42 μg/L[214]	Herbicide	Shifu et al. 2006[215]
Methamidophos: 	Rv: 46.43 ng/L [216]	Insecticide	Wei et al. 2008 [217] Zhang et al. 2002 [216]
Tetracycline: 	WTI:48 μg/L[23] WTE:3.6 μg/L[23]	Antibiotic	Zhu et al. 2013 [24]

¹The cross reference work derives from **Manuela Romero**'s co-supervised Bachelor's Thesis *Atomistic Simulation of Water Contaminants on Amorphous TiO₂ Surface Models*, **2018**.

Table 4.2: Pharmaceuticals treated with TiO₂. **Gr:** Ground Water, **Ma:** Marine Water, **SW:** Surface waters, **Rv:** River Water, **WTI:** Water treatment influents, **WTE¹:** Water treatment effluents. Red colors refer to pollutants investigated in this work.

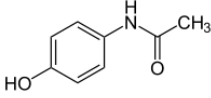
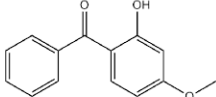
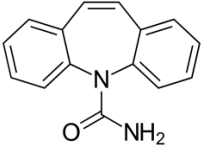
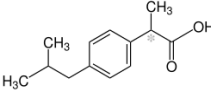
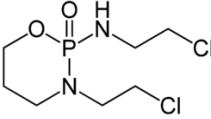
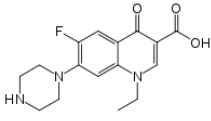
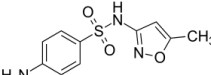
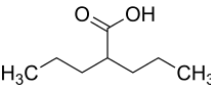
Contaminant	Concentration	Application	TiO ₂ Literature
Acetaminophen/ Paracetamol : 	WTI: 0.5 mg/L WTE: 62µg/L	Analgesic	Deluna et al. 2016 [9] Abdelwahab et al. 2017 [218] Jallaoui et al. 2017 [10]
Benzophenone : 	WTI :7.8µg/L[219] WTE:700ng/L[219]	Suncreams Food Packing	Zuniga-Benitez et al. 2016 [220]
Carbamazepine : 	SW: 93 ng/L[35] Gr: 76 ng/L [35] WTI: 83.5µg/L[23]	Anticonvulsant	Doll et al. [11] Im et al.[12]
Ibuprofen: 	WTI: 55.9µg/L[23] WTE: 14.6µg/L[23]	Anti-inflammatory	Chen et al.2018[13]
Ifosfamid Oxazasphosphorine: 	WTE:2.9 µg/L [221] SW:0.14ng/L	Chemotherapy	Lai et al 2015 [221]
Norfloaxine: 	SW: 231 ng/L[222]	Antibiotic	Sayed et al. 2016 [223]
Sulfamethoxazole : 	WTI: 11.5µg/L[23] WTE 3µg/L[23]	Antibiotic	Giannakis et al. 2017 [224]
Valproic Acid : 	WTI: 50mg/L[225]	Anticonvulsant	Haranaka-Funai et al. 2017 [225]

Table 4.3: Industrial chemicals treated with TiO₂. **Gr:** Ground Water, **Ma:** Marine Water, **SW:** Surface waters, **Rv:** River Water, **WTI:** Water treatment influents, **WTE¹:** Water treatment effluents. Red colors refer to pollutants investigated in this work.

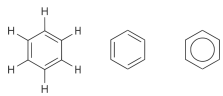
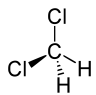
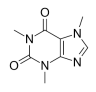
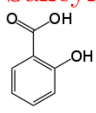
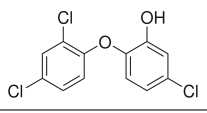
Contaminant	Concentration	Application	TiO ₂ Literature
Benzene: 	Ma:20 ng/L[16] Rv:800 ng/L [16] Gr:0.30mg/L [16]	Precursor in the Chemical Industry	Montoya et al.2013 [14] Schneider et al.2014 [15]
Dichloromethane: 	SW: 1- 743 μg/L[17]	Chemical Solvent	Borisch et al. 2004[18]

Table 4.4: Daily usage products treated with TiO₂. **Gr:** Ground Water, **Ma:** Marine Water, **SW:** Surface waters, **Rv:** River Water, **WTI:** Water treatment influents, **WTE¹:** Water treatment effluents. Red colors refer to pollutants investigated in this work.

Contaminants	Concentration	Application	TiO ₂ Literature
Caffeine : 	WTI:113.2μg/L [23] WTE:51.7 μg/L [23]	Stimulants	Arfanis et al. 2016 [19]
Salicylic Acid: 	WTI: 164.4 μg/L[23] WTE:10μg/L [23]	Cosmetics	Arfanis et al. 2016 [19]
Triclosan: 	SW: 62ng/L [34]	Antibacterial	Son et al. 2009 [226]

Among the listed pollutants, nine of them were chosen from the four different categories. They are highlighted in the tables in red. Their investigation was performed through static and dynamic FF interactions on a large amorphous TiO₂ surface.

The global pharmaceutical market has experienced a strong growth over the last years [227]. Acetaminophen (ACE) [228, 229], ibuprofen (IBU) [230] and

carbamazepine (CRB) [231] are among the most administered medicines belonging to this category, with consumption surpassing even 15000 t/year in case of IBU. The first two substances are suited for pain relief and anti-inflammatory actions, whereas the latter is an anticonvulsant for epilepsy treatments. Once injected and after their release in the human body, up to 58 – 68% of ACE, 15% of IBU, 10% of CRB as well as their metabolites are introduced to aquatic environments through disposal by the excretory system. They can be considered water contaminants due to their several negative effects: ACE can induce proliferation of breast cancer cells [218], IBU can strongly affect the photosynthesis of aquatic plants as well as the reproduction of aquatic animals [13] and CRB at uncontrolled rates can cause the Stevens-Johnson syndrome or associated diseases [12, 231].

Dangerous chemicals can also be found in industrial plants during their production chains. A major example are benzene (BEN) and dichloromethane (DCL), with applications such as fuel additives [232] and production of adhesives [17], respectively. When released through the factory effluents or from petrol spills in case of BEN, they get easily spread into water sources. While BEN provides high risks of cancer at concentrations above $1 \mu\text{g/L}$ [16], DCL is potentially able to destroy the stratospheric ozone by releasing chlorine into atmosphere [18]. Potentially environmentally hazardous chemicals are also found in everyday products such as energy drinks and cosmetics. Among the world's most consumed daily usage substances are caffeine (CAF) [20] and salicylic acid (SLC) [19]. The former has a stimulating effect on the nervous system, while the latter is used in make-up and for skin products. Due to their frequent use, these substances reach water sources very easily. Too high a dose of CAF in the human body can be lethal and toxicity thresholds have already been reached for some aquatic organisms [233, 21]. The environmental release of SLC affects instead phenomena such as photosynthesis and ion transport of some aquatic plants, risking harmful effects in case of high rates [22, 23].

The agriculture and livestock sectors are also rich of harmful organic chemicals. These include pesticides and insecticides for plants, but also medicines for animals. Glyphosate (GGG) is a very potent non-selective herbicide [27], whereas tetracycline (TTR) is a widely used breeding antibiotic [25]. Through processes of percolation to groundwater and expulsion by the excretory system, both substances respectively reach water sources at large concentrations [29, 30, 31]. While GGG may cause carcinogenic effects in humans along with many other diseases [28, 234, 235, 236], TTR and its mix with other anthropogenic contaminants affect aquatic plants such as green algae [26].

According to our knowledge, no theoretical nor computational studies of the aforementioned molecules have been conducted on TiO_2 surfaces. It is therefore necessary to achieve information through computational chemistry that could shed a light on the experimental results. In a sample used in a laboratory the amount of pollutants studied can reach very high concentrations. While this causes difficulties in collecting meaningful data, it also reminds us of the importance of statistics. When dealing with a single molecule on a surface in a simplicistic model, one cannot be certain that its adsorption configuration is the one that would occur with the highest probability. Although it does represent

a minimum point for the potential energy of the system, it is unlikely to be a global one. For this reason, methods that can explore the energy landscape as fully as possible are often used under the ergodic hypothesis. According to it, the time spent by a molecule in a thermodynamic system in the phase space volume of microstates of the same energy is proportional to the volume itself after a sufficiently long time. In other words, if one had infinite simulation time available, the probability of the molecule changing its state to another would tend to 1, ending up with all possible available configurations.

Another way to approach the problem is given by statistical multi-sampling. Instead of considering a single molecule in all its possible states, multiple molecules are distributed in different initial arrangements. Exploiting a sufficiently high number of molecules, assuming that they are inserted into the system in positions and configurations mutually independent, a Molecular Dynamics (MD) simulation can then be performed in order to study their temporal evolution. In this way it is not only possible to observe the different adsorption modes at various points on the surface, but also to estimate how many of these molecules do not adsorb or are attracted to each other more than to the surface, creating competition. In order to proceed with such a method, we have to rely on big systems and long MDs. The use of FF methods is therefore the most suited approach.

4.1 Theoretical background

The methods used in this chapter are based on the FF theory, on which both static rotational analysis simulations and dynamic simulations consisting of the multi-sampling approach were based. FF principles are here introduced with specific reference in the construction of the potential of the Hamiltonian, which is the key element that provides the main characteristics of the system.

4.1.1 Force Fields

In force fields (FF), the potential V of the Hamiltonian introduced in the chapter 2 is divided into two parts: one contains the intramolecular bonding information and the other the non-bonded intermolecular interaction [26, 81, 237, 189].

Bonded interactions:

- *Bonds.* The potential referred to bonds between atoms is a second order Taylor approximation around the minimum of the curve

$$V_b(\vec{R}_i, \vec{R}_j) = K_{ij}(R_{ij} - R_0)^2, \quad (4.1)$$

where k_B is the ab-initio parametrized or experimentally determined elastic constant, R_0 is the distance at equilibrium and $R_{ij} = \|\vec{R}_i(t) - \vec{R}_j(t)\|$ is the distance between the centers of the two atoms, as in fig. 4.1. This potential is the same of Hook's law for elastic forces and small oscillatory behaviors and therefore describes the binding interaction quite adequately.

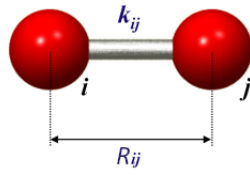


Figure 4.1: Bond formed between two atoms at positions \vec{R}_i and \vec{R}_j . Image from reference [238].

- *Angles.* Excluding trivial cases such as, for example, H_2 , O_2 and so on, most molecules are composed of more than two atoms. In principle, ideally one would consider the oscillating effect of the interaction between all the atoms in the system. However, this would complicate the overall potential and consequently the computational speed. Among the interactions to be considered, however, are the angles formed by three atoms (fig. 4.2), as their oscillatory behavior is fundamental in many situations. A classic

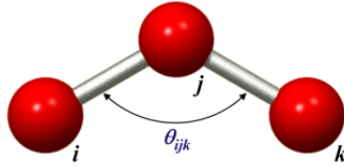


Figure 4.2: Angle formed between three atoms at positions \vec{R}_i , \vec{R}_j and \vec{R}_k . Image from reference [238].

example is the water molecule that, when free in the system at a certain temperature, decreases and increases in an oscillating way the angle spaced by the oxygen and the two hydrogen atoms. Also in this case, therefore, the use of Hook's law helps in terms of a well-approximated description. This time, however, the potential depends on three position vectors:

$$V_a(\vec{R}_i, \vec{R}_j, \vec{R}_k) = K_{ij k}(\theta_{ij k} - \theta_0)^2 \quad (4.2)$$

Again, the K_a constant has to be parametrized with ab-initio methods or determined experimentally. Here θ_0 represents the angle at its energetically minimum position, whereas $\theta_{ij k}$ is the time-dependent one. The latter can be trigonometrically defined as

$$\theta(\vec{R}_i, \vec{R}_j, \vec{R}_k) = \arccos \frac{(\vec{R}_j - \vec{R}_i) \cdot (\vec{R}_j - \vec{R}_k)}{R_{ji} R_{jk}},$$

where the atom j is here considered as the central one.

- *Dihedrals.*

A dihedral can be thought of as the extension of the concept of angle in a three dimensional space. It is defined as the portion of space between two half-planes (faces) having the same edge as their origin. In chemistry, this corresponds to the angle between planes through two sets of three atoms, having two atoms in common. Dihedrals, are the last, fundamental

interaction that cannot be avoided. In fact, they allow the description of the torsion of the molecule or a part of it. A torsion can be of proper or improper character. In the first case, one has a quartet of consecutively bonded atoms (fig. 4.3). This mainly allows to constrain the rotation

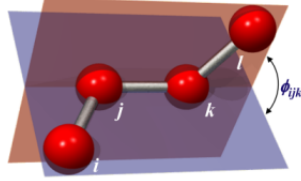


Figure 4.3: Dihedral describing a proper torsion, formed between four atoms at positions \vec{R}_i , \vec{R}_j , \vec{R}_k and \vec{R}_l . Image from reference [238].

around a bond. In order to describe this kind of torsion, we first need to define the normal vectors belonging to the two planes:

$$\vec{m} = \frac{\vec{R}_{lk} \times \vec{R}_{jk}}{\|\vec{R}_{lk} \times \vec{R}_{jk}\|}$$

$$\vec{n} = \frac{\vec{R}_{ij} \times \vec{R}_{jk}}{\|\vec{R}_{ik} \times \vec{R}_{jk}\|}$$

At this point, one can define the torsional angle ϕ_{ijkl} either through its cosine or sine functions as it follows:

$$\cos \phi_{ijkl} = \vec{m} \cdot \vec{n}$$

$$\sin \phi_{ijkl} = (\vec{m} \times \vec{n}) \cdot \frac{\vec{R}_{jk}}{\|\vec{R}_{jk}\|}$$

According to the official convention, the angle on its own is then given by

$$\phi_{ijkl} = -\arctan \frac{\sin \phi_{ijkl}}{\cos \phi_{ijkl}}$$

The potential which describes proper dihedral should then be defined as a function able of taking into account the energetic minima provided by the tilting of the two planes. One way to approximate this curve is given by a cosine formalism:

$$V_{prp.}(\vec{R}_i, \vec{R}_j, \vec{R}_k, \vec{R}_l) = K_{ijkl}^C [1 + \cos(n_{ijkl}\phi_{ijkl} - \phi_0)] \quad (4.3)$$

Here, the constant K_{ijkl}^C refers to the cosine description and it is a parameter identified either with ab-initio calculations or experimentally. The term n_{ijkl} is instead the so-called *multiplicity*, a positive, non-zero, real number indicating the amount of energetic minima as the bonds rotates on a period of $T = 2\pi$. Finally, ϕ_0 is the torsional angle at a starting equilibrium position of choice. In the second case of improper torsion, this is given by any other torsion occurring between four atoms not successively

bonded, as shown in fig. 4.4. This is used to understand, for instance, the

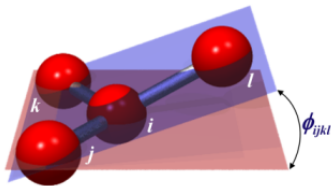


Figure 4.4: Dihedral describing an improper torsion, formed between four atoms at positions \vec{R}_i , \vec{R}_j , \vec{R}_k and \vec{R}_l . Image from reference [238].

chirality present in the molecule. Due to its functionality, an improper torsion only has one minimum in its description. Hence, a second-order approximation following Hook's law is sufficient for a proper description:

$$V_{imp.}(\vec{R}_i, \vec{R}_j, \vec{R}_k) = K_{ijk}(\phi_{ijkl} - \phi_0)^2 \quad (4.4)$$

The description of the torsional angle ϕ_{ijkl} and ϕ_0 is the same as in the case of proper torsion, since it still depends on exactly the same two planes. Again, the constant K_{ijk} shall be identified either with ab-initio methods or experimentally.

Non-bonded interactions:

- *Electrostatic.* The first of the two non-bonded interactions considered is the electrostatic one (fig. 4.5). Each i -th ion present in the system, in

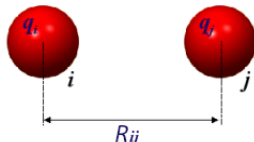


Figure 4.5: Electrostatic interaction between two atoms at positions \vec{R}_i and \vec{R}_j , with total charges q_i and q_j , respectively. Image from reference [238].

fact, possesses a total charge q_i . This is provided by experimental data or by charges deduced through ab-initio methods (for instance Mullikan or Bader charges), as it is deduced from the electronic distribution in the molecular orbitals and any dipole present in the molecule. In fact, more electronegative atoms attract electrons more than those with lower electronegativity, resulting in an uneven total charge distribution. The use of the classical coulombic potential is therefore an appropriate choice for the description of this interaction:

$$V_E(\vec{R}_i, \vec{R}_j) = \frac{q_i q_j}{4\pi\epsilon R_{ij}} \quad (4.5)$$

In the above expression, the term ϵ represents the dielectric constant in the medium. This value can become $\epsilon_0 = 8.85 \cdot 10^{-12} \text{ C}^2/\text{Nm}^2$ in case of a system in vacuum, otherwise it solely depends on the implicit

solvent used. In principle, electrostatic interactions are infinite and should take into account even atoms that are far away from each other. Since the coulombic interaction decreases hyperbolically to zero with increasing distance, it is a good choice to consider an energy cut-off beyond which it is no longer calculated. Usually this distance is set between a range of 0.8 - 1.2 nm, as it is thought to be sufficiently long to ensure no strong affections from atoms further than that [189, 237].

- *Van der Waals.* The second and final non-bonded intramolecular interaction consists of Van der Waals (VdW) forces. This is an effect due to correlations in the fluctuating polarizations of nearby particles, as shown in fig. 4.6. When the electron density temporarily shifts to one side of

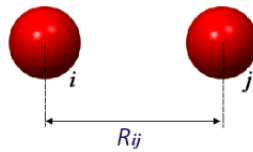


Figure 4.6: Van der Waals interaction between two atoms at positions \vec{R}_i and \vec{R}_j . Image from reference [238].

the nucleus of an atom, in fact, it develops a transient charge able to either attract or repel a nearby atom. Despite being the weakest form of interaction, VdW potentials shall not be treated as negligible terms: their collective effects, if any, may contribute in the total energy of the system. The usual way of describing VdW contributions is given either by Lennard-Jones or Buckingham potentials. In the first case, the formula is given by the difference of two hyperbole, one of grade 12 and the other of grade 6:

$$V_{LJ}(\vec{R}_i, \vec{R}_j) = 4\varepsilon_{ij} \left[\left(\frac{\sigma_{ij}}{R_{ij}} \right)^{12} - \left(\frac{\sigma_{ij}}{R_{ij}} \right)^6 \right] \quad (4.6)$$

Here, the term ε_{ij} is the well depth at the minimum $r_m = 2^{\frac{1}{6}}\sigma_{ij}$ of the potential. This corresponds to the equilibrium attraction. The parameter σ_{ij} shall instead be identified with ab-initio methods or experimentally. Its meaning is the separation for which the energy between the two particles is zero. Although the Lennard-Jones potential only consists in a pair-function, it yet describes well the VdW forces. In fact, the first hyperbola ensures a very strong repulsion at a very close distance, which then disappears quickly when the two particles are far away. Other powers can be chosen, but 12 and 6 are the conventional ones.

The Buckingham potential is another empirical potential proposed by Richard Buckingham as a simplification of the Lennard-Jones potential. Its mathematical expression is given by the following formula:

$$V_{Bh}(\vec{R}_i, \vec{R}_j) = A_{ij}e^{-B_{ij}R_{ij}} - \frac{C_{ij}}{R_{ij}^6}. \quad (4.7)$$

The three terms A_{ij} , B_{ij} and C_{ij} are in this case the parameters that shall be provided either experimentally or with ab-initio methods. The function

follows the same concept of the Lennard-Jones potential, with an additive exponential term for the repulsive part instead of the hyperbola of grade 12. Thanks to it, the Buckingham potential describes slightly better the repulsion of the VdW interactions, but it remains more expensive to be computed.

VdW forces, like electrostatic ones, have also in principle an infinite operating range. While a distance of 0.4 nm is needed to obtain a repulsive VdW interaction, it is sufficient to move the atoms away beyond 0.6 nm to no longer observe any kind of effect. Hence, a cut-off energy of about 0.6 nm can be used.

Once described all the bonded and non-bonded components of the total potential acting on the system, we can sum them up to obtain the following intrinsic expression:

$$\begin{aligned}
 V(\vec{R}_1, \vec{R}_2, \dots, \vec{R}_N) = & \sum_i^{N-1} \sum_{j>i}^N V_b(\vec{R}_i, \vec{R}_j) + \\
 & + \sum_i^{N-2} \sum_{j>i}^{N-1} \sum_{k>j}^N V_a(\vec{R}_i, \vec{R}_j, \vec{R}_k) + \\
 & + \sum_i^{N-3} \sum_{j>i}^{N-2} \sum_{k>j}^{N-1} \sum_{l>k}^N \left[V_{prp.}(\vec{R}_i, \vec{R}_j, \vec{R}_k, \vec{R}_l) + V_{imp.}(\vec{R}_i, \vec{R}_j, \vec{R}_k, \vec{R}_l) \right] + \\
 & + \sum_i^{N-1} \sum_{j>i}^N V_E(\vec{R}_i, \vec{R}_j) + \\
 & + \sum_i^{N-1} \sum_{j>i}^N V_{LJ}(\vec{R}_i, \vec{R}_j)
 \end{aligned}$$

Here, the Lennard-Jones potential was taken into account for the VdW contribution, as it is the standard choice of many simulation programs [237, 189].

4.2 Calculations protocols

The computational settings used in this chapter are listed below.

Force Fields parameters

The structures of the water contaminants was taken from the PubChem data base [239]. The water pollutants were constructed in their reduced configuration such that they possessed a neutral total charge ².

²The FF routine for the rotational analysis was conducted by [Manuela Romero](#)'s in her co-supervised Bachelor's Thesis *Atomistic Simulation of Water Contaminants on Amorphous TiO2 Surface Models*, 2018. Dynamic calculations were performed by [Maria von Einem](#), the results of which were analyzed through a Python script created on my own.

The FF parameters were generated using Antechamber, implemented in the AMBER program package [237] based on the *AMBER99SB* FF. The partial charges were calculated with GAUSSIAN98 (6-31G*) [240] and were adjusted according to the RESP scheme common for AMBER FF. The molecules were then minimized to the closest local minimum of the potential energy through the FF of AMBER retrieved from GAFF [241].

The TiO_2 surface used has a size of $8.18 \times 9.55 \text{ nm}^2$, namely $\approx 78.12 \text{ nm}^2$ [207]. This was created by cutting a single rutile model in a completely arbitrary manner [207]. After that, the crystal was heated up to 500 K through an annealing procedure, for a duration of 200 ps which produced a final amorphous structure. Some reactive water was further distributed on the surface according to the model implemented by Köppen et al. [128]. For a physical pH of 7.4, the absolute density of charge was 0.35 e/nm^2 . Note that the TiO_2 model was functionalized on just the upper side, meaning that adsorption events on the upper side are not significative for the selected pH value.

Rotational analysis

The molecules were placed at an arbitrary position and height over the surface³. They were then rotated along the combination of two angles α and β of 45° referred to perpendicular planes. A single MD step was here performed, which allowed the system not to have enough time to evolve dynamically, by leaving the structure of the molecule unchanged. In this way it is possible to calculate the force acting on the molecule at each orientation. This was done by summing up the z-coordinate of the single force acting on each atom in the contaminant. A positive force corresponds to a repulsion from the surface and vice versa. In principle, the larger the molecule, the more likely it is to observe a high total force. Atoms without significant z components however do not contribute significantly, therefore this simple approach still remains representative.

The procedure was iterated at different heights by keeping the same vertical reference over the surface, as shown in fig. 4.7. The reference height of 0 \AA was considered in the z-coordinate of the most exposed surface atom. Therefore, a negative distance means that the molecule dropped below this level, but still it did not enter the bulk or directly overlapped the TiO_2 surface atoms.

MD settings

The timestep set for the MD was set to 2 fs, allowing simulations up to 110 ns within a reasonable computational time. The sampling frequency was of 10 ps for simulations of 10 or 110 ns and it was dropped down to 1 ps in case of 1 ns dynamics in order to achieve a nice definition for a denser-framing approach.

The equilibration of the system was performed over 0.2 ns within an NpT ensemble and 0.5 ns in NVT ensemble at room temperature using first the Berendsen barostat and then the velocity rescaling thermostat [189].

³The FF routine for the rotational analysis was conducted by **Manuela Romero**'s during her co-supervised Bachelor's Thesis *Atomistic Simulation of Water Contaminants on Amorphous TiO_2 Surface Models*, **2018**.

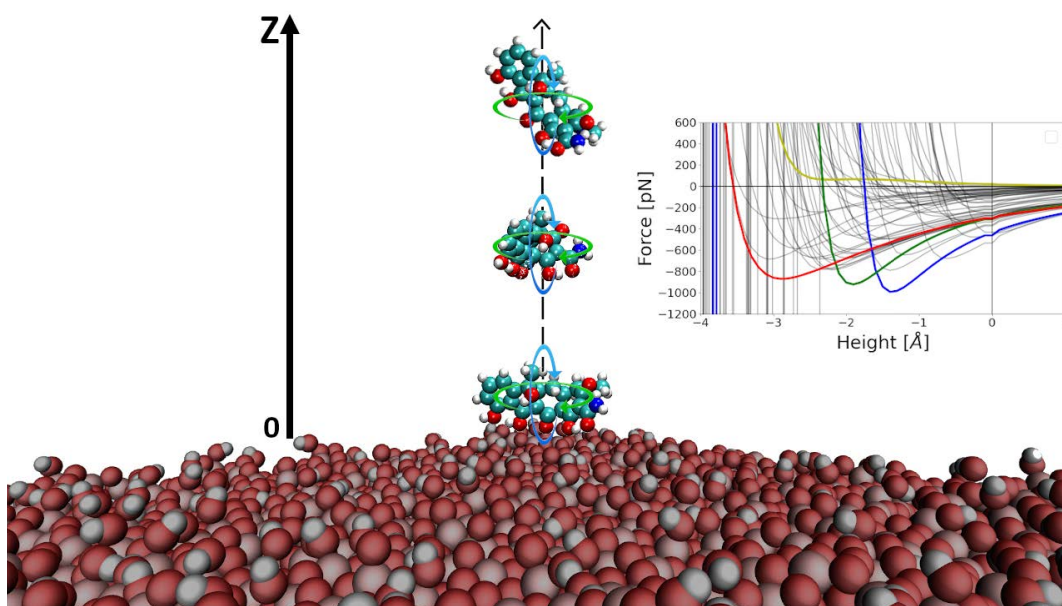


Figure 4.7: Scheme of the rotational analysis routine⁴ for TTR. The molecule is placed at a random position above the amorphous surface and it is rotated by 45° along two axis at different heights. The energy is then evaluated and force-distance curves are generated by finite differences.

The systems with 25 contaminants on the titanium dioxide surfaces were first calculated in AMBER [237] for 100 ps in an implicit solvent environment using the Generalized Born model. All further calculations were performed with the GROMACS program package [189] which allowed to fill up the cell with the TIP3P explicit solvent.

4.3 Force-distance curves

A good starting point for identifying adsorption configurations is to proceed with the static rotational analysis⁴. In this way it is possible to find an estimate of the attraction force as well as initial guesses for dynamic calculations. In figure 4.8 the force-distance curves are reported for the 9 selected organic water pollutants. The intensity of the minimum of the respective force-distance curves along with any functional groups driving the adsorption are listed in tab. 4.5. Careful observations of the results lead to four different possibilities. The first consists of a weak force (below 300 pN) and barely distinguishable orientations. This brings up the conclusion that molecules such as BEN and DCL do not feel a strong attraction nor a significant interaction with the TiO_2 surface. In a dynamic environment, where water solvent is also present and the ambient temperature of the system leads to non-negligible entropy, it can be expected that these two molecules will not be able to bond in a strong way to the material.

⁴The FF routine for the rotational analysis was conducted by [Manuela Romero](#)'s during her co-supervised Bachelor's Thesis *Atomistic Simulation of Water Contaminants on Amorphous TiO_2 Surface Models*, 2018.

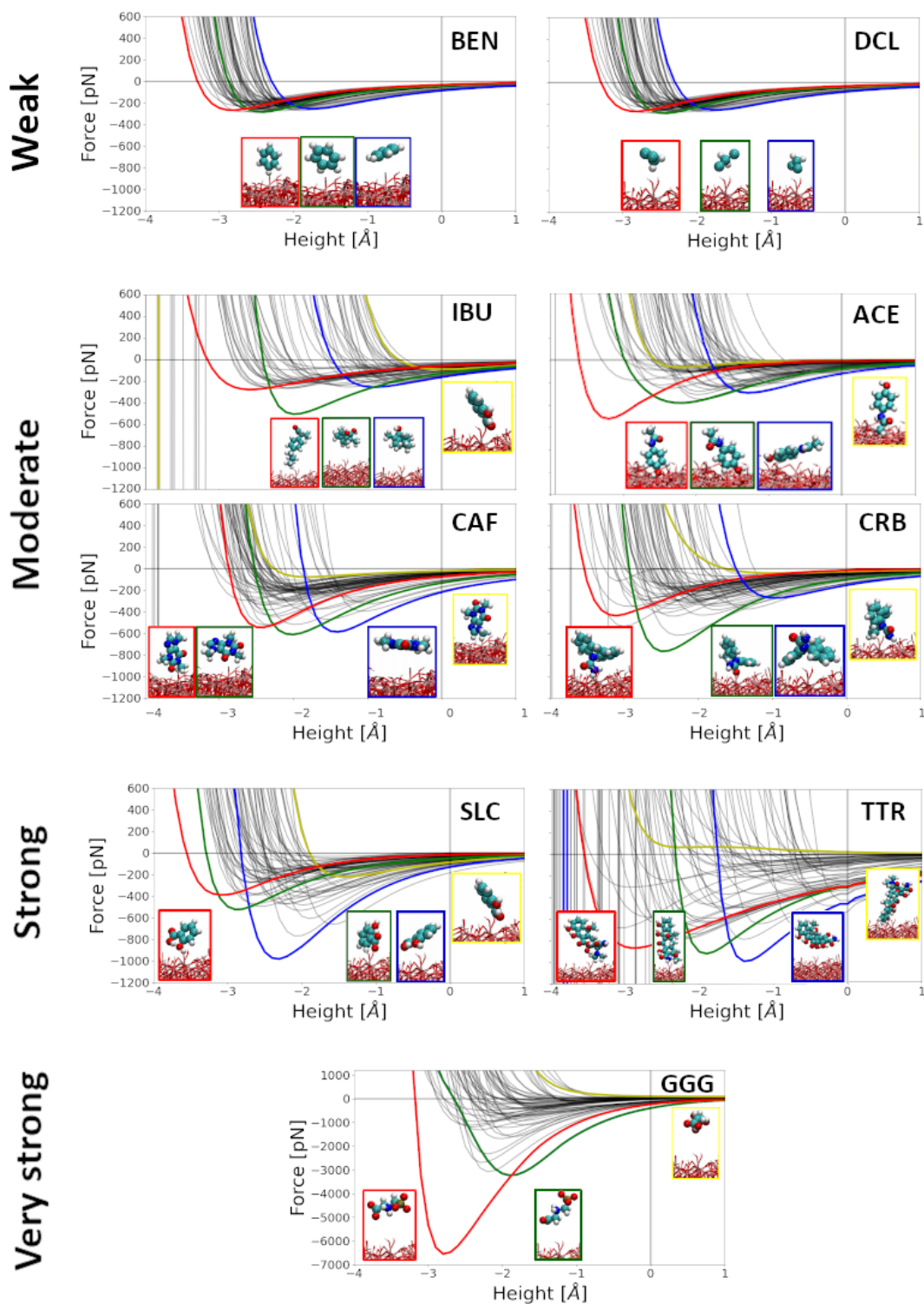


Figure 4.8: Force-distance curves of benzene (BEN), dichloromethane (DCL), ibuprofen (IBU), acetaminophen (ACE), caffeine (CAF), carbamazepine (CRB), salicylic acid (SLC), tetracycline (TTR) and glyphosate (GGG). The results refer to a physiological pH value of 7.4. Red, green and blue curves correspond to the most attractive configurations with major changes at different heights. In yellow the least attractive configuration is depicted⁵.

Table 4.5: Increasing intensities of the attractive forces and identification of the driving functional group towards adsorption.

Contaminant	Force [pN]	Driving functional group
BEN	-290	indistinguishable
DCL	-290	indistinguishable
IBU	-500	indistinguishable
ACE	-535	hydroxyl
CAF	-600	indistinguishable
CRB	-780	carboxamide
SLC	-1000	carboxyl
TTR	-1000	carboxamide
GGG	-6500	carboxyl, amino, phosphate

There are then forces with a moderate intensity (between 500 and 800 pN). Some of them, such as CAF and IBU, are not able to identify a precise orientation: for certain curves they tend to be positioned vertically and for others horizontally, corresponding to a similar force intensity. It is then challenging to predict here what to expect from a dynamic simulation, as all these orientations may actually correspond to adsorption possibilities. On the other hand, ACE and CRB tend to position themselves vertically on TiO₂ with their hydroxyl and carboxyl groups, respectively. The presence of a highly oriented adsorption indicates a higher likelihood of remaining at the surface than for CAF and IBU. The same is even more expected for SLC and TTR, which possess a high attraction towards the surface driven by the carboxyl and carboxamide groups, respectively.

Finally, it was surprising to observe how strong the force-distance curves for GGG (6500 pN) are, of which a precise adsorption configuration is also well defined. It is possible here to recognize how the molecule tends to position itself horizontally towards the surface, making all three of its main functional groups interact: the carboxyl, amine and phosphate groups. It is remarkable, however, that even for the second configuration identified the intensity of the force (3200 pN) is much greater than in any other molecule investigated. In this case it is the carboxyl group that is bonded to the surface, leaving the rest of the structure in a nearly vertical position.

Due to the simplicity of this approach, one key factor must be taken into account. This rotational analysis routine was actually developed with the intention of observing the major adsorption configurations of macroproteins, such as Lysozyme⁵. In this case, it works adequately due to the size of the adsorbate. Regardless of whether the surface has kinked sites, reconstructions or charged groups, the extent of the macroprotein is so large that it is only taken into account in global terms and is not particularly affected. When performing this type of analysis on organic pollutants, as in this thesis, it must therefore be

⁵The force-distance curves were computed using a modified version of a Python script originally developed by Nils Hildebrand in his PhD thesis *Molecular Dynamics Simulations of the Protein Adsorption Process on Oxides*, 2017.

remembered that the results obtained may strongly depend on the specific surface position in which the molecule is placed. Despite this, the method remains valid to understand the magnitude of the total force acting on the adsorbate and to have a first rough estimate on which functional groups are those that feel the greatest attraction. Multi-sampling approaches can be used to solve the problem of position dependence on the surface, as explained in the next section.

4.4 Dynamic multi-sampling

The statistical multi-sample approach performed consists of the regular distribution of 25 contaminants of the same species over the amorphous surface of TiO_2 at a height of 4 Å in an explicit water solvent at the physiological pH of 7.4. The molecules were placed equidistant from each other at distances of 7 Å and 15° rotations in order to simulate different types of orientations⁶. An example of this starting configuration is shown for GGG in fig. 4.9. Classical

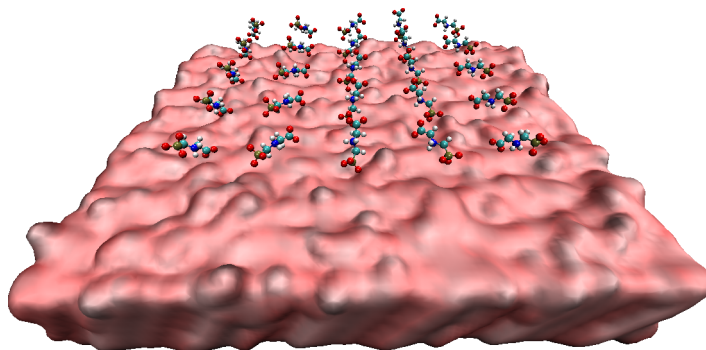


Figure 4.9: The 25 GGG molecules over the amorphous TiO_2 surface are here shown at the starting of the dynamical approach. The contaminants are equally spaced and they differ for rotations of 15° between one another.

MDs at 300 K were then performed for 10 ns with a sampling frequency of 10 ps. The results were analyzed through a Python script that allowed to report the relative residence rate at height intervals of 5 Å and the dynamic trend of the center of mass of each molecule. A total of three types of behaviors were then identify: no adsorption, formation of clusters, and adsorption of single molecules. The results for the 25 pollutants by species are shown in tab. 4.6.

Table 4.6: List of the 25 pollutants per species with their respective adsorption modes.

Mode	Contaminants
no adsorption	BEN, DCL
clustering	CAF, CRB, IBU, TTR
adsorption	ACE, SLC, GGG

⁶The regular distribution of the 25 contaminants in the dynamic calculations performed by [Maria von Einem](#) was generated through a Python script developed by [Manuela Romero](#).

The first category includes BEN and DCL. Since the very beginning of the MDs, the 25 molecules of each pollutant have barely interacted with the surface, never forming an attraction that would hold them for more than 0.5 ns. As shown in fig. 4.10, the contaminants were uniformly distributed within the space occupied by the slab and its repeated image, which is filled with explicit solvent.

This behavior confirms what was expected from the rotational analysis.

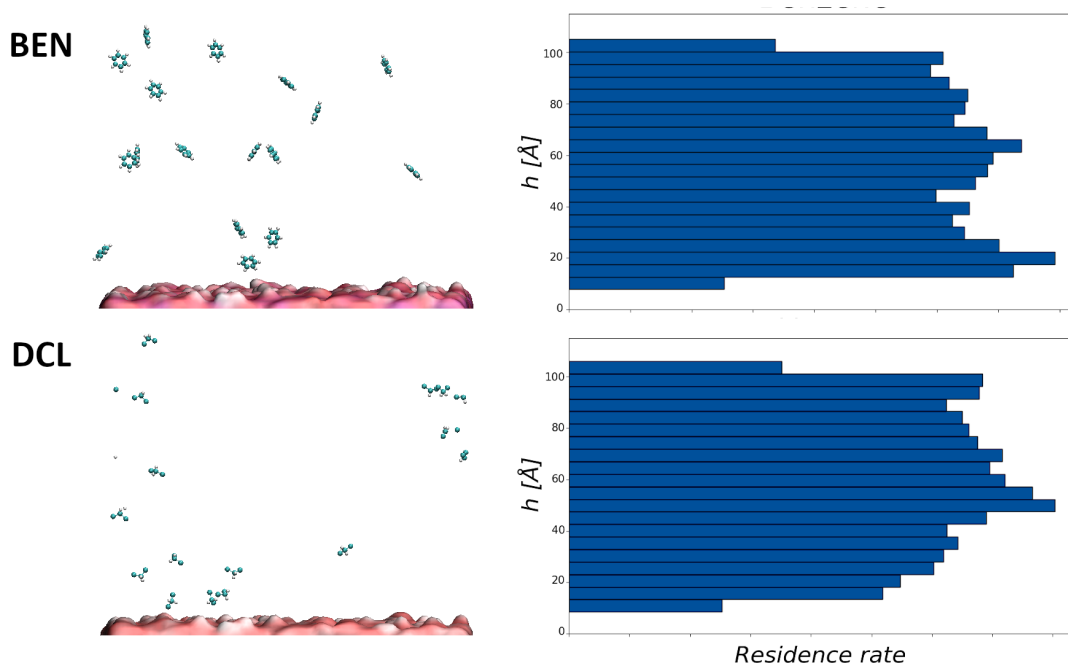


Figure 4.10: BEN: snapshot of the BEN molecules at the end of a 10 ns simulation. DCL: snapshot of the DCL molecules at the end of a 10 ns simulation ⁷. The histograms represent the residence rates of adsorption at the surface over a total time of 10 ns, evaluated on the z-coordinate of the center of mass of each molecule.

As many as four of the nine molecules investigated formed clusters during their simulation. This is a very significant data as it teaches us how the competition between pollutants can be a game changer in reactions such as adsorption and, consequently, degradation. Structures of this type could never have been found through a single pollutant study, which reinforces the importance of having access to statistical methods such as the multi-sampling done in this chapter. The final clusters are shown in fig. 4.11. Simulations of CAF, CRB and IBU have been extended 100 ns longer to better observe the dynamic evolution of the system.

The most impressive structure is provided by CAF, which resembles that of a DNA double-helix. The chemical composition and shape of a single CAF molecule belongs to the class of purine ring systems. Here we find also adenosine and guanine, nucleobasis of DNA. It is therefore reasonable, yet surprising, that a similar base stacking of CAF molecules forms in a dynamic environment. From the beginning of the simulation, CAF leaves the TiO_2 surface to start forming the structure.

⁷The FF MD simulations were performed by Maria von Einem, the results of which were analyzed through a Python script created on my own.

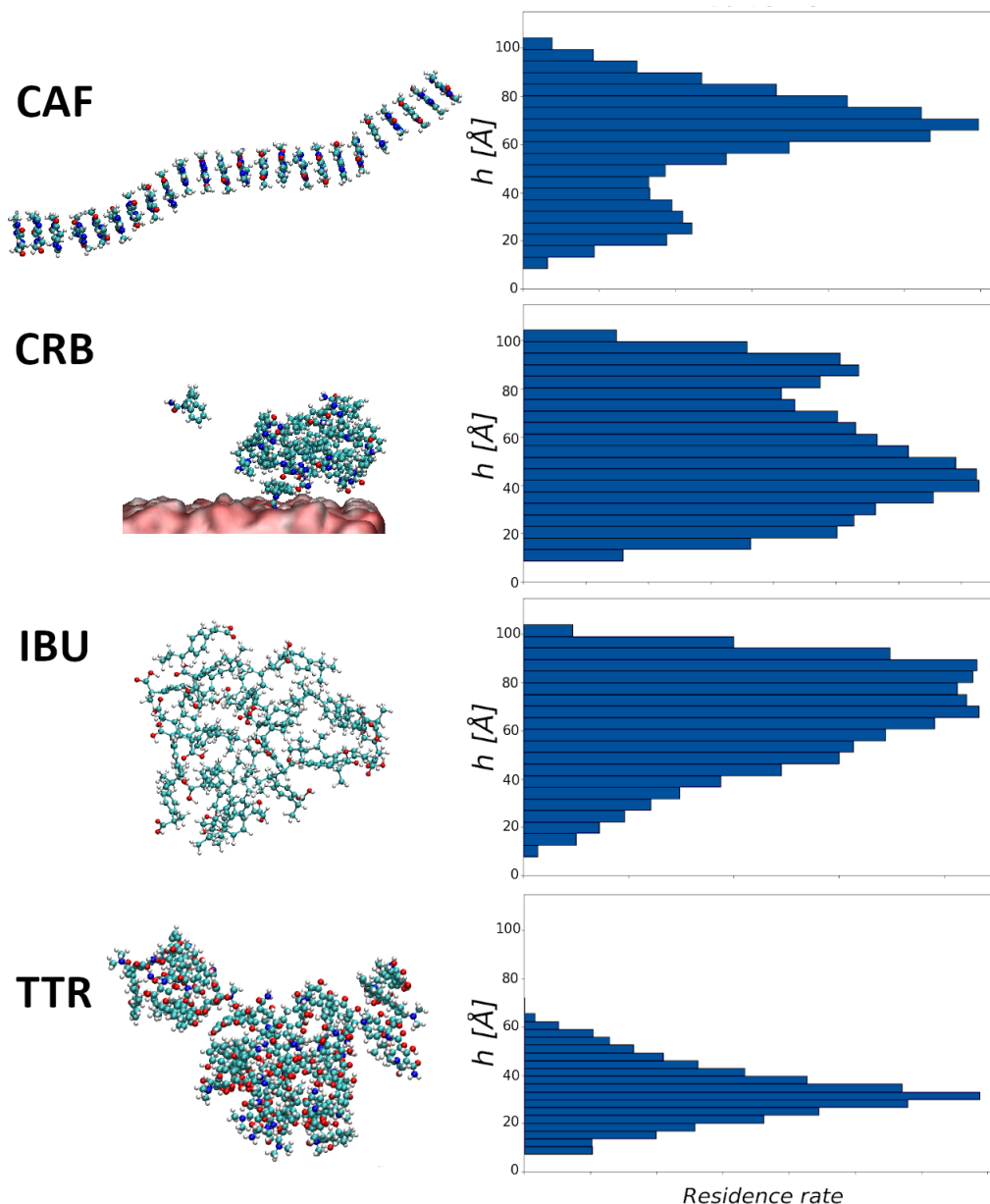


Figure 4.11: CAF: snapshot of the cluster formed by CAF molecules after 100 ns, which resembles the structure of a DNA molecule. CRB: snapshot of the amorphous cluster formed by CRB molecules after 110 ns, which also adsorbed at the surface for 7.4 ns. IBU: snapshot of the amorphous cluster formed by IBU molecules after 110 ns, which adsorbed at the surface for 3.7 ns. TTR: snapshot of the amorphous cluster formed by TTR molecules after 10 ns⁷. The histograms represent the residence rates of adsorption at the surface over a total time of 110 ns (10 ns in case of TTR), evaluated on the z-coordinate of the center of mass of each molecule.

Another contaminant that immediately forms a cluster, albeit an amorphous one, is TTR. Of all the TTR molecules in the system, only one adsorbs to the TiO_2 surface, distributing its skeleton horizontally and away from the cluster. This orientation recalls the one marked by the red curve in the rotational analysis, but it also evolves dynamically in the others (blue and green) before detaching from the surface.

Finally, both CRBs and IBUs share the commonality of creating a cluster that is attracted to the material in its entirety. In contrast to the cases mentioned so far, some CRB and IBU molecules are adsorbed by the surface at regular intervals, and then detached afterwards. In the meantime, the other molecules in the water network start to form two amorphous-looking clusters. These two macromolecules then interact with the surface from time to time, even managing to break up the first layers of water on it and thus creating direct adsorption. In the case of CRB, it is a single carboxamide group that drives the reaction, and then lets the structure lay horizontally and break away. The longest interaction identified for CRB is a whopping 7.4 ns. In the case of IBU it is impossible to identify a specific mediator group in the outermost part of the cluster: once in contact with the surface, it continues to turn on itself without indicating a more stable configuration than the others. This type of cluster remains bonded up to a maximum of 3.7 ns. It is interesting to note that the interaction of CRB and IBU clusters with the surface is still consistent with the predicted attractive functional groups of the respective rotational analyses.

For most of the time, the molecules of ACE SLC and GGG were subject to the strong entropy of the system and remained in the explicit water solvent between the surface and its repeated image. As shown in the two graphs in fig. 4.12, adsorption events were nevertheless present and therefore ACE and SLC belong to this category. The simulations have been again extended 100 ns longer in all three cases. Most adsorptions were mediated by water and were therefore

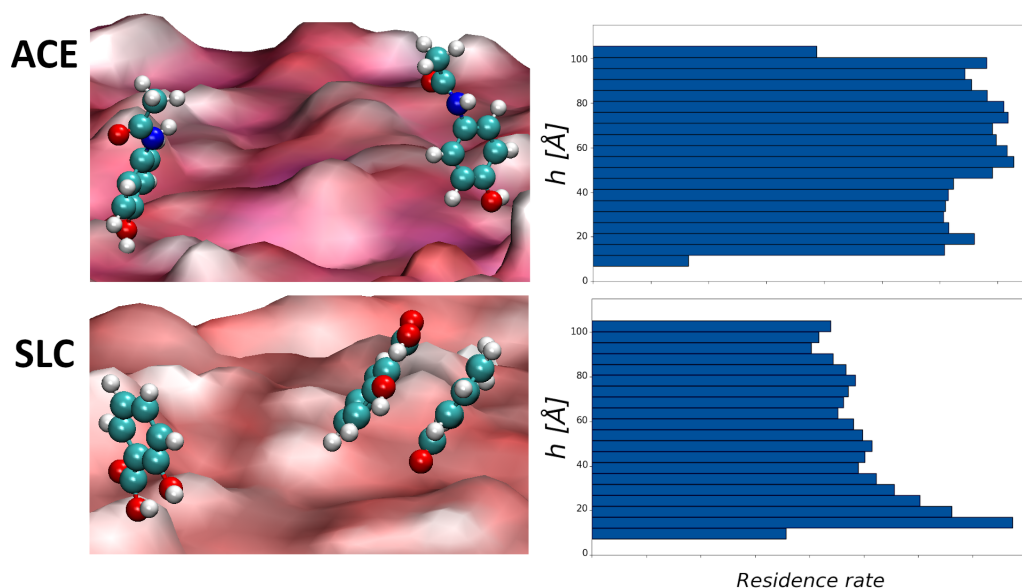


Figure 4.12: ACE: snapshot of two ACE molecules adsorbing at the surface vertically with their hydroxyl group. SLC: snapshot of three SLC molecules adsorbing at the surface: two of them bond vertically with their carboxyl group, another with the opposite part of the phenolic ring⁸. The histograms represent the residence rates of adsorption at the surface over a total time of 110 ns, evaluated on the z-coordinate of the center of mass of each molecule.

⁸Dynamic calculations were performed by Maria von Einem, the results of which were analyzed through a Python script created on my own.

rather weak due to an indirect interaction with the surface. The water molecules played in fact the role of a physical barrier that could not be easily overcome. When this happened, the molecules tended to position themselves vertically, as predicted by the static analysis. In case of ACE, the adsorption was always driven by the hydroxyl group and only rarely with horizontal configurations which did not stand for more than 5.0 ns. Also SLC confirmed the attraction given by the carboxyl group bonded up to 6 ns, but here adsorption events conducted by the opposite part of the phenolic ring could also be detected for less than 1 ns. Although no interactions between contaminants of the same species was identified for ACE close to each other, in case of SLC this happened instead quite often. The molecules formed a double-layered structure with an horizontal attraction of one on top of the other. We can therefore state that it is a principle of clustering, as the new structure was rather stable and did not break apart easily.

To better observe the type of adsorption for ACE, the simulation window was restricted to 1 ns out of the total 110 ns range. Here, the MD was performed with a denser framing rate so that the interactions with the surface could be detected more accurately. This simulation was cropped by considering the frame of fig. 4.12 (a) as the initial configuration. They were positioned vertically as predicted by the red curve of our rotational analysis. In the middle of the simulation (0.5 ns) no ACEs were adsorbed to the surface anymore. However, two of them still sensed the attractive force from TiO_2 , distributing one horizontally and the other with the amino group downward. Both of these configurations were identified by the rotational analysis, represented by rather weak force-distance curves (blue and yellow). At the end of this simulation with dense framing (1 ns), up to 5 molecules adsorbed to the surface were observed. Here, the main configuration was the one identified by the phenolic ring on the surface. Despite the presence of 3 molecules around the same adsorption site, as shown in fig. 4.13 (left side), no interaction was detected between them. This is an indication that ACE does not possess competitive behavior with its peer molecules. The

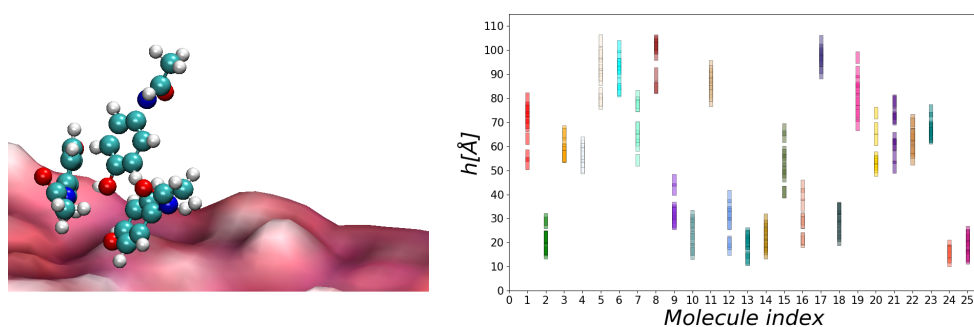


Figure 4.13: Overview of the dense-framing simulation of ACE at 1 ns ⁹. Three ACE molecules are found very close at the end of the simulation. The time evolution of each of the 25 ACE molecules in the simulation of 10 ns is shown, evaluated on the z-coordinate of the center of mass and sampled every 1 ns.

average position of the center of mass for each of the 25 molecules is shown

⁹Dynamic calculations were performed by Maria von Einem, the results of which were analyzed through a Python script created on my own.

with a different color is shown in fig. 4.13 (right side). It can be seen that the molecules that were already adsorbed at the beginning always remained near the surface, even when slightly detached. This is given by the fact that, due to the presence of the explicit water solvent, an ACE molecule is unable to diffuse away from the TiO₂ surface. The remaining molecules float in the explicit solvent or bind to the top of the slab model, which has no statistical significance as explained in the theoretical background section of this chapter.

4.4.1 A special mention: glyphosate

Of all the contaminants investigated, glyphosate represents the strongest case of adsorption. The results of the 110 ns MD simulation are shown in fig. 4.14.

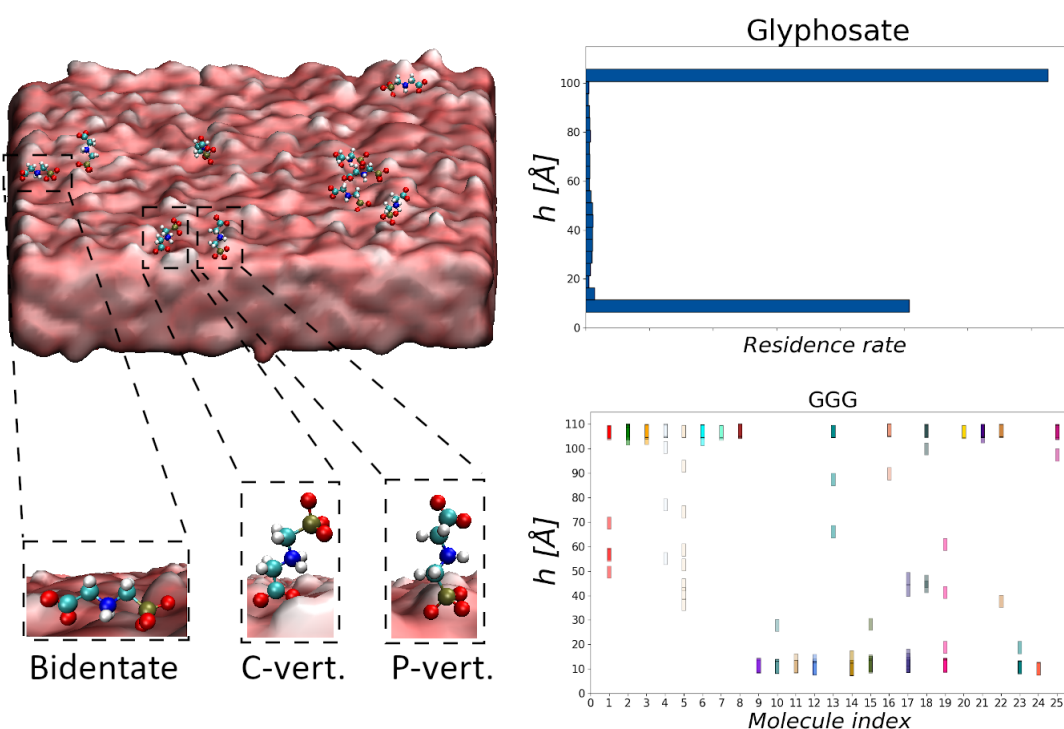


Figure 4.14: Left side: Final snapshot of the GGG simulation after 110 ns¹⁰. The three main adsorption configurations are highlighted and named after Bidentate, C-vertical and P-vertical. Top right: the histogram represents the residence rate of adsorption at the surface over a total time of 110 ns, evaluated on the z-coordinate of the center of mass of each molecule. Bottom right: time evolution of each of the 25 GGG molecules in the simulation of 110 ns, evaluated on the z-coordinate of the center of mass and sampled every 10 ns.

From the very beginning, 5 molecules were observed adsorbed steadily in contact with the surface. One of the 5 molecules bonded straight away in an horizontal fashion at the surface. In this case both the phosphate and carboxyl groups were in contact with the surface: for this reason the configuration has been named *bidentate*. The 4 other GGG molecules positioned themselves vertically interacting to the surface with the carboxyl group only. This configuration was

¹⁰Dynamic calculations were performed by Maria von Einem, the results of which were analyzed through a Python script created on my own.

called *C-vertical*. Due to the entropy of the system at 300 K, however, also the C-vertical orientations moved to bidentate modes after 10 ns. Here, the bond provided by the carboxyl group proved to be weaker than the one of the phosphate group. Some molecules thus raised the carboxyl moiety towards the water network, remaining in a vertical position with the phosphate group only bound to the surface. Such a structure was labeled as *P-vertical*. Within less than 3 ns, though, also all P-vertical configurations returned to bidentated ones. In the meantime other pollutants approached the surface directly in a P-vertical fashion. At the end of 110 ns, on the charged TiO₂ surface 5 bidentate structures, 4 P-verticals and 1 C-vertical could be identified, as shown in the bottom right side of fig. 4.14. The remaining 15 pollutants still felt a strong attraction from the TiO₂, binding to it in the opposite side of the slab model.

The high adsorption of GGG given by a horizontal configuration was already clear from the static results of the rotational analysis, where the intensity of the force was almost one order of magnitude higher than the others. Moreover, the C-vertical mode found in the same analysis is still representative on an attraction higher than any other pollutant.

Once again, the importance of using a dynamic environment with many molecules is confirmed in order to observe events that otherwise would not be identified¹¹. This is the existence of the P-vertical structure that rotational analysis failed to detect although it turned out to be more stable than the C-vertical. Nevertheless, the bidentate structure remains the most stable orientation that needs further investigation at even more advanced theoretical levels. To do this it is necessary to rely on quantum mechanics methods such as DFT, which is not able to handle an amorphous surface without falling into the regular repetition of the structure due to PBCs. However, a viable candidate structure is rutile-(110), which is also widely used in the lab to conduct experiments. A detailed investigation of the adsorption and possible degradations of GGG was therefore carried out and reported in the chapter 5, where we focused on the identified bident structure precisely on rutile-(110).

4.5 Summary

In this chapter, 9 different water contaminants were investigated in both static and dynamic terms. The rotational analysis provided initial guesses on which molecules had the highest adsorption propensity as well as on their possible binding orientations to an amorphous TiO₂ surface. Through long classical MD simulations of 25 pollutants of the same species it was possible to compare the results of the rotational analysis with a dynamic statistical approach. This multi-sampling analysis identified three types of molecule-surface interactions: no adsorption, clustering and singular adsorption. In most cases, the initial guesses predicted by the static approach were also confirmed by the dynamic approach. During the adsorption events, in fact, other orientations driven by functional groups different from those found through the rotational analysis were

¹¹Dynamic calculations were performed by Maria von Einem, whereas their histogram and time-evolution analysis was done through a Python script created on my own.

hardly found. The most striking exception is given by GGG which, showing a much higher adsorption than the other molecules, identified a new configuration (P-vertical) not found by the rotational analysis. The dynamic approach has also allowed to detect very interesting situations of clustering between pollutants of the same species, as in the case of CAF that resembles the structure of a DNA chain.

Despite the good agreement between the two methods, it must be remembered that they possess certain limitations. The FF approach does not allow direct electronic exchange and bases its strengths on harmonic conjectures. It is therefore necessary to supplement these approaches with more advanced levels of theory, such as DFT. On the other hand, without the approach of multi-sampling or FF MDs, it would be unthinkable in ab-initio methods to exploit simulations of even 1 ns and systems of such a large size. This means that, in DFT as well as other ab-initio methods, one could never have detected for instance the competitive behavior of CAF. Moreover, results derived from rotational analysis may depend strongly on the position above TiO_2 in which the molecule has been placed. Since the surface is amorphous the force-distance curves obtained at another site would not only change in intensity, but even the orientations they represent could be different.

During chapter 5, the FF studies performed so far regarding the GGG molecule will be supplemented with in-depth investigations at the ab-initio level on a pristine rutile-(110) surface. In this way it is possible to achieve a complete picture not only of the way of adsorption of GGG, but also of its possible degradation. It is our hope that the development of this top-down analytical approach will be a precursor to similar future investigations on the other pollutants as well as on different surfaces.

CHAPTER 5

Adsorption and degradation of glyphosate on rutile-(110)

The results presented in this chapter have been made public on [ChemRxiv.org](https://chemrxiv.org) [5].

Glyphosate (GGG) is one of the most controversial compounds used in the agriculture sector. This non-selective crop-desiccant was immediately successful after its discovery in 1970 [242]. The herbicides introduced before were less efficient and even more harmful when compared to GGG, which was then a very appealing alternative. The scientific reports of those times started praising it and wanted to highlight its extraordinary properties rather than focus on the harm to human health [243, 244, 245, 246]. For instance, it has been outlined how the product possesses a relatively low penetration in the soil, down to 15 cm and rarely deeper [247, 248, 249]. Natural degradation provided by the action of subsurface bacteria was also reported [249, 250, 251, 252]. Precisely because of its several advantages, the scientific community is still undecided about the dangerousness of GGG. The main opinion agrees, however, that it is a highly harmful substance [27, 234, 235]. As shown in fig. 5.1, the research on this molecule has been increasing over time [27]. Neurological issues, epilepsy and diseases of the endocrine system remains among the top concerns [236, 235, 28]. Especially the possibility of provoking cancers in humans remains the most fought discussion [253]. All these concerns led the European Commission to renew the approval of GGG for only 5 years, with a new assessment taking place already in 2022 [254].

The degradation process of GGG in soil has captured the attention of the scientific community and has been the subject of intense research. This crop-desiccant has a half-life of about 35 days for environments with a pH of 6.5

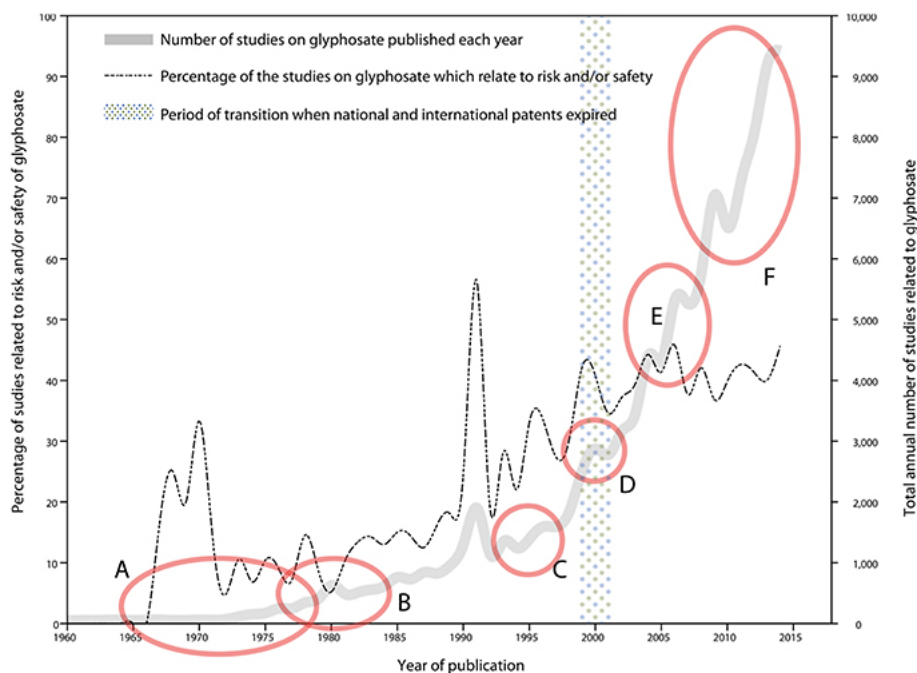


Figure 5.1: Numbers of publications on glyphosate (GGG) over time. Graph taken from the work of Cuhra et al. [27]. A: Period of development, approval and patenting. B: Initial safety assessments. C: Advent of glyphosate-tolerant-crops. D: Several important reviews on health and ecotoxicology documenting low toxicity. E: Emerging evidence on crop damage, residue accumulation and impact on non-target organisms. F: Evidence on complex effect.

- 7.5 and temperatures raging between 340 - 350 K. To date, the existence of two main pathways has been reported [255, 256, 257, 252]. The first well recognized reaction corresponds to the production of *aminomethylphosphonic acid* (AMPA) and *glycolic / glyoxylic acid*. This degradation occurs in case the N-C bond close to the carboxyl group of GGG gets disrupted. By breaking the P-C bond instead, *sarcosine* and *orthophosphate* are formed. Finally, calculations performed with density functional theory (DFT) by Catão et al. [256] reported that is the C-C bond the most likely to break in a water environment. Depending on the protonation state of GGG (e.g. its pK_s value), a different number of water molecules proved to be directly involved in the reaction, which resulted into methyl-AMPA. The role of water has been also highlighted experimentally, suggesting a hydrolytic character of the degradation process [258, 255]. Moreover, the reaction barriers proposed in Catão's study suggests that the mechanism can in principle be activated with photocatalysis. The photo-degradation of GGG is a well-accepted procedure that has been already observed in the laboratory [259, 260, 261, 236, 60]. According to the experimental studies, the AMPA way is the one of thermal degradation whereas the sarcosine way occurs in case of photocatalytic decay. These results do need however further theoretical investigations and Catão's work is one of the very few computational works present in literature.

The interaction with TiO_2 may represent the most optimal way to degrade GGG under UV light. Ilina et al. [61] conducted an investigation on the interaction

of TiO₂-rutile and anatase nanoparticles (NPs) in water when in presence of both GGG and AMPA. The study was conducted in the dark, so that they could prevent any induced photocatalytic mechanism. The two compounds were added together in the sample containing the NPs, which was then shaken by hand and allowed to settle for 24 h. It was observed that the TiO₂ NPs massively contribute in the degradation of the two pollutants. According to them, the phosphate group was primarily responsible for interacting with the NPs, stabilizing the adsorption. The same conclusion was also obtained by experiments conducted on other metal oxides [235, 256, 262]. As stated in Ilina's work, though, "little is known about the role of the involved functional groups" upon degradation. It is therefore necessary to proceed with more supporting information through more theoretical studies at the atomistic level.

In this chapter, different levels of theory were combined to investigate the adsorption and degradation of GGG on the surface of rutile-(110) introduced in chapter 3 [183], which was further extended in size for the classical MDs. The applied methods range from classical simulations, e.g. Force Fields (FF), to *ab initio* approaches, such as DFT, and TD-DFT. In the first case, the use of Newtonian equations only ensured the possibility to work with a significantly large statistical sample consisting in 25 GGG molecules as in the approach used in chapter 4. This allowed to conjecture an educated guess of what the most stable adsorption configurations should look like, which were then further investigated on the quantum mechanical level. After analyzing the adsorption energies, the electronic structure and the torsional contribution of the GGG-TiO₂ interface at its most attractive configuration, a mechanism of photocatalytic degradation was further suggested. This was accomplished by creating a cluster model of the rutile-(110) and investigated via TD-DFT.

5.1 Theoretical background

The computational treatment of systems involving excited states is very expensive [52]. Usually the most used methods are based on DFT calculations with hybrid exchange-correlation functionals, such as PBE0 [167, 168] or HSE06 [166]. However, here the self-consistent error does not allow to achieve sufficiently precise results. The implementation of the Hubbard correction U [263, 264] can solve the problem, but the outcome becomes dependent on the choice of parameters used. On the other hand, these methods have the great advantage of being able to deal with periodic systems or with systems bigger than those usually treated with first principle calculations. Here the combination of the Bethe-Salpeter [265, 266] approach with the GW approximation [267, 268, 269] as well as the time-dependent DFT (TD-DFT) [270], are limited to non-periodic systems. Another well known technique is to address the problem on only the involved active species, with the assumption of independent holes and electrons. In these terms, the exciton can be calculated as a triplet state, forcing the localization of the electron in a few surface layers by freezing the corresponding atoms. Other methods, such as Δ SCF [271], are also possible. All of these approaches are however restricted to static calculations only.

5.1.1 Molecular analysis

In this section the main analytical tools used to analyse the bidentate \perp configuration are introduced.

Bader net atomic charges

Together with the success of DFT in the early 60s, the electron density also gave raise to the Quantum Theory of Atoms in Molecules (QTAM) [272]. The main developer was Bader and his working group. According to this theory, it is possible to accurately describe the geometrical structure of a molecular system by investigating the topology of the electron density $\rho_{\vec{R}}(\vec{r})$, where \vec{r} represents an arbitrary position of an electron and \vec{R} is a parameter for an ionic position. Especially the interaction of nuclei, in fact, predominantly affects the topology of the electron density, allowing the detection of their positions as well as chemical bonds with use of electronic properties only. This means that a knowledge of the curvatures and critical points of ρ directly reflects the aspect of the molecules in the system, as shown in fig. 5.2.

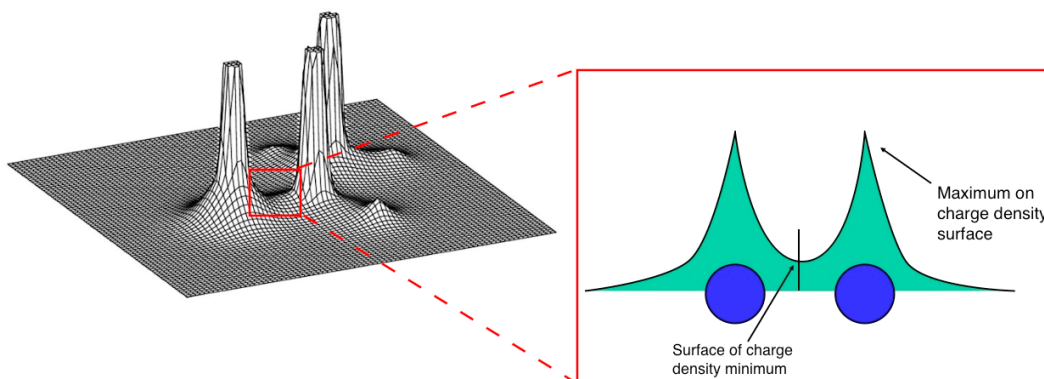


Figure 5.2: Electron density surface seen from a three-dimensional point of view. The bond between two atoms is highlighted to show a section of the electron density behavior. The first image is taken from reference [273], the second from reference [274].

Since the electron density is a scalar quantity, its critical points can be found in positions \vec{r}_0 such that

$$\nabla\rho(\vec{r}_0) = \vec{0} \quad (5.1)$$

Their classification as minima, maxima or saddle points follows then by the study of the eigenvalues of the Hessian matrix $H(\vec{r}_0)$. Thanks to the spectral theorem and with use of diagonalization procedures such as Gram-Schmidt or other LAPACK routines [275], it is possible to find the principal axes of curvatures $\lambda_1, \lambda_2, \lambda_3$. These eigenvalues are associated with a duple (ω, σ) for each critical point. The number ω is the rank and it consists in the number of non-zero eigenvalues. The term σ is the signature of the critical point, which is defined as the algebraic sum of the signs of the eigenvalues. Topologically stable critical points must be associated with positive eigenvalues, meaning that $\omega = 3$. This leaves 4 possibilities based on the entries of σ : $(3, -3)$, $(3, -1)$, $(3, 1)$, $(3, 3)$. Especially the first two of them are of main interest. The case

of $(3, -3)$ corresponds to a point the neighborhood of which has all the three curvatures negative. This is then a maximum in the electron density which in turn coincides to the nuclei positions. Singularities accounting for $(3, -1)$ have two negative curvatures and a positive one. It is a saddle point corresponding to a situation in which ρ is a maximum in a plane and a minimum perpendicularly to it. Such points are found between pairs of nuclei and are therefore directly connected to the concept of chemical bonds. For this reason, they are called *bond critical points*: pairs of gradient paths originating at these positions determine unique lines which connect neighbouring ions (attractors). Finally, the last two signature cases $(3, 1)$ and $(3, 3)$ correspond to another saddle point usually found in ring structures and to a local minimum, respectively.

Thanks to the bond critical points it is possible to approximately find the total electronic charge around each atom in the system by use of an expectation value. Since atoms in molecules have proven to be connected by surfaces in which the gradient vector field lies perpendicular to them, the following zero-flux interaction holds:

$$\nabla\rho(\vec{r}) \cdot n(\vec{r}) = \vec{0} \quad \forall \vec{r} \text{ between two bounded atoms} \quad (5.2)$$

This property allows to make well use of the expectation value of any atomic observable \hat{A} over a surface subspace Ω .

$$A(\Omega) = \langle A \rangle_{\Omega} = \frac{n}{2} \int_{\Omega} [\psi^*(\vec{r})\hat{A}\psi(\vec{r}) + (\hat{A}\psi(\vec{r}))^*\psi(\vec{r})] d\xi \quad (5.3)$$

with $d\xi$ being an infinite surface element of parametrization and n the total number of electrons in the system. By properly integrating and dividing the surfaces so that they coincide at the edges with the bond critical points it is possible to define the Bader net atomic charges:

$$q(\Omega) = (Z_{\Omega} - N(\Omega))e \quad (5.4)$$

where Z_{Ω} is the atomic number of the considered ion and $N(\Omega) = \int_{\Omega} \rho(\vec{r})d\xi$ is the averaged number of electrons. Adding all the Bader net atomic charges allows then to evaluate the total charge around the molecule.

Judgment of Energy DIstribution (JEDI)

Whenever a molecule gets involved in any reaction it is subjected not only to electronic exchange, but to major torsional mutations as well. Compared to its stable gas phase configuration, an interaction with other elements of the system actually creates some strain in its bonds, angles and dihedrals. An understanding of how much energy is stored in them is a useful information as it can shed a light on possible further mechanisms such as degradation. To date there are no experimental methods able to measure such features in a proper way and only few theoretical models have been proposed during the years [276, 277, 278].

The Judgment of Energy DIstribution (JEDI) is a quantum chemical tool that allows to analyze the distribution of strain energy in mechanically deformed

molecules [279, 280, 281]. This energy is a function of the changes in the redundant internal coordinates of the system. They are linear combinations of the minimum number of internal coordinates (bond lengths, bond angles, dihedrals) necessary for a complete description of the normal modes. In this sense, *redundant* is used because they add up to the $3N - 6$ degrees of freedom, although some of them can be zero [282].

Given $\{q\}_{i=1}^M$ redundant internal coordinates for a given molecule, the energy stored by each of them is defined through the Hessian matrix of $\vec{q} = (q_1, q_2, \dots, q_M)$ under the harmonic approximation, which holds for small stretches and bends:

$$\Delta E_{\text{harm}} = \frac{1}{2} \sum_{i=1}^M \sum_{j=1}^M \left. \frac{\partial^2 V(\vec{q})}{\partial q_i \partial q_j} \right|_{\vec{q}=\vec{q}_0} dq_i dq_j = \frac{1}{2} \sum_{i=1}^M \sum_{j=1}^M H_{ij}(\vec{q}_0) dq_i dq_j \quad (5.5)$$

In the above expression, $V(\vec{q})$ is the potential of the system in redundant coordinates and \vec{q}_0 corresponds to the equilibrium geometry before any torsion occurs. It is actually possible to move from infinitesimal $dq_i dq_j$ to finite differences $\Delta q_i \Delta q_j$ in order to work numerically on this quantity. Given the contribution of the force along the i -th component of an arbitrary \vec{q}_k ,

$$\vec{F}_i(\vec{q}_k) = -\nabla V(\vec{q}) \Big|_{\vec{q}=\vec{q}_k}, \quad (5.6)$$

it is possible to compute its associated energy per redundant coordinate needed to deform \vec{q}_0 to \vec{q}_k :

$$\Delta E_i = \int_{q_{0,i}}^{q_{k,i}} \vec{F}_i(\vec{q}_0) dq_i = - \int_{q_{0,i}}^{q_{k,i}} \nabla V(\vec{q}) \Big|_{\vec{q}=\vec{q}_0} dq_i \quad (5.7)$$

With use of a Taylor expansion of $V(\vec{q})$ around \vec{q}_0 up to the second order, we then obtain the finite difference version of equation 5.5 for a single contribution i :

$$\Delta E_i = \frac{1}{2} \sum_{i=1}^M \sum_{j=1}^M H_{ij}(\vec{q}_0) \Delta q_i \quad (5.8)$$

The harmonic total energy can then be reproduced by adding up all the contributions:

$$\Delta E_{\text{harm}} = \sum_{j=1}^M \Delta E_j \quad (5.9)$$

JEDI needs three inputs to start a calculation. The first two consist of the geometry optimized structures of the gas-phase molecule in a stable equilibrium configuration and that of the deformed structure. These two calculations are usually obtained by DFT methods, but JEDI is not restricted to this level of theory. The most expensive calculation is the computation of the Hessian, which needs to be positive defined and without artifacts such as imaginary frequencies. This requires very low energy convergence criteria, even on the order of 10^{-8} eV. Once the Hessian in Cartesian coordinates \vec{r} is computed, it is possible to transform it into redundant internal coordinates \vec{q} through the use of Wilson's

B matrix [283]:

$$H(\vec{q}) = (B^T)^\dagger H(\vec{r}) B^\dagger \quad (5.10)$$

5.1.2 Defining reaction pathways

In this section we introduce two methods used primarily for the study of free energy reaction barriers. In contrast to metadynamics, which often requires computational time not accessible to DFT because of the large statistical sampling it requires, steered MD and NEB can be used with reasonable effort.

Steered Molecular Dynamics

The steered MD approach was developed to observe the dynamic evolution of macromolecules, such as proteins, when one of their parts is subjected to an external force that deforms its structure [284]. Once the atoms to be pulled or compressed are identified, it is possible to bind them through a Hooke's law in which the spring evolves according to a given velocity $\frac{d\vec{\xi}(t)}{dt}$ provided a priori, where $\vec{\xi}$ is the constrained collective variable. Among the available methods there is the constant applied force method or the constant pulling (pushing) velocity method. In VASP the calculation is made by the second approach with use of a direct linear increment of the collective variable. Since we are interested in bond disruption, in this case

$$\vec{\xi} = \vec{R}_1 - \vec{R}_2 \quad (5.11)$$

corresponds to the bond distance between two atoms at positions \vec{R}_1 and \vec{R}_2 . The manual stretch is then applied by pulling (pushing) the two atoms simultaneously along their binding directions for a given time. In case of opposite repulsion, this would correspond to

$$\begin{cases} \vec{R}_1(t + \Delta t) = \vec{R}_1(t) - \frac{d}{dt}\vec{\xi}\Delta t \\ \vec{R}_2(t + \Delta t) = \vec{R}_2(t) + \frac{d}{dt}\vec{\xi}\Delta t \end{cases} \quad (5.12)$$

Note that the selected speed is an extremely important variable. In fact, it must be small enough to ensure that all other atoms in the system can interact with the molecule while it is undergoing linear deformation. On the other hand, it must be large enough to ensure adequate computational time to achieve the maximum selected stretch.

It is possible to define the resulting work needed to carry out the reaction from the initial state $\vec{\xi}(t_0)$ to the final one $\vec{\xi}(t_f)$ as

$$W = \int_{\xi(t_0)}^{\xi(t_f)} \left(\frac{\partial V(\{\vec{R}_I\}_I)}{\partial \xi} \right) \dot{\xi} dt \quad (5.13)$$

where $\xi = \|\dot{\vec{\xi}}\|$ and $\dot{\xi}$ is its time derivative. For an infinitesimally small velocity this actually would correspond to the free-energy difference between the two

states. For the purpose of this work, though, steered MDs have been used to dynamically sample degradation reactions in terms of initial and final products rather than energetically. Nudged elastic band (NEB) calculations have been performed to achieve such an information.

Nudged Elastic Band (NEB)

Given two stable and well defined configurations of the same system, it is possible to evaluate the energy barrier of the reaction from one to another through a NEB calculation [285, 286]. The necessary assumption is that both the initial and final states are in a geometrically and electrically optimized structure, which means they are local minima of the system free energy. The NEB approach allows to identify the minimum energy path (MEP) between those two states. This is defined as the way to go with the absolute least amount of energy effort. One of its properties is that it must necessarily pass through at least one first order saddle point of the free energy, as shown schematically in fig. 5.3 (a).

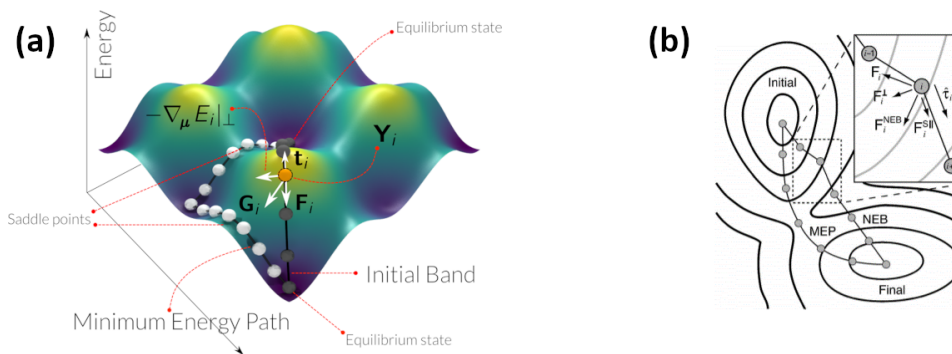


Figure 5.3: Initial imaging of a NEB to find the MEP between two equilibrium states in a three dimensional (a) [285] and two-dimensional (b) [286] perspective.

The basic idea of a NEB is to replace the parallel component of the force acting on a point of the system, which contributes in moving it away from the MEP, with that of an elastic force that does not make it move away from it. This projection is what gives the name *nudged* to the method.

The calculation is set up according to the following steps. First, the segment connecting the two minima \vec{R}_0 and \vec{R}_n is divided into $n - 1$ equispaced images, also called replicas. The number n must be decided a priori: the larger it is, the more accurate the convergence of the method will be, but also the slower. The images are then mutually connected to each other through springs with some constant k (also decided a priori) that decides how stiff the interaction is. Their elastic force is defined using three images, so that equal spacing is guaranteed even in regions with large curvature:

$$\vec{F}_i^{(S)} = -k \left[(\vec{R}_{i+1} - \vec{R}_i) - (\vec{R}_i - \vec{R}_{i-1}) \right] = -k(\vec{R}_{i+1} - 2\vec{R}_i - \vec{R}_{i-1}) \quad (5.14)$$

Being the union of steepest descent walks from a saddle point, at each point along the path the total force follows a direction parallel to it. In all its perpendicular directions (degrees of freedom) the energy is than stationary. It is

therefore reasonable to consider only the component of the real force \vec{F}_i acting on \vec{R}_i that is perpendicular to the path and try to bring it to zero. In order to do this, the tangent unit vector $\vec{\tau}_i = \vec{t}_i / \|\vec{t}_i\|$ needs to be defined between two images, where

$$\vec{t}_i = \frac{\vec{R}_{i+1} - \vec{R}_i}{\|\vec{R}_{i+1} - \vec{R}_i\|} + \frac{\vec{R}_i - \vec{R}_{i-1}}{\|\vec{R}_i - \vec{R}_{i-1}\|} \quad (5.15)$$

The perpendicular component of the total force is then described by eliminating the parallel one from the gradient of the potential:

$$\vec{F}_i^\perp = -\nabla V(\vec{R}_i) + \underbrace{(\nabla V(\vec{R}_i) \cdot \vec{\tau}_i)}_{\nabla V^\parallel(\vec{R}_i)} \vec{\tau}_i = -\nabla V^\perp(\vec{R}_i) \quad (5.16)$$

The total NEB force acting on the image \vec{R}_i is then given by

$$\vec{F}_i^{\text{NEB}} = \vec{F}_i^{(S)\parallel} - \nabla V^\perp(\vec{R}_i) \quad (5.17)$$

where the parallel component of the force was obtained through

$$\vec{F}_i^{(S)\parallel} = k[(\vec{R}_{i+1} - 2\vec{R}_i + \vec{R}_{i-1}) \cdot \vec{\tau}_i] \cdot \vec{\tau}_i \quad (5.18)$$

Elastic calculations with no nudging projection give spring forces which make the band too rigid and prevent it from converging to the actual MEP by causing a sliding away of the images from the high energy regions towards the minima [287].

Another artifact has been observed consisting in the generation of never converging kinked sites when the force parallel to the MEP has a value much larger respect to the perpendicular component [286]. A solution to this is given by a new definition of the tangent vector \vec{t}_i as

$$\begin{cases} \vec{R}_{i+1} - \vec{R}_i & \text{if } V_{i+1} > V_i > V_{i-1} \\ \vec{R}_i - \vec{R}_{i-1} & \text{if } V_{i+1} < V_i < V_{i-1} \end{cases} \quad (5.19)$$

which is what is currently implemented in the VTST [287, 288] code used in our work.

The NEB method provides a rather good description of the MEP, but it can evaluate the rate constant for the transition with major errors. This corresponds to the highest identified saddle point, namely the highest maximum of the potential energy along the MEP, which in turn is also the height of the reaction barrier. The shape of the energy along the MEP is in fact given by interpolation schemes and must be refined for the identification of the value close to a saddle point. The climbing image method [287] is an accurate procedure that solves the issue yet maintaining constant both MEP's shape and the computational effort. After a NEB is performed up to a certain convergence criterion, the image which is closest to the saddle point, say $\vec{R}_{i_{\text{max}}}$, is selected. A new NEB is then started, but the force acting on $\vec{R}_{i_{\text{max}}}$ shall now be defined in a way that the image actually climbs up the surface along the elastic bands and goes down

in their perpendicular direction:

$$\vec{F}_{i_{\max}} = -\nabla V(\vec{R}_{i_{\max}}) + [2\nabla V(\vec{R}_{i_{\max}}) \cdot \vec{t}_{i_{\max}}] \vec{t}_{i_{\max}} \quad (5.20)$$

The other images act then as the one degree of freedom necessary to maximize the energy up to the saddle point.

The last refinement that allows to find the saddle point with a very high precision is given by the dimer method [289, 290]. One that the two images \vec{R}_1 and \vec{R}_2 closest to a saddle point have been identified within a NEB, eventually with use of the climbing image protocol, the dimer can be defined. It consists of the pair (\vec{R}_1, \vec{R}_2) , which possess very similar coordinates and are spaced slightly by a fixed value ΔR along $\vec{\tau}$:

$$\begin{cases} \vec{R}_1 = \vec{R} + \Delta R \vec{\tau} \\ \vec{R}_2 = \vec{R} - \Delta R \vec{\tau} \end{cases} \quad (5.21)$$

where $\vec{R} = \frac{\vec{R}_1 + \vec{R}_2}{2}$ corresponds to their common midpoint, as shown in fig. 5.4 (a). The algorithm starts then to look for the saddle point by moving the center

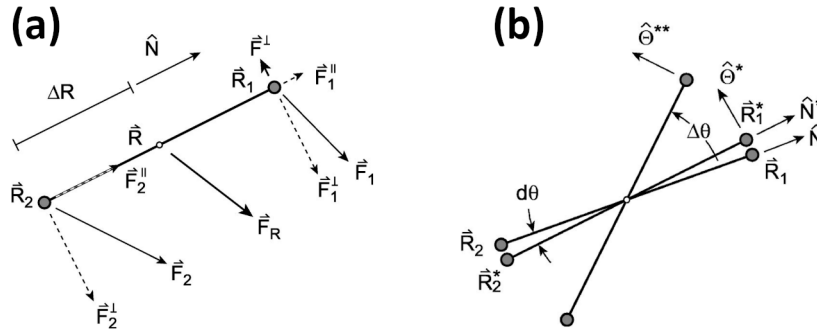


Figure 5.4: (a) Representation of the dimer together with the forces acting on it. (b) Schematic illustration of dimer rotation. Images taken from reference [289]

\vec{R} of the dimer uphill with both a translation and a rotation. At each new rigid location, the potential $V(\vec{R})$ acting on the center of the dimer is defined as

$$V(\vec{R}) = \frac{V(\vec{R}_1) - V(\vec{R}_2)}{2} + \frac{\Delta R}{4} [\vec{F}(\vec{R}_1) - \vec{F}(\vec{R}_2)] \cdot \vec{\tau} \quad (5.22)$$

which is derived from the finite difference formula representing the curvature. Note that, although one refers to \vec{R} , all the evaluated quantities actually come from the two images \vec{R}_1 and \vec{R}_2 only. The rotation of the dimer follows with a single iteration towards the minimum energy configuration. This can be performed with a Newton minimization algorithm. A small angle $d\theta$ is first selected to allow a finite difference estimate of the rotational force \vec{F}' :

$$F' = \frac{d\vec{F}}{d\theta} \approx \left\| \frac{\vec{F}^* \cdot \hat{\Theta}^* - \vec{F} \cdot \hat{\Theta}}{d\theta} \right\|_{\theta = \frac{d\theta}{2}} \quad (5.23)$$

In the above expression, $\vec{F}^* = \vec{F}_1^* - \vec{F}_2^*$ is the difference of the updated forces, whereas $\hat{\Theta}^*$ and $\hat{\Theta}$ are the updated and original unit vectors within the plane of rotation. The rotation then follows with a bigger angle

$$\Delta\theta \approx \frac{\vec{F} \cdot \hat{\Theta} + \vec{F}^* \cdot \hat{\Theta}^*}{-2F'} \quad (5.24)$$

obtained from the Newton method in order to bring the force within the plane to zero.

The efficiency of the dimer method strongly depends on the algorithm used to perform the rotation. For the first steps the Newton approach is a valid choice, but when the saddle points starts getting closer to the dimer the conjugate gradient algorithm brings to a faster convergence [289].

5.1.3 Time-Dependent Density Functional Theory (TD-DFT)

Ab-initio methods such as DFT start from the study of the time-independent (non-relativistic) Schrödinger equation. The lack of a time dependency is justified by the fact that the potential of the system reflects conservative forces, so the original Schrödinger equation can be decoupled into a time dependent and a stationary independent part. The elimination of the time variable allows to find stationary GS through the development of the Kohn-Sham equations A.22 and then recover the information through the Born-Oppenheimer approximation (see appendix). Twenty years after the introduction of DFT, Runge and Gross [291] derived a formulation taking into account the time dependency in a very similar way. They were able to show that the concept behind the first Hohenberg-Kohn theorem can be extended in the time domain as well.

Theorem 3 (Runge and Gross theorem). *Given the time-dependent electronic Schrödinger equation*

$$\hat{H}_{ee}(t) |\Psi(\{\vec{r}_i\}_i, t)\rangle = i \frac{\partial}{\partial t} |\Psi(\{\vec{r}_i\}_i, t)\rangle \quad (5.25)$$

where $\hat{H}_{ee}(t)$ is the time-dependent electron Hamiltonian operator, there exists a bijection between the time-dependent electronic density

$$\rho_{\Psi}(\vec{r}, t) = n \int_{\mathbb{R}^{3(n-1)}} \Psi^*(\vec{r}_1, \dots, \vec{r}_n, t) \Psi(\vec{r}_1, \dots, \vec{r}_n, t) d\vec{r}_1 \dots d\vec{r}_{j-1} d\vec{r}_{j+1} \dots d\vec{r}_n \quad (5.26)$$

and the time-dependent external potential $V_{ext}(\vec{r}, t)$ of the system.

Although the proof of this theorem is far from being trivial, its consequences are quite straightforward as they follow the same way of DFT. It is in fact possible to create a time-dependent non-interacting particle system of fermions, the Kohn-Sham system, which arises exactly the same time-dependent electron density of the original one. Assuming that the functions in play are v-representable,

it is then possible to write down the time-dependent Kohn-Sham equations

$$i \frac{\partial}{\partial t} |\psi_j(\vec{r}, t)\rangle = \left[-\frac{\hbar^2}{2m_e} \Delta_{\vec{r}} + V_{\text{eff}}[\rho, \Psi_0](\vec{r}, t) \right] |\psi_j(\vec{r}, t)\rangle \quad (5.27)$$

where $\{|\psi_j\rangle\}_j$ are the Kohn-Sham orbitals and $V_{\text{eff}}[\rho, \Psi_0](\vec{r}, t)$ is an effective potential following the same logic of that in DFT. Note that the dependency to the initial state $\Psi_0 = \Psi(\vec{r}, 0)$ is a completely new feature of TD-DFT. This characteristic is inherited from the time-dependent Schrödinger equation itself, which is formally solvable only by having the information at $t = 0$. The initial state is therefore also the starting point for solving the time-dependent Kohn-Sham equations and it is usually taken as a Slater determinant of single-particle orbitals $\{|\psi_j(\vec{r}, 0)\rangle\}_j$. It is then important that this function reproduces the initial density ρ , such as in DFT, but also its first time derivatives.

TD-DFT finds its applications in several fields, but the most studied one is that of spectroscopy and excitations [270]. The time-dependent external potential can in fact derive not only from electrostatic interactions, but also from light emissions such as laser pulses hitting the particles. At $t = 0$ the system is in its GS, but when the first pulse comes this is not anymore the case. Due to the initial weakness of the laser (electric) field, perturbation theory can be applied once the exchange-correlation energy in the vicinity of the GS is known. This corresponds to the frequency-dependent linear response method, which allows to compute excitations and spectra. If $\delta V_{\text{ext}}(\vec{r}, t)$ is the applied perturbation on $V_{\text{ext}}(\vec{r}, 0)$, then the response of the electron density (but also of any other observable) can be expressed through a Taylor expansion:

$$\rho(\vec{r}, t) = \rho_{\text{GS}}(\vec{r}) + \rho_1(\vec{r}, t) + \rho_2(\vec{r}, t) + \dots \quad (5.28)$$

In case of linear response, the series gets truncated at the first order, which also explains the name of it. The first order term is found by the following expression:

$$\rho_1(\vec{r}, t) = \int_0^{+\infty} \int \chi(\vec{r}t, \vec{r}'t') \delta V_{\text{ext}}(\vec{r}', t') d\vec{r}' dt' \quad (5.29)$$

where χ is the density-density response function, defined as

$$\chi(\vec{r}t, \vec{r}'t') = \left. \frac{\delta \rho(\vec{r}, t)}{\delta V_{\text{ext}}(\vec{r}', t')} \right|_{V_{\text{ext}}(\vec{r}, 0)} \quad (5.30)$$

Since the system starts at its GS, the electron density can be written as a functional $\rho[V_{\text{ext}}](\vec{r}, t)$ of the external potential as there is no dependency from the initial state, like in DFT. The same applies then to V_{ext} and χ as functionals of ρ_{GS} .

Thanks to the fact that the time-dependent Kohn-Sham equations allow to compute a formally correct electron density, the exact response $\rho_1(\vec{r}, t)$ can be found from that of the non-interacting system:

$$\rho_1(\vec{r}, t) = \int_0^{+\infty} \chi_{\text{eff}}(\vec{r}t, \vec{r}'t') \delta V_{\text{eff}}(\vec{r}', t') d\vec{r}' dt' \quad (5.31)$$

In the above expression, δV_{eff} is the effective time-dependent potential evaluated to the first order by perturbing the energy, whereas χ_{eff} corresponds to the density-density response function in the non-interacting system with unperturbed density ρ_{GS} :

$$\chi_{\text{GS}}(\vec{r}t, \vec{r}'t') = \left. \frac{\delta \rho(\vec{r}, t)}{\delta V_{\text{eff}}(\vec{r}', t')} \right|_{V_{\text{eff}}[\rho_{\text{GS}}](\vec{r})} \quad (5.32)$$

The true density response can then be evaluated from the Kohn-Sham system by the first order change in the time-dependent Kohn-Sham effective potential:

$$\rho_{\text{eff}}(\vec{r}, t) = \delta V_{\text{ext}}(\vec{r}, t) + \int \frac{\rho_1(\vec{r}, t)}{\|\vec{r} - \vec{r}'\|} d\vec{r}' + \int_0^{+\infty} \int f_{\text{xc}}[\rho_{\text{GS}}](\vec{r}t, \vec{r}'t') \rho_1(\vec{r}', t') d\vec{r}' dt' \quad (5.33)$$

where the time-dependent exchange-correlation kernel f_{xc} has been defined as

$$f_{\text{xc}}[\rho_{\text{GS}}](\vec{r}t, \vec{r}'t') = \left. \frac{\delta V_{\text{xc}}[\rho](\vec{r}, t)}{\delta \rho(\vec{r}', t')} \right|_{\rho=\rho_{\text{GS}}} \quad (5.34)$$

Equation 5.33 again correlates the interacting and the non-interacting system: the exact linear density response $\rho_1(\vec{r}, t)$ is found by that of the non-interacting system to the effective perturbation $\delta V_{\text{eff}}(\vec{r}, t)$.

The linear response formalism allows the investigation of closed-shell systems and their singlet excitations. Triplet states are also useful to be investigated, as the localization of the electron in a few surface layers can be forced by freezing the corresponding atoms. The description of this kind of interaction still relies on linear response, but needs to be extended to take into account spin effects more extensively.

From periodic systems to clusters

The TD-DFT calculations performed in our work did not rely on the supercell approach, but rather on that of clusters. They consist of cropping a relatively small number of atoms from the bulk structure of a solid and investigating its reactions, such as adsorption of a molecule, as if it were a single "supermolecule" with no PBCs. The main advantage is that one can use sophisticated quantum chemistry techniques able to characterize electron correlation effects as well as excited states [292, 293, 294]. Cluster approaches are also widely used to investigate local defects such as vacancies [295, 296, 297], since the lack of the repetition of a supercell does not allow them to be infinitely reproduced. On the other hand, cluster structures should be generated with extreme attention to the truncated parts. The risk of taking few atoms into account is that of creating a structure with a high amount of undercoordinations. This would basically correspond to a surface in all directions, with a small room for bulk atoms to stabilize the cluster. If too many atoms are considered, though, the computational effort increases. A cluster that is sufficiently small but stable must therefore be constructed.

There are mainly three methods for building up such a structure [292]. *Free* clusters are the most straightforward way to go. They consist of a rather small cropped part of the crystal without any modification. This means that they are heavily subject to the selected size, which can be iteratively increased to prove the validity of the model. Since most of their atoms are surface atoms, though, they often need to be extended to big sizes before being stabilized. Another approach is that of *hydrogen saturated* clusters, which consist of small crystals with their dangling bonds saturated by H atoms. In this way it is possible to limit problems related to cluster size and boundary effects such as in free clusters. However, also in this case it is necessary to verify the stability of the saturation. It has been proven that for covalently bonded systems such as TiO₂ sizes up to 9 Ti and 18 O atoms were needed before finding a reliable model of rutile-(110).

The most preferred and widely used method is that of *embedded* clusters [298, 299, 300, 68, 301]. The whole system is here composed by three parts. First, the crystal gets cropped in a structure representing the quantum cluster. Here the region close to the adsorption site is treated with quantum chemical methods such as DFT. Chemical bonds as well as eventual modifications of the quantum cluster structure upon adsorption must be in a good agreement with a reference supercell or experimental system. This comparison leads then to the decision of the quantum cluster size and shape. The structure is then embedded in an extended point charge field (PCF) reproducing the correct Madelung potential when close to the surface. This is done by positioning the point charges in a way that coincides with the lattice points of the crystal in vacuum. The formal charges are often taken from the stoichiometry of the system: for TiO₂ they count as +2 for Ti and -1 for O atoms. Finally, it is necessary to find a way to avoid strong attractions between valence electrons of the surface atoms and the point charges. A boundary region around the quantum cluster is then created, in which repulsive effective core potentials (ECPs), pseudopotentials (PPs) or model potentials (MPs) are applied to mitigate the problem.

5.2 Calculations protocols

The computational settings used in this chapter are listed below.

FF settings

The FF parameters used in the description of GGG were implemented through the AMBER program package [237] based on the AMBER99SB FF ¹. The program Gaussian16 was used to compute the partial charges with the use of the 6-31G* basis set [240]. They were further adjusted within the usual RESP scheme present in AMBER. The final values are reported in fig. 5.5.

To increase the sampling of the adsorption modes, quenched annealing between 300 and 500 K of 10 cycles for 2 ns in total were added.

¹The settings of GGG within the FF calculation protocol were carried out by Maria von Einem, while Wilke Dononelli took care of the calculation of the charges with Gaussian16 [240]

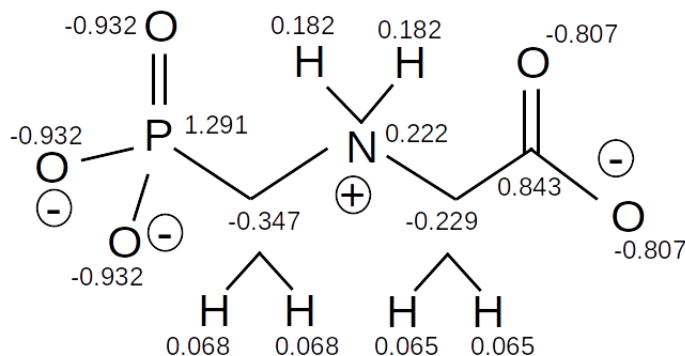


Figure 5.5: Distribution of the RESP partial charges on GGG computed from Gaussian16 (6-31G*)¹. Image created by [Maria von Einem](#) for ref. [5].

Extended rutile-(110) surface

The rutile-(110) slab model investigated in chapter 3 was extended in the xy-plane in order to perform FF calculations. It consisted of a 10×7 repetition of the optimized unit cells of $8.90 \times 13.19 \text{ \AA}^2$, which turned out in a simulation cell of $89.03 \times 92.32 \times 125.00 \text{ \AA}^3$. For ab-initio calculations the same slab of chapter 3 was taken into account.

Adsorption energies

The evaluation of the adsorption energy required as reference system the GGG molecule at a certain distance from the rutile-(110) slab model. This distance was optimized by evaluating the difference in the adsorption energies through a comparison of several settings: standard VASP calculations, with an implicit solvent [190], with the DFT-D3 correction term of Grimme [172, 173] and with a combination Impl. + DFT-D3. The procedure was the following: first, the molecule of GGG was inserted at a distance of 11 \AA between its center and the first perpendicular surface atom of rutile-(110). The system was then geometry optimized for each of the aforementioned settings. The GGG molecule was then shifted up of +1 \AA with a rigid movement and a new geometry optimization followed. The protocol was repeated for three times, until a distance of 14 \AA has been reached (see fig. 5.6). The resulting adsorption energy differences are shown in tab. 5.1. From the calculations it is clear that the main influence is

Distance (\AA)	Std. (eV)	Impl. (eV)	DFT-D3 (eV)	Impl. + D3 (eV)
12	-0.13	-0.01	-0.13	0.00
13	-0.76	-0.01	-0.23	-0.01
14	-2.16	-0.02	-0.46	-0.01

Table 5.1: Energetic differences of GGG far from the surface evaluated with standard VASP calculations, with an implicit solvent [190], with the DFT-D3 correction term of Grimme [172, 173] and with a combination Impl. + DFT-D3 at different distances. The setting used in our results is highlighted in bold.

given by the presence of the implicit solvent, which can handle the zwitterionic

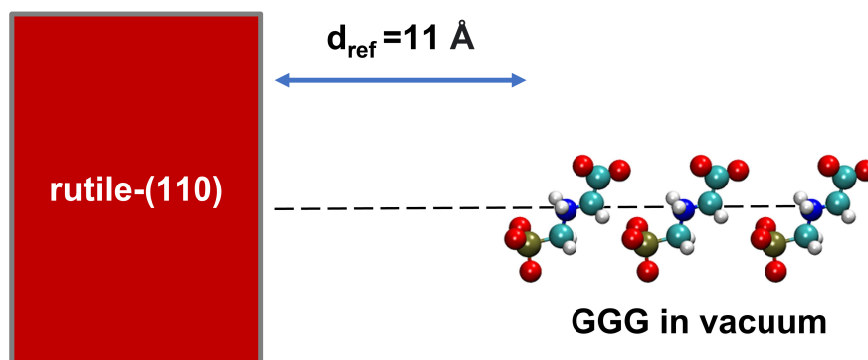


Figure 5.6: Scheme of the protocol used to optimize the distance between GGG and rutile-(110). The most stable configuration was taken as a reference system for the computation of the adsorption energies.

character of the GGG molecule. To maintain an acceptable substitute reference of the molecule in the gas phase, the 14 Å distance was chosen. Finally, although the presence of the DFT-D3 correction term affects the calculations to a lesser extent, it was still retained to remain consistent with the setting used in ab-initio MD with explicit water solvent, where VdW corrections have more influence.

Bader charge analysis

The Bader net atomic charges computed in this work were performed with the VTST software developed by Henkelman’s group [274]. Numerically, a partitioning of the electron density via a grid into Bader volumes is needed. This is performed by an algorithm following steepest ascent paths along the gradient, distributed at each grid point. Once a maximum is reached, the algorithm stops and proceed to other paths defining the whole surface. The method is efficient, robust and scales linearly with the number of grid points.

JEDI settings

The JEDI analysis performed in this work used the relaxed geometry generated by optimizing GGG freely in solution² This does not correspond to the global gas-phase minimum, but rather to the local torsional conformation closest to bidentate \perp . Only through this structure it was in fact possible to obtain a Hessian matrix without imaginary frequencies, allowing the JEDI analysis to be carried out. The real strain energy upon adsorption is therefore actually higher than the one calculated. This artifact, though, does not change our conclusions at least from a qualitative point of view.

The bidentate \perp configuration without the surface was taken as the mechanically strained structure.

²All JEDI calculations were performed by **Tim Stauch**, the results of which were interpreted and analyzed together with the other co-authors [5].

Steered MD

The GGG molecule in its bidentate \perp structure was placed on the explicitly solvated slab model of rutile-(110) obtained in chapter 3. In order to do this, five water molecules were removed from the surface and the solvent network to leave enough space for GGG to directly be in contact with the rutile slab. An NVT simulation at 320 K was then performed for 1 ps, followed by a 4 ps NVE one which guaranteed the thermodynamic stability of the bidentate \perp structure on TiO_2 in an aquatic environment also at the DFT level. The pulling in the steered MD lasted for 1.25 ps at 320 K in all studied cases, corresponding to a bond widening of 1.25 Å. The pulling velocity was set to 1 Å/ps to ensure that water could recombine or relax through the changed structure. After that, the resulting fragments were move freely within an unconstrained MD for a time different from reaction to reaction.

NEB settings

All initial and final configurations were geometrically optimized to energy differences of 10^{-3} eV before starting any kind of NEB or dimer calculation.

The N-C bond break of the bidentate \perp structure has been investigated with a NEB composed by 15 images. The method started without activating the climbing image procedure for energy differences down to 10^{-2} eV; after this error the protocol was activated until an accuracy of 10^{-3} eV. The dimer method was then activated to find the exact position of the saddle point, which was defined with a high precision of 10^{-9} eV.

The same procedure was applied to the C-C bond break with 8 images without the dimer refinement.

The P-C bond break was optimized using the dimer method only ³.

Cluster properties

An embedded cluster model was created to investigate the photocatalytic properties and photo-degradation of GGG on rutile-(110)⁴. The structure is shown in fig. 5.7 This was constructed based on the periodic DFT rutile-(110) model optimized in 3. The central quantum cluster part consisted of a charged $\text{Ti}_{27}\text{O}_{54}[\text{O}_{34}]^{68-}$ fragment, with both Ti and O atoms fully coordinated in order to avoid the generation of artificial dangling bonds. The embedding environment was created with a total of 71247 within a half-sphere PCF cropped from the supercell model preserving charge neutrality and were arranged in a way that could reproduce the TiO_2 lattice parameters. A charge value of +2 was assigned to Ti atoms, whereas it was of -1 for O atoms to provide a good description of the long-term Coulomb potential. Atomic charge values were taken instead of the correspondent oxidation states [68]. Overpolarization effects were prevented with use of a boundary region between the quantum cluster and the corresponding PCF. This consisted of 113 ECPs positioned at the Ti atoms in the PCF close to the quantum cluster [302]. To achieve net charge neutrality, two separate shell

³The P-C dimer calculation was performed by Wilke Dononelli, who was also of great help in the validation of the two NEBs.

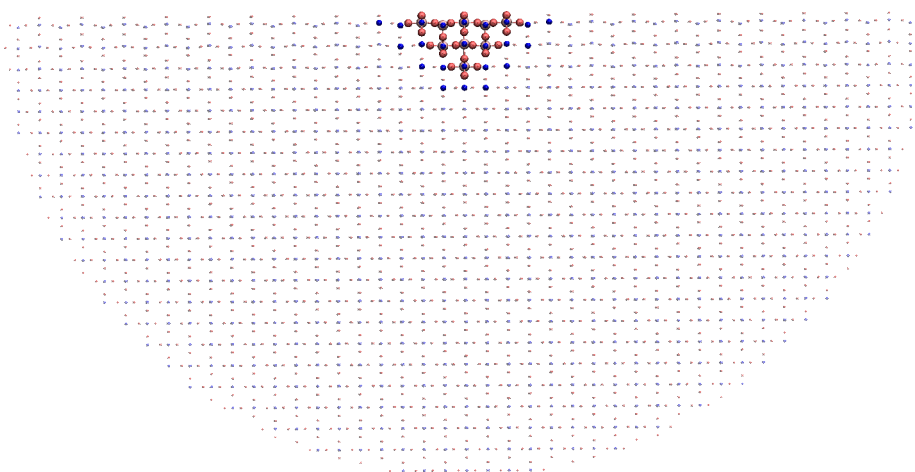


Figure 5.7: Front view of the cluster model. The quantum region ($\text{Ti}_{27}\text{O}_{54}[\text{O}_{34}]^{68-}$) is described by brushed metal atoms, whereas the 113 ECPs are in thick blue dots. The surrounding PCF is represented with 71247 fine transparent blue (negative) and red (positive) dots ⁴.

divided the ECP atoms. The outer shell was defined with the same charge values of the PCFs, namely +2. The inner shell, having to compensate also the charges belonging to the quantum cluster, had a value of +2.27 per ECP atom.

In order to compare the quantum cluster properties with that of the rutile-(110) periodic model, a geometry optimization of the 14 atoms belonging to the first layer was performed. Both the electronic (band gap) and geometrical (bond lengths) values are reported in tab. 5.2. The comparison between the

Table 5.2: Band gap and bond lengths values of the periodic slab model of rutile-(110) and the embedded cluster constructed from it ⁴.

Approach	Band gap (eV)	P-C (Å)	N-C (Å)	C-N (Å)	C-C (Å)
PBC	1.75	1.89	1.49	1.51	1.57
Cluster	2.15	1.94	1.50	1.51	1.58

two models provides a good agreement, which means that the cluster model can be trusted to investigate the electronic excitation.

The calculations were performed using the software ORCA [303] with a pob-TZVP basis set [304]. The ECP and SDD potentials included in ORCA were used. In order to compare with DFT results, the exchange-correlation functional of choice was PBE [162] with the DFT-D3 dispersion term of Grimme [172, 173].

TD-DFT and triplet state settings

The TD-DFT calculations were performed using the same settings of the cluster model⁵ The auxiliary basis set Def2-SVP/C was also used with the RIJCOSX

⁴The cluster model was created by Luca Gerhards, the properties of which were then compared together with the periodic rutile-(110) structure.

⁵TD-DFT and triplet state calculations were performed by Luca Gerhards on the cluster model he created by cropping the DFT periodic rutile-(110) structure.

approximation [305]. The description of the reaction trajectories in the triplet state was performed by a scan along the reaction coordinate with 6 steps. In addition, a state-averaged complete active space self-consistent field calculation (CAS(2,2) [306, 303]) was performed to validate both the excitations in the TD-PBE spectrum and the triplet state. Here, the highest occupied molecular orbital (HOMO) and the lowest unoccupied molecular orbital (LUMO) from the PBE ground state calculation was used in the active space.

5.3 Adsorption of glyphosate on rutile-(110)

The static and especially dynamic approaches carried out in chapter 4 have proven the great attraction that binds GGG to an amorphous TiO_2 surface. The adsorption configurations identified are certainly an excellent starting point for a possible degradation procedure, but they need more detailed investigations passing through ab-initio methods such as DFT. For this to happen, however, it is necessary to change the TiO_2 surface to a more regular one. The amorphous structure is in fact filled with kinked sites and H^+ / OH^- ions present on the surface to mimic a pH value of 7.4, which are impossible to reproduce in small models subjected to PBC conditions. For this reason, the in-depth GGG search on TiO_2 was performed on the rutile-(110) slab introduced in chapter 3.

The first step consisted of performing the same multi-sampling procedure of chapter 4 to see whether adsorption orientations similar to those identified on the amorphous surface or new ones appeared. This time two separate simulations of 25 GGG molecules at 300 K for 110 ns were performed on rutile-(110)⁶. In one system the molecules were inserted with their symmetry axis along the structure parallel to the rows of bridging O atoms, in the other perpendicular. In both initial configurations the 7 Å distance and 15° rotation was still maintained between them. In this way it was possible to have an overall statistic of 50 components in two opposite situations, increasing the quality of the sample. The last frame of one of the two simulations is showed in fig. 5.8, where the identified adsorption configurations are also highlighted. The amount of adsorbed molecules and the different adsorption modes were studied through a Python script. The time evolution of the distance of the center of the molecule from the surface and of two perpendicular angles of reference has been observed and analyzed. Through use of a histogram it was possible to observe the percentage of molecules in a given configuration, scanned over all 110 ns (fig. 5.9 (a)). The second graph, represented in a heat-map fashion, provides information on the transformations from one adsorption mode to another during the entire MD calculation (fig. 5.9 (b)).

As many as 47 of the 50 molecules analyzed remained adsorbed to the surface with a direct bond for most of the simulation time, whereas two of them adsorbed indirectly on top of the first water layer. The strong attraction of GGG to the rutile can be directly compared to the sample obtained in chapter 4, in which 15 of them were attracted by the upper slab of the amorphous

⁶Classical MD calculations were performed by Maria von Einem. She has also developed the Python script for the heat-map and histograms of fig. 5.9 and 5.10 with criteria for the identification of the different modes that were decided together.

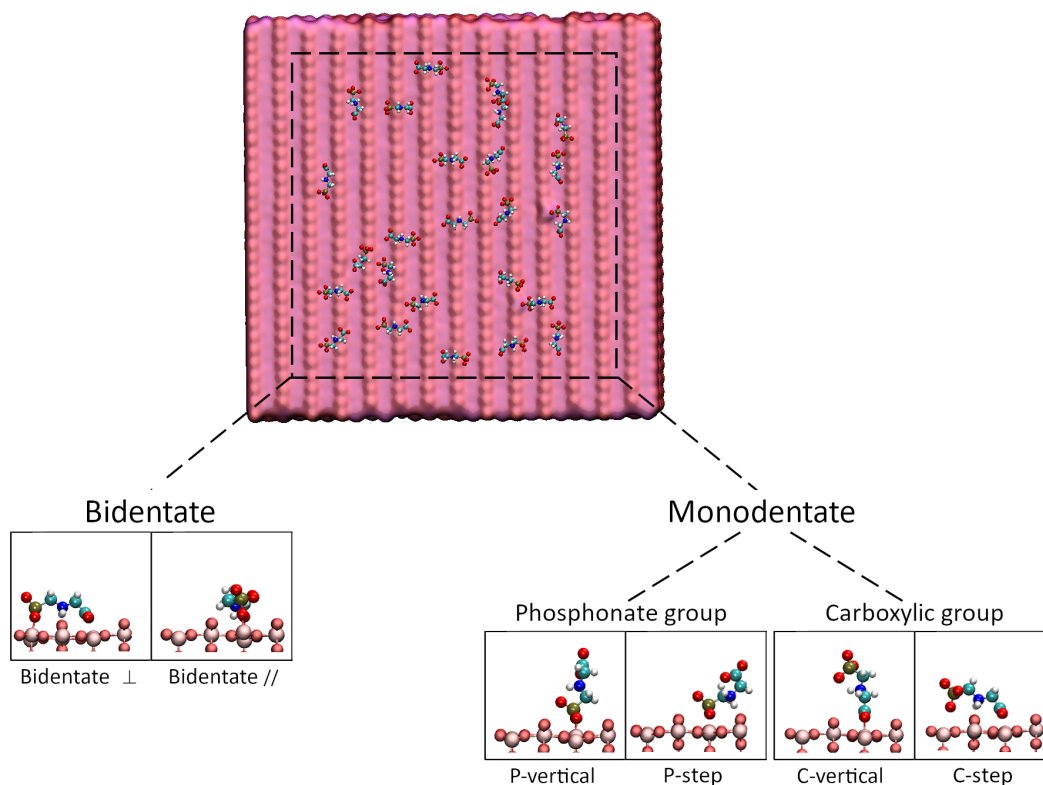


Figure 5.8: Final snapshot of the MD simulation with the GGG molecules starting at perpendicular positions to the surface bridging O rows⁶. Two main adsorption modes were identified here, namely bidentate and monodentate. They got further divided in different categories: bidentate \perp , bidentate \parallel , P-vertical, P-step, C-vertical and C-step.

surface and only 10 by the lower slab having the distribution of H^+ and OH^- ions. This suggests that lack of a charged surface, such as in this case, allows GGG molecules to be attracted easily. The adsorption orientations identified on the amorphous surface were also found on the rutile-(110). In this situation, however, thanks to the regularity of the slab models, it was possible to detect them with a better definition. GGG molecules bonded to the surface firmly due to the presence of the charged functional groups. Two types of adsorption have been observed: bidentate adsorption and monodentate adsorption, as illustrated at the bottom left and bottom right sides of fig. 5.8, respectively. At the bidentated configurations, both ends of the molecule are adsorbed to surface titanium atoms either at different sides of two bridging O atoms (Bid. \perp) or within the same row (Bid. \parallel). For a monodentated configuration, a strong differentiation between a binding driven by the phosphate or the carboxylic group could be identified. Here the molecule can be placed directly in a vertical position (P-vertical and C-vertical) through O-Ti bonds and without involving other functional groups, or slightly bent (P-step and C-step). In this case it is the amine group in the middle of the GGG structure that interacts with rutile by forming hydrogen bonds with the surface O atoms.

Among all the described situations the bidentated modes dominated the sample, as analyzed in fig. 5.9 (a). It is also remarkable to observe that half of the

50 total molecules bonded in the bidentate \perp mode, whereas only one third of them in the bidentate \parallel one. In fig. 5.9 (b) the time evolution for each of the

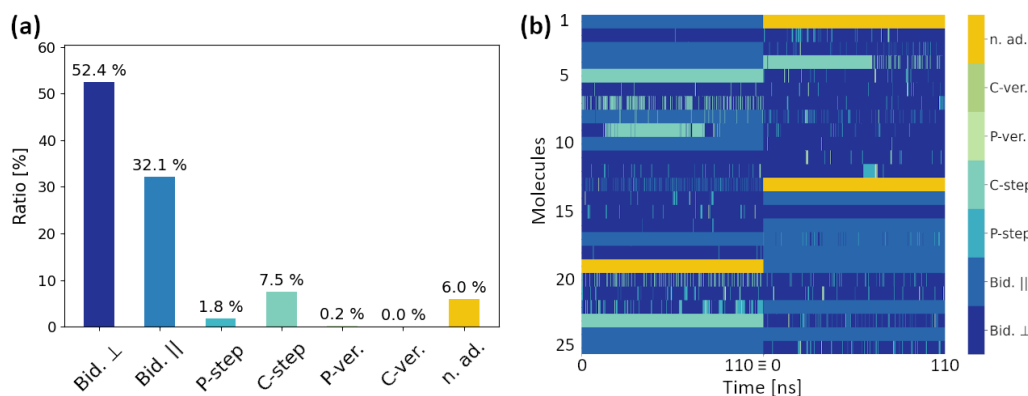


Figure 5.9: (a) Distribution of the detected adsorption modes evaluated from 50 GGG molecules for a simulation time of 110 ns with a sampling frequency of 10 ps⁷. (b) Time evolution of the adsorption modes of 25 molecules per half of the diagram for a simulation time of 110 ns with a sampling frequency of 10 ps. Image created by [Maria von Einem](#) for ref. [5].

25 GGG molecules in their respective simulations is represented in a heat-map fashion. The plot clearly shows how stable the bidentate configurations are: 23 and 14 molecules out of 50 remains adsorbed in their bidentate \perp and bidentate \parallel configurations, respectively, for the whole 110 ns. Especially the bidentate \perp mode shows in some cases slight changes to other modes which turn back within a short time. Monodentated orientations are also representative of a stable adsorption, such as the 3 molecules in the C-step configuration which maintain it for the entire computation. Note that the C-vertical configuration actually never appeared in the MD simulations, but its existence was nonetheless conjectured by chemical intuition, and its structure was subsequently analyzed along with other.

Two 1 ns simulations with a denser-framing sampling of 1 ps were created by cropping a time window from the 110ns long MDs in order to observe with more details the evolution of both systems. The results are shown in fig. 5.10.

Here it is possible again to observe the stability of the bidentated modes, but the resolution now allows a better understanding of the dynamic evolution of the monodentated ones. The GGG molecules at index 22 (a) and 21 (b) begin in a P-vertical way, but after 100 ps their amine group starts feeling the attraction towards the surface bringing to a P-step configuration. This becomes within time more and more frequent until the bond is well established and the molecule ends up in a bidentate \perp structure. Similar behaviors were also observed in chapter 4 for the amorphous surface, albeit in a coarser fashion. On the contrary, the C-vertical configuration does not change its orientation during the simulation and rather stays stable at its position but for some rare exceptions such as the molecule at index 7(a), in which the orientation keeps

⁷Classical MD calculations were performed by [Maria von Einem](#). She has also developed the Python script for the heat-map and histograms of fig. 5.9 and 5.10 with criteria for the identification of the different modes that were decided together.

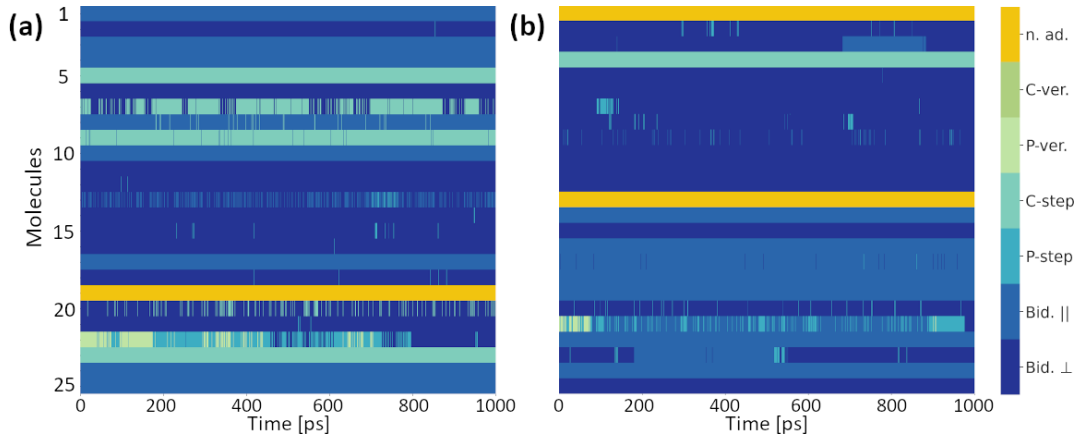


Figure 5.10: Time evolution of the adsorption modes of 25 molecules for a simulation time of 1 ns and a denser sampling frequency of 1 ps ⁷. (a) System with the GGG molecules starting parallel to the surface bridging O rows. (b) System with the GGG molecules starting perpendicular to the surface bridging O rows. Image created by [Maria von Einem](#) for ref. [5].

oscillating with a bidentate \perp one. We assume then that for the P-vertical configurations the attraction of the central amino directly leads to a bidentated mode and happens more rarely for modes driven by the carboxyl group. This explains the low rate of monodentated adsorptions coming from the phosphate group in the histogram of fig. 5.9 (a).

The six configurations were reproduced on the smaller original rutile-(110) slab model in order to achieve an in-depth electronic information with DFT calculations. After performing a geometry optimization, their adsorption energy to the surface was evaluated through the following formula:

$$\Delta E_{\text{ads}} = E_{\text{GGG distant from rutile}} - E_{\text{GGG on rutile}} \quad (5.35)$$

The energy contribution $E_{\text{GGG distant from rutile}}$ is representative of a previously optimized GGG molecule in a vacuum cell of the same size by a global minimum search procedure ⁸. In other words, this corresponds to GGG's gas phase configuration. Note that, due to the charged background in our system, the use of the standard formula for the adsorption energy used in chapter 3 for H_2O molecules on TiO_2 would actually need an additional term of charge correction, say E_{corr} . The computation of the adsorption energy was then rather performed by taking into account the fact that $E_{\text{GGG distant from rutile}} \approx E_{\text{GGG}} + E_{\text{rutile}} + E_{\text{corr}}$. Here the term $E_{\text{GGG distant from rutile}}$ refers to the system with GGG positioned at a distance of 14\AA from rutile. The second energy, $E_{\text{GGG on rutile}}$, is representative of the molecule once adsorbed at the surface. This, when inserted in the simulation cell at the distance of 14\AA from the slab, did not show any major changes.

The adsorption energies are reported in the first line of tab. 5.3. As expected

⁸The global minimum search procedure was performed by [Wilke Dononelli](#) using ORCA [303] and was further refined in VASP to be consistent with the other DFT calculations.

Table 5.3: Adsorption energies and Bader net atomic charges of the optimized structures of GGG on rutile-(110).

	Vacuum	Bid. \perp	Bid.	P-stp.	C-stp.	P-ver.	C-ver.
ΔE_{ads} (eV)		-3.06	-2.48	-2.92	-1.67	-2.62	-1.94
Charge ($\frac{e}{\text{Bohr}^3}$)	-1.94	-1.12	-1.10	-1.26	-1.33	-1.25	-1.49

from the classical MDs, the bidentate \perp structure promoted the highest attraction. Monodentated configurations driven by the phosphate group follow immediately after, but their presence has a very low rate due to the fast decay to a bidentated mode, as previously explained in the denser-framing simulation. On the other hand, both arrangements based on carboxylic moiety showed the lowest adsorption energies. In this case, it is not straightforward to move from the C-vertical or C-step configuration into a bidentate one, which confirms their minor presence in the histogram of fig. 5.9 (a).

Bader net atomic charges of the six configurations were computed and listed in the second line of tab. 5.3) in order to visualize how much charge remained in the various adsorption configurations. In case of the bidentate adsorption modes, the charge located at the GGG reduces of about 1 eV, whereas in the monodentated ones is higher. Also from the electronic point of view, then, the bidentated configurations confirm the results obtained with FF calculations.

5.4 Properties of the bidentate \perp mode

Thanks to both the aforementioned classical dynamic analysis and the static analysis the stability of the adsorption configurations has been well understood. Since the interest lies in the search for possible degradation pathways, it is necessary to dig deeper in the matter and investigate where the electronic exchange actually takes place and what is the mechanical torsion the molecule is subjected to. Being the most probable configuration to occur, the focus from here on will be on the bidentate mode \perp only.

In order to analyze in more detail the charge transfer occurring in this interaction, its electron density difference was evaluated⁹. This is shown in fig. 5.11, where the difference was integrated in the y-direction and projected along the xz plane. At a first glance, one immediately notice that the pollutant is embedded in a blue cloud. The P-C, C-C, C-N and N-C bonds inside the molecule felt then a strong loss of charge. The surroundings of rutile surface atoms, on the other hand, tended towards red colors. It is here clear that the two adsorption sites provided by the phosphate and carboxyl groups are then driving the interaction. The charge was directly transferred from the O atoms of GGG to the 5-fold coordinated Ti surface atoms. The electrons were then transported towards the inner structure and distributed among the first bulk layers. The same can be observed for the amino group, in which the transfer was slightly weaker. The latter was driven by the two H-bonds formed between GGG and

⁹The Python script used to compute the charge transfer was written and provided by Wilke Dononelli, who also helped in its interpretation together with the other co-authors [5]

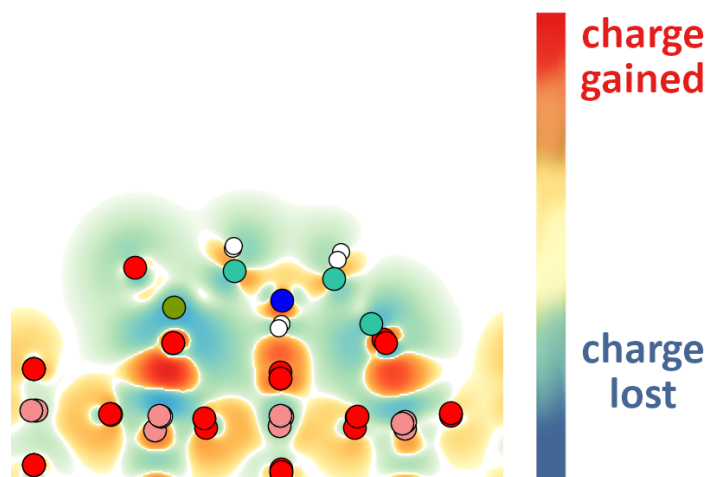


Figure 5.11: The integrated charge density differences are plotted for bidentate \perp ⁹. Blue areas indicate regions with decreased electron density and red areas with increased electron density.

the O_{bridge} atoms, that were then carrying the charge inside the rutile structure as well. The formation of these four O-Ti bonds, together with the two additional hydrogen bonds, leads to a weakening of the P-C and C-C bonds in GGG. This indicates that the two bonds may potentially break during a degradation process induced by adsorption at the surface. However, this type of analysis is not sufficient to give us an adequate conclusion.

In past works, it has been found that torsional motions can weaken chemical bonds by preconditioning them for rupture [307]. Since in the bidentate \perp conformation the structure of GGG is far from its correspondent gas phase global equilibrium, a strong strain within the molecule shall be expected. The GGG molecule, in its bidentate \perp configuration, was grabbed out from the rutile surface and embedded in an explicit water solvent. Through a MD simulation at 320 K with a duration of 2.5 ps, the structure dynamically relaxed over time until it reached its thermodynamic equilibrium. A frontal and top view of the two final conformations is shown in fig. 5.12 At this point, the principal bonds and dihedral angles within it were measured, averaged along the last 1 ps of simulation time. By evaluating the differences between these averages and the respective values of the static bidentate \perp configuration at the surface, the largest changes could be detected (see tab. 5.4). No significant changes were identified in the major bonds (P-C, C-N, N-C, and C-C, starting from the phosphate group towards the carboxyl group), with differences less than 0.03\AA . The dihedral angles, indices of torsion, also remained stable with variations smaller than 8° , except in case of the dihedral involving the C-C bond and one of the two O atoms of the carboxyl group. In it, a remarkable difference of about 54° was measured.

In order to understand how much strain corresponded to the torsion in the C-C bond, a rotation along its axis was performed. Based on a 10° step, the energy was calculated each time using a simple single point calculation. The results are shown in fig. 5.13 (b). The configuration corresponding to 0° corresponds to the dynamic relaxation in the explicit solvent. As can be observed, this is a

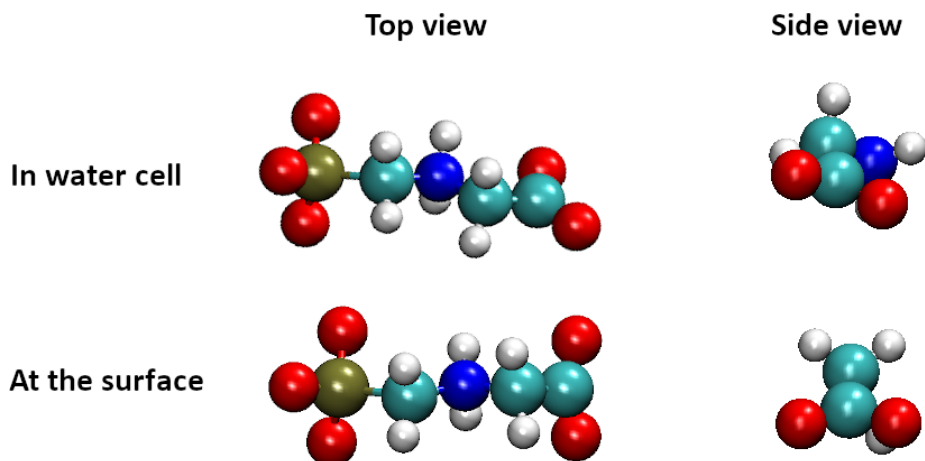


Figure 5.12: Comparison between the relaxed GGG structure in a dynamic water environment and the bidentate \perp configuration. In both the top (left column) and side view (right column) the two molecules were aligned along the phosphate group.

Table 5.4: Measured bond and dihedral differences between the relaxed GGG structure in a dynamic water environment and the bidentate \perp configuration. The greatest dihedral difference is marked in bold.

	In water cell	At the surface	Difference
Bonds (Å)			
P-C	1.89	1.87	0.02
C-N	1.49	1.51	-0.02
N-C	1.51	1.50	0.01
C-C	1.57	1.54	0.03
Dihedrals (°)			
O-P-C-N	184.09	179.74	4.34
P-C-N-C	184.72	192.70	-7.98
C-N-C-C	179.82	171.75	8.07
N-C-C-O	264.11	209.89	54.22

minimum of the strain in the bond. The bidentate \perp structure is instead close to a point of maximum. Thus, when the molecule approaches the surface, its C-C bond shall possess a very high strain.

The structural deformations of the bidentate \perp mode were then investigated by terms of JEDI analysis [279, 280, 281]¹⁰ The resulting values are reported in fig. 5.13 (a). It can be observed that the adsorption leads to a strain of 1.67 eV, which is actually overestimated of about 10% by the JEDI protocol and then justifies the assumption of the harmonic. The highest contribute to the strain energy is stored in the C-C bond as well as in the P-C and N-C bonds with smaller amounts. It can then be concluded that the energy gained through the bidentate \perp configuration overcompensates the strain energy in the gas phase by storing the strain predominantly in the C-C bond.

¹⁰All JEDI calculations were performed by **Tim Stauch**, the results of which were interpreted and analyzed together with the other co-authors [5].

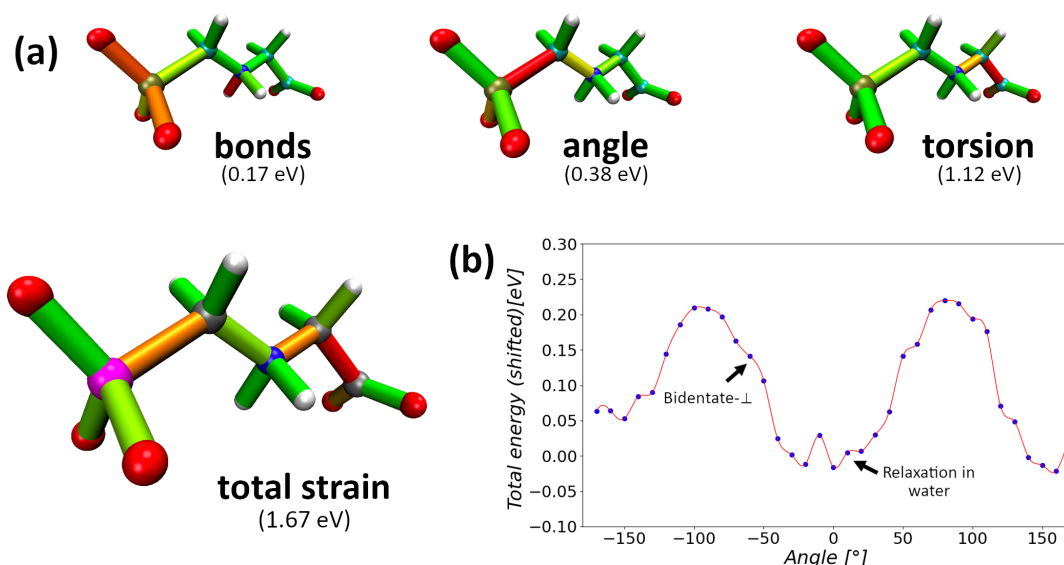


Figure 5.13: (a) JEDI analysis of the bidentate \perp configuration of GGG on rutile (110)¹⁰: the strain of the bonds, angles and torsions has been computed and summed up in the bottom left panel. The color code ranges from green (no strain) to red (high strain). (b) The major strain in the bidentate \perp configuration is in the torsional motion of the C-C bond at the carboxyl group. This rotated of 54° from the equilibrium structure in solution in order to reach the optimal adsorption mode.

Through this analysis it seems clear that the main probability of breakage is in this chemical bond. As we will show in the next section, the C-C bond is actually one of the bonds least likely to activate degradation. Water molecules around the bidentate \perp structure, which were not present in the charge transfer and torsional analysis, do in fact play an active role changing the conjectures made up to this point.

5.5 Degradation of the bidentate \perp mode

Both the energy and strain analysis made it clear that, if the molecule can be torn apart, then this must start from one of the main bonds. Starting from the phosphate group to the carboxyl group, they are here named as the P-C, C-N, N-C, C-C bonds. In this section, we will proceed with manually breaking these bonds and then evaluate their actual realization through the respective reaction barriers. We will then proceed with TD-DFT calculations to understand if photocatalytic activation promotes a different type of degradation than that identified in GS.

5.5.1 Thermal degradation

The static study of charge transfer and strain led to the conclusion that any bond breakage occurs primarily at the C-C site. However, it should not be forgotten that the bidentate configuration \perp , as well as the others, have been identified within an aqueous environment. The explicit solvent not only represents a

barrier to be overcome in the adsorption reaction at the surface, but may in principle be a key key to the stabilization of the structure.

To observe this, two ab-initio MDs at 320 K were performed. The first one lasted for 8.4 ps and was carried out with the optimized bidentate \perp structure at the surface embedded in an implicit solvent. Here, the carboxyl group left its adsorption position heading towards the vacuum after 1.5 ps and the P-step configuration was observed. Right afterward, also the amine group slacked the attraction to rutile and the structure ended up being in the P-vertical one. Note that P-vertical configurations appeared in the explicit solvent FF sample with a percentage of 0.2% over 110 ns. It is therefore very unlikely that a DFT calculation without explicit water molecules produced this result without a specific reason: the explicit solvent must stabilize the structure. This was confirmed by the second MD, in which the bidentate \perp conformation at the surface was embedded in the same water network identified in chapter 3 for rutile-(110). Here the calculation lasted just for 2.4 ps due to the expensive simulation time. This time, the bidentate \perp structure did not leave rutile, indeed suggesting that the presence of water in the system is an active element in maintaining the arrangement, as it represents barrier not possible to overcome at such a temperature. This leads to another important conclusion: the possibility of water molecules being an active part of a degradation process cannot be ruled out either.

Four steered MD simulations (one pull for each main bond) at 320 K were then performed in the same explicit water environment to study the eventual degradation reaction. In this way it was possible to observe water reactions dynamically already during the pulling of the bonds. The final, optimized fragments are shown in the bottom part of fig. 5.14.

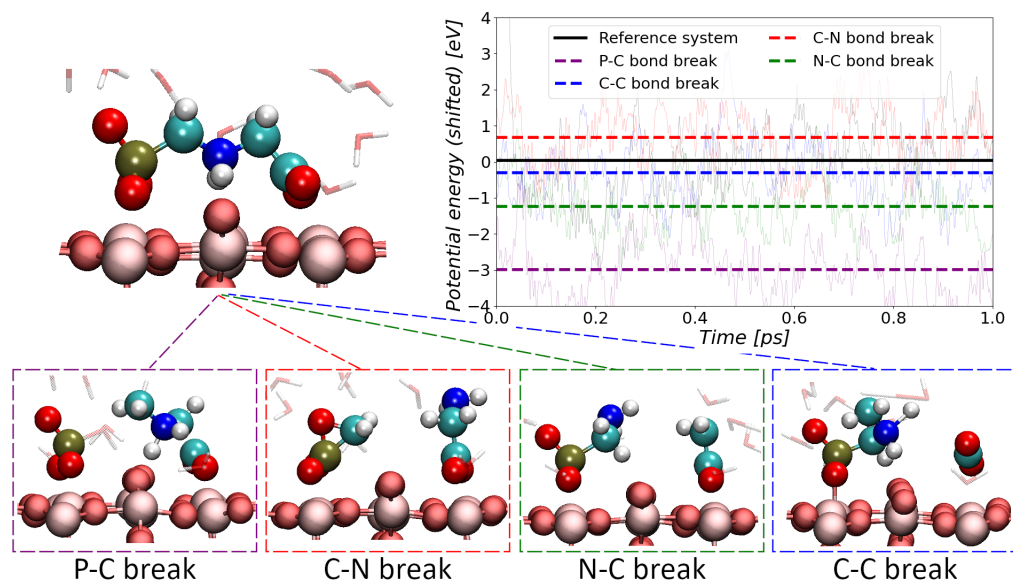


Figure 5.14: Initial and final configurations of the bidentate \perp structure after the action of the steered MDs together with the four final snapshots of the following unconstrained MDs. The graph represents the averaged potential energy of the system over the last picosecond of each simulation. The black line corresponds to the averaged potential energy on the bidentate \perp structure without any pulling.

- **P-C.** The P-C bond disruption is recognized experimentally as the sarcosine pathway and in the laboratory has been identified as the one that can be induced by photocatalytic activation [60].

This steered MD was actually the only one leaving out three ending fragments instead of two, as shown in fig. 5.15. Already after 1.1 ps during the

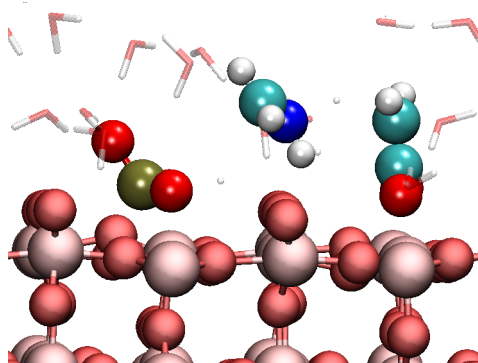


Figure 5.15: Final snapshot of the P-C bond break performed with the same steered MD routine used for C-N, N-C and C-C. The lack of a proper relaxation time for water led to the formation of three ionic fragments. The modified protocol included an additional distance between a H₂O molecule and the phosphate group, the resulting structure of which is reported in fig. 5.14.

pulling we observed that the sarcosine part (C₃H₆NO₂) broke its N-C bond as well. Hence, at the end of the steered MD three fragments were formed, respectively composed by phosphate (PO₃), methaniminium (CH₄N) and athenperoxyd (C₂H₂O₂). The unconstrained MD that followed lasted 7.7 ps, a rather long time in order to observe eventual recombinations. The two outermost molecules (PO₃ and C₂H₂O₂) remained steadily adsorbed to the surface through their original bonds. In the phosphate group the P atom created an additional bond to a 2-fold coordinated surface O atom, whereas the central C₃H₆NO₂ fragment underwent meanwhile a strong rotation. First, both the two hydrogen bonds of the NH₂ part with the bridging O atoms broke. Then, after rotating on its position, a new hydrogen bond was formed between the unadsorbed O atom in the PO₃ molecule. This did not stand for a long time (0.6 ps), letting methaniminium to complete its rotation and lie horizontally on the surface with two new hydrogen bonds onto the previous bridging O atoms. This last interaction, though, was rather weak as the hydrogen bond belonging to the C atom was right afterwards disrupted.

The unfolding of sarcosine not only is inconsistent with expectations coming from experimental data [60], but it also produces two highly unstable fragments. We assume that this final configuration formed due to the absence of a water molecule capable of rapidly binding to the phosphate group within the pulling time, stabilizing the charges involved. However, a repetition of the simulation with a lower pulling rate does not guarantee

that a different reaction will take place, since it could also be an unfavorable initial configuration in which the water molecules are not close enough to the phosphate group.

For this reason the simulation was carried out again with the addition of a push between the O atom of the first water molecule above the phosphate group and the P atom. This new steered MD lasted 1 ps, corresponding to 1 Å of O-P approach and simultaneous P-C bond separation. In the pushing-and-pulling procedure, the amino group of the GGG broke a hydrogen bond with the surface and put itself at an upward slant. During the following unconstrained MD, which lasted 2.3 ps, the water molecule broke into OH⁻, binding to the phosphate group, performing a proton flip towards the CH₂ moiety of the sarcosine. This moiety then initiated a slight twist, moving away from the phosphate group. After 0.6 ps, the amino group undertook a rotation, breaking the remaining hydrogen bond to reform soon after with the second H atom. The overall structure remained thermodynamically stable, with the methyl group CH₃ created again positioning itself in the direction of the phosphate group.

- **C-N.** To our knowledge, there are no experimental data to a possible disrupture of this bond.

Almost immediately after the onset of the steered MD, at a time of 0.5 ps, a change within the phosphate group was observed: the unadsorbed O atom moved to a central position between the P and C atoms. It then created a further bond with the latter, compacting the structure. On the other resulting glycinate (C₂H₄NO₂) fragment the break of the two hydrogen bonds with the surface could be observed. This molecule tilted onto a more vertical position, remaining then stable for the rest of the 5.5 ps long MD. Here, one H₂O molecule of the solvent stabilized the fragment by forming a hydrogen bond with the NH₂ part. The same occurred with the central O atom in the other formed structure, the methylene-phosphate-like molecule (CH₂O₃P).

- **N-C.** This reaction is the one that follows the most well-known pathway of AMPA, which is scientifically recognized as the one to occur thermally. The compound was indeed created by stretching the N-C bond. The final result depended however heavily on the action of the water in the surrounding solvent. While the pulling was still in progress, at a time of 0.7 ps, an H₂O molecule dissociated. This was located exactly between the phosphate and carboxyl groups, the latter mirrored along the (010) axis by the PBC. An H atom of the molecule detached to be adsorbed by a bridging O atom. Thus, a second water molecule in the vicinity recovered the loss by yielding one of its hydrogen atoms. The remaining OH⁻ hydroxyl formed a bond with the athylenperoxid fragment (C₂H₂O₂) via its O atom. Finally, the restored H₂O formed a hydrogen bond with the unadsorbed O atom of AMPA instead. The entire structure then remained stable for the entire following unconstrained MD of 3.5 ps. It is important to observe that, if it was not for the active water molecules,

by breaking AMPA along its P-C bond the three fragments of the P-C steered MD would be again obtained.

- **C-C.** According to the static analysis performed, the C-C bond should be the one most prone to breakage given the strong strain it possesses. The theoretical work of Catao et al. [256] also identifies in this bond the most likely photocatalytic activation for the molecule embedded in a water environment.

Right after the pulling, it was clear the intention of the formed carbon dioxide (CO_2) to reconnect with the main fragment. The latter, though, started rotating and moved aside with its CH_2 part, while keeping stable the two hydrogen bonds of the amino group. The CO_2 molecule then created a new hydrogen bond between one of its two O atoms and one of the H atoms in the amino group, forcing the detachment of the latter from the surface. In the meantime, one H_2O molecule belonging to the solvent split, triggering a Grotthuss mechanism. One proton moved to the CH_2 in the main fragment. The remaining OH^- got transferred through the water chain reaction to the CO_2 molecule, which had previously broken the newly created hydrogen bond. For the rest of the MD of 4.7 ps, no further dynamic changes could be identified. This "proton circuit" corresponds exactly to the one observed already by Catao et al. [256] without the contribute, though, of any surface.

On the top-right panel of Fig. 5.14, the graph shows the averaged potential energy of each studied system over its last picosecond of unconstrained MD. In this way, it is possible to observe which configuration proved to be more thermodynamically stable. Here, the black line represents the reference system, which corresponds to the averaged potential energy on the last picosecond of the bidentate \perp structure on rutile in the explicit solvent. Although the noise and entropy provoked by the surrounding explicit water molecules are high, the initial setting was the same in all the four cases. The positive difference of +0.67 eV shows that the C-N bond is the only unfavorable one with respect to the reference system. The C-C bond break, on the other hand, is quite close to the averaged bidentate \perp value, with a value of -0.31 eV. The N-C bond break follows then with a difference of -1.23 eV, whereas it is of -2.98 eV for the P-C bond break. The lowest potential energy therefore suggests that the P-C bond break is the most dynamically stable, but it does not mean that it is also the most likely to get disrupted. To obtain this information, it is necessary to analyze the energy barriers of the break reaction.

Static studies via a combination of NEBs or dimer method were performed on the three bonds shown to possess lower potential energy than the reference value in dynamic environment. The results are shown under "thermal degradation" in the first column of Fig. 5.16.

¹¹The calculations of the triplet state were performed by Luca Gerhards and further discussed together with the other co-authors [5].

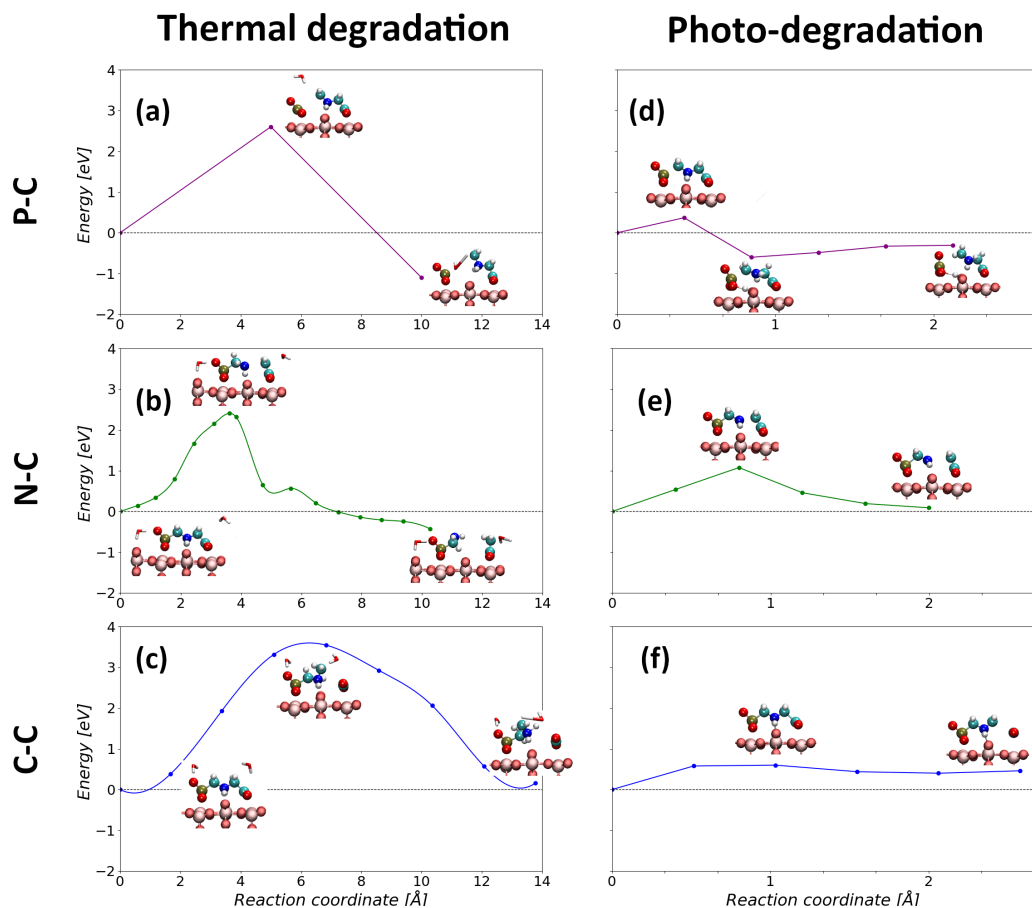


Figure 5.16: Left column: (a) final curves corresponding to a GS dimer optimization of the P-C bond break, (b) a GS NEB calculation with dimer of the N-C bond break through 15 images and (c) a GS NEB of the C-C bond break through 8 images. Right column: final curves corresponding to triplet calculations of bond breaking through 6 steps for P-C (d), N-C (e) and C-C (f) ¹¹.

The final structure of the P-C (fig. 5.16 (a)) bond breaking was optimized and the transition state evaluated through a dimer method ¹². Here a single water molecule is involved which, as in the steered MD, gives up a proton to sarcosine when it binds with the phosphate group. The height of the reaction barrier is 2.68 eV for a favorable final product of -1.08 eV relative to the initial \perp bidentate structure. As on-going research, a NEB is currently being prepared that can help observe a refinement of the minimum energy pathway (MEP) and possibly identify intermediate minimum points.

A NEB composed of 15 images was actually carried out and refined by dimer method regarding N-C bond breaking (fig. 5.16 (b)). The initial and final states were taken from the bidentate \perp structure and the final product of the steered MD, respectively. In general, the MEP followed by the NEB described a similar trajectory to that of the steered MD with following unconstrained MD. The reaction barrier here is 2.40 eV for a final product having -0.43 eV lower potential energy than the initial one.

¹²The P-C dimer calculation (fig. 5.16 (a)) was performed by Wilke Dononelli, who was also of great help in the validation of the two NEBs.

Investigation of C-C bonding was performed through a NEB consisting of 8 images (fig. 5.16 (c)). Again, the initial and final products were taken directly from the corresponding steered MD. The trajectory corresponding to MEP is again analogous to that observed during steered MD with following unconstrained MD. This is the only case, however, where the final state has a similar (slightly more unfavorable) energy than the initial one, with a difference of 0.16 eV. The reaction barrier was 3.54 eV, although this value is only close to the saddle point. We observe that according to Catão et al. [256] the C-C bond breaking should occur with a 3.33 barrier in the case where water is not involved, otherwise it drops to 2.00 eV. Thus, the existence of another MEP that makes this reaction more favorable cannot be ruled out. The structure of GGG studied by the authors, moreover, is not the bidentate \perp and has no interaction with a surface.

The results of this analysis allow us to conjecture which bond is most likely to break in the case of interaction with at least one water molecule. We immediately observe that, unexpectedly from what was found through the analysis of the electronic and torsion properties of the bidentate \perp structure, the C-C bond is actually the least likely to break among the three. Furthermore, although the sarcosine path product is more stable than the AMPA pathway, it is the latter that possesses the lowest reaction barrier. Both energy values are however lower than the 3.40 eV corresponding to a wavelength of 365 nm of the usual photocatalytic processes. Up to date, most of researchers were not able to overcome this barrier for glyphosate or other degradation products [256, 308, 309, 60]. Considering also the value of the reaction barrier of the C-C bond as within this range, we can say that all the reactions investigated have the potential to be photoinduced.

Finally, we observe that the stability trend dictated by the potentials during the dynamic simulation was respected (see fig. 5.14). The values of the final products are higher than those found previously because the water inside the dynamic cell forms stable bonds at both sides of the rutile-(110) surface, strengthening the overall equilibrium, which is not the case with an implicit solvent such as in the NEB calculations.

5.5.2 Photo-degradation

The presence of water during the degradation processes was a major influence in understanding which pathway is the more likely to occur thermally at the GS level of theory. It is now necessary to investigate whether the N-C bond turns out to be the favorable one even in case of ES or whether it is the P-C, as predicted by the experimental literature [60].

In order to study the photocatalytic behavior and the accompanying destabilization of bonds in the bidentate \perp structure, the total DOS of the adsorbed system has been compared to the pristine as shown in fig. 5.17. It can be observed that a slight reduction of the band gap is induced upon adsorption, leading to a value of 1.59 eV compared to the 1.75 eV of rutile-(110) found in chapter 3. This means that the presence of GGG on the surface actually promotes photocatalytic activation. Note however that the underestimation

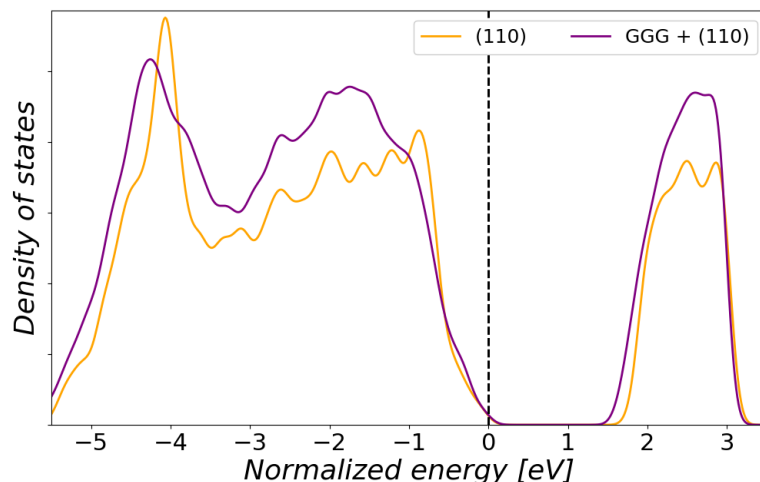


Figure 5.17: Total density of states (DOS) of rutile-(110) (orange) with and without adsorption (purple). The band gap shifts from 1.75 eV to 1.59 eV upon adsorption, meaning that there is a higher likelihood of photocatalytic activation. The curves were smeared with Gaussians and shifted to the VBE.

of the band gap is a well known behavior for the PBE functional [163, 310]. The method selected to perform ES analysis was TD-DFT¹³ by reproducing the GGG-TiO₂ interface was first reproduced on a rutile-(110) cluster. Here, a direct comparison between the crystalline highest occupied molecular orbital (HOMO) near the Fermi energy shows an equivalent hybridization between the orbitals of the bidentate \perp structure and the surface band, as reported in fig. 5.18. This result then well supports the charge transfer into the surface dis-

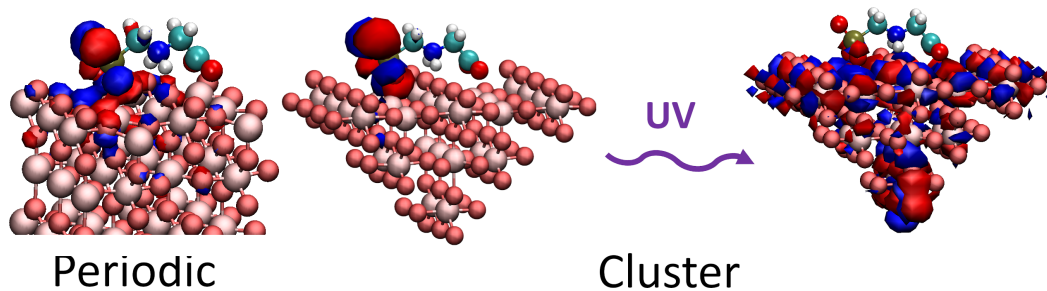


Figure 5.18: Schematic effects of excitation on the orbitals. The HOMO level crystalline orbitals at the Γ -point of the GS periodic structure (left) are compared to the cluster model in both GS (central) and ES (right). Negative isovalues are displayed in blue, positive ones in red. In the GS the isovalue is ± 0.015 e/ \AA^3 , whereas in the ES it was set to ± 0.007 to better visualize the 3d-Ti orbitals¹³.

cussed in the previous section in section 5.4. The strong localization of the HOMO level at the phosphate group is a clear indication of the destabilization of the P-C bond in case a photo-induced excitation takes place. As visible from the virtual bands of TiO₂, an excitation into the unoccupied Ti-d-bands from

¹³TD-DFT calculations were performed by Luca Gerhards on the cluster model he created by cropping the DFT periodic rutile-(110) structure.

the occupied hybridization bands might in fact occur.

In fig. 5.19, a comparison between the absorption spectra of the pristine rutile-(110) surface and the adsorbed GGG molecule is reported. The calculated

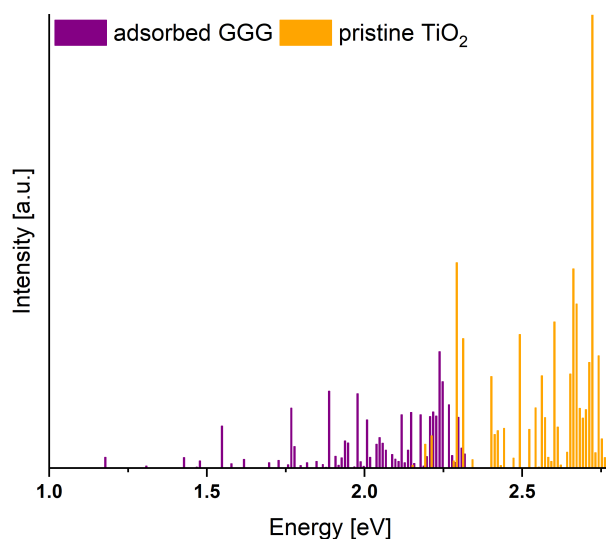


Figure 5.19: Comparison between the TD-DFT spectra of the bidentate \perp configuration (purple) with the cluster model rutile-(110) surface (orange)¹³. At its interaction with the surface, the first electronic excitation can be detected at 1.14 eV, while for the pristine TiO₂ they it occurs at 2.15 eV. Image created by Luca Gerhards for ref. [5].

spectra indicate that the excitation energy is significantly lowered by the binding of the adsorbant. The pristine surface has its first electronic excitation at 2.15 eV, which is close to the calculated band gap of the calculations with periodic boundary conditions (1.75 eV, see 3). The adsorbed GGG shows its first electronic excitations at 1.14 eV, which is also not far from the calculated band gap of 1.59 eV of the system (see fig. 5.17). An investigation of the character of the transitions makes it then clear that the HOMO is involved in several excitations. Therefore, the charge transfer into the d-bands of TiO₂ in this case occurs leading to an even more charged adsorbate, which destabilizes the bonds in the molecule by reducing the electron density of the bidentate \perp configuration. This suggests that the experimental investigations of the photocatalytic degradation under irradiation of the system [60] are confirmed. The simulations indicate in fact that, after the photocatalytic excitation, the P-C bond might break, leading to the degradation products of sacrosine and orthophosphate.

A more detailed investigation of this excitation was performed with a triplet state calculation of the system¹⁴, which is an approach already been successfully used in previous works to describe photocatalytic reactions [311, 312]. As shown for the ES of fig. 5.18, the phosphate and 3d-Ti orbitals formed a superposition. One electron is then transferred to the 3d conduction band of TiO₂, thus weakening the P-C bond. Hence, a P-C break should be expected to be the favorable one under photo-excitation.

¹⁴Triplet state calculations were performed by Luca Gerhards on the cluster model he created by cropping the DFT periodic rutile-(110) structure.

To describe the trajectories of all three bond breaks, a scan was performed along the reaction coordinate in the triplet state through 6 geometrically optimized steps. They consisted of stretching and breaking bonds of interest followed by geometry optimizations for each image. The final resulting curves are reported in the right column of fig. 5.3 under the label of photo-degradation.

A comparison of the two occupied orbitals in the triplet state with the electronic excitation in the TD-PBE spectra (see 5.19) reveals that it corresponds to the ES. In contrast to thermal degradation, this time it is the P-C bond (fig. 5.16 (d)) that provides the least reaction barrier, with a very low activation value of 0.37 eV. The destabilization through excitation at the phosphate group is in fact localized and for this reason it provides a reduced energy of the bond break. The resulting product, corresponding to the third data point, promoted a proton transfer from the amino group. The H atom, remaining bound to the surface O bridging, strengthens the configuration by forming a hydrogen bond with the phosphate group. The energy of this state is -0.60 eV lower than the initial energy.

In contrast, the N-C bond break (fig. 5.16 (e)) is the one that demonstrates having the highest activation barrier with a value of 1.08 eV. In this case the energy corresponding to the final product is basically coincident with the initial one (0.09 eV), indicating its possible reversibility. Here the structure is similar to the final steered MD, except that the amino group remains bound to the surface. This is likely due to the lack of an interaction with the water molecule, which plays an important active role in the thermal reaction.

Finally, the bond C-C ((fig. 5.16 (f))) which was expected to break from the mechanical point of view, shows a reaction barrier of 0.60 eV which is lower than that corresponding to N-C but higher than that of P-C. In contrast to the other two cases, however, here the final product is slightly higher in energy (+0.40 eV). This suggests that the reaction is not favorable and can easily return to its initial state once photocatalytically activated. Again, the absence of water molecules affects the final structure and it cannot be ruled out that with them the reaction barrier would be lowered, as suggested by Catao et al. for GGG in the gas phase [256].

Electronic properties such as the spin densities of the products at the transition states need of course further investigations, which are part of the on-going research.

5.6 Summary

In the present chapter we used atomistic simulation methods to investigate the adsorption of GGG on the rutile-(110) surface. The molecule showed a high adsorption to the surface especially in its bidentate \perp mode, which confirmed the expectations of chapter 4 at the amorphous surface. This configuration was then taken as representative and further investigated both in terms of charge transfer and strain analysis in order to get a hint on the location of the most probable bond break to occur under external mechanical forces. In the first case a transfer of roughly one electron was observed from the functional groups binding to the surface atoms, leaving the molecule at the phosphate, carboxylic

and amine groups. This charge is distributed into the rutile's bulk, where it gets then dissipated. The strain analysis identified the C-C bond as the major strain location, which suggested in a first place that this would be the most likely break to occur.

When thermal effects came into play, though, this assumption was refuted. Through steered MD simulations and following NEB/dimer calculations it has been proved that, from the thermodynamic point of view, the N-C bond is the most likely to break. This confirms the experimental data, which suggest the AMPA pathway as the one to be taken in dark conditions [61, 60].

In order to understand the photo-degradation, a cluster model was developed to perform TD-DFT simulations. The cluster simulations were in good agreement with the DFT simulations in terms of ground state properties (band gap and HOMO-levels) as well as in the comparison of the geometrically optimized structures. Here not only the DOS showed a reduction of the band gap upon adsorption, but also the TD-DFT spectrum had its first signal in the same regime. This suggested a high likelihood for the bidentate \perp structure to proceed in a photocatalytic reaction, which was confirmed by triplet states calculations. Experimental results were again confirmed here for activation by light [60], indicating the sarcosine pathway as the most favorable, corresponding to P-C bond disruption.

CHAPTER 6

Conclusions and final remarks

The presence of pollutants in water resources is one of the biggest environmental problems humanity has ever faced [6, 7, 8]. There is no single quick and easy solution able to tackle it, but rather a precise and detailed study based on experimental and computational data is needed. With our work we have made a substantial contribution to it with the establishment of an analytical protocol that spans several theoretical levels. The combination of FF, DFTB, DFT and TD-DFT methods has indeed allowed us to shed a light on the phenomenon of adsorption and degradation in an efficient way both in terms of accuracy and computational time. While the multi-sampling approach allows us to simultaneously study the dynamic evolution of several molecules in one system, ab-initio methods can focus on the most statistically significant result, investigating its quantum properties in both the GS and ES (see fig. 6.1). The power of this

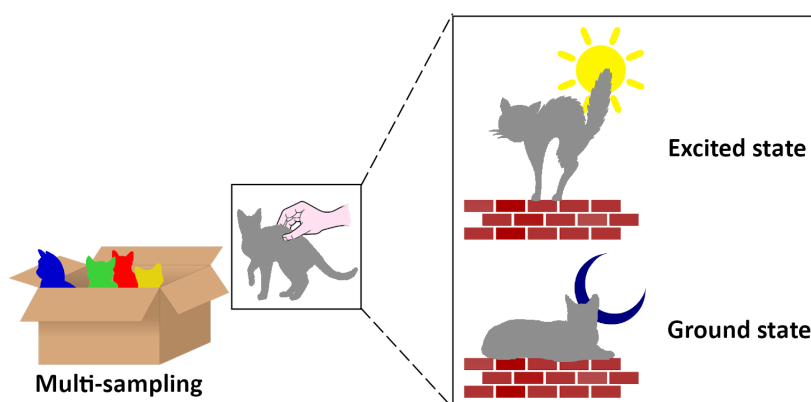


Figure 6.1: Scheme of how the protocol developed in the thesis works. From a multi-sampling method, one representative configuration is taken out to be investigated at the surface more in detail both in the GS and ES.

combination is in the fact that the limitations of one method cancel out with the advantages of the other and vice versa. This is the case with the dependence on a parameterization for FF or DFTB as well as for ab-initio methods, such as DFT or TD-DFT, due to the lack of ability to investigate systems of sizes and times in the nano-scale.

The experimental results speak for themselves [40, 42, 43, 44, 45, 46, 55, 56]: TiO_2 is a material with outstanding properties, capable of adsorbing most water contaminants and promoting their degradation through photocatalytic activity. Both processes are not at all trivial to describe as they incur several complexities. Through the study of the selected 9 pollutants we have shown that there are multiple obstacles occurring during the phase of surface approaching. The highly ordered first water layer represents for instance a barrier that must be overcome in order to proceed with direct adsorption modes to TiO_2 . However, it is often an indirect adsorption the one taking place, which can easily turn out in a new diffusion of the contaminants into the aquatic environment. Next to this pollutant-water competition, the molecules itself can also interact with each other. This results in molecular arrangements, or clusters, that can no longer identify a precise adsorption site on TiO_2 . The molecules that, however, do feel a strong attraction towards the surface and therefore remain adsorbed for at least more than 5–10 ns, bind to it through precise functional groups. By first observing the force-distance curves and then the duration and frequency of adsorption of these contaminants, we assume the existence of a ranked ladder that quantifies their binding strength. Starting from the most weakly attracted to the most strongly attracted, we identified the hydroxyl, carboxyl, carboxamide and phosphate groups (see 6.2). As with amino acids, adsorption depends

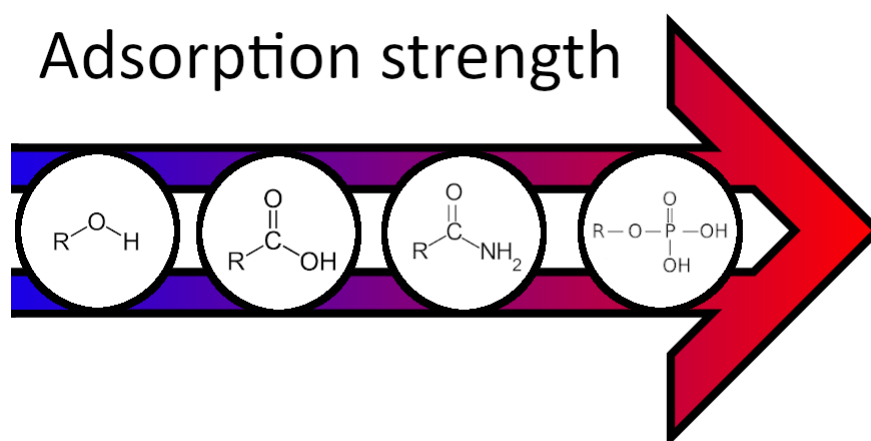


Figure 6.2: According to our static and dynamic analysis on the 9 pollutants, the phosphate group (GGG) is the one providing the most stable adsorption mode to the TiO_2 surface. It is followed by the carboxamide (CRB), carboxyl (GGG, SLC) and hydroxyl (ACE) groups.

primarily on functional groups and less on the backbone structure [211, 206, 207, 209, 208, 210, 212]. It is therefore entirely justifiable, as well as beneficial, to exploit the results obtained on the interaction of amino acids with TiO_2 , of which the literature continues to be enriched for applications in the medical field, to investigate the adsorption of water pollutants.

Although the presence of a specific functional group indicates the intensity with which a molecule adsorbs to the surface, this does not provide any kind of information on what the most likely degradation pathway will be. The GGG molecule has indeed been shown to possess a very strong attraction force with TiO_2 due to the presence of both the phosphate and carboxyl functional groups [5], but the identification of the most likely bond break upon degradation required detailed ab-initio analysis. The recognition of the bond in which the most torsional strain resides provided very important information about the conformation of the molecule, but this was not yet sufficient to state that it was also the most likely to break. The solvent around the adsorption configuration in fact not only serves to sustain the molecule at the surface, but is an active part of the degradation reaction through proton transfers and stabilization of the fragments produced. This was observed in our work with respect to thermal activation in GS, but it cannot be excluded that it could also occur in ES. Here, though, all water molecules adsorbing to the surface need an ES treatment as well, since due to the homocatalytic cleavage a co-adsorbate can be neglected due to a lack of formation of ionic charges. This results in a complex system, which would then need a much higher computational effort.

It is exactly the need to insist on developing ever more efficient methods that makes scientific research as challenging as exciting. One goal that should be achieved in the near future is to find an approach able to handle nanoscale systems without losing ab-initio information. Semi-empirical techniques such as DFTB are a promising prospect that is garnering increasing success [82]. Through the study of the properties of two different reconstructed rutile surfaces [183] we have shown that this method is indeed able to find results comparable to those of DFT, but unfortunately it still finds gaps in the correct description of hydrogen bonds while maintaining the same type of parameterization. Assuming to achieve this information and to reach a comparable representation also for the organic molecule - TiO_2 interface interaction, it would then be possible to study the adsorption and degradation in an even more extensive way. As reported in our work, in fact, each surface cut has different electronic properties and can therefore promote other types of reaction pathways. A study conducted on reconstructed, defective or doped surfaces would require, on the other hand, simulations that can only be achieved through semi-empirical methods.

The complexities to consider within the system are not limited to this. In the multi-sampling method considered in our research, molecules of the same species were taken into account in order to study their statistically more frequent adsorption mode. The eventual creation of clusters among the pollutants, however, opens up the way to other simulations in which the contaminants included in the sample are of different species (see fig. 6.3). Their interaction could in fact create new macromolecules with completely different properties compared to the original components. Would they feel the attraction of the surface even more strongly or would they rather stay in the solvent? How would the kinked sites of an amorphous or reconstructed surface affect any adsorption and degradation of this heterogeneous cluster? Again, a comparison of FF approaches with suitable semi-empirical methods would be an optimal way to find that out.

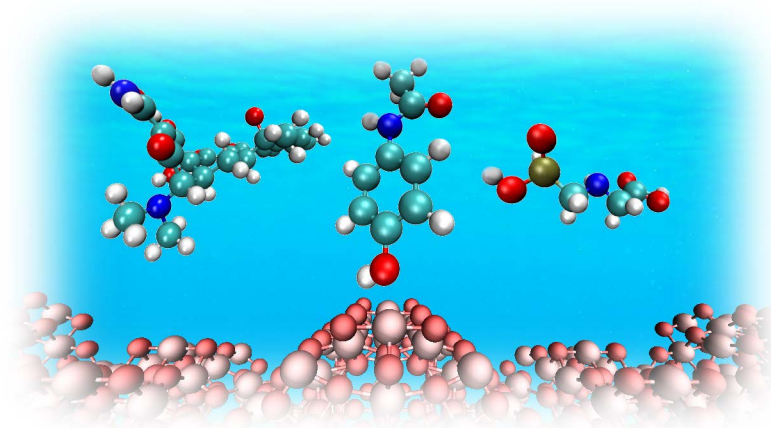


Figure 6.3: Example of a perspective for future calculations. The (001)-rec model is considered as the irregular surface on which to investigate the in-water dynamic trends of three pollutants of different species (TTR, ACE, GGG). Ideally, the simulation should be performed in DFTB to maintain ab-initio information.

Another key factor is the pH. Experimentally, it is known how the surface charge of TiO_2 changes according to the pH of the system [39, 10, 19, 12, 24, 13, 60, 55, 24, 61]. Our FF simulations were based on the physiological pH of 7.4, but it is necessary to continue with investigations also under basic and acidic conditions. Where exactly does the pH dependence reported in the degradation rates come from? Is it perhaps due to the high percentage of surface hydroxyls which then affect the adsorption modes? Does the electron transfer present at the contaminant- TiO_2 interface observed in this work change due to a charged surface? The difficulty in answering these questions, however, lies in the ab-initio representation which, given the small size of the surface and the presence of PBC, would not be able to have a distribution of hydroxyls and protons that accurately reproduce the desired pH without incurring fictitious mistakes.

In conclusion, although our study has been able to give an explanation of several phenomena, other exciting perspectives are already on the horizon. This, however, is the fate of scientific research: for each given answer, new questions await.

Appendix

Proofs of theorems and insights related to the sections of theoretical backgrounds described during the thesis are given in this appendix chapter.

Born-Oppenheimer approximation

The Hamiltonian operator of the many-body problem is very complex and its computational application inefficient. For this reason, it is possible to apply a first assumption, called Born-Oppenheimer approximation [86]. It is based on the fact that the masses M_I of the ions are much larger than that of an electron m_e . In the lightest case of the hydrogen atom, in fact, the nucleus (a proton) has a mass 1836 times heavier than that of the electron. The higher order of magnitude allows us to assume that while electrons perform their motion, protons remain basically stationary. Born-Oppenheimer's idea is then to calculate in quantum terms the solutions of the Schrödinger equation given only by the electron Hamiltonian operator \hat{H}_e . This recalls the same operator of eq. 3.2, but takes into account the position vectors \vec{R}_I as parameters and not as variables:

$$\hat{H}_e = \underbrace{-\frac{\hbar^2}{2m_e} \sum_{i=1}^n \Delta_i}_{\text{electronic kinetic term}} + \underbrace{\sum_{i=1}^{n-1} \sum_{j>i}^n \frac{e^2}{\|\vec{r}_i - \vec{r}_j\|}}_{\text{electron-electron interaction}} - \underbrace{\sum_{I=1}^N \sum_{i=1}^n \frac{e^2 Z_I}{\|\vec{R}_I - \vec{r}_i\|}}_{\text{electron-ion interaction}} \quad (\text{A.1})$$

$$= \hat{K} + V_{\text{ee}} + V_{\text{ext}}$$

Note that terms depending purely on the ionic coordinates, namely the ionic kinetic operator and the ion-ion interaction, are simply eliminated, as they would be constants. By writing the formula compactly, we will from now on refer to \hat{K} as the kinetic operator, to V_{ee} as the electron-electron repulsion and to V_{ext} as the external potential. The latter is a very important term that will be the key turning point in DFT theory. In the same way, we shift $\{\vec{R}_H\}_H$ from being variables to parameters in the total wavefunction

$$\left| \Psi(\{\vec{R}_H(t)\}_H, \{\vec{r}_h(t)\}_h) \right\rangle := \left| \Psi_{\{\vec{R}_H(t)\}_H}(\{\vec{r}_h(t)\}_h) \right\rangle := \left| \Psi(\{\vec{r}_h(t)\}_h) \right\rangle, \quad (\text{A.2})$$

which allows us to write down the stationary electronic Schrödinger equation:

$$\hat{H}_e |\Psi\rangle = E |\Psi\rangle \quad (\text{A.3})$$

The quantum system, therefore, reduces to $3n$ and not $3(N + n)$ degrees of freedom. Of course, for the purposes of ab-initio MD, the ions in the system must still move. Given their much slower than electronic motion, the Born-Oppenheimer approximation assumes that it can be treated with Newton's classical equations. The potential of the system referred to by the forces at each numerical integration step, called the Born-Oppenheimer potential $V_{\text{B-O}}(\{\vec{r}_h\}_h, \{\vec{R}_H\}_H)$, corresponds to the ground state (GS) of the expectation value of the electronic Hamiltonian operator:

$$M_I \frac{d^2}{dt^2} \vec{R}_I = -\nabla_I V_{\text{B-O}}(\{\vec{r}_h\}_h, \{\vec{R}_H\}_H) = -\nabla_I \min_{\Psi \in Q} \langle \Psi | \hat{H}_e | \Psi \rangle \quad (\text{A.4})$$

In the above formula, Q is the set of $L^2(\mathbb{R}^{3n}) = \{\Psi : \mathbb{R}^{3n} \rightarrow \mathbb{C} \mid \int_{\mathbb{R}^{3n}} \Psi < +\infty\}$ in which the wavefunctions are properly normalized to 1.

Proof of Rayleigh-Ritz principle

We report again the Rayleigh-Ritz principle [156] and give a proof of it.

Theorem 4 (Rayleigh-Ritz principle). *Given the many-body, stationary, electronic Schrödinger equation, the expectation value of the electronic hamiltonian operator \hat{H}_e on any wavefunction cannot be lower than the GS energy of the system.*

Proof. First, we can multiply both term of eq. A.3 by $\langle \Psi |$. Analytically speaking, this corresponds, according to the formalism of Dirac's *bra-ket*, to calculating the expectation value by integral.

$$\hat{H}_e |\Psi\rangle = E |\Psi\rangle \Rightarrow \langle \Psi | \hat{H}_e | \Psi \rangle = \langle \Psi | E | \Psi \rangle$$

Since the energy E is a real number and not a function, it can be taken out of the integral and made explicit.

$$\langle \Psi | \hat{H}_e | \Psi \rangle = E \langle \Psi | \Psi \rangle \Rightarrow E = \frac{\langle \Psi | \hat{H}_e | \Psi \rangle}{\langle \Psi | \Psi \rangle}$$

The GS energy E_{GS} , per definition, is the lowest energy of the system given by a normalized wavefunction. Hence, we have that

$$E > E_{\text{GS}} = \min_{\Psi \in Q} \langle \Psi | \hat{H}_e | \Psi \rangle$$

□

Explicitation of V_{ext} in terms of ρ

We provide a derivation of how the term V_{ext} in the Hamiltonian operator can be rewritten explicitly in terms of the electronic density.

We start writing its expectation value for the GS wave-function:

$$\begin{aligned} \langle \Psi_0 | V_{\text{ext}} | \Psi_0 \rangle &= \int_{\mathbb{R}^{3n}} \Psi_0^*(\vec{r}_1, \dots, \vec{r}_n) \Psi_0(\vec{r}_1, \dots, \vec{r}_n) \sum_{i=1}^n \sum_{I=1}^N \frac{Ze^2}{\|\vec{r}_i - \vec{R}_I\|} d\vec{r}_1 \dots d\vec{r}_n = \\ &= \int_{\mathbb{R}^{3n}} \|\Psi_0(\vec{r}_1, \dots, \vec{r}_n)\|^2 \sum_{i=1}^n \sum_{I=1}^N \frac{Ze^2}{\|\vec{r}_i - \vec{R}_I\|} d\vec{r}_1 \dots d\vec{r}_n \end{aligned}$$

By developing the summation in i term by term, we can break the integral into n integrals thanks to Fubini's theorem:

$$\begin{aligned} \langle \Psi_0 | V_{\text{ext}} | \Psi_0 \rangle &= \int_{\mathbb{R}^3} \sum_{I=1}^N \frac{Z_I e^2}{\|\vec{r}_1 - \vec{R}_I\|} \underbrace{\left(\int_{\mathbb{R}^{3(n-1)}} \|\Psi_0(\vec{r}_1, \dots, \vec{r}_n)\|^2 d\vec{r}_2 \dots d\vec{r}_n \right)}_{\frac{1}{n} \rho_{\Psi_0}(\vec{r}_1)} d\vec{r}_1 + \\ &\dots + \int_{\mathbb{R}^3} \sum_{I=1}^N \frac{Z_I e^2}{\|\vec{r}_n - \vec{R}_I\|} \underbrace{\left(\int_{\mathbb{R}^{3(n-1)}} \|\Psi_0(\vec{r}_1, \dots, \vec{r}_{n-1})\|^2 d\vec{r}_1 \dots d\vec{r}_{n-1} \right)}_{\frac{1}{n} \rho_{\Psi_0}(\vec{r}_n)} d\vec{r}_n \end{aligned}$$

For the purposes of integration, however, there is no difference between \vec{r}_i , so that we can simply define them as $\vec{r}_i = \vec{r}$. In this way we can add up all the electronic densities and get

$$\langle \Psi_0 | V_{\text{ext}} | \Psi_0 \rangle = \mathcal{N} \frac{1}{\mathcal{N}} \int_{\mathbb{R}^3} \sum_{I=1}^N \underbrace{\frac{Z_I e^2}{\|\vec{r} - \vec{R}_I\|}}_{V_{\text{ext}}(\vec{r})} \rho_{\Psi_0}(\vec{r}) d\vec{r}, \quad (\text{A.5})$$

where we can recognize in $\sum_{I=1}^N \frac{Z_I e^2}{\|\vec{r} - \vec{R}_I\|}$ the external potential acting on one single electron at a position \vec{r} .

Proof of the first theorem of Hohenberg-Kohn

We report again the first theorem of Hohenberg-Kohn and give a proof of it.

Theorem 5 (first theorem of Hohenberg-Kohn). *Given the many-body, stationary, electronic Schrödinger equation, there exists a bijection between the GS electronic density $\rho_{\Psi_0}(\vec{r})$ and the external potential $V_{\text{ext}}(\vec{r})$ of the system.*

Proof. \Rightarrow

This implication is trivial. In fact, if $\rho_{\Psi_0}(\vec{r})$ is known, then the functional $V_{\text{ext}}[\rho]$

is immediately obtainable as defined in eq. A.5:

$$V_{\text{ext}} : \rho_{\Psi}(\vec{r}) \mapsto V[\rho] = \int_{\mathbb{R}^3} \sum_{I=1}^N \frac{Z_I e^2}{\|\vec{r} - \vec{R}_I\|} \rho_{\Psi}(\vec{r}) d\vec{r} \quad (\text{A.6})$$

Please note that this definition does not imply that ρ has to be the one referred to the GS energy. This is strictly required, though, in the opposite implication. \Leftarrow R.A.A.

Let us suppose that there exist two different systems, namely two different Hamiltonian operators, \hat{H}_e and \hat{H}'_e given rise to the same GS electronic density $\rho_{\Psi_0}(\vec{r}) = \rho'_{\Psi'_0}(\vec{r})$. Due to the nature of the kinetic operator and of the electron-electron interaction, we have that $\hat{K} = \hat{K}'$ as well as $V_{\text{ee}} = V_{\text{ee}'}$. What distinguishes the two Hamiltonian operators are then the different external potentials $V_{\text{ext}}(\vec{r})$ and $V'_{\text{ext}}(\vec{r})$:

$$\hat{H}'_e = \hat{H}_e + V'_{\text{ext}} - V_{\text{ext}} \quad (\text{A.7})$$

In terms of expectation values, the two ground states are given by

$$E_{\text{GS}} = \langle \Psi_0 | \hat{H}_e | \Psi_0 \rangle \quad (\text{A.8})$$

$$E'_{\text{GS}} = \langle \Psi'_0 | \hat{H}'_e | \Psi'_0 \rangle \quad (\text{A.9})$$

Hence, if we evaluate the energy of the first system for the GS wavefunction Ψ'_0 of the second, we obtain per definition an energy higher than E_{GS} . By using eq. A.7, we obtain the following expression:

$$\begin{aligned} E_{\text{GS}} &< \langle \Psi'_0 | \hat{H}_e | \Psi'_0 \rangle = \langle \Psi'_0 | \hat{H}'_e + V_{\text{ext}} - V'_{\text{ext}} | \Psi'_0 \rangle \\ &= \langle \Psi'_0 | \hat{H}'_e | \Psi'_0 \rangle + \langle \Psi'_0 | V_{\text{ext}} - V'_{\text{ext}} | \Psi'_0 \rangle \\ &\Rightarrow E_{\text{GS}} < E'_{\text{GS}} + \langle \Psi'_0 | V_{\text{ext}} - V'_{\text{ext}} | \Psi'_0 \rangle \end{aligned} \quad (\text{A.10})$$

With a similar argument, one can also prove that

$$E'_{\text{GS}} < E_{\text{GS}} - \langle \Psi_0 | V_{\text{ext}} - V'_{\text{ext}} | \Psi_0 \rangle \quad (\text{A.11})$$

By summing up term by term in expressions A.10 and A.11, we explicitly obtain:

$$\begin{aligned} E_{\text{GS}} + E'_{\text{GS}} &< E_{\text{GS}} + E'_{\text{GS}} + \\ &+ \int_{\mathbb{R}^3} [V_{\text{ext}}(\vec{r}) - V'_{\text{ext}}(\vec{r})] \rho'_{\Psi'_0}(\vec{r}) d\vec{r} - \int_{\mathbb{R}^3} [V_{\text{ext}}(\vec{r}) - V'_{\text{ext}}(\vec{r})] \rho_{\Psi_0}(\vec{r}) d\vec{r} \end{aligned} \quad (\text{A.12})$$

Since $\rho_{\Psi_0}(\vec{r}) = \rho'_{\Psi'_0}(\vec{r})$, though, the latter two terms cancel out, leaving

$$E_{\text{GS}} + E'_{\text{GS}} < E_{\text{GS}} + E'_{\text{GS}} , \quad (\text{A.13})$$

which is absurd. Therefore, a unique potential must exist to determine ρ . \square

Derivation of Kohn-Sham equations

We proceed with the construction of a dummy system in which the electrons do not interact with each other, as in the HF approximation. It is assumed, however, that they still provide the same density ρ as the interacting system. The Hamiltonian operator of the non-interacting system will then be given by

$$\hat{H}^{(s)} = \hat{K}^{(s)} + V_{\text{ext}}^{(s)} = \sum_{i=1}^n \left(-\frac{\hbar^2}{2m_e} \Delta_i + \sum_{I=1}^N \frac{Z_I e^2}{\|\vec{r}_i - \vec{R}_I\|} \right), \quad (\text{A.14})$$

which it is solvable since it does not have the electron-electron repulsion term V_{ee} . An exact GS solution is given by the HF wavefunction, which uses the Slater determinant to respect Pauli's exclusion principle:

$$\Psi^{\text{HF}}(\{\vec{r}_h\}_h) = \frac{1}{\sqrt{n!}} \begin{vmatrix} \psi_1(\vec{r}_1) & \psi_1(\vec{r}_2) & \dots & \psi_1(\vec{r}_n) \\ \psi_2(\vec{r}_1) & \dots & \dots & \psi_2(\vec{r}_n) \\ \vdots & \ddots & \ddots & \vdots \\ \psi_n(\vec{r}_1) & \dots & \dots & \psi_n(\vec{r}_n) \end{vmatrix} \quad (\text{A.15})$$

In the above expression, $\psi_i(\vec{r}_i)$ represents the eigenstates of each electron. For this wavefunction, the electronic GS density is given by

$$\rho_{\Psi^{\text{HF}}}(\vec{r}) = \sum_{i=1}^n \|\psi_i\|_{\mathbb{C}}^2 \quad (\text{A.16})$$

The question is now how to relate the non-interacting system to the original, interacting one. We can start writing the non-interacting system as functionals of ρ :

$$E^{(s)}[\rho] = \hat{K}^{(s)}[\rho] + \int_{\mathbb{R}^3} V_{\text{ext}}^{(s)}(\vec{r}) \rho(\vec{r}) d\vec{r} \quad (\text{A.17})$$

Due to the non-interacting characteristic of the fictitious system, we are able to describe the kinetic operator explicitly thanks to the Slater determinant:

$$\hat{K}^{(s)}[\rho] = \frac{\hbar^2}{2m_e} \sum_{i=1}^n \int_{\mathbb{R}^3} \psi_i(\vec{r}) \Delta_{\vec{r}} \psi_i^*(\vec{r}) d\vec{r} \quad (\text{A.18})$$

We ask, now, how incisive is the difference between the kinetic energy of the interacting system \hat{K} and that of the non-interacting $\hat{K}^{(s)}$. If the electron correlation is low, HF's method gives a very good approximation of the GS energy E_{GS} . The "kinetic correlation" effects actually make up a very small part of the kinetic energy, with the most significant part being the $\hat{K}^{(s)}[\rho]$ functional. A similar approach can be made regarding the term V_{ee} . Enclosed within it are all the "classical" and "non-classical" effects of the electrostatic potential. It is possible to extract the Coulomb functional $J[\rho]$ from the HF approach and assign to the remaining term, the so-called *exchange-correlation*

functional $E_{\text{xc}}[\rho]$, an unknown form.

$$V_{\text{ee}}[\rho] = J[\rho] + E_{\text{xc}}[\rho] = \int_{\mathbb{R}^3} \int_{\mathbb{R}^3} \frac{\rho(\vec{r})\rho(\vec{r}')}{\|\vec{r} - \vec{r}'\|} d\vec{r}d\vec{r}' + E_{\text{xc}}[\rho] \quad (\text{A.19})$$

In the exchange-correlation functional we have included all the effects of the many-body character of the true electron system and it is what gives to DFT the necessity to proceed with at least some approximations. We can then define the Kohn-Sham energy functional as

$$E_{\text{KS}}[\rho] = T^{(s)}[\rho] + V_{\text{ext}}[\rho] + J[\rho] + \underbrace{E_{\text{xc}}[\rho]}_{\text{unknown}} \quad (\text{A.20})$$

Therefore, by minimizing this energy one can find the GS energy of the system. Thanks to Euler-Lagrange equation and the variational approach, we can obtain a derivation that depends on the single-state wavefunctions belonging to the Slater determinant [A.15](#). In order to do this we proceed with the functional derivative over ρ :

$$\frac{\delta \hat{K}^{(s)}[\rho]}{\delta \rho} + \underbrace{V_{\text{ext}}(\vec{r}) + \frac{\delta J[\rho]}{\delta \rho} + \frac{\delta E_{\text{xc}}[\rho]}{\delta \rho}}_{V_{\text{eff}}(\vec{r})} = \frac{\delta E_{\text{KS}}[\rho]}{\delta \rho} \quad (\text{A.21})$$

The term V_{eff} was here defined and it is called *effective potential*. We observe that the interacting system can be treated in the same way as an independent particle system, provided, however, that the efficacious potential plays a role analogous to that of $V_{\text{ext}}(\vec{r})$ of the fictitious system, governed by the equation $\frac{\delta \hat{K}^{(s)}[\rho]}{\delta \rho} + V_{\text{ext}}^{(s)}(\vec{r}, \rho) = \frac{\delta E^s[\rho]}{\delta \rho}$. Since both of the systems have, per construction, the same extreme ρ_{GS} , we can apply once again HF approach to obtain the famous Kohn-Sham equations:

$$\left[-\frac{\hbar^2}{2m_e} \Delta_{\vec{r}} + V_{\text{eff}}[\rho](\vec{r}) \right] |\psi(\vec{r})\rangle = \varepsilon_i |\psi(\vec{r})\rangle \quad (\text{A.22})$$

Plane-waves and Bloch's theorem

The integer span space generated by the primitive lattice vectors, i.e. the collection of all vectors of the kind [3.14](#), is the so-called *Bravais lattice* \mathcal{B} . Next to this set, which is real and can be visualized as a direct manifestation of the unit cell, it is possible to assign a set that occurs instead in Fourier space. In quantum physics, in fact, the use of the Fourier transform has the very important significance of allowing one to move from spatial observables $\{\vec{r}_h\}_h$ to momentum observables $\{\vec{p}_h\}_h$. These second variables are associated with wave-vectors $\{\vec{k}_h\}_h$, which allow us to observe how the wavefunctions extend through the crystal as a wave. Therefore, we define *reciprocal space* \mathcal{R} the collection of wave-vectors \vec{G} that make a generic plane wave $\psi_{\vec{G}}(\vec{r}) = e^{i\vec{G}\cdot\vec{r}}$ periodic in \vec{R} . In

order to satisfy this property, we have that:

$$\begin{aligned} \psi_{\vec{G}}(\vec{r}) = \psi_{\vec{G}}(\vec{r} + \vec{R}) &\iff e^{i\vec{G}\cdot\vec{r}} = e^{i\vec{G}\cdot(\vec{r}+\vec{R})} \iff e^{i\vec{G}\cdot\vec{R}} = 1 \\ &\iff \vec{G} \cdot \vec{R} = 0 \iff \vec{G} \cdot \vec{R} = 2\pi h, \text{ with } h \in \mathbb{Z} \end{aligned}$$

Therefore, this space is generated by $\vec{b}_1, \vec{b}_2, \vec{b}_3$ such that

$$\vec{a}_i \cdot \vec{b}_j = 2\pi\delta_{ij} \quad (\text{A.23})$$

These inverse-space vectors can be explicitly calculated:

$$\begin{aligned} \vec{b}_1 &= 2\pi \frac{(\vec{a}_2 \times \vec{a}_3)}{\vec{a}_1 \cdot (\vec{a}_2 \times \vec{a}_3)} \\ \vec{b}_2 &= 2\pi \frac{(\vec{a}_3 \times \vec{a}_1)}{\vec{a}_2 \cdot (\vec{a}_3 \times \vec{a}_1)} \\ \vec{b}_3 &= 2\pi \frac{(\vec{a}_1 \times \vec{a}_2)}{\vec{a}_3 \cdot (\vec{a}_1 \times \vec{a}_2)} \end{aligned} \quad (\text{A.24})$$

In the same way as before, we can then reach each point of the reciprocal space by an integer linear combination of the primitive reciprocal lattice vectors:

$$\vec{G} = m_1\vec{b}_1 + m_2\vec{b}_2 + m_3\vec{b}_3, \quad m_1, m_2, m_3 \in \mathbb{Z} \quad (\text{A.25})$$

Note that the reciprocal space is a real Bravais lattice as well. Moreover, the volumes of the two sets are connected to each other by the following relation:

$$\Omega_{\text{RUC}} = \left\| \vec{b}_1 \cdot (\vec{b}_2 \times \vec{b}_3) \right\| = \frac{(2\pi)^3}{\left\| \vec{a}_1 \cdot (\vec{a}_2 \times \vec{a}_3) \right\|} = \frac{(2\pi)^3}{\Omega_{\text{PUC}}} \quad (\text{A.26})$$

with Ω_{RUC} and Ω_{PUC} being the volumes of the reciprocal unit cell and primitive unit cell, respectively. The application of a Fourier transformation on a general function $f(\vec{r})$ with periodicity of the lattice space can be written down as a vector sum instead of an integral (due to the integer character of the lattices):

$$f(\vec{r}) = \sum_{\vec{G} \in \mathcal{R}} f(\vec{G}) e^{i\vec{G}\cdot\vec{r}} \quad (\text{A.27})$$

with $f(\vec{G})$ being the Fourier transform components of f . The periodic nature of these functions is what makes the electronic study of crystal structures accessible and computationally simplified [154].

Theorem 6 (Bloch's theorem). *Given the many-body, stationary, electronic Schrödinger equation, if the potential in the single-particle hamiltonian has the translational periodicity of the Bravais lattice, namely*

$$V^{sp}(\vec{r} + \vec{R}) = V^{sp}(\vec{r}), \text{ with } \vec{R} \in \mathcal{B} \quad (\text{A.28})$$

then the single-particle wavefunctions have the same symmetry. up to a phase factor:

$$\psi_{\vec{k}}(\vec{r} + \vec{R}) = e^{i\vec{k}\cdot\vec{R}}\psi_{\vec{k}}(\vec{r}) \quad (\text{A.29})$$

In other words, each single-particle wavefunction can be expressed as the product of the phase factor multiplied by the functions $u_{\vec{k}}(\vec{r} + \vec{R}) = u_{\vec{k}}(\vec{r})$ which have the full translational periodicity of the Bravais lattice:

$$\psi_{\vec{k}}(\vec{r}) = e^{i\vec{k}\cdot\vec{r}}u_{\vec{k}}(\vec{r}) \quad (\text{A.30})$$

We therefore define any wavefunction that satisfies Bloch's theorem as *Bloch function* (or *Bloch state*). We can now solve the single-particle Schrödinger equation with use of Bloch functions, namely:

$$\left[-\frac{\hbar^2}{2m_e}\Delta_{\vec{r}} + \frac{\hbar^2}{2m_e}\|\vec{k}\|^2 + V^{\text{sp}}(\vec{r}) \right] u_{\vec{k}}(\vec{r}) = \varepsilon_{\vec{k}}u_{\vec{k}}(\vec{r}) \quad (\text{A.31})$$

Solving the above equation provides an explicit definition of $u_{\vec{k}}(\vec{r})$, which can then be multiplied by the factor $e^{i\vec{k}\cdot\vec{r}}$ to obtain the solution of the original single-particle equation. The great advantage of Bloch's theorem is the possibility of solving the equation for \vec{r} within the primitive unit cell of the crystal only, because every other value of the wavefunction outside of it can be obtain with use of periodicity.

Thanks to Bloch's theorem we can now work on periodic systems limiting the computational cost. Another piece of information suggested by the consequences of the theorem is the importance of plane-waves, which forms the phase factor in $\psi_{\vec{k}}(\vec{r})$, without its normalization term: $1/\sqrt{\Omega_{\text{PUC}}}e^{i\vec{k}\cdot\vec{r}}$. Its integral over the volume Ω_{PUC} coincides with a uniform probability, from which the term "plane" comes from:

$$\begin{aligned} \int_{\Omega_{\text{PUC}}} \left\| \frac{1}{\sqrt{\Omega_{\text{PUC}}}} e^{i\vec{k}\cdot\vec{r}} \right\|_{\mathbb{C}}^2 dx dy dz &= \\ \frac{1}{\Omega_{\text{PUC}}} \int_{\Omega_{\text{PUC}}} e^{-i\vec{k}\cdot\vec{r}} e^{i\vec{k}\cdot\vec{r}} dx &= \frac{1}{\Omega_{\text{PUC}}} \int_{\Omega_{\text{PUC}}} dx dy dz = 1 \end{aligned} \quad (\text{A.32})$$

Hence, the description is of total delocalization: at each point of Ω_{PUC} we have a probability of 1 of finding one electron of defined momentum $\vec{p} = \hbar\vec{k}$. Despite this, plane-waves are for many reasons among the most widely used basis sets in DFT. First, since plane-waves are the solution of the Schrödinger equation for the free particle, it has historically been decided to take it as a model for more constructed cases as well. Many elements in fact exhibit a band structure that can be interpreted as in the case of the free electron, such as metallic s and p elements. The second reason is practical: the energy and Hamiltonian expressions of the system are simple to implement under this scheme. Linked to this is a high computational speed, as the use of the (fast) Fourier transform is made straightforward due to the particular structure of the plane-waves.

DFT-D2 dispersion correction term

In order to properly describe the DFT-D3 approach, it is necessary to explain how DFT-D2 works. The most challenging task in creating VdW dispersion corrections is the right definition of an energetic damping function f_d for each pair of atoms. In DFT-D2 this is expressed through use of an exponential function:

$$f_d^{(\text{D2})}(\|\vec{R}_I - \vec{R}_J\|) = \frac{1}{1 + e^{-d \left(\frac{\|\vec{R}_I - \vec{R}_J\|}{R_{0,IJ}^{\text{D2}}} \right)}} \quad (\text{A.33})$$

In the above expression, d is a parameter representing the damping factor (usually set to 20), whereas $R_{0,IJ}^{\text{D2}}$ is the sum of the atomic VdW radii for the two elements I and J . We can then add to the Kohn-Sham total energy of the system $E^{(\text{DFT})}$ the correction term

$$E_{\text{disp}}^{(\text{D2})} = -\frac{1}{2} s_6 \sum_{I=1}^N \sum_{J=1}^N \frac{C_{6,IJ}^{(\text{D2})}}{\|\vec{R}_I - \vec{R}_J\|^6} f_d^{(\text{D2})}(\|\vec{R}_I - \vec{R}_J\|) \quad (\text{A.34})$$

such that the new, corrected energy is then given by $E_{\text{corr}}^{(\text{DFT-D2})} = E^{(\text{DFT})} + E_{\text{disp}}^{(\text{D2})}$. The quantities $C_{6,IJ}^{(\text{D2})}$ are coupled dispersion coefficients derived from single ones, namely $C_{6,I}^{(\text{D2})}$ and $C_{6,J}^{(\text{D2})}$, through the relation

$$C_{6,IJ}^{(\text{D2})} = \sqrt{C_{6,I}^{(\text{D2})} C_{6,J}^{(\text{D2})}} \quad (\text{A.35})$$

Single coefficients are tabulated for most elements and they represent, together with the functional-dependent scaling factor s_6 as well as a cut-off distance to truncate the direct lattice summation, parameters that one has to specify a priori.

Approximations in DFTB

In order to introduce the tight-binding approach, which involves how the atomic orbitals shall be treated, we have first to derive approximations to the charge fluctuations and repulsive terms.

The charge fluctuation energy is a mixture of the Coulomb interaction and exchange-correlation contributions, both due to oscillations in $\delta\rho$. To handle this term, we start dividing the volume of the system V into volumes related to each atom, $\{V_I\}_I$. In this way, an integral over V can be obtained as a sum of N integrals over V_I . The form of these volumes is case-specific and, since they are mere geometrical quantities, in each of them we can find an excess/deficiency of electrons. This is defined as $\Delta q_I = q_I - q_I^0$, where q_I is the actual number of electrons in V_I and q_I^0 is the number of valence electrons for the neutral atom I . A rough estimate of Δq_I can be obtained as

$$\Delta q_I \approx \int_{V_I} \delta\rho(\vec{r}) \delta r, \quad (\text{A.36})$$

which means that

$$\delta\rho(\vec{r}) = \sum_{I=1}^N \Delta q_I \delta\rho_I(\vec{r}) \quad (\text{A.37})$$

In this last expression, the $\delta\rho_I(\vec{r})$ represent normalized variations of the local density in the atom I : they tell how the density profile of a given atom changes upon charging. A knowledge of such functions is not known and can only be assumed a priori. In this formulation, we define them as Gaussians of the form

$$\delta\rho_I(\vec{r}) = \frac{1}{(2\pi\sigma_I^2)^{3/2}} e^{-\frac{r^2}{2\sigma_I^2}}, \quad (\text{A.38})$$

where σ_I is the standard deviation. Thanks to the applied volumetric partition in $\{V_I\}_I$, we can now convert the double integral in 3.32 into a sum over atom pairs. Its result depends on whether $I = J$ or not.

- $I = J$.

In this case, $E_{\text{coul}}[\delta\rho]$ assumes the following expression:

$$\frac{1}{2} \Delta q_I^2 \int \int_{V_I \times V_I} \left(\frac{\delta^2 E_{\text{xc}}[\rho_0]}{\delta\rho\delta\rho'} + \frac{1}{\|\vec{r} - \vec{r}'\|} \right) \delta\rho_I \delta\rho'_I d\vec{r} d\vec{r}' \quad (\text{A.39})$$

We now recall that, in general, the energy of an atom I can be expressed as a function of Δq_I by Taylor expansion:

$$\begin{aligned} E(\Delta q_I) &\approx E_0 + \frac{\partial E}{\partial \Delta q_I} \Delta q_I + \frac{1}{2} \frac{\partial^2 E}{\partial \Delta q_I^2} \Delta q_I^2 \\ &= E_0 + \chi_I \Delta q_I + \frac{1}{2} U_I \Delta q_I^2 \end{aligned} \quad (\text{A.40})$$

The factor χ_I represents the electronegativity of the atom, whereas U_I is the so-called Hubbard term. By comparing eqs. A.39 and A.40, we observe that the integral is actually U_I , so that

$$E_{\text{coul.}}[\delta\rho] = \frac{1}{2} U_I \Delta q_I^2 \quad (\text{A.41})$$

- $I \neq J$

In this second case, contributions belonging to the exchange-correlation term vanish, leaving out

$$\frac{1}{2} \Delta q_I \Delta q_J \int \int_{V_I \times V_J} \frac{1}{\|\vec{r} - \vec{r}'\|} \delta\rho_I \delta\rho'_J d\vec{r} d\vec{r}' \quad (\text{A.42})$$

as expression for $E_{\text{coul.}}[\delta\rho]$. With our previous assumption on the Gaussian form of $\delta\rho_I$, this becomes

$$E_{\text{coul.}}[\delta\rho] = \frac{1}{2} \frac{\text{erf}(C_{IJ} \|\vec{R}_I - \vec{R}_J\|)}{\|\vec{R}_I - \vec{R}_J\|} \Delta q_I \Delta q_J, \quad (\text{A.43})$$

with C_{IJ} appropriately defined coefficients.

In conclusion, the charge fluctuation term can be rewritten as

$$E_{\text{coul.}}[\delta\rho] = \frac{1}{2} \sum_{I=1}^N \sum_{J=1}^N \gamma_{IJ}(\|\vec{R}_I - \vec{R}_J\|) \Delta q_I \Delta q_J, \quad (\text{A.44})$$

where $\gamma_{IJ}(\|\vec{R}_I - \vec{R}_J\|)$ is given by

$$\begin{cases} U_I & \text{if } I = J \\ \frac{\text{erf}(C_{IJ} \|\vec{R}_I - \vec{R}_J\|)}{\|\vec{R}_I - \vec{R}_J\|} & \text{if } I \neq J \end{cases} \quad (\text{A.45})$$

We must now shortly deal with the repulsion term E_{rep} , which contains the interactions between ions. However, within it there is also a contribution due to exchange-correlation interactions, in which all the core-electron effects are displayed. The main idea here is to approximate the whole term in a repulsive function V_{rep}^{IJ} which depends only on atomic numbers, exactly as it is already for the ionic-ionic potential. This may seem like a crude approach, but it is actually well justified. By partitioning the volume V in N atomic volumes as before, in fact. the Hartree term

$$\frac{1}{2} \int \int_{\mathbb{R}^6} \frac{\delta\rho_0(\vec{r}) \delta\rho'_0(\vec{r}')}{\|\vec{r} - \vec{r}'\|} d\vec{r} d\vec{r}' \quad (\text{A.46})$$

can be discretized as a sum over atom pairs, each depending on atomic numbers alone. This is possible because $\rho_0(\vec{r})$ itself depends on them and is spherically symmetric for free atoms. The whole repulsive term can then be approximated as

$$E_{\text{rep}} = \sum_{I=1}^{N-1} \sum_{J>I}^N V_{\text{rep}}^{IJ}(\|\vec{R}_I - \vec{R}_J\|), \quad (\text{A.47})$$

with $V_{\text{rep}}^{IJ}(\|\vec{R}_I - \vec{R}_J\|)$ obtained by fitting to higher level of theory, such as DFT or HF.

Derivation of the chemical potential μ_{O}

We derive the classical definition of the chemical potential μ_{O} for an ideal gas, which will then be representative for the oxygen reservoir. Let $U(S, V, n)$ be the internal energy of the system, where S is the entropy, V the volume and

$n = n_1 + n_2 + \dots + n_i + \dots + n_N$ the number of particles per N different species. The definitions of temperature T , pressure p and chemical potential of the i -th species μ_i are computed through the differential:

$$dU = \underbrace{\frac{\partial U}{\partial S}}_T dS + \underbrace{\frac{\partial U}{\partial V}}_{-p} dV + \sum_{i=1}^N \underbrace{\frac{\partial U}{\partial n_i}}_{\mu_i} dn_i \quad (\text{A.48})$$

An extension of eq. 3.42 leads then to

$$G(T, p) = \sum_{i=1}^N n_i \mu_i \quad (\text{A.49})$$

which holds true since we are in an ideal gas. On the other hand, the Gibbs free energy can also be written as $G = U + pV - TS$. We can then proceed differentiating both of its two expressions, which have to coincide in the end:

$$\begin{cases} dG = \sum_{i=1}^n (\mu_i dn_i + n_i d\mu_i) \\ dG = dU + p dV + V dp - T dS - S dT \end{cases} \quad (\text{A.50})$$

In the second equation, we can make use of the differential A.48 to obtain

$$\begin{aligned} dG &= T dS - p dV + \sum_{i=1}^N \mu_i + p dV + V dp - T dS - S dT \\ &= \sum_{i=1}^N \mu_i + V dp - S dT \end{aligned} \quad (\text{A.51})$$

By comparing the two different expressions of the same quantity dG and assuming that T is constant ($dT = 0$), we then conclude the following relationship:

$$\sum_{i=1}^n n_i d\mu_i = V dp \quad (\text{A.52})$$

We can now think of p as composed by the sum of each contribution p_i , meaning that $dp = \sum_{i=1}^n dp_i$. Moreover, since we in an ideal gas we can make use of

$$p_i V = n_i k_B T \Rightarrow V = \frac{n_i k_B T}{p_i} \quad (\text{A.53})$$

to obtain the following differential equation, which holds true $\forall i = 1, 2, \dots, N$:

$$\begin{aligned} V dp_i = n_i d\mu_i &\Rightarrow \frac{n_i k_B T}{p_i} dp_i = n_i d\mu_i \\ &\Rightarrow k_B T \frac{dp_i}{p_i} = d\mu_i \\ \int_{\mu_i^0}^{\mu_i} d\mu'_i &= k_B T \int_{p^0}^{p_i} \frac{dp'_i}{p'_i} \end{aligned} \quad (\text{A.54})$$

where μ_i^0 and p^0 are reference values of the i -th chemical potential and pressure, respectively. The solution of the integral for the chemical potential of an oxygen molecule is then given by

$$\mu_{\text{O}_2}(T, p) = \mu_{\text{O}_2}^0 + k_B T \ln\left(\frac{p_{\text{O}_2}}{p^0}\right) \quad (\text{A.55})$$

However, we are interested in finding the chemical potential of a single oxygen atom μ_{O} . Since the surface is supposed to be in equilibrium with the oxygen gas reservoir, we have that $\mu_{\text{O}}^{\text{surf}} = \mu_{\text{O}}^{\text{gas}}$, because of $\text{O} + \text{O} \rightarrow \text{O}_2$. For the chemical potential we are interested in then $\mu_{\text{O}} = \frac{1}{2}\mu_{\text{O}_2}$ shall hold which, when inserted in equation A.55 leads to the following, final expression:

$$\mu_{\text{O}}(T, p) = \mu_{\text{O}}^0 + \frac{1}{2}k_B T \ln\left(\frac{p_{\text{O}_2}}{p^0}\right) \quad (\text{A.56})$$

Bibliography

- [1] A.E. Schwarz et al. “Sources, transport, and accumulation of different types of plastic litter in aquatic environments: A review study”. In: *Marine Pollution Bulletin* 143 (2019), pp. 92–100. ISSN: 0025-326X. DOI: <https://doi.org/10.1016/j.marpolbul.2019.04.029>.
- [2] Imogen E. Napper et al. “Reaching New Heights in Plastic Pollution Preliminary Findings of Microplastics on Mount Everest”. In: *One Earth* 3.5 (2020), pp. 621–630. ISSN: 2590-3322. DOI: <https://doi.org/10.1016/j.oneear.2020.10.020>.
- [3] Wen Yi Chia et al. “Nature’s fight against plastic pollution: Algae for plastic biodegradation and bioplastics production”. In: *Environmental Science and Ecotechnology* 4 (2020), p. 100065. ISSN: 2666-4984. DOI: <https://doi.org/10.1016/j.ese.2020.100065>.
- [4] Philipp Wanner. “Plastic in agricultural soils – A global risk for groundwater systems and drinking water supplies? – A review”. In: *Chemosphere* 264 (2021), p. 128453. ISSN: 0045-6535. DOI: <https://doi.org/10.1016/j.chemosphere.2020.128453>.
- [5] Filippo Balzaretti et al. *Charge-Transfer Promoted Fixation of Glyphosate on TiO₂ - a Multiscale Approach*. Apr. 2021. DOI: [10.26434/chemrxiv.14465436.v1](https://doi.org/10.26434/chemrxiv.14465436.v1).
- [6] Eline Boelee et al. “Water and health: From environmental pressures to integrated responses”. In: *Acta Tropica* 193 (2019), pp. 217–226. ISSN: 0001-706X. DOI: <https://doi.org/10.1016/j.actatropica.2019.03.011>.
- [7] Ang Li et al. “Water pollution from food production: lessons for optimistic and optimal solutions”. In: *Current Opinion in Environmental Sustainability* 40 (2019). System dynamics and sustainability, pp. 88–94. ISSN: 1877-3435. DOI: <https://doi.org/10.1016/j.cosust.2019.09.007>.

- [8] Guilherme Gomes-Silva et al. "Water pollution affects fish community structure and alters evolutionary trajectories of invasive guppies (*Poecilia reticulata*)". In: *Science of The Total Environment* 730 (2020), p. 138912. ISSN: 0048-9697. DOI: <https://doi.org/10.1016/j.scitotenv.2020.138912>.
- [9] Mark Daniel G. de Luna et al. "Photocatalytic oxidation of acetaminophen using carbon self-doped titanium dioxide". In: *Sustainable Environment Research* (2016). DOI: <http://dx.doi.org/10.1016/j.serj.2016.02.001>.
- [10] Nabil Jallouli et al. "Photocatalytic degradation of paracetamol on TiO₂ nanoparticles and TiO₂/cellulosic fiber under UV and sunlight irradiation". In: *Arabian Journal of Chemistry* (2017). DOI: <https://doi.org/10.1016/j.arabjc.2014.03.014>.
- [11] Tusnela E Doll and Fritz H Frimmel. "Kinetic study of photocatalytic degradation of carbamazepine, clofibric acid, iomeprol and iopromide assisted by different TiO₂ materials determination of intermediates and reaction pathways". In: *Water Research* (2004). DOI: [10.1016/j.watres.2003.11.009](https://doi.org/10.1016/j.watres.2003.11.009).
- [12] Jong Kwon Im et al. "Carbamazepine Degradation by Photolysis and Titanium Dioxide Photocatalysis". In: *Water Environment Research* (2012). DOI: <https://doi.org/10.2175/106143012X13373550427273>.
- [13] Meijuan Chen and Wei Chu and Jingzi Beiyuan and Yu Huang. "Enhancement of UV assisted TiO₂ degradation of ibuprofen using Fenton hybrid process at circumneutral pH". In: *Chinese Journal of Catalysis* (2018). DOI: [https://doi.org/10.1016/S1872-2067\(18\)63070-0](https://doi.org/10.1016/S1872-2067(18)63070-0).
- [14] Juan Felipe Montoya et al. "Catalytic Role of Surface Oxygens in TiO₂ Photooxidation Reactions: Aqueous Benzene Photooxidation with TiO₂ under Anaerobic Conditions". In: *The Journal of Physical Chemistry Letters* (2012). DOI: <http://dx.doi.org/10.1021/jz400580b>.
- [15] Jenny Schneider et al. "Understanding TiO₂ Photocatalysis: Mechanisms and Materials". In: *Chemical Reviews* (2014). DOI: <http://dx.doi.org/10.1021/cr5001892>.
- [16] World Health Organization. "Benzene in Drinking Water". In: *Background document for development of WHO Guidelines for Drinking-water Quality* (2003).
- [17] World Health Organization. "Dichloromethane in Drinking Water". In: *Background document for development of WHO Guidelines for Drinking-water Quality* (2003).
- [18] John Borisch et al. "TiO₂ photocatalytic degradation of dichloromethane: An FTIR and solid-state NMR study". In: *Journal of Physical Chemistry B - J PHYS CHEM B* 108 (May 2004). DOI: [10.1021/jp037066b](https://doi.org/10.1021/jp037066b).

- [19] Michalis K. Arfanis et al. “Photocatalytic degradation of salicylic acid and caffeine emerging contaminants using titania nanotubes”. In: *Chemical Engineering Journal* (2017). DOI: <http://dx.doi.org/10.1016/j.cej.2016.06.098>.
- [20] I Buerge et al. “Caffeine, an anthropogenic marker for wastewater contamination of surface waters”. In: *Environmental Science and Technology* (2003). DOI: <https://doi.org/10.1021/es020125z>.
- [21] Thomas Bruton et al. “Fate of Caffeine in the ENvironment nd Ecotoxicological CONsiderationss”. In: *Contaminats of Emerging Concern in the Environment: Ecologicaland Human Health Considerations* (2010).
- [22] AC Vlot, DA Dempsey, and DF Klessig. “Salicylic Acid, a multifaceted hormone to combat disease”. In: *Annual Review of Phytopathology* (2009). DOI: [10.1146/annurev.phyto.050908.135202](https://doi.org/10.1146/annurev.phyto.050908.135202). PMID19400653.
- [23] Ngoc Han Tran, Martin Reinhard, and Karina Yew-Hoong Ginc. “Occurrence and fate of emerging contaminants in municipal wastewater treatment plants from different geographical regions-a review”. In: *Water Research* (2017). DOI: <https://doi.org/10.1016/j.watres.2017.12.029>.
- [24] Xiang-Dong Zhu et al. “Photocatalytic degradation of tetracycline in aqueous solution by nanosized TiO₂”. In: *Chemosphere* (2013). DOI: <http://dx.doi.org/10.1016/j.chemosphere.2013.02.066>.
- [25] G H Safari et al. “Photocatalytic degradation of tetracycline using nano-sized titanium dioxide in aqueous solution”. In: *International Journal of Environmental Science and Technology* (2015). DOI: <https://doi.org/10.1007/s13762-014-0706-9>.
- [26] Miguel Gonzalez-Pleiter et al. “Toxicity of five antibiotics and their mixtures towards photosynthetic aquatic organisms: Implications for environmental risk assessment”. In: *Water Research* (2013). DOI: <https://doi.org/10.1016/j.watres.2013.01.020>.
- [27] Marek Cuhra, Thomas Bøhn, and Petr Cuhra. “Glyphosate: Too Much of a Good Thing?” In: *Frontiers in Bioscience* 4 (Mar. 2016). DOI: [10.3389/fenvs.2016.00028](https://doi.org/10.3389/fenvs.2016.00028).
- [28] Sean X. Naughton and Alvin V. Terry. “Neurotoxicity in acute and repeated organophosphate exposure”. In: *Toxicology* 408 (2018), pp. 101–112. ISSN: 0300-483X. DOI: <https://doi.org/10.1016/j.tox.2018.08.011>.
- [29] Nancy Trautmann, Keith Porter, and Robert Wagenet. “Pesticides: Health Effects in Drinking Water”. In: (Dec. 1985). URL: <https://hdl.handle.net/1813/3335>.
- [30] José de Castro Lima et al. ““Modern agriculture” transfers many pesticides to watercourses: a case study of a representative rural catchment of southern Brazil”. In: *Environmental Science and Pollution Research* 27 (Apr. 2020). DOI: [10.1007/s11356-019-06550-8](https://doi.org/10.1007/s11356-019-06550-8).

- [31] Muhammad Syafrudin et al. “Pesticides in Drinking Water—A Review”. In: *International Journal of Environmental Research and Public Health* 18 (Jan. 2021), p. 468. DOI: [10.3390/ijerph18020468](https://doi.org/10.3390/ijerph18020468).
- [32] Peter Matthiesen and Peter E. Gibbs. “Critical appraisal of the evidence for tributyltin-mediated endocrine disruption in mollusks”. In: *Environmental Toxicology and Chemistry* (1998). DOI: <https://doi.org/10.1002/etc.5620170106>.
- [33] Bruce Petrie, Ruth Barden, and Barbara Kasprzyk-Hordern. “A review on emerging contaminants in wastewaters and the environment: Current knowledge, understudied areas and recommendations for future monitoring”. In: *Water Research* (2016). DOI: <http://dx.doi.org/10.1016/j.watres.2014.08.053>.
- [34] Sara Castiglioni et al. “Mass balance of emerging contaminants in the water cycle of a highly urbanized and industrialized area of Italy”. In: *Water Research* (2017). DOI: <https://doi.org/10.1016/j.watres.2017.12.047>.
- [35] Lei Yang et al. “Occurrence, distribution, and attenuation of pharmaceuticals and personal care products in the riverside groundwater of the Beiyun River of Beijing, China”. In: *Environmental Science and Pollution Research* (2017). DOI: <https://doi.org/10.1007/s11356-017-8999-0>.
- [36] Christos Comninellis et al. “Advanced oxidation processes for water treatment: advances and trends for R&D”. In: *Journal of chemical technology and biotechnology* (2008). DOI: <http://dx.doi.org/10.1185/03007999709113322>.
- [37] Paspaltsis I et al. “Titanium dioxide photocatalytic inactivation of prions”. In: *Journal General Virology* (2006). DOI: <https://doi.org/10.1099/vir.0.81746-0>.
- [38] Blanco-Galvez J, Fernandez-Ibagnes P, and Malato-Rodriguez S. “Solar photocatalytic detoxification and disinfection of water: recent overview”. In: *Journal of Solar Energy Eng* (2007). DOI: <https://doi.org/10.1115/1.2390948>.
- [39] Ulrike Diebold. “The surface science of titanium dioxide”. In: *Surface Science Reports* 48 (2003), pp. 53–229. DOI: [10.1016/S0167-5729\(02\)00100-0](https://doi.org/10.1016/S0167-5729(02)00100-0).
- [40] Shifu Chen and Yunzhang Liu. “Study on the photocatalytic degradation of glyphosate by TiO₂ photocatalyst”. In: *Chemosphere* 67 (Apr. 2007), pp. 1010–7. DOI: [10.1016/j.chemosphere.2006.10.054](https://doi.org/10.1016/j.chemosphere.2006.10.054).
- [41] Vincenzo Augugliaro et al. “Overview on oxidation mechanisms of organic compounds by TiO₂ in heterogeneous photocatalysis”. In: *Journal of Photochemistry and Photobiology C: Photochemistry Reviews* 13 (Sept. 2012), pp. 224–245. DOI: [10.1016/j.jphotochemrev.2012.04.003](https://doi.org/10.1016/j.jphotochemrev.2012.04.003).

- [42] M. Visa, Luminita Isac, and Anca Duta. “New fly ash TiO₂ composite for the sustainable treatment of wastewater with complex pollutants load”. In: *Applied Surface Science* 339 (June 2015). DOI: [10.1016/j.apsusc.2015.02.159](https://doi.org/10.1016/j.apsusc.2015.02.159).
- [43] Marta Cruz et al. “Bare TiO₂ and graphene oxide TiO₂ photocatalysts on the degradation of selected pesticides and influence of the water matrix”. In: *Applied Surface Science* 416 (Nov. 2015). DOI: [10.1016/j.apsusc.2015.09.268](https://doi.org/10.1016/j.apsusc.2015.09.268).
- [44] Khalid Umar et al. “Synthesis of visible light active doped TiO₂ for the degradation of organic pollutants—methylene blue and glyphosate”. In: *Journal of Analytical Science and Technology* 7 (Dec. 2016). DOI: [10.1186/s40543-016-0109-2](https://doi.org/10.1186/s40543-016-0109-2).
- [45] Ying Yang, Qinzuo Deng, and Yongli Zhang. “Comparative study of low-index 101-TiO₂, 001-TiO₂, 100-TiO₂ and high-index 201-TiO₂ on glyphosate adsorption and photo-degradation”. In: *Chemical Engineering Journal* 360 (Oct. 2018). DOI: [10.1016/j.cej.2018.10.219](https://doi.org/10.1016/j.cej.2018.10.219).
- [46] Goutham Rangarajan et al. “Present applications of titanium dioxide for the photocatalytic removal of pollutants from water: A review”. In: *Journal of Environmental Management* 270 (Sept. 2020). DOI: [10.1016/j.jenvman.2020.110906](https://doi.org/10.1016/j.jenvman.2020.110906).
- [47] R. Lindsay C. L. Pang and G. Thornton. “Structure of Clean and Adsorbate-Covered Single-Crystal Rutile TiO₂ Surfaces”. In: *Chem. Rev.* 113 (2013), pp. 3887–3948. DOI: [10.1021/cr300409r](https://doi.org/10.1021/cr300409r).
- [48] Kyriakos Bourikas, Christos Kordulis, and Alexis Lycourghiotis. “ChemInform Abstract: Titanium Dioxide (Anatase and Rutile): Surface Chemistry, Liquid-Solid Interface Chemistry, and Scientific Synthesis of Supported Catalysts”. In: *Chemical Reviews* 114 (Oct. 2014), 97549823. DOI: [10.1021/cr300230q](https://doi.org/10.1021/cr300230q).
- [49] Sofia A. Alves et al. “Synthesis of calcium-phosphorous doped TiO₂ nanotubes by anodization and reverse polarization: A promising strategy for an efficient biofunctional implant surface”. In: *Applied Surface Science* 399 (2017), pp. 682–701. ISSN: 0169-4332. DOI: <https://doi.org/10.1016/j.apsusc.2016.12.105>.
- [50] Radium Ikono et al. “Enhanced bone regeneration capability of chitosan sponge coated with TiO₂ nanoparticles”. In: *Biotechnology Reports* 24 (2019), e00350. ISSN: 2215-017X. DOI: <https://doi.org/10.1016/j.btre.2019.e00350>.
- [51] Tejasri Yarlagadda et al. “Recent Developments in the Field of Nanotechnology for Development of Medical Implants”. In: *Procedia Manufacturing* 30 (2019). Digital Manufacturing Transforming Industry Towards Sustainable Growth, pp. 544–551. ISSN: 2351-9789. DOI: <https://doi.org/10.1016/j.promfg.2019.02.077>.

- [52] Annapaola Migani and Lluís Blancafort. “Theoretical Studies of Photochemistry on TiO₂ Surfaces”. In: (Jan. 2017). DOI: [10.1016/B978-0-12-409547-2.13205-6](https://doi.org/10.1016/B978-0-12-409547-2.13205-6).
- [53] Igor Beinik et al. “Water Dissociation and Hydroxyl Ordering on Anatase TiO₂(001)–(1 × 4)”. In: *Phys. Rev. Lett.* 121 (20 Nov. 2018), p. 206003. DOI: [10.1103/PhysRevLett.121.206003](https://doi.org/10.1103/PhysRevLett.121.206003).
- [54] Yucheng Lan, Yalin Lu, and Zhifeng Ren. “Mini review on photocatalysis of titanium dioxide nanoparticles and their solar applications.” In: *Nano Energy* 2 (Jan. 2013), pp. 1031–1045. DOI: <https://doi.org/10.1016/j.nanoen.2013.04.002>.
- [55] Ke Dai et al. “Photocatalytic Degradation and Mineralization of Commercial Methamidophos in Aqueous Titania Suspension”. In: *Environment Science and Technology* (2008). DOI: <https://doi.org/10.1021/es702268p>.
- [56] Svetlana Ilina et al. “Investigations into titanium dioxide nanoparticle and pesticide interactions in aqueous environments”. In: *Environmental Science: Nano* 4 (2017), pp. 2555–2065. DOI: [10.1039/c7en00445a](https://doi.org/10.1039/c7en00445a).
- [57] Alaa A.F. Husain et al. “A review of transparent solar photovoltaic technologies”. In: *Renewable and Sustainable Energy Reviews* 94 (2018), pp. 779–791. ISSN: 1364-0321. DOI: <https://doi.org/10.1016/j.rser.2018.06.031>.
- [58] A.V. Emeline et al. “Chapter 1 - Heterogeneous Photocatalysis: Basic Approaches and Terminology”. In: *New and Future Developments in Catalysis*. Ed. by Steven L. Suib. Amsterdam: Elsevier, 2013, pp. 1–47. ISBN: 978-0-444-53872-7. DOI: <https://doi.org/10.1016/B978-0-444-53872-7.00001-7>.
- [59] Xiaolan Kang et al. “Titanium Dioxide: From Engineering to Applications”. In: *Catalysts* 9.2 (2019). ISSN: 2073-4344. DOI: [10.3390/catal9020191](https://doi.org/10.3390/catal9020191).
- [60] Mohammad Muneer and Colin Boxall. “Photocatalyzed degradation of a pesticide derivative glyphosate in aqueous suspensions of titanium dioxide”. In: *International Journal of Photoenergy* 2008 (2008), p. 197346. DOI: <https://doi.org/10.1155/2008/197346>.
- [61] Svetlana Ilina et al. “Investigations into titanium dioxide nanoparticle and pesticide interactions in aqueous environments”. In: *Environ. Sci.: Nano* 4 (Aug. 2017). DOI: [10.1039/C7EN00445A](https://doi.org/10.1039/C7EN00445A).
- [62] Joan Borràs-Ferrís et al. “TiO₂ Nanostructures for Photoelectrocatalytic Degradation of Acetaminophen”. In: *Nanomaterials* 9 (Apr. 2019), p. 583. DOI: [10.3390/nano9040583](https://doi.org/10.3390/nano9040583).
- [63] J.W. Deneer. “Toxicity of mixtures of pesticides in aquatic systems”. In: *Pest Manag. Sci* (2000). DOI: [https://doi.org/10.1002/\(SICI\)1526-4998\(200006\)56:6<516::AID-PS163>3.0.CO;2-0](https://doi.org/10.1002/(SICI)1526-4998(200006)56:6<516::AID-PS163>3.0.CO;2-0).

- [64] M Junghans et al. “Application and validation of approaches for the predictive hazard assessment of realistic pesticide mixtures”. In: *Aquatic Toxicology* (2006). DOI: <https://doi.org/10.1016/j.aquatox.2005.10.001>.
- [65] S I Rodney, R S Teed, and D R J Moore. “Estimating the Toxicity of Pesticide Mixtures to Aquatic Organisms : A Review”. In: *Human Ecological Risk Assessment Int Journal* (2013). DOI: <https://doi.org/10.1080/10807039.2012.723180>.
- [66] Michael Feig et al. “Challenges and opportunities in connecting simulations with experiments via molecular dynamics of cellular environments”. In: *Journal of Physics: Conference Series* 1036 (June 2018), p. 012010. DOI: [10.1088/1742-6596/1036/1/012010](https://doi.org/10.1088/1742-6596/1036/1/012010).
- [67] Annapaola Migani and Lluís Blancafort. “What Controls Photocatalytic Water Oxidation on Rutile TiO₂(110) under Ultra-High-Vacuum Conditions?” In: *Journal of the American Chemical Society* 139.34 (2017). PMID: 28768408, pp. 11845–11856. DOI: [10.1021/jacs.7b05121](https://doi.org/10.1021/jacs.7b05121).
- [68] Thorben Petersen and Thorsten Klüner. “Water Adsorption on Ideal Anatase-TiO₂(101) – An Embedded Cluster Model for Accurate Adsorption Energetics and Excited State Properties”. In: *Zeitschrift für Physikalische Chemie* 234.5 (2020), pp. 813–834. DOI: [doi:10.1515/zpch-2019-1425](https://doi.org/10.1515/zpch-2019-1425).
- [69] S. Koeppen and W. Langel. “Simulation of the interface of (1 0 0) rutile with aqueous ionic solution”. In: *Surface Science* (2006). DOI: [http://dx.doi.org/10.1016/j.susc.2006.02.042](https://dx.doi.org/10.1016/j.susc.2006.02.042).
- [70] Carla E. Giacomelli, Marcelo J. Avena, and Carlos P. De Pauli. “Aspartic acid adsorption onto TiO₂ particles surface. Experimental data and model calculations”. In: *Langmuir* 11.9 (1995), pp. 3483–3490. DOI: [10.1021/la00009a034](https://doi.org/10.1021/la00009a034).
- [71] George Panagiotou et al. “Mapping the surface (hydr)oxo-groups of titanium oxide and its interface with an aqueous solution: The state of the art and a new approach”. In: *Advances in colloid and interface science* 142 (May 2008), pp. 20–42. DOI: [10.1016/j.cis.2008.04.003](https://doi.org/10.1016/j.cis.2008.04.003).
- [72] A. Volkova et al. “Electrosurface characteristics of titanium dioxide in solutions of simple electrolytes: I. Effect of nature of counterions on adsorption and electrokinetic parameters of TiO₂”. In: *Colloid Journal - COLLOID J-ENGL TR* 72 (Dec. 2010), pp. 743–748. DOI: [10.1134/S1061933X10060037](https://doi.org/10.1134/S1061933X10060037).
- [73] Jenny Holmberg et al. “Surface charge and interfacial potential of titanium dioxide nanoparticles: Experimental and theoretical investigations”. In: *Journal of colloid and interface science* 407 (June 2013). DOI: [10.1016/j.jcis.2013.06.015](https://doi.org/10.1016/j.jcis.2013.06.015).
- [74] Hongbo Shi et al. “Titanium dioxide nanoparticles: A review of current toxicological data”. In: *Particle and fibre toxicology* 10 (Apr. 2013), p. 15. DOI: [10.1186/1743-8977-10-15](https://doi.org/10.1186/1743-8977-10-15).

- [75] Daniele Selli et al. “Water Multilayers on TiO₂ (101) Anatase Surface: Assessment of a DFTB-Based Method”. In: *Journal of Chemical Theory and Computation* 13 (July 2017). DOI: [10.1021/acs.jctc.7b00479](https://doi.org/10.1021/acs.jctc.7b00479).
- [76] Christie Sayes et al. “Correlating Nanoscale Titania Structure with Toxicity: A Cytotoxicity and Inflammatory Response Study with Human Dermal Fibroblasts and Human Lung Epithelial Cells”. In: *Toxicological sciences : an official journal of the Society of Toxicology* 92 (Aug. 2006), pp. 174–85. DOI: [10.1093/toxsci/kfj197](https://doi.org/10.1093/toxsci/kfj197).
- [77] David Warheit et al. “Pulmonary toxicity study in rats with three forms of ultrafine-TiO”. In: *Toxicology* 230 (Feb. 2007), pp. 90–104. DOI: [10.1016/j.tox.2006.11.002](https://doi.org/10.1016/j.tox.2006.11.002).
- [78] Chengbin Xue et al. “Nano Titanium Dioxide Induces the Generation of ROS and Potential Damage in HaCaT Cells Under UVA Irradiation”. In: *Journal of nanoscience and nanotechnology* 10 (Dec. 2010), pp. 8500–7. DOI: [10.1166/jnn.2010.2682](https://doi.org/10.1166/jnn.2010.2682).
- [79] Jana Petković et al. “DNA damage and alterations in expression of DNA damage responsive genes induced by TiO₂ nanoparticles in human hepatoma HepG2 cells”. In: *Nanotoxicology* 5 (Nov. 2010), pp. 341–53. DOI: [10.3109/17435390.2010.507316](https://doi.org/10.3109/17435390.2010.507316).
- [80] Helgi Ingólfsson et al. “The power of coarse graining in biomolecular simulations”. In: *Wiley Interdisciplinary Reviews: Computational Molecular Science* 4 (May 2014). DOI: [10.1002/wcms.1169](https://doi.org/10.1002/wcms.1169).
- [81] Raymond Kapral and Giovanni Ciccotti. “Molecular dynamics”. In: Dec. 2005, pp. 425–441. ISBN: 9780444517197. DOI: [10.1016/B978-044451719-7/50059-7](https://doi.org/10.1016/B978-044451719-7/50059-7).
- [82] Pekka Koskinen and Ville Mäkinen. “Density-functional tight-binding for beginners”. In: *Computational Materials Science* 47 (Oct. 2009). DOI: [10.1016/j.commatsci.2009.07.013](https://doi.org/10.1016/j.commatsci.2009.07.013).
- [83] M. Elstner et al. “Self-consistent-charge density-functional tight-binding method for simulations of complex materials properties”. In: *Phys. Rev. B* 58 (11 Sept. 1998), pp. 7260–7268. DOI: [10.1103/PhysRevB.58.7260](https://doi.org/10.1103/PhysRevB.58.7260).
- [84] B. Hourahine et al. “DFTB+, a software package for efficient approximate density functional theory based atomistic simulations”. In: *The Journal of Chemical Physics* 152.12 (2020), p. 124101. DOI: [10.1063/1.5143190](https://doi.org/10.1063/1.5143190).
- [85] Kyle Baseden and Jesse Tye. “Introduction to Density Functional Theory: Calculations by Hand on the Helium Atom”. In: *Journal of Chemical Education* 91 (Dec. 2014), pp. 2116–2123. DOI: [10.1021/ed5004788](https://doi.org/10.1021/ed5004788).
- [86] M. Born and W. Heisenberg. “Zur Quantentheorie der Molekeln”. In: *Annalen der Physik* 379 (Mar. 1927), pp. 1–31. DOI: [10.1002/andp.19243790902](https://doi.org/10.1002/andp.19243790902).
- [87] Francisco Fernández. *The Born-Oppenheimer approximation*. Mar. 2019. DOI: [10.13140/RG.2.2.21650.91840](https://doi.org/10.13140/RG.2.2.21650.91840).

- [88] D.R. Bowler and T Miyazaki. “O(N) methods in electronic structure calculations”. In: *Reports on progress in physics. Physical Society (Great Britain)* 75 (Mar. 2012), p. 036503. DOI: [10.1088/0034-4885/75/3/036503](https://doi.org/10.1088/0034-4885/75/3/036503).
- [89] P. Hohenberg and W. Kohn. “Inhomogeneous Electron Gas”. In: *Phys. Rev.* 136 (3B Nov. 1964), B864–B871. DOI: [10.1103/PhysRev.136.B864](https://doi.org/10.1103/PhysRev.136.B864).
- [90] W. Kohn and L. J. Sham. “Self-Consistent Equations Including Exchange and Correlation Effects”. In: *Phys. Rev.* 140 (4A Nov. 1965), A1133–A1138. DOI: [10.1103/PhysRev.140.A1133](https://doi.org/10.1103/PhysRev.140.A1133).
- [91] D. R. Hartree. “The Wave Mechanics of an Atom with a Non-Coulomb Central Field. Part II. Some Results and Discussion”. In: *Mathematical Proceedings of the Cambridge Philosophical Society* 24.1 (1928), pp. 111–132. DOI: [10.1017/S0305004100011920](https://doi.org/10.1017/S0305004100011920).
- [92] J. C. Slater. “The Self Consistent Field and the Structure of Atoms”. In: *Phys. Rev.* 32 (3 Sept. 1928), pp. 339–348. DOI: [10.1103/PhysRev.32.339](https://doi.org/10.1103/PhysRev.32.339).
- [93] V. Fock. “Näherungsmethode zur Lösung des quantenmechanischen Mehrkörperproblems”. In: *Zeitschrift für Physik* 61.1-2 (Jan. 1930), pp. 126–148. DOI: [10.1007/BF01340294](https://doi.org/10.1007/BF01340294).
- [94] V. Brázdová and D.R. Bowler. *Atomistic Computer Simulations: A Practical Guide*. Wiley. ISBN: 9783527671830.
- [95] Loup Verlet. “Computer "Experiments" on Classical Fluids. I. Thermodynamical Properties of Lennard-Jones Molecules”. In: *Phys. Rev.* 159 (1 July 1967), pp. 98–103. DOI: [10.1103/PhysRev.159.98](https://doi.org/10.1103/PhysRev.159.98).
- [96] E. J. W. Verwey. “Theory of the Stability of Lyophobic Colloids.” In: *The Journal of Physical and Colloid Chemistry* 51.3 (1947), pp. 631–636. DOI: [10.1021/j150453a001](https://doi.org/10.1021/j150453a001).
- [97] B. Derjaguin and L. Landau. “Theory of the stability of strongly charged lyophobic sols and of the adhesion of strongly charged particles in solutions of electrolytes”. In: *Progress In Surface Science* 43.1 (Aug. 1993), pp. 30–59. DOI: [10.1016/0079-6816\(93\)90013-L](https://doi.org/10.1016/0079-6816(93)90013-L).
- [98] Alexey Onufriev, Donald Bashford, and David Case. “Modification of the Generalized Born Model Suitable for Macromolecules”. In: *J. Phys. Chem. B* 104 (Apr. 2000), pp. 3712–3720. DOI: [10.1021/jp994072s](https://doi.org/10.1021/jp994072s).
- [99] Alexey Onufriev, Donald Bashford, and David Case. “Exploring Protein Native States and Large-Scale Conformational Changes with a Modified Generalized Born Model”. In: *Proteins* 55 (May 2004), pp. 383–94. DOI: [10.1002/prot.20033](https://doi.org/10.1002/prot.20033).
- [100] H. Berendsen et al. “Interaction Models for Water in Relation to Protein Hydration”. In: 1981. DOI: https://doi.org/10.1007/978-94-015-7658-1_21.

- [101] Michael W. Mahoney and W. L. Jorgensen. “A five-site model for liquid water and the reproduction of the density anomaly by rigid, nonpolarizable potential functions”. In: *Journal of Chemical Physics* 112 (2000), pp. 8910–8922. DOI: <https://doi.org/10.1063/1.481505>.
- [102] Saeed Izadi, Ramu Anandakrishnan, and Alexey Onufriev. “Building Water Models: A Different Approach”. In: *Journal of Physical Chemistry Letters* 5 (Oct. 2014), pp. 3863–3871. DOI: [10.1021/jz501780a](https://doi.org/10.1021/jz501780a).
- [103] Frank H. Stillinger and Aneesur Rahman. “Improved simulation of liquid water by molecular dynamics”. In: *The Journal of Chemical Physics* 60.4 (1974), pp. 1545–1557. DOI: [10.1063/1.1681229](https://doi.org/10.1063/1.1681229).
- [104] E. Duboué-Dijon et al. “A practical guide to biologically relevant molecular simulations with charge scaling for electronic polarization”. In: *The Journal of Chemical Physics* 153.5 (2020), p. 050901. DOI: [10.1063/5.0017775](https://doi.org/10.1063/5.0017775).
- [105] K.F Hayes and J.O Leckie. “Modeling ionic strength effects on cation adsorption at hydrous oxide/solution interfaces”. In: *Journal of Colloid and Interface Science* 115.2 (1987), pp. 564–572. ISSN: 0021-9797. DOI: [https://doi.org/10.1016/0021-9797\(87\)90078-6](https://doi.org/10.1016/0021-9797(87)90078-6).
- [106] Ian C. Bourg and Garrison Sposito. “Molecular dynamics simulations of the electrical double layer on smectite surfaces contacting concentrated mixed electrolyte (NaCl–CaCl₂) solutions”. In: *Journal of Colloid and Interface Science* 360.2 (2011), pp. 701–715. ISSN: 0021-9797. DOI: <https://doi.org/10.1016/j.jcis.2011.04.063>.
- [107] P. P. Ewald. “Die Berechnung optischer und elektrostatischer Gitterpotentiale”. In: *Annalen der Physik* 369.3 (Jan. 1921), pp. 253–287. DOI: [10.1002/andp.19213690304](https://doi.org/10.1002/andp.19213690304).
- [108] Tom Darden et al. “New tricks for modelers from the crystallography toolkit: The particle mesh Ewald algorithm and its use in nucleic acid simulations”. In: *Structure (London, England : 1993)* 7 (Apr. 1999), R55–60. DOI: [10.1016/S0969-2126\(99\)80033-1](https://doi.org/10.1016/S0969-2126(99)80033-1).
- [109] Giovanni Bussi, Davide Donadio, and Michele Parrinello. “Canonical Sampling Through Velocity Rescaling”. In: *The Journal of chemical physics* 126 (Feb. 2007), p. 014101. DOI: [10.1063/1.2408420](https://doi.org/10.1063/1.2408420).
- [110] Herman Berendsen et al. “Molecular-Dynamics with Coupling to An External Bath”. In: *The Journal of Chemical Physics* 81 (Oct. 1984), p. 3684. DOI: [10.1063/1.448118](https://doi.org/10.1063/1.448118).
- [111] Shūichi Nosé. “A molecular dynamics method for simulations in the canonical ensemble”. In: *Molecular Physics* 52.2 (1984), pp. 255–268. DOI: [10.1080/00268978400101201](https://doi.org/10.1080/00268978400101201).
- [112] Hans C. Andersen. “Molecular dynamics simulations at constant pressure and/or temperature”. In: *The Journal of Chemical Physics* 72.4 (1980), pp. 2384–2393. DOI: [10.1063/1.439486](https://doi.org/10.1063/1.439486).

- [113] Jonas Moellmann et al. “A DFT-D study of structural and energetic properties of TiO₂ modifications”. In: *Journal of Physics: Condensed Matter* 24.42 (Oct. 2012), p. 424206. DOI: [10.1088/0953-8984/24/42/424206](https://doi.org/10.1088/0953-8984/24/42/424206).
- [114] Matteo Monai, Tiziano Montini, and Paolo Fornasiero. “Brookite: Nothing New under the Sun?” In: *Catalysts* 7.10 (2017). DOI: [10.3390/catal7100304](https://doi.org/10.3390/catal7100304).
- [115] Dorian Hanaor and Charles Sorrell. “Review of the Anatase to Rutile Phase Transformation”. In: *Journal of Materials Science* 46 (Feb. 2011), pp. 855–874. DOI: [10.1007/s10853-010-5113-0](https://doi.org/10.1007/s10853-010-5113-0).
- [116] Tim Luttrell et al. “Why is Anatase a Better Photocatalyst Than Rutile? - Model Studies on Epitaxial TiO₂ Films”. In: *Scientific reports* 4 (Feb. 2014), p. 4043. DOI: [10.1038/srep04043](https://doi.org/10.1038/srep04043).
- [117] H. Perron et al. “Optimisation of accurate rutile TiO₂ (110), (100), (101) and (001) surface models from periodic DFT calculation”. In: *Theor. Chem. Acc* 117 (2007), pp. 565–574. DOI: [10.1103/PhysRevLett.77.3865](https://doi.org/10.1103/PhysRevLett.77.3865).
- [118] A Kiejna, T Pabisiak, and S W Gao. “The energetics and structure of rutile TiO₂(110)”. In: *Journal of Physics: Condensed Matter* 18.17 (Apr. 2006), pp. 4207–4217. DOI: [10.1088/0953-8984/18/17/009](https://doi.org/10.1088/0953-8984/18/17/009).
- [119] Frédéric Labat, Philippe Baranek, and Carlo Adamo. “Structural and Electronic Properties of Selected Rutile and Anatase TiO₂ Surfaces: An ab Initio Investigation”. In: *Journal of Chemical Theory and Computation* 4.2 (2008), pp. 341–352. DOI: [10.1021/ct700221w](https://doi.org/10.1021/ct700221w).
- [120] Daiping Song et al. “Molecular Dynamics Study on Surface Structure and Surface Energy of Rutile TiO₂ (110)”. In: *Applied Surface Science* 255 (Mar. 2009), pp. 5702–5708. DOI: [10.1016/j.apsusc.2008.12.062](https://doi.org/10.1016/j.apsusc.2008.12.062).
- [121] F. Allegretti et al. “Adsorption Bond Length for H₂O on TiO₂(110): A Key Parameter for Theoretical Understanding”. In: *Phys. Rev. Lett.* 95 (22 Nov. 2005), p. 226104. DOI: [10.1103/PhysRevLett.95.226104](https://doi.org/10.1103/PhysRevLett.95.226104).
- [122] Zong-Yan Zhao. “Single Water Molecule Adsorption and Decomposition on the Low-Index Stoichiometric Rutile TiO₂ Surfaces”. In: *The Journal of Physical Chemistry C* 118.8 (2014), pp. 4287–4295. DOI: [10.1021/jp500177n](https://doi.org/10.1021/jp500177n).
- [123] Giulia Serrano et al. “Molecular Ordering at the Interface Between Liquid Water and Rutile TiO₂(110)”. In: *Advanced Materials Interfaces* 2.17 (2015), p. 1500246. DOI: <https://doi.org/10.1002/admi.201500246>.
- [124] Fabrizio Gala, L. Agosta, and Giuseppe Zollo. “Water Kinetics and Clustering on the (101) TiO₂ Anatase Surface”. In: *The Journal of Physical Chemistry C* 120.1 (2016), pp. 450–456. DOI: [10.1021/acs.jpcc.5b10934](https://doi.org/10.1021/acs.jpcc.5b10934).

- [125] Enrico Berardo and Martijn A. Zwijnenburg. “Modeling the Water Splitting Activity of a TiO₂ Rutile Nanoparticle”. In: *The Journal of Physical Chemistry C* 119.24 (2015), pp. 13384–13393. DOI: [10.1021/acs.jpcc.5b01512](https://doi.org/10.1021/acs.jpcc.5b01512).
- [126] Ye-Fei Li and Annabella Selloni. “Pathway of Photocatalytic Oxygen Evolution on Aqueous TiO₂ Anatase and Insights into the Different Activities of Anatase and Rutile”. In: *ACS Catalysis* 6.7 (2016), pp. 4769–4774. DOI: [10.1021/acscatal.6b01138](https://doi.org/10.1021/acscatal.6b01138).
- [127] Lorenzo Agosta, Erik G. Brandt, and Alexander P. Lyubartsev. “Diffusion and reaction pathways of water near fully hydrated TiO₂ surfaces from ab initio molecular dynamics”. In: *The Journal of Chemical Physics* 147.2 (2017), p. 024704. DOI: [10.1063/1.4991381](https://doi.org/10.1063/1.4991381).
- [128] S. Köppen and W. Langel. “Simulation of the interface of (100) rutile with aqueous ionic solution”. In: *Surface Science* 600.10 (May 2006), pp. 2040–2050. DOI: [10.1016/j.susc.2006.02.042](https://doi.org/10.1016/j.susc.2006.02.042).
- [129] W. Friedrichs et al. “Adsorption of Collagen Nanofibrils on Rough TiO₂: A Molecular Dynamics Study”. In: *Adv. Eng. Mat.* 13.10 (2011), pp. 335–342. DOI: [10.1002/adem.201080123](https://doi.org/10.1002/adem.201080123).
- [130] W. Friedrichs, W. Langel, and S. Köppen. “Adsorption of Collagen Nanofibrils on Rough TiO₂: A Molecular Dynamics Study”. In: *Surf. Sci.* 617 (2013), pp. 42–52. DOI: [10.1016/j.susc.2013.07.010](https://doi.org/10.1016/j.susc.2013.07.010).
- [131] Rentao Mu et al. “Structural motifs of water on metal oxide surfaces”. In: *Chem. Soc. Rev.* 46 (7 2017), pp. 1785–1806. DOI: [10.1039/C6CS00864J](https://doi.org/10.1039/C6CS00864J).
- [132] Danilo González et al. “Water Adsorption on MO₂ (M = Ti, Ru, and Ir) Surfaces. Importance of Octahedral Distortion and Cooperative Effects”. In: *ACS Omega* 4.2 (2019), pp. 2989–2999. DOI: [10.1021/acsomega.8b03350](https://doi.org/10.1021/acsomega.8b03350).
- [133] Marie-Pierre Gageot, Michiel Sprik, and Marialore Sulpizi. “Oxide/water interfaces: How the surface chemistry modifies interfacial water properties”. In: *Journal of physics. Condensed matter : an Institute of Physics journal* 24 (Mar. 2012), p. 124106. DOI: [10.1088/0953-8984/24/12/124106](https://doi.org/10.1088/0953-8984/24/12/124106).
- [134] Thorben Petersen and Thorsten Klüner. “Photodesorption of H₂O from Anatase-TiO₂ (101) - A Combined Quantum Chemical and Quantum Dynamical Study”. In: *The Journal of Physical Chemistry C* XXXX (Apr. 2020). DOI: [10.1021/acs.jpcc.0c01926](https://doi.org/10.1021/acs.jpcc.0c01926).
- [135] Nitin Kumar et al. “Hydrogen Bonds and Vibrations of Water on (110) Rutile”. In: *The Journal of Physical Chemistry C* 113.31 (2009), pp. 13732–13740. DOI: [10.1021/jp901665e](https://doi.org/10.1021/jp901665e).
- [136] Li-Min Liu et al. “Structure and dynamics of liquid water on rutile TiO₂(110)”. In: *Phys. Rev. B* 82 (16 Oct. 2010), p. 161415. DOI: [10.1103/PhysRevB.82.161415](https://doi.org/10.1103/PhysRevB.82.161415).

- [137] Julian Schneider and Lucio Colombi Ciacchi. “Specific Material Recognition by Small Peptides Mediated by the Interfacial Solvent Structure”. In: *Journal of the American Chemical Society* 134.4 (2012), pp. 2407–2413. DOI: [10.1021/ja210744g](https://doi.org/10.1021/ja210744g).
- [138] Ting Zheng et al. “A DFT study of water adsorption on rutile TiO₂ (110) surface: The effects of surface steps”. In: *The Journal of Chemical Physics* 145.4 (2016), p. 044702. DOI: [10.1063/1.4958969](https://doi.org/10.1063/1.4958969).
- [139] Hideyuki Kamisaka and Koichi Yamashita. “The surface stress of the (110) and (100) surfaces of rutile and the effect of water adsorbents”. In: *Surface Science* 601.21 (2007), pp. 4824–4836. ISSN: 0039-6028. DOI: <https://doi.org/10.1016/j.susc.2007.07.033>.
- [140] Leonard A. Harris and Andrew A. Quong. “Molecular Chemisorption as the Theoretically Preferred Pathway for Water Adsorption on Ideal Rutile TiO₂(110)”. In: *Phys. Rev. Lett.* 93 (8 Aug. 2004), p. 086105. DOI: [10.1103/PhysRevLett.93.086105](https://doi.org/10.1103/PhysRevLett.93.086105).
- [141] J.B. Cohen P. Zschack and Y.W. Chung. “Structure of the TiO₂ (100) 1 X 3 surface determined by glancing angle X-ray diffraction and low energy electron diffraction”. In: *Surface Science* 262 (1992), pp. 395–408. DOI: [10.1126/science.aat6752](https://doi.org/10.1126/science.aat6752).
- [142] Philip J.D Lindan and N.M Harrison. “The structure of the reduced rutile TiO₂(100) 1×3 reconstruction”. In: *Surface Science* 479.1 (2001), pp. L375–L381. ISSN: 0039-6028. DOI: [https://doi.org/10.1016/S0039-6028\(01\)01005-6](https://doi.org/10.1016/S0039-6028(01)01005-6).
- [143] Nobuhiro Sawai, Kohei Yamasue, and Yasuo Cho. “Atomic Scale Imaging of TiO₂ (100) Reconstructed Surfaces by Noncontact Scanning Nonlinear Dielectric Microscopy”. In: *Japanese Journal of Applied Physics* 51 (Nov. 2012), p. 121801. DOI: [10.1143/jjap.51.121801](https://doi.org/10.1143/jjap.51.121801).
- [144] R. H. Tait and R. V. Kasowski. “Ultraviolet photoemission and low-energy-electron diffraction studies of TiO₂ (rutile) (001) and (110) surfaces”. In: *Phys. Rev. B* 20 (12 Dec. 1979), pp. 5178–5191. DOI: [10.1103/PhysRevB.20.5178](https://doi.org/10.1103/PhysRevB.20.5178).
- [145] L.E. Firment. “Thermal faceting of the rutile TiO₂(001) surface”. In: *Surface Science* 116.2 (1982), pp. 205–216. ISSN: 0039-6028. DOI: [https://doi.org/10.1016/0039-6028\(82\)90428-9](https://doi.org/10.1016/0039-6028(82)90428-9).
- [146] Holger Nörenberg, F. Dinelli, and G.A.D. Briggs. “Network-like (72×2)R45° surface reconstruction on rutile TiO₂(001) by non-equilibrium self-organization”. In: *Surface Science* 436.1 (1999), pp. L635–L640. DOI: [https://doi.org/10.1016/S0039-6028\(99\)00718-9](https://doi.org/10.1016/S0039-6028(99)00718-9).
- [147] Ken-ichi Fukui, Ryugo Tero, and Yasuhiro Iwasawa. “Atom-Resolved Structures of TiO₂(001) Surface by Scanning Tunneling Microscopy”. In: *Japanese Journal of Applied Physics* 40 (June 2001), pp. 4331–4333. DOI: [10.1143/JJAP.40.4331](https://doi.org/10.1143/JJAP.40.4331).

- [148] Ryugo Tero, Ken Fukui, and Yasuhiro Iwasawa. “Atom-Resolved Surface Structures and Molecular Adsorption on $\text{TiO}_2(001)$ Investigated by Scanning Tunneling Microscopy”. In: *The Journal of Physical Chemistry B* 107.14 (2003), pp. 3207–3214. DOI: [10.1021/jp0222090](https://doi.org/10.1021/jp0222090).
- [149] Y. Wang et al. “Atomically flat reconstructed rutile $\text{TiO}_2(001)$ surfaces for oxide film growth”. In: *Applied Physics Letters* 108.9 (2016), p. 091604. DOI: [10.1063/1.4942967](https://doi.org/10.1063/1.4942967).
- [150] Luc Museur et al. “Surface structuring of rutile TiO_2 (100) and (001) single crystals with femtosecond pulsed laser irradiation”. In: *J. Opt. Soc. Am. B* 35 (Oct. 2018), pp. 2600–2607. DOI: [10.1364/JOSAB.35.002600](https://doi.org/10.1364/JOSAB.35.002600).
- [151] Yasuro Ikuma et al. “Surface X-ray diffraction study of annealed single-crystal rutile TiO_2 (001) surface”. In: *Ionics* 25 (Sept. 2018), pp. 1879–1886. DOI: [10.1007/s11581-018-2692-2](https://doi.org/10.1007/s11581-018-2692-2).
- [152] Longxia () Wu et al. “Surface chemistry and photochemistry of small molecules on rutile $\text{TiO}_2(001)$ and $\text{TiO}_2(011)-(2 \times 1)$ surfaces: The crucial roles of defects”. In: *The Journal of Chemical Physics* 152.4 (2020), p. 044702. DOI: [10.1063/1.5135945](https://doi.org/10.1063/1.5135945).
- [153] Longxia Wu, Cong Fu, and Weixin Huang. “Surface chemistry of TiO_2 connecting thermal catalysis and photocatalysis”. In: *Physical Chemistry Chemical Physics* 22 (Apr. 2020). DOI: [10.1039/C9CP07001J](https://doi.org/10.1039/C9CP07001J).
- [154] E. Kaxiras. *Atomic and Electronic Structure of Solids*. Cambridge University Press, 2003. ISBN: 9780521523394.
- [155] C. David Sherrill and Henry F. Schaefer. “The Configuration Interaction Method: Advances in Highly Correlated Approaches”. In: ed. by Per-Olov Löwdin et al. Vol. 34. *Advances in Quantum Chemistry*. Academic Press, 1999, pp. 143–269. DOI: [https://doi.org/10.1016/S0065-3276\(08\)60532-8](https://doi.org/10.1016/S0065-3276(08)60532-8).
- [156] A.W. Leissa. “The historical bases of the Rayleigh and Ritz methods”. In: *Journal of Sound and Vibration* 287.4 (2005), pp. 961–978. ISSN: 0022-460X. DOI: <https://doi.org/10.1016/j.jsv.2004.12.021>.
- [157] F. Jensen. *Introduction to Computational Chemistry*. Wiley, 2006. ISBN: 9780470011867.
- [158] S. H. Vosko, L. Wilk, and M. Nusair. “Accurate spin-dependent electron liquid correlation energies for local spin density calculations: a critical analysis”. In: *Canadian Journal of Physics* 59 (Aug. 1980), p. 1200. DOI: [10.1139/p80-159](https://doi.org/10.1139/p80-159).
- [159] J. P. Perdew and Alex Zunger. “Self-interaction correction to density-functional approximations for many-electron systems”. In: 23.10 (May 1981), pp. 5048–5079. DOI: [10.1103/PhysRevB.23.5048](https://doi.org/10.1103/PhysRevB.23.5048).
- [160] Lee A. Cole and J. P. Perdew. “Calculated electron affinities of the elements”. In: 25.3 (Mar. 1982), pp. 1265–1271. DOI: [10.1103/PhysRevA.25.1265](https://doi.org/10.1103/PhysRevA.25.1265).

- [161] John P. Perdew and Yue Wang. “Accurate and simple analytic representation of the electron-gas correlation energy”. In: 45.23 (June 1992), pp. 13244–13249. DOI: [10.1103/PhysRevB.45.13244](https://doi.org/10.1103/PhysRevB.45.13244).
- [162] John P. Perdew, Kieron Burke, and Matthias Ernzerhof. “Generalized Gradient Approximation Made Simple”. In: *Phys. Rev. Lett.* 77 (18 Oct. 1996), pp. 3865–3868. DOI: [10.1103/PhysRevLett.77.3865](https://doi.org/10.1103/PhysRevLett.77.3865).
- [163] John P. Perdew. “Density functional theory and the band gap problem”. In: *International Journal of Quantum Chemistry* 28.S19 (1985), pp. 497–523. DOI: [10.1002/qua.560280846](https://doi.org/10.1002/qua.560280846).
- [164] K. Kim and K. D. Jordan. “Comparison of Density Functional and MP2 Calculations on the Water Monomer and Dimer”. In: *The Journal of Physical Chemistry* 98.40 (1994), pp. 10089–10094. DOI: [10.1021/j100091a024](https://doi.org/10.1021/j100091a024).
- [165] P. J. Stephens et al. “Ab Initio Calculation of Vibrational Absorption and Circular Dichroism Spectra Using Density Functional Force Fields”. In: *The Journal of Physical Chemistry* 98.45 (1994), pp. 11623–11627. DOI: [10.1021/j100096a001](https://doi.org/10.1021/j100096a001).
- [166] Jochen Heyd, Gustavo E. Scuseria, and Matthias Ernzerhof. “Hybrid functionals based on a screened Coulomb potential”. In: 118.18 (May 2003), pp. 8207–8215. DOI: [10.1063/1.1564060](https://doi.org/10.1063/1.1564060).
- [167] John P. Perdew, Matthias Ernzerhof, and Kieron Burke. “Rationale for mixing exact exchange with density functional approximations”. In: *The Journal of Chemical Physics* 105.22 (1996), pp. 9982–9985. DOI: [10.1063/1.472933](https://doi.org/10.1063/1.472933).
- [168] Carlo Adamo and Vincenzo Barone. “Toward reliable density functional methods without adjustable parameters: The PBE0 model”. In: 110.13 (Apr. 1999), pp. 6158–6170. DOI: [10.1063/1.478522](https://doi.org/10.1063/1.478522).
- [169] Robert B. Leighton. “The Vibrational Spectrum and Specific Heat of a Face-Centered Cubic Crystal”. In: *Reviews of Modern Physics* 20.1 (Jan. 1948), pp. 165–174. DOI: [10.1103/RevModPhys.20.165](https://doi.org/10.1103/RevModPhys.20.165).
- [170] A.N. W et al. *Solid State Physics*. HRW international editions. Holt, Rinehart and Winston, 1976. ISBN: 9780030839931.
- [171] P. E. Blöchl. “Projector augmented-wave method”. In: *Phys. Rev. B* 50 (24 Dec. 1994), pp. 17953–17979. DOI: [10.1103/PhysRevB.50.17953](https://doi.org/10.1103/PhysRevB.50.17953).
- [172] Stefan Grimme et al. “A consistent and accurate ab initio parametrization of density functional dispersion correction (DFT-D) for the 94 elements H-Pu”. In: *The Journal of Chemical Physics* 132 (). DOI: [10.1063/1.3382344](https://doi.org/10.1063/1.3382344).
- [173] Stefan Grimme, Stephan Ehrlich, and Lars Goerigk. “Effect of the damping function in dispersion corrected density functional theory”. In: *Journal of Computational Chemistry* 32.7 (2011), pp. 1456–1465. DOI: <https://doi.org/10.1002/jcc.21759>. eprint: <https://onlinelibrary.wiley.com/doi/pdf/10.1002/jcc.21759>.

- [174] Alexandre Tkatchenko and Matthias Scheffler. “Accurate Molecular Van Der Waals Interactions from Ground-State Electron Density and Free-Atom Reference Data”. In: *Phys. Rev. Lett.* 102 (7 Feb. 2009), p. 073005. DOI: [10.1103/PhysRevLett.102.073005](https://doi.org/10.1103/PhysRevLett.102.073005).
- [175] Victor G. Ruiz et al. “Density-Functional Theory with Screened van der Waals Interactions for the Modeling of Hybrid Inorganic-Organic Systems”. In: *Phys. Rev. Lett.* 108 (14 Apr. 2012), p. 146103. DOI: [10.1103/PhysRevLett.108.146103](https://doi.org/10.1103/PhysRevLett.108.146103).
- [176] Lars Goerigk. “Chapter 6 - A Comprehensive Overview of the DFT-D3 London-Dispersion Correction”. In: *Non-Covalent Interactions in Quantum Chemistry and Physics*. Ed. by Alberto Otero de la Roza and Gino A. DiLabio. Elsevier, 2017, pp. 195–219. ISBN: 978-0-12-809835-6. DOI: <https://doi.org/10.1016/B978-0-12-809835-6.00007-4>.
- [177] Karsten Reuter and Matthias Scheffler. “Composition and structure of the RuO₂(110) surface in an O₂ and CO environment: Implications for the catalytic formation of CO₂”. In: *Phys. Rev. B* 68 (4 July 2003), p. 045407. DOI: [10.1103/PhysRevB.68.045407](https://doi.org/10.1103/PhysRevB.68.045407).
- [178] R. Heid et al. “Anomalous lattice dynamics of ruthenium”. In: *Phys. Rev. B* 61 (18 May 2000), pp. 12059–12062. DOI: [10.1103/PhysRevB.61.12059](https://doi.org/10.1103/PhysRevB.61.12059).
- [179] Claudine Noguera. “Polar oxide surfaces”. In: *Journal of Physics: Condensed Matter* 12.31 (July 2000), R367–R410. DOI: [10.1088/0953-8984/12/31/201](https://doi.org/10.1088/0953-8984/12/31/201).
- [180] D. R. Stull, H. Prophet, and United States. *JANAF thermochemical tables [electronic resource] / D.R. Stull and H. Prophet, project directors*. English. 2d ed. U.S. Dept. of Commerce, National Bureau of Standards Washington, D.C, 1971.
- [181] Frédéric Labat et al. “Density functional theory analysis of the structural and electronic properties of TiO₂ rutile and anatase polytypes: Performances of different exchange-correlation functionals”. In: *The Journal of Chemical Physics* 126.15 (2007), p. 154703. DOI: <https://doi.org/10.1063/1.2717168>.
- [182] G. Kresse and J. Furthmüller. “Efficient iterative schemes for ab initio total-energy calculations using a plane-wave basis set”. In: *Phys. Rev. B* 54 (1996), pp. 11169–11186.
- [183] Filippo Balzaretto et al. “Water Reactions on Reconstructed Rutile TiO₂: A Density Functional Theory/Density Functional Tight Binding Approach”. In: *The Journal of Physical Chemistry C* 125.24 (2021), pp. 13234–13246. DOI: [10.1021/acs.jpcc.1c00871](https://doi.org/10.1021/acs.jpcc.1c00871). eprint: <https://doi.org/10.1021/acs.jpcc.1c00871>. URL: <https://doi.org/10.1021/acs.jpcc.1c00871>.
- [184] *List of functionals and coefficients for zero-damping*. <https://www.chemie.uni-bonn.de/pctc/mulliken-center/software/dft-d3/functionals>.

- [185] Grygoriy Dolgonos et al. “An Improved Self-Consistent-Charge Density-Functional Tight-Binding (SCC-DFTB) Set of Parameters for Simulation of Bulk and Molecular Systems Involving Titanium”. In: *Journal of Chemical Theory and Computation* 6.1 (2010), pp. 266–278. DOI: [10.1021/ct900422c](https://doi.org/10.1021/ct900422c).
- [186] P. Souvatzis, O. Eriksson, and M. I. Katsnelson. “Anomalous Thermal Expansion in α -Titanium”. In: *Phys. Rev. Lett.* 99 (1 July 2007), p. 015901. DOI: [10.1103/PhysRevLett.99.015901](https://doi.org/10.1103/PhysRevLett.99.015901).
- [187] V. Wang et al. *VASPKIT: A Pre- and Post-Processing Program for VASP code*. [ArXiv:1908.08269v2](https://arxiv.org/abs/1908.08269v2). 2019.
- [188] Soohaeng Yoo, Xiao Cheng Zeng, and Sotiris S. Xantheas. “On the phase diagram of water with density functional theory potentials: The melting temperature of ice Ih with the Perdew–Burke–Ernzerhof and Becke–Lee–Yang–Parr functionals”. In: *The Journal of Chemical Physics* 130.22 (2009), p. 221102. DOI: [10.1063/1.3153871](https://doi.org/10.1063/1.3153871).
- [189] M. J. Abraham et al. *GROMACS User Manual version 2016.4*. 2017.
- [190] K. Mathew, V. S. Chaitanya Kolluru, and R. G. Hennig. *VASPsol: Implicit solvation and electrolyte model for density-functional theory*. 2018. DOI: [10.5281/zenodo.2555053](https://doi.org/10.5281/zenodo.2555053).
- [191] K. Mathew et al. “Implicit solvation model for density-functional study of nanocrystal surfaces and reaction pathways.” In: *J. Chem. Phys.* 140 (2014), p. 084106. DOI: [10.1063/1.4865107](https://doi.org/10.1063/1.4865107).
- [192] K. Mathew et al. “Implicit self-consistent electrolyte model in plane-wave density-functional theory.” In: *J. Chem. Phys.* 151 (2019), p. 234101. DOI: [10.1063/1.5132354](https://doi.org/10.1063/1.5132354).
- [193] H. Fox et al. “Bulk and Surface Properties of Rutile TiO₂ from Self-Consistent-Charge Density Functional Tight Binding”. In: *Journal of Chemical Theory and Computation* 6.2 (2010), pp. 499–507. DOI: [10.1021/ct900665a](https://doi.org/10.1021/ct900665a).
- [194] Sam De Waele et al. “Error estimates for density-functional theory predictions of surface energy and work function”. In: *Phys. Rev. B* 94 (23 Dec. 2016), p. 235418. DOI: [10.1103/PhysRevB.94.235418](https://doi.org/10.1103/PhysRevB.94.235418).
- [195] Peter Deák et al. “Optimized hybrid functionals for defect calculations in semiconductors”. In: *Journal of Applied Physics* 126.13 (2019), p. 130901. DOI: [10.1063/1.5110643](https://doi.org/10.1063/1.5110643).
- [196] Regina Lushtinetz et al. “Adsorption of Phosphonic Acid at the TiO₂ Anatase (101) and Rutile (110) Surfaces”. In: *Journal of Physical Chemistry C* 113 (Apr. 2009), pp. 5730–5740. DOI: [10.1021/jp8110343](https://doi.org/10.1021/jp8110343).
- [197] Puja Goyal et al. “Molecular Simulation of Water and Hydration Effects in Different Environments: Challenges and Developments for DFTB Based Models”. In: *The Journal of Physical Chemistry B* 118.38 (2014), pp. 11007–11027. DOI: [10.1021/jp503372v](https://doi.org/10.1021/jp503372v).

- [198] Jens Laube et al. “Dependencies of the Adhesion Forces between TiO₂ Nanoparticles on Size and Ambient Humidity”. In: *The Journal of Physical Chemistry C* 121.28 (2017), pp. 15294–15303. DOI: [10.1021/acs.jpcc.7b05655](https://doi.org/10.1021/acs.jpcc.7b05655).
- [199] Ashley N. Shultz et al. “Comparative second harmonic generation and X-ray photoelectron spectroscopy studies of the UV creation and O₂ healing of Ti³⁺ defects on (110) rutile TiO₂ surfaces”. In: *Surface Science* 339.1 (1995), pp. 114–124. ISSN: 0039-6028. DOI: [https://doi.org/10.1016/0039-6028\(95\)00650-8](https://doi.org/10.1016/0039-6028(95)00650-8).
- [200] A. Fujishima, T. N. Rao, and D. A. Tryk. “Titanium dioxide photocatalysis”. In: *Journal of Photochemistry and Photobiology C: Photochemistry Reviews* 1.1 (2000), pp. 1–21. ISSN: 1389-5567. DOI: [https://doi.org/10.1016/S1389-5567\(00\)00002-2](https://doi.org/10.1016/S1389-5567(00)00002-2).
- [201] A. Mills and M. Crow. “A Study of Factors that Change the Wettability of Titania Films”. In: *International Journal of Photoenergy* 2008 (Jan. 2008). DOI: [10.1155/2008/470670](https://doi.org/10.1155/2008/470670).
- [202] Julian Schneider and Lucio Colombi Ciacchi. “A Classical Potential to Model the Adsorption of Biological Molecules on Oxidized Titanium Surfaces”. In: *Journal of Chemical Theory and Computation* 7.2 (2011), pp. 473–484. DOI: [10.1021/ct1004388](https://doi.org/10.1021/ct1004388).
- [203] Maciej Smiechowski. “Molecular hydrogen solvated in water – A computational study”. In: *The Journal of Chemical Physics* 143 (Dec. 2015), p. 244505. DOI: [10.1063/1.4938571](https://doi.org/10.1063/1.4938571).
- [204] Emmerich. Wilhelm, Rubin. Battino, and Robert J. Wilcock. “Low-pressure solubility of gases in liquid water”. In: *Chemical Reviews* 77.2 (1977), pp. 219–262. DOI: [10.1021/cr60306a003](https://doi.org/10.1021/cr60306a003).
- [205] Svea große Holthaus et al. “Atomistic Simulations of the ZnO(1210)/Water Interface: A Comparison between First-Principles, Tight-Binding, and Empirical Methods”. In: *Journal of Chemical Theory and Computation* 8.11 (2012), pp. 4517–4526. DOI: [10.1021/ct3007106](https://doi.org/10.1021/ct3007106).
- [206] N. A. Hildebrand. “Molecular Dynamics Simulations of the Protein Adsorption Process on Oxides”. In: *PhD Thesis* (2017).
- [207] Ludmilla Derr et al. “Physisorption of alpha chymotrypsin on SiO₂ and TiO₂: A comparative study via experiments and molecular dynamics simulations”. In: *Biointerphases* (2016). DOI: <http://dx.doi.org/10.1116/1.4940701>.
- [208] Susan Köppen, Oliver Bronkalla, and Walter Langel. “Adsorption Configurations and Energies of Amino Acids on Anatase and Rutile Surfaces”. In: *Journal of Physical Chemistry C - J PHYS CHEM C* 112 (Aug. 2008). DOI: [10.1021/jp803354z](https://doi.org/10.1021/jp803354z).
- [209] Evren Ataman et al. “Adsorption of L-cysteine on rutile TiO₂(110)”. In: *Surface Science* 605 (Jan. 2011), pp. 179–186. DOI: [10.1016/j.susc.2010.10.017](https://doi.org/10.1016/j.susc.2010.10.017).

- [210] Imali Mudunkotuwa and Vicki Grassian. “Histidine Adsorption on TiO₂ Nanoparticles: An Integrated Spectroscopic, Thermodynamic and Molecular-Based Approach Towards Understanding Nano-Bio Interactions.” In: *Langmuir : the ACS journal of surfaces and colloids* 30 (June 2014). DOI: [10.1021/la500722n](https://doi.org/10.1021/la500722n).
- [211] Sebastian Schwaminger et al. “Experimental characterization and simulation of amino acid and peptide interactions with inorganic materials”. In: *Engineering in Life Sciences* 18 (July 2017). DOI: [10.1002/elsc.201700019](https://doi.org/10.1002/elsc.201700019).
- [212] McQuillan A.J. Roddick-Lanzilotta AD. “An in Situ Infrared Spectroscopic Investigation of Lysine Peptide and Polylysine Adsorption to TiO₂ from Aqueous Solutions.” In: *J Colloid Interface Sci.* 217(1) (1999), pp. 194–202. DOI: <https://doi.org/10.1006/jcis.1999.6367>.
- [213] Shi Tong Han et al. “Photocatalytic decomposition of acephate in irradiated TiO₂ suspensions”. In: *Journal of Hazardous Materials* (2008). DOI: <https://doi.org/10.1016/j.jhazmat.2008.07.077>.
- [214] Jaime Rendon-von Osten and Ricardo Dzul-Caamal. “Glyphosate Residues in Groundwater, Drinking Water and Urine of Subsistence Farmers from Intensive Agriculture Localities: A Survey in Hopelchen, Campeche, Mexico”. In: *International Journal of Environmental Research and Public Health* (2017). DOI: <https://doi.org/10.3390/ijerph14060595>.
- [215] Chen Shifu and Liu Yunzhang. “Study on the photocatalytic degradation of glyphosate by TiO₂ photocatalyst”. In: *Chemosphere* (2006). DOI: <https://doi.org/10.1016/j.chemosphere.2006.10.054>.
- [216] Zhang Zulin et al. “Determination and load of organophosphorus and organochlorine pesticides at water from Jiulong River Estuary, China”. In: *Marine Pollution Bulletin* (2002). DOI: [https://doi.org/10.1016/S0025-326X\(02\)00094-2](https://doi.org/10.1016/S0025-326X(02)00094-2).
- [217] Liu Wei et al. “Titanium dioxide mediated photocatalytic degradation of methamidophos in aqueous phase”. In: *Journal of Hazardous Materials* (2009). DOI: <https://doi.org/10.1016/j.jhazmat.2008.07.140>.
- [218] Aboel-Magd Abdel-Wahab, Al-Sayed Al-Shirbini, and Osama Nasr Omima Mohamed. “Photocatalytic degradation of paracetamol over magnetic flower-like TiO₂/Fe₂O₃ core-shell nanostructures”. In: *Journal of Photochemistry and Photobiology A: Chemistry* (2017). DOI: <https://doi.org/10.1016/j.jphotochem.2017.07.030>.
- [219] K Fent, A Zenker, and M Rapp. “Widespread occurrence of estrogenic UV-filters in aquatic ecosystems in Switzerland”. In: *Environmental Pollution* (2010). DOI: <https://doi.org/10.1016/j.envpol.2009.11.005>.

- [220] Henry Zuniga-Benitez, Carolina Aristizabal-Ciro, and Gustavo A. Pegnuela. "Heterogeneous photocatalytic degradation of the endocrine-disrupting chemical Benzophenone-3: Parameters optimization and by-products identification". In: *Journal of Environmental Management* (2016). DOI: <http://dx.doi.org/10.1016/j.jenvman.2015.11.047>.
- [221] Wei-Po Lai, Hank Hui-Hsiang Lin, and Angela Yu-Chen Lin. "TiO₂ Photocatalytic degradation and transformation of oxazaphosphorine drugs in an aqueous environment". In: *Journal of Hazardous Materials* (2015). DOI: <http://dx.doi.org/10.1016/j.jhazmat.2015.01.045>.
- [222] S Zhao et al. "Temporal Spatial Variation and partitioning Prediction of Antibiotics in Surface Water and Sediments from the Intertidal Zones of the Yellow River Delta". In: *Science of the Total Environment* (2016).
- [223] Murtaza Sayed et al. "Efficient Photocatalytic Degradation of Norfloxacin in Aqueous Media by Hydrothermally Synthesized Immobilized TiO₂ /Ti Films with Exposed 001 Facets". In: *The Journal of Physical Chemistry* (2016). DOI: <http://dx.doi.org/10.1021/acs.jpca.6b09719>.
- [224] Stefanos Giannakis, Sami Rtimi, and Cesar Pulgarin. "Light-Assisted Advanced Oxidation Processes for the Elimination of Chemical and Microbiological Pollution of Wastewaters in Developed and Developing Countries". In: *Molecules* (2017). DOI: <https://doi.org/10.3390/molecules22071070>.
- [225] Daniel Haranaka-Funai et al. "Photocatalytic treatment of valproic acid sodium salt with TiO₂ in different experimental devices: An economic and energetic comparison". In: *Chemical Engineering Journal* (2017). DOI: <http://dx.doi.org/10.1016/j.cej.2017.06.148>.
- [226] Hyun-Seok Son, Gwangpyo Ko, and Kyung-Duk Zoh. "Kinetics and mechanism of photolysis and TiO₂ photocatalysis of triclosan". In: *Journal of Hazardous Materials* (2009). DOI: <http://dx.doi.org/10.1016/j.jhazmat.2008.11.107>.
- [227] *Revenue of the worldwide pharmaceutical market from 2001 to 2020*. <https://www.statista.com/statistics/263102/pharmaceutical-market-worldwide-revenue-since-2001/>.
- [228] N. Muir et al. "Comparative bioavailability of aspirin and paracetamol following single dose administration of soluble and plain tablets". In: *Current Medical Research and Opinion* (1997).
- [229] Karl Fent, Anna Weston, and Daniel Caminada. "Ecotoxicology of Human Pharmaceuticals". In: *Aquatic toxicology (Amsterdam, Netherlands)* 76 (Mar. 2006), pp. 122–59. DOI: [10.1016/j.aquatox.2005.09.009](https://doi.org/10.1016/j.aquatox.2005.09.009).
- [230] J H Zeng et al. "Degradation of pharmaceutical contaminant ibuprofen in aqueous solution by cylindrical wetted wall corona discharge". In: *Chemical Engineering Journal* (2015).
- [231] Faisal Hai et al. "Carbamazepine as a Possible Anthropogenic Marker in Water: Occurrences, Toxicological Effects, Regulations and Removal by Wastewater Treatment Technologies". In: *Water* 10 (Jan. 2018). DOI: [10.3390/w10020107](https://doi.org/10.3390/w10020107).

- [232] W. Slooff. “Integrated criteria document benzene.” In: *Institute of Public Health and Environmental Protection Neatherlands* (1988).
- [233] A Nehlig, JL Daval, and G Debry. “Caffeine and the central nervous system Mechanisms of action, biochemical, metabolic, and psychostimulant effects”. In: *Brain Research Reviews* (1992).
- [234] Robin Mesnage, Charles Benbrook, and Michael Antoniou. “Insight into the confusion over surfactant co-formulants in glyphosate-based herbicides”. In: *Food and Chemical Toxicology* 128 (Apr. 2019). DOI: [10.1016/j.fct.2019.03.053](https://doi.org/10.1016/j.fct.2019.03.053).
- [235] Kamalesh Sen. “5 - A comprehensive review of glyphosate adsorption with factors influencing mechanism: Kinetics, isotherms, thermodynamics study”. In: Nov. 2020, pp. 93–125. ISBN: 978-0-12-819671-7. DOI: [10.1016/B978-0-12-819671-7.00005-1](https://doi.org/10.1016/B978-0-12-819671-7.00005-1).
- [236] Manoj Silva and Jonas Baltrusaitis. “Destruction of emerging organophosphate contaminants in wastewater using the heterogeneous iron-based photo-Fenton-like process”. In: *Journal of Hazardous Materials Letters* 2 (2021), p. 100012. ISSN: 2666-9110. DOI: <https://doi.org/10.1016/j.hazl.2020.100012>.
- [237] *Amber Tools 12 Reference Manual*. English. 537 pp.
- [238] *The PumMa website*. <http://cbio.bmt.tue.nl/pumma/index.php>.
- [239] *The PubChem website*. <https://pubchem.ncbi.nlm.nih.gov/>.
- [240] H. B. Schlegel et al. M. J. Frisch G. W. Trucks. *Gaussian~16 Revision C.01*. 2016.
- [241] Junmei Wang et al. “Development and Testing of a General AMBER Force Field”. In: *Journal of computational chemistry* 25 (July 2004), pp. 1157–74. DOI: [10.1002/jcc.20035](https://doi.org/10.1002/jcc.20035).
- [242] DD Baird. “Introduction of a new broad spectrum post emergence herbicide class with utility for herbaceous perennial weed control”. In: *Proceedings of the 26th North Central Weed Conference (Kansas City, USA, 7-9 December 1971)* (1971).
- [243] H.C. Steinrücken and N. Amrhein. “The herbicide glyphosate is a potent inhibitor of 5-enolpyruvylshikimic acid-3-phosphate synthase”. In: *Biochemical and Biophysical Research Communications* 94.4 (1980), pp. 1207–1212. ISSN: 0006-291X. DOI: [https://doi.org/10.1016/0006-291X\(80\)90547-1](https://doi.org/10.1016/0006-291X(80)90547-1).
- [244] Martin R. Boocock and John R. Coggins. “Kinetics of 5-enolpyruvylshikimate-3-phosphate synthase inhibition by glyphosate”. In: *FEBS Letters* 154.1 (1983), pp. 127–133. ISSN: 0014-5793. DOI: [https://doi.org/10.1016/0014-5793\(83\)80888-6](https://doi.org/10.1016/0014-5793(83)80888-6).
- [245] C C Smart et al. “Selective overproduction of 5-enol-pyruvylshikimic acid 3-phosphate synthase in a plant cell culture which tolerates high doses of the herbicide glyphosate.” In: *Journal of Biological Chemistry* 260.30 (1985), pp. 16338–16346. ISSN: 0021-9258. DOI: [https://doi.org/10.1016/S0021-9258\(17\)36242-7](https://doi.org/10.1016/S0021-9258(17)36242-7).

- [246] C S Gasser et al. “Structure, expression, and evolution of the 5-enolpyruvylshikimate-3-phosphate synthase genes of petunia and tomato.” In: *Journal of Biological Chemistry* 263.9 (1988), pp. 4280–4287. ISSN: 0021-9258. DOI: [https://doi.org/10.1016/S0021-9258\(18\)68922-7](https://doi.org/10.1016/S0021-9258(18)68922-7).
- [247] M Meyer et al. “Transport and degradation of glyphosate in a midwestern tile-drained watershed, Sugar Creek, Indiana.” In: *229th American Chemical Society National Meeting, San Diego CA, US: American Chemical Society*. (2005).
- [248] Harry Vereecken. “Mobility and Leaching of Glyphosate: A Review”. In: *Pest management science* 61 (Dec. 2005), pp. 1139–51. DOI: [10.1002/ps.1122](https://doi.org/10.1002/ps.1122).
- [249] Antonio Cerdeira and Stephen Duke. “Effects of glyphosate-resistant crop cultivation on soil and water quality”. In: *GM crops* 1 (Jan. 2010), pp. 16–24. DOI: [10.4161/gmcr.1.1.9404](https://doi.org/10.4161/gmcr.1.1.9404).
- [250] R.L. Haney, Scott Senseman, and F.M. Hons. “Effect of Roundup Ultra on Microbial Activity and Biomass from Selected Soils”. In: *Journal of Environmental Quality* 31 (May 2002), pp. 730–735. DOI: [10.2134/jeq2002.7300](https://doi.org/10.2134/jeq2002.7300).
- [251] Mara Grube, Uldis Kalnenieks, and Olga Muter. “Metabolic response of bacteria to elevated concentrations of glyphosate-based herbicide”. In: *Ecotoxicology and Environmental Safety* 173 (2019), pp. 373–380. ISSN: 0147-6513. DOI: <https://doi.org/10.1016/j.ecoenv.2019.02.045>.
- [252] Simranjeet Singh et al. “Herbicide Glyphosate: Toxicity and Microbial Degradation”. In: *International Journal of Environmental Research and Public Health* 17 (Nov. 2020). DOI: [10.3390/ijerph17207519](https://doi.org/10.3390/ijerph17207519).
- [253] Jose Tarazona et al. “Glyphosate toxicity and carcinogenicity: a review of the scientific basis of the European Union assessment and its differences with IARC”. In: *Archives of toxicology* 91 (Aug. 2017). DOI: [10.1007/s00204-017-1962-5](https://doi.org/10.1007/s00204-017-1962-5).
- [254] Per Kudsk and Solvejg Kopp Mathiassen. “Pesticide Regulation in the European Union and the Glyphosate Controversy”. In: *Weed Science* 68.3 (2020), pp. 214–222. DOI: [10.1017/wsc.2019.59](https://doi.org/10.1017/wsc.2019.59).
- [255] Jeff Schuette. “Environmental fate of Glyphosate”. In: *Environmental Monitoring Pest Management, Department of Pesticide Regulation, Sacramento* (1998).
- [256] Anderson Catão and Alejandro López-Castillo. “On the Degradation Pathway of Glyphosate and Glycine”. In: *Environmental Science: Processes Impacts* 20 (June 2018). DOI: [10.1039/C8EM00119G](https://doi.org/10.1039/C8EM00119G).
- [257] Stephen O. Duke. “Glyphosate: environmental fate and impact”. In: *Weed Science* 68.3 (2020), pp. 201–207. DOI: [10.1017/wsc.2019.28](https://doi.org/10.1017/wsc.2019.28).
- [258] W. Kollman and R. Segawa. “Interim Report of the Pesticide Chemistry Database”. In: *Department of Pesticide Regulation: Environmental Protection Agency, Sacramento, California* (1995).

- [259] Ying Yang et al. “Comparative study of glyphosate removal on goethite and magnetite: Adsorption and photo-degradation”. In: *Chemical Engineering Journal* 352 (2018), pp. 581–589. ISSN: 1385-8947. DOI: <https://doi.org/10.1016/j.cej.2018.07.058>.
- [260] Zhengfang Zhang et al. “High mineral adsorption of glyphosate versus diethyl phthalate and tetracycline, during visible light photodegradation with goethite and oxalate”. In: *Environmental Chemistry Letters* 17 (Mar. 2019). DOI: [10.1007/s10311-019-00877-x](https://doi.org/10.1007/s10311-019-00877-x).
- [261] Patricia Garcia-Muñoz et al. “Reaction pathways, kinetics and toxicity assessment during the photocatalytic degradation of glyphosate and myclobutanil pesticides: Influence of the aqueous matrix”. In: *Chemical Engineering Journal* 384 (2020), p. 123315. ISSN: 1385-8947. DOI: <https://doi.org/10.1016/j.cej.2019.123315>.
- [262] Melissa S. Caetano et al. “Understanding the inactivation process of organophosphorus herbicides: A DFT study of glyphosate metallic complexes with Zn^{2+} , Ca^{2+} , Mg^{2+} , Cu^{2+} , Co^{3+} , Fe^{3+} , Cr^{3+} , and Al^{3+} ”. In: *International Journal of Quantum Chemistry* 112.15 (2012), pp. 2752–2762. DOI: <https://doi.org/10.1002/qua.23222>. eprint: <https://onlinelibrary.wiley.com/doi/pdf/10.1002/qua.23222>.
- [263] J. Hubbard and Brian Hilton Flowers. “Electron correlations in narrow energy bands”. In: *Proceedings of the Royal Society of London. Series A. Mathematical and Physical Sciences* 276.1365 (1963), pp. 238–257. DOI: [10.1098/rspa.1963.0204](https://doi.org/10.1098/rspa.1963.0204).
- [264] F.H.L. Essler et al. *The One-Dimensional Hubbard Model*. Cambridge University Press. ISBN: 9781139441582.
- [265] E. E. Salpeter and H. A. Bethe. “A Relativistic Equation for Bound-State Problems”. In: *Phys. Rev.* 84 (6 Dec. 1951), pp. 1232–1242. DOI: [10.1103/PhysRev.84.1232](https://doi.org/10.1103/PhysRev.84.1232).
- [266] Maurizia Palummo et al. “The Bethe-Salpeter equation: A first-principles approach for calculating surface optical spectra”. In: *Journal of Physics: Condensed Matter* 16 (Sept. 2004), S4313. DOI: [10.1088/0953-8984/16/39/006](https://doi.org/10.1088/0953-8984/16/39/006).
- [267] Lars Hedin. “New Method for Calculating the One-Particle Green’s Function with Application to the Electron-Gas Problem”. In: *Phys. Rev.* 139 (3A Aug. 1965), A796–A823. DOI: [10.1103/PhysRev.139.A796](https://doi.org/10.1103/PhysRev.139.A796).
- [268] Wilfried G. Aulbur, Lars Jönsson, and John W. Wilkins. “Quasiparticle Calculations in Solids”. In: ed. by Henry Ehrenreich and Frans Spaepen. Vol. 54. *Solid State Physics*. Academic Press, 2000, pp. 1–218. DOI: [https://doi.org/10.1016/S0081-1947\(08\)60248-9](https://doi.org/10.1016/S0081-1947(08)60248-9).
- [269] F Aryasetiawan and O Gunnarsson. “TheGWmethod”. In: *Reports on Progress in Physics* 61.3 (Mar. 1998), pp. 237–312. DOI: [10.1088/0034-4885/61/3/002](https://doi.org/10.1088/0034-4885/61/3/002).

- [270] Miguel Marques et al. *Fundamentals of Time-Dependent Density Functional Theory*. Vol. 837. Jan. 2012. ISBN: 978-3-642-23517-7. DOI: [10.1007/978-3-642-23518-4](https://doi.org/10.1007/978-3-642-23518-4).
- [271] Jeppe Gavnholt et al. “Delta Self-Consistent Field as a method to obtain potential energy surfaces of excited molecules on surfaces”. In: *Physical Review B* 78 (Aug. 2008). DOI: [10.1103/PhysRevB.78.075441](https://doi.org/10.1103/PhysRevB.78.075441).
- [272] R.F.W. Bader. *Atoms in Molecules: A Quantum Theory*. International Ser. of Monogr. on Chem. Clarendon Press. ISBN: 9780198558651.
- [273] Louis J Farrugia. “Topological Analysis of Electron Density”. In: *University of Glasgow* (2007).
- [274] Graeme Henkelman, Andri Arnaldsson, and Hannes Jonsson. “A Fast and Robust Algorithm for Bader Decomposition of Charge Density”. In: *Computational Materials Science - COMPUT MATER SCI* 36 (June 2006), pp. 354–360. DOI: [10.1016/j.commatsci.2005.04.010](https://doi.org/10.1016/j.commatsci.2005.04.010).
- [275] E. Anderson. *LAPACK Users' Guide*. Miscellaneous Bks. Society for Industrial and Applied Mathematics, 1992. ISBN: 9780898712940.
- [276] Gerald Lim H. W., Michael Wortis, and Ranjan Mukhopadhyay. “Stomatocyte–discocyte–echinocyte sequence of the human red blood cell: Evidence for the bilayer–couple hypothesis from membrane mechanics”. In: *Proceedings of the National Academy of Sciences* 99.26 (2002), pp. 16766–16769. ISSN: 0027-8424. DOI: [10.1073/pnas.202617299](https://doi.org/10.1073/pnas.202617299).
- [277] Jia Li et al. “Spectrin-Level Modeling of the Cytoskeleton and Optical Tweezers Stretching of the Erythrocyte”. In: *Biophysical journal* 88 (June 2005), pp. 3707–19. DOI: [10.1529/biophysj.104.047332](https://doi.org/10.1529/biophysj.104.047332).
- [278] Raja Paul et al. “Propagation of Mechanical Stress through the Actin Cytoskeleton toward Focal Adhesions: Model and Experiment”. In: *Biophysical journal* 94 (Mar. 2008), pp. 1470–82. DOI: [10.1529/biophysj.107.108688](https://doi.org/10.1529/biophysj.107.108688).
- [279] Tim Stauch and Andreas Dreuw. “A quantitative quantum-chemical analysis tool for the distribution of mechanical force in molecules”. In: *J. Chem. Phys.* 140 (2014), p. 134107. ISSN: 1089-7690. DOI: [10.1063/1.4870334](https://doi.org/10.1063/1.4870334).
- [280] Tim Stauch and Andreas Dreuw. “On the use of different coordinate systems in mechanochemical force analyses”. In: *J. Chem. Phys.* 143 (2015), p. 074118. DOI: [10.1063/1.4928973](https://doi.org/10.1063/1.4928973).
- [281] Tim Stauch and Andreas Dreuw. “Quantum Chemical Strain Analysis For Mechanochemical Processes”. In: *Acc. Chem. Res.* 50 (2017), pp. 1041–1048. DOI: [10.1021/acs.accounts.7b00038](https://doi.org/10.1021/acs.accounts.7b00038).
- [282] Moumita Majumder and SADASIVAM MANOGARAN. “Redundant internal coordinates, compliance constants and non-bonded interactions - Some new insights”. In: *Journal of Chemical Sciences* 125 (Feb. 2013). DOI: [10.1007/s12039-012-0357-7](https://doi.org/10.1007/s12039-012-0357-7).

- [283] E.B. Wilson, J.C. Decius, and P.C. Cross. *Molecular Vibrations: The Theory of Infrared and Raman Vibrational Spectra*. Dover Books on Chemistry Series. Dover Publications, 1980. ISBN: 9780486639413.
- [284] M.S. Kemp. *An Introduction to Molecular Dynamics*. Physics research and technology. Nova Science Publishers, Incorporated, 2019. ISBN: 9781536160543.
- [285] David Cortés-Ortuño et al. “Thermal stability and topological protection of skyrmions in nanotracks”. In: *Scientific Reports* 7 (June 2017). DOI: [10.1038/s41598-017-03391-8](https://doi.org/10.1038/s41598-017-03391-8).
- [286] Hannes Jonsson. “Improved Tangent Estimate in the Nudged Elastic Band Method for Finding Minimum Energy Paths and Saddle Points”. In: *J. Chem. Phys.* 113 (Dec. 2000), pp. 9978–9985. DOI: [10.1063/1.1323224](https://doi.org/10.1063/1.1323224).
- [287] Blas Uberuaga and Hannes Jonsson. “A Climbing Image Nudged Elastic Band Method for Finding Saddle Points and Minimum Energy Paths”. In: *J. Chem. Phys.* 113 (Dec. 2000), pp. 9901–9904. DOI: [10.1063/1.1329672](https://doi.org/10.1063/1.1329672).
- [288] Daniel Sheppard et al. “A generalized solid-state nudged elastic band method”. In: *The Journal of chemical physics* 136 (Feb. 2012), p. 074103. DOI: [10.1063/1.3684549](https://doi.org/10.1063/1.3684549).
- [289] Graeme Henkelman and Hannes Jónsson. “A dimer method for finding saddle points on high dimensional potential surfaces using only first derivatives”. In: *The Journal of Chemical Physics* 111.15 (1999), pp. 7010–7022. DOI: [10.1063/1.480097](https://doi.org/10.1063/1.480097).
- [290] Penghao Xiao, Daniel Sheppard, and Jutta Rogal. “Solid-state dimer method for calculating solid-solid phase transitions”. In: *The Journal of chemical physics* 140 (May 2014), p. 174104. DOI: [10.1063/1.4873437](https://doi.org/10.1063/1.4873437).
- [291] Erich Runge and E. K. U. Gross. “Density-Functional Theory for Time-Dependent Systems”. In: *Phys. Rev. Lett.* 52 (12 Mar. 1984), pp. 997–1000. DOI: [10.1103/PhysRevLett.52.997](https://doi.org/10.1103/PhysRevLett.52.997).
- [292] Volker Staemmler. “The Cluster Approach for the Adsorption of Small Molecules on Oxide Surfaces”. In: July 2005, pp. 219–256. DOI: [10.1007/b104404](https://doi.org/10.1007/b104404).
- [293] Simone Salustro et al. “Comparison between cluster and supercell approaches: the case of defects in diamond”. In: *Theoretical Chemistry Accounts* 136 (Mar. 2017). DOI: [10.1007/s00214-017-2071-5](https://doi.org/10.1007/s00214-017-2071-5).
- [294] Letizia Chiodo et al. “Structure, electronic, and optical properties of TiO₂ atomic clusters: An ab initio study”. In: *The Journal of chemical physics* 135 (Dec. 2011), p. 244704. DOI: [10.1063/1.3668085](https://doi.org/10.1063/1.3668085).
- [295] Javier Carrasco et al. “Bulk and surface oxygen vacancy formation and diffusion in single crystals, ultrathin films, and metal grown oxide structures”. In: *The Journal of chemical physics* 125 (Sept. 2006), p. 074711. DOI: [10.1063/1.2335842](https://doi.org/10.1063/1.2335842).

- [296] Annalisa D’Ercole et al. “Embedded-Cluster Study of Hydrogen Interaction with an Oxygen Vacancy at the Magnesium Oxide Surface”. In: *The Journal of Physical Chemistry B* 103.19 (1999), pp. 3872–3876. DOI: [10.1021/jp990117d](https://doi.org/10.1021/jp990117d).
- [297] Asbjörn M. Burow et al. “Point defects in CaF₂ and CeO₂ investigated by the periodic electrostatic embedded cluster method”. In: *The Journal of Chemical Physics* 130.17 (2009), p. 174710. DOI: [10.1063/1.3123527](https://doi.org/10.1063/1.3123527).
- [298] C. Pisani et al. “Embedded-cluster and super-cell treatment of charged defects in crystals”. In: *Journal of Electron Spectroscopy and Related Phenomena* 69.1 (1994), pp. 1–12. ISSN: 0368-2048. DOI: [https://doi.org/10.1016/S0368-2048\(14\)80003-0](https://doi.org/10.1016/S0368-2048(14)80003-0).
- [299] Maija M. Kuklja, Frank J. Zerilli, and Peter Sushko. “Embedded Cluster Model: Application to Molecular Crystals”. In: *MRS Proceedings* 800 (2003), AA6.2. DOI: [10.1557/PROC-800-AA6.2](https://doi.org/10.1557/PROC-800-AA6.2).
- [300] T. Goumans et al. “An embedded cluster study of the formation of water on interstellar dust grains”. In: *Physical chemistry chemical physics : PCCP* 11 (Aug. 2009), pp. 5431–6. DOI: [10.1039/b816905e](https://doi.org/10.1039/b816905e).
- [301] Wilke Dononelli and Thorsten Klüner. “Analyzing the local basis set superposition error for CO adsorbed on rutile(110)”. In: *International Journal of Quantum Chemistry* 121.2 (2021), e26428. DOI: <https://doi.org/10.1002/qua.26428>.
- [302] Daniel Berger et al. “Embedded-cluster calculations in a numeric atomic orbital density-functional theory framework”. In: *The Journal of chemical physics* 141.2 (2014), p. 024105. DOI: <https://doi.org/10.1063/1.4885816>.
- [303] Frank Neese et al. “The ORCA quantum chemistry program package”. In: *The Journal of Chemical Physics* 152.22 (2020), p. 224108. DOI: <https://doi.org/10.1063/5.0004608>.
- [304] Michael F Peintinger, Daniel Vilela Oliveira, and Thomas Bredow. “Consistent Gaussian basis sets of triple-zeta valence with polarization quality for solid-state calculations”. In: *Journal of Computational Chemistry* 34.6 (2013), pp. 451–459. DOI: <https://doi.org/10.1002/jcc.23153>.
- [305] Arnim Hellweg et al. “Optimized accurate auxiliary basis sets for RI-MP2 and RI-CC2 calculations for the atoms Rb to Rn”. In: *Theoretical Chemistry Accounts* 117.4 (2007), pp. 587–597. DOI: <https://doi.org/10.1007/s00214-007-0250-5>.
- [306] G Herzberg and A Monfils. “The dissociation energies of the H₂, HD, and D₂ molecules”. In: *Journal of Molecular Spectroscopy* 5.1 (1961), pp. 482–498. ISSN: 0022-2852. DOI: [https://doi.org/10.1016/0022-2852\(61\)90111-4](https://doi.org/10.1016/0022-2852(61)90111-4).
- [307] Tim Stauch and Andreas Dreuw. “Knots “Choke Off” Polymers upon Stretching”. In: *Angew. Chem. Int. Ed.* 55 (2016), pp. 811–814. ISSN: 14337851. DOI: [10.1002/anie.201508706](https://doi.org/10.1002/anie.201508706).

- [308] Friestad H. O. Lund-Høie K. “Photodegradation of the Herbicide Glyphosate in Water”. In: *Bull Environ Contam Toxicol.* 36 (5 1986), pp. 723–729. DOI: [10.1007/BF01623575](https://doi.org/10.1007/BF01623575).
- [309] Deb Jaisi et al. “Mechanisms of Bond Cleavage during Manganese Oxide and UV Degradation of Glyphosate: Results from Phosphate Oxygen Isotopes and Molecular Simulations”. In: *Journal of Agricultural and Food Chemistry* 64 (Oct. 2016), pp. 8474–8482. DOI: [10.1021/acs.jafc.6b02608](https://doi.org/10.1021/acs.jafc.6b02608).
- [310] Peter Deák et al. “Optimized hybrid functionals for defect calculations in semiconductors”. In: *Journal of Applied Physics* 126.13 (2019), p. 130901. DOI: [10.1063/1.5110643](https://doi.org/10.1063/1.5110643).
- [311] Yongfei Ji, Bing Wang, and Yi Luo. “A comparative theoretical study of proton-coupled hole transfer for H₂O and small organic molecules (CH₃OH, HCOOH, H₂CO) on the Anatase TiO₂(101) surface”. In: *The Journal of Physical Chemistry C* 118 (Sept. 2014), pp. 21457–21462. DOI: [10.1021/jp505854t](https://doi.org/10.1021/jp505854t).
- [312] T. Klüner L. Gerhards. “Quantum chemical investigation of photocatalytical sulfoxidation of hydrocarbons on TiO₂”. In: *Under review* (2021).